Nanomaterial-based approaches to the study of membrane signaling

By

Kristina Elizabeth Kitko

Dissertation

Submitted to the Faculty of the

Graduate School of Vanderbilt University

in partial fulfillment of the requirements

for the degree of

DOCTOR OF PHILOSOPHY

in

Interdisciplinary Materials Sciences

December 15, 2018

Nashville, TN

Approved:

Qi Zhang, Ph.D.

Yaxiong Xu, Ph.D.

Sandra J. Rosenthal, Ph.D.

Erin S. Calipari, Ph.D.

D. Greg Walker, Ph.D.

To my mom, for all the years of sacrifice so that I could have this moment.

ACKNOWLEDGEMENTS

I would not be here – nor where I'm headed in the future – without the support of my advisor. Qi, thank you for making what many would consider a risky decision and taking a chance on an engineer with no formal training in biology. Learning and growing as a microscopist were why I started graduate school, and I could not have done so in a better environment. You also introduced me to the world of neuroscience, and through that I have found something that I wake up every day content in the knowledge that the journey ahead will also be my passion in life. To my labmates, thank you for showing me the ropes. I would not have been able to call myself half the biologist that I am without your shared knowledge and wisdom on an almost daily basis. And to Danielle Bailey for being a constant thought partner, cheerleader, proofreader, and partner in my quantum dot journey.

I am grateful to so many whom I have interacted with during my time at Vanderbilt, be it collaborators or through joint meetings or departmental events. Yaxiong Xu, Tu Hong, and several others in the Xu lab have enabled the vast majority of my dissertation research. Anne Kenworthy and Krishan Raganathanun have been invaluable sources of feedback as I learned and generally sought to put my research into the context of membrane biophysics. Sandy Rosenthal and lab have made my quantum dot work possible. To Oleg Kovtun, James McBride, and Louis Thal, thank you for always being sources of much advice and feedback. I would not have been able to navigate the past few years without the constant support of Greg Walker and Sarah Ross and so many others in and around the IMS program. To Joey Barnett, Heidi Hamm, Karen Gieg, and so many others in Vanderbilt pharmacology, thank you for making me feel like I was welcome and for your endless support and feedback of my work.

I am especially grateful to Erin Calipari, who has given me so much more than just space to write in her lab; Erin has been the greatest possible example of the kind of scientist I want to be – thank you for your supportiveness, openness, candor, and wisdom. To the Calipari lab – watching you grow and flourish is a wonderful experience for me on a daily basis. I cannot thank you enough for your welcoming attitudes, advice, and guidance. Gunes, Amy, Lillian, Alberto, Stephanie, Kim, Christy, and others – am I so indebted to all of you.

To my wonderful friends – all of you have made this possible. My science ladies for all of the late night cocktails and early morning coffees, Susan, Kat, Alyssa, Jenny, and so many more: you kept me running and were a constant source of inspiration! To Max for walking in and upending my routine, and for Saturdays of football fun. To Todd, for being as much family as moral support. To Wilson and Dan for all of the conversations, advice, and fun paper links as I close this chapter. Science twitter, I have met so many amazing people this way – excited to keep in touch with all of you. Josh Fessel, you and I will always be in touch, so happy that you are pursuing your dreams. To my amazing family, you weren't really sure what I was doing most of the time, but you were unconditionally supportive. Lastly, to Christopher, I am only writing these words because of your unending patience and love; you inspire me every single day. When I think I can't, you are the voice in my head telling me I can.

TABLE OF CONTENTS

Page

LIST OF TABLES

Table Page

LIST OF FIGURES

Figure Page

LIST OF ABBREVIATONS

AFM, atomic force microscopy
ATP, adenosine triphosphate
BODIPY, boron-dipyrromethene
CI, confidence interval
CNT, carbon nanotube
FRET, Forster resonance energy transfer
FLIM, fluorescence lifetime imaging microscopy
FOV, field of view
FCF, full-collapse fusion
FRF, fast and reversible fusion
G, graphene
GNFs, graphene nanoflakes
GO, graphene oxide
GP, generalized polarization
GPMV, giant plasma membrane vesicle
MβCD, methyl-β-cyclodextrin
ptDNA, Phosphorothioate DNAs
PVP, polyvinylpyrrolidone
Qdot, quantum dot
rGO, reduced graphene oxide
SDS, sodium dodecyl sulfate
TEM, transmission electron microscopy
TFC, TopFluor cholesterol
TFPC, TopFluor phosphocholine
TFSM, TopFluor sphingomyelin

Chapter 1

Graphene-based nanomaterials and the brain

Introduction

The promises of nanomedicine are extensive. Graphene, the first true two-dimensional material to exist in isolation, is the type of new nanomaterial that results in interest for novel biomedical applications. From Michael Chrichton's tragic protagonist in *The Terminal Man* to the recent growth in start-up companies seeking to transfer consciousness, the fictive present and future call to mind visions of devices that enable neural interfacing and control. Although these ideas may create questions as to ethics for neuroscience in the future, the current state-of-the-art for implanted devices is far more limited in scope. Progress in brain-computer interfaces holds great promise for patients following stroke (Ramos-Murguialday, Broetz et al. 2013), to control prosthetic limbs (Hochberg, Serruya et al. 2006, Donoghue, Nurmikko et al. 2007), with the motor degeneration characteristic of Parkinson's disease (Little, Pogosyan et al. 2013), and for a number of other disorders and diseases (Chaudhary, Birbaumer et al. 2016). Graphene may be poised for incorporation into such devices. As the presence of graphene becomes more widespread and commonplace across the biomedical sciences, the relatively larger body of work detailing the biological effects of carbon nanotubes may serve as a template guiding the utility of graphene for biological applications (Kostarelos, Bianco et al. 2009).

Graphene-based materials for interfacing with the peripheral nervous system have been reviewed elsewhere (Domínguez-Bajo, González-Mayorga et al. 2017). We instead focus on new directions for application to the central nervous system. This review is limited to preclinical applications, although graphene and graphene-based devices may someday advance to clinical

implementation. We begin with an overview of graphene manufacturing advances, applications to hybrid materials systems as well as drug delivery strategies. This is followed by an overview of work performed with non-murine models. Finally, the interaction of graphene with murine neural systems, both *in vivo* and *in-vitro* is examined. Despite a sizable body of work, to date there remain many unresolved questions as to cytotoxicity and the mechanisms underlying the graphene-cellular interaction that must be addressed moving forward.

Manufacturing advances

2D graphite was long believed to be relegated to the realm of theoreticians and condensed matter physicists, as the thermodynamic stability of such crystals was believed to be prohibitive for their existence (Geim and Novoselov 2007). 2D graphite – or graphene – was first isolated through mechanical exfoliation (Novoselov, Geim et al. 2004, Novoselov, Jiang et al. 2005). These small sheets provided the ability to study transport in this new class of material (Novoselov, Geim et al. 2004), but the small size of the sheets (< 10 μm) necessitated the development of alternative approaches that would produce graphene in sizes large enough for practical transistor-based applications. Of note, for high quality single and few layer graphene sheets, mechanical exfoliation remains the process of choice for transport measurements to date.

The development of chemical-vapor deposition as a manufacturing strategy (Li, Cai et al. 2009, Reina, Jia et al. 2009) allows the production of graphene with higher areal coverage than was previously possible with exfoliation-based methods. To date, the majority of devices that demonstrate compatibility for *in vivo* imaging use single or multi-layer graphene produced via chemical vapor deposition (Kuzum, Takano et al. 2014, Park, Schendel et al. 2014, Du, Wu et al. 2015, Park, Brodnick et al. 2016, Park, Ness et al. 2017). Indeed, advances in CVD technology

have allowed the production of rectangular graphene sheets with a cross-length as long as 30 inches (Bae, Kim et al. 2010). Although these large size sheets should be of sufficient size for any neural application, the solution transfer process often results in alteration of the properties of the graphene sheet (Suk, Kitt et al. 2011, Suk, Lee et al. 2013). Thus, continued research into scalable transfer of CVD graphene or alternative processes (Pang, Mendes et al. 2017) should help generate more reliably responsive devices. Additionally, ensuring that devices are processed in such a way as to remain relatively sterile is a necessary step to consider for long-term interfacing.

As an alternative to the large-scale growth of graphene, it is now possible to produce large quantities of single-layer and multi-layer graphene through bulk exfoliation (Hernandez, Nicolosi et al. 2008, Li, Müller et al. 2008, Lotya, Hernandez et al. 2009, Shih, Vijayaraghavan et al. 2011, Paton, Varrla et al. 2014). Graphite in a colloidal suspension can be sonicated to yield thin flakes (G), ranging from single to a few layers. A variety of solvents are compatible with this approach – and more recently it has been demonstrated that G and graphene oxide (GO) can be exfoliated directly into biological media (Castagnola, Zhao et al. 2018). GO flakes produced by this method are more largely monolayer than G flakes, however oxidization comes with costs, for example, reduced carrier mobility. Flakes of graphene produced by exfoliation, while not matching the transport properties of micromechanical isolation, can be considered graphene, as no chemical functionalization is required. Thus, G flakes may prove advantageous for applications where the electronic properties of graphene are not of primary importance but where large quantities of G are desirable.

Graphene oxide

The ease with which GO can be chemically modified remains of interest for drug delivery and bio-scaffolding applications. A number of different processes have been developed to produce bulk quantities of GO flakes (Brodie 1860, Hummers and Offeman 1958), although GO is traditionally produced through the reduction of bulk graphite in the presence of both acids and oxidants (Park and Ruoff 2009). Reduction of GO yields graphene-like sheets (rGO) which improve electrical conductivity, (Stankovich, Dikin et al. 2007), but the electronic properties of rGO still lag far behind those of pure graphene, even with the numerous efforts that have been made via modifying annealing processes to improve the figures of merit. The inherently lower electrical conductivity and inability to greatly increase it has resulted in less interest to date in the use of GO as an electrode material. Indeed, even chemical reduction of GO to rGO yields room temperature conductivity values 3 orders of magnitude below that measured for pristine G (Gómez-Navarro, Weitz et al. 2007). Mobility values for GO produced via the Hummers method are ~850 $cm^2/(V\ s)$, but other methods report a device mobility of around ~1-10 $cm^2/(V\ s)$ (Eda, Fanchini et al. 2008, Wang, Chia et al. 2008, Su, Xu et al. 2009). Importantly, future device design may take into account contact resistance in production, as use of all-carbon transistors improves both electron and hole mobility relative to using gold electrodes (Wang, Ang et al. 2010), which may prove a more practical approach to improving device performance. Further attempts to reduce GO to graphene-like sheets via chemical (Li, Wang et al. 2009, Moon, Lee et al. 2010) or thermal (Becerril, Mao et al. 2008, Jung, Field et al. 2009, Barroso-Bujans, Alegría et al. 2010) processing have improved the fraction of graphitic areas in the structure, but also introduced nanoscale holes and defects that deleteriously affect final performance. rGO's improved device characteristics also come at the cost of a reduction in hydrophilicity (Rourke, Pandey et al. 2011), and surface properties remain an important consideration for bio-interfacing applications. It was recently

demonstrated that solution-exfoliated GO flakes could be processed to recover properties more resembling those of CVD-graphene. Reduction of the concentration of in-plane oxygen via 1-2 s microwave pulses produced 2D and G peaks closer to those of graphene and greatly increased electron and hole carrier mobility to ~1000 $cm^2/(V\ s)$ in a FET (Voiry, Yang et al. 2016). Thus, the ability to modify in-plane oxygen concentration to improve electronic properties may open new doors to the use of GO and GO-based materials for sensor applications.

Similar to applications for the photoluminescence of CNTs (Welsher, Liu et al. 2008), the photoluminescence of GO may be useful in for optical readout and/or in combination with drug delivery. The photoluminescence of GO, which arises from bond disorder throughout the structure, which induces energy gaps (Cao, Meziani et al. 2013), is to some extent a tunable property, depending on the oxidization state (Luo, Vora et al. 2009). This stands in contrast to the lack of photoluminescent emission observed for defect-free G. GO luminescence is broadband in as-prepared samples, with a wide peak across the visible spectrum (Luo, Vora et al. 2009, Qian, Wang et al. 2012). PEGylated GO sheets exhibit intrinsic near infrared red (NIR) photoluminescence (Sun, Liu et al. 2008), a property of great interest for *in vivo* imaging applications due to the enhanced light penetration in this wavelength range. It has been more recently demonstrated that GO also exhibits photoluminescence under both 2-photon and 3-photon excitation (Qian, Wang et al. 2012), in addition to the broad photoluminescence in the visible range. By exploiting the ability of GO to undergo a 2-photon process, Qian et al. imaged PEGylated-GO nanoparticles in a skull-removed whole brain to a depth of 300 μm. Growth in the commercial availability of three-photon sources may lead to studies at even greater depths within the intact rodent brain. As new advances in genetic engineering and microscopy enable deeper and faster cellular resolution imaging in head fixed or freely moving specimens, it is likely GO/G-based imaging will also move toward

applications compatible with this type of experiment. Although the broadband nature of the emission from GO may be somewhat of a limiting factor for multiplexing multiphoton imaging processes, advances in hyperspectral detection and fast fluorescence lifetime detection may help to make GO of greater utility for *in vivo* brain imaging.

Graphene/polymer composite materials & applications

Polymer electronics remain of great interest to ultimately offer an alternative to traditional materials to minimize mechanical mismatch between cells/tissue and the recording probe (for a more in-depth discussion see (Rivnay, Wang et al. 2017)). Elastic modulus mismatch between brain tissue and recording device leads to increased tissue damage both upon insertion and during chronic interface (Polikov, Tresco et al. 2005), as the elastic moduli of brain tissue (~150 kPa) and an implanted electrode (~150 GPa for silicon) differ by six orders of magnitude. Thus, much current research has focused on the ability to better match the modulus of electrodes to that of brain tissue (for a more in-depth review on interfacing tissue with electrodes see Fattahi et al. (Fattahi, Yang et al. 2014)). Graphene electrodes have been of interest for such designs, as it can be incorporated into flexible electronics (Fiori, Bonaccorso et al. 2014); and for applications in the brain, where techniques like optogenetics and calcium imaging require optical access to brain regions of interest, the large degree of optical transparency of single or few-layer G may be uniquely advantageous.

PEDOT

Poly(3,4-ethylene dioxythiophene)(PEDOT) is an electroconductive polymer produced from 3,4-ethylene dioxythiophene (EDOT) monomers. Polymerization results in a positively-

charged backbone, whereby negatively charged materials can then be incorporated to balance charge. Neurons embedded in PEDOT matrices remain viable for around 1 week (Richardson-Burns, Hendricks et al. 2007) and neurons grown on PEDOT-based substrates show unaltered electrophysiological characteristics (membrane potential, membrane capacitance, input resistance) after 21 DIV (Cellot, Lagonegro et al. 2015). Although the surface charge of graphene limits its utility in PEDOT-based composites without further surface modification, the negative surface charge of graphene oxide may be better adaptable to such composites. PEDOT/GO composites have been used as electrode coatings to improve sensitivity and decrease the lower detection limit of dopamine in fast-scan cyclic voltammetry (Taylor, Robbins et al. 2017), a widely-used technique for measuring dopamine release in rodents *in vivo* (Robinson, Venton et al. 2003). Carbon nanotube-PEDOT composites have also been demonstrated to perform well in interfacing applications (Jan, Hendricks et al. 2009, Luo, Weaver et al. 2011). PEDOT-coated microelectrode arrays show good performance characteristics and lowered impedance relative to iridium oxide (IrOx), suggesting potential for long-term neural interfacing applications (Wilks, Richardson-Burns et al. 2009). As both GO and CNT incorporation into PEDOT-based composites has improved overall performance, future work may seek to fabricate composite polymer electrodes.

Chitosan

Chitosan composites have been demonstrated both for GO (Yang, Tu et al. 2010, Bao, Pan et al. 2011) and for rGO (Fang, Long et al. 2010). It can be produced in relatively abundant quantities from the deacetylation of chitin. Like with many polymers, applications may be limited by the low mechanical strength of the material. GO as a nanofiller is one route to achieve enhanced mechanical properties. Chitosan-GO nanocomposites can be assembled in a manner of ways. pH-

responsive functionality is possible with chitosan (Yi, Wu et al. 2005); increased pH leads to amine deprotonation, decharging of the polymer, and ultimately insolubility. Interestingly, preparations of such suspensions seem to be greatly affected by the preparation method: addition of GO to chitosan yields a uniform suspension while addition of chitosan to GO yields agglomerations (Fang, Long et al. 2010). This is due to the way that excess GO will create bridges between sheets via multiple attachment points on the polymer chains. Reducing GO allows chitosan attachment by zwitterionic interactions and hydrogen bonding between the remaining oxygen groups of the rGO and the amino and hydroxyl groups of chitosan. The reversibility of the molecular chain interactions with GO sheets between different pH values may provide an opportunity to modulate graphene-based composite materials within different cellular compartments. This could potentially allow for pH-based assembly strategies in acidic intracellular compartments (e.g. late endosomes, lysosomes), where chitosan would stabilize GO composites relative to higher pH extracellular spaces.

Hydrogels

The use of graphene for regenerative approaches has been reviewed previously (Ding, Liu et al. 2015), however the pace of new methodologies in neuroscience has opened new directions for scaffolding technologies, with a particular resurgence in hydrogel-based techniques for connectomics applications (Chung, Wallace et al. 2013, Chen, Tillberg et al. 2015). G/GO and other nanomaterials may be of interest for cleared or expanded tissue applications where added structural stability is desirable. Composite scaffolds for regenerative medicine remain and area of great interest. Hydrogels can be chemically tuned to impart different surface properties, for example to modify surface charge or conductivity, before functionalization to GO (Liu, Miller et

al. 2017). Biomolecules such as DNA can also be incorporated via stacking interactions (Xu, Wu et al. 2010), enabling payload delivery within the hydrogel matrix. This is one possible route to achieve more biologically realistic synthetic minimal brain circuits, which to date have largely been limited in structure to two-dimensional culture systems or proteins or liposomes (Adamala, Martin-Alarcon et al. 2016). Overall mechanical strength can be tailored by the degree to which G/GO are incorporated, with mechanical strength being inversely correlated to the amount of swelling in the composite.

Local delivery of polymerized materials may someday be a route to a new form of tissue scaffolding *in vivo*. In such applications, graphene and graphene-based materials may play a multifunctional role, both as structural support and as part of a stimulation or recording device.

Graphene in 'stretchable' electronics applications

Advances in both computational and analytical models have recently begun to enable the fabrication of nanoscale semiconductor materials that will tolerate relatively large amounts of strain (Su, Ping et al. 2017, Yu, Yan et al. 2017), advances in the manufacturing of graphene may allow similar structures to be produced (Wang, Boutilier et al. 2017). Although measurements of second-order stiffness in graphene have yielded in-plane stiffness values of ~340 N/m (Lee, Wei et al. 2008), crumpling from static wrinkling in free-standing graphene at biologically relevant temperatures effectively reduces this value (Nicholl, Conley et al. 2015). p-type doping of graphene may be one way forward for flexible graphene electrodes, as it decreases sheet resistance and increases the effective work function (Han, Kwon et al. 2016). Multilayer-based approaches using graphene may also improve stretchability performance through strain relaxation (Won, Hwangbo et al. 2014). In fact, the addition of graphene 'nanoscrolls' between layers in transparent

transistors showed improved performance under strain relative to monolayer graphene (Liu, Chortos et al. 2017).

Drug delivery applications and conjugation strategies

Chemical modifications for drug delivery applications

G/GO have been most widely demonstrated for cancer-related drug delivery applications (Liu, Robinson et al. 2011, Liu, Zhao et al. 2017), however, the chemical and surface modifications used to enable loading and release may also be used to enable new applications in the brain. The ability to harness hydrophobic interactions and pi-pi stacking to deliver aromatic, hydrophobic compounds may extend the utility of graphene for brain-specific drug delivery beyond simply proof-of-concept. For example, polyethylene glycol modification (PEGylation) of GO results in excellent solution stability (Liu, Robinson et al. 2008). Alternative strategies also include PAMAM functionalization of both GO (Gu, Guo et al. 2017) and G (Quintana, Montellano et al. 2011) and hyperbranched polyglycerol (hPG) (Tu, Wycisk et al. 2017). Amide linkage between GO and chitosan yields sheets that are relatively stable in cell culture media for up to 48 h (Bao, Pan et al. 2011), an example of a myriad of alternative approaches to stabilize G/GO in aqueous solution. Dextran can also be used to increase the hydrophilicity of GO via amine modification and EDC coupling chemistry (Zhang, Yang et al. 2011). GO functionalized with cyclodextrin molecules, again via pi-pi adsorption, reduced to G sheets in an ammonia solution also serves as an effective peptide carrier (Dong, Li et al. 2013). Thus, the versatility of pi-pi adsorption onto G/GO surfaces allows for a wide scope of possible molecular delivery types.

Chemical reaction methods can also be selected to control the location of functional groups onto G sheets. 1,3-dipolar cycloaddition results in conjugation within the large central area of the

sheets, whereas amide concentration reactions concentrate conjugates to the edges of G sheets (Quintana, Montellano et al. 2011). Azide modified dopamine has been used for simultaneous capping and reduction of GO (Kaminska, Das et al. 2012), where the aromatic structure of the dopamine molecule likely interacts via pi-stacking on the surface. As many monoamines contain contain aromatic groups, molecules such as serotonin, cathecholamine, and epinephrine may find utility as stabilizers for GO while also acting to alter neural function.

Although click chemistry opens new doors to functionalization strategies for G/GO, approaches that utilize a copper catalyst elicit concern regarding toxicity to living tissue (Baskin, Prescher et al. 2007).

Interestingly, the overall surface charge of a GO sheet was shown to play a role in the effectiveness of intracellular drug delivery. Positively-charged aminolated surfaces were shown to be more effective at releasing DOX in intracellular compartments than negatively charged sulfonated surfaces (Tu, Wycisk et al. 2017). Given the relative ease of modifying the surface charge of GO, this may be a new avenue to site-specific intracellular drug release. The different surface characteristics across a graphene sheet may also be a useful strategy for orthogonal delivery of different classes of compound: the negatively charged surface regions may better adsorb positively charged molecules while the outer edges, decorated with carboxyl groups, can for example be modified with zwitterionic lipid vesicles (Wang, Liu et al. 2013).

Payload delivery

The delivery of various forms of genetic payload has been demonstrated as a possible application for G/GO-based materials, however, to date, low transduction efficiencies limit the utility of graphene in comparison to traditional methods for genetic delivery. For example,

chitosan-stabilized GO sheets had a lower transfection efficiency for luciferase transduction into HeLa cells (Bao, Pan et al. 2011) compared to traditional methods. Polymer-based assemblies are some of the most widely used nanomaterial strategies for transduction, and relative to polymer-based approaches, GO used to attach plasmid DNA and PEI shows improved transfection efficiency (Feng, Zhang et al. 2011). Graphene can also bind ssDNA, although cannot bind dsDNA to the same extent. This property has been exploited to deliver hairpin-shaped DNA into cells, which will be unloaded upon interaction with an mRNA target (Lu, Zhu et al. 2010). GO has also been employed as a delivery vehicle for aptamers, delivering an ATP binding aptamer (Wang, Li et al. 2010) to cells. G/GO may ultimately be most advantageous for applications where simultaneous delivery of both genetic payloads and pharmacological compounds is desirable. For example Polyamidoamine (PAMAM) functionalized GO was demonstrated as a vehicle for both Doxorubicin (DOX) and shRNA (Gu, Guo et al. 2017) delivery.

Photothermal therapy

Reduced graphene oxide (rGO) has been exploited for its photothermal properties for drug delivery. Chitosan/rGO composites were shown to deliver drug payloads on a timescale of minutes; addition of rGO to Chitosan acts to increase the photothermal absorption of the composite with respect to chitosan alone (Matteini, Tatini et al. 2014). Here, DOX delivery to HeLa cells was increased with short-pulse laser illumination. DOX has also been loaded onto GO for photothermal delivery in a glioma-bearing rat model (Liu, Shen et al. 2013, Dong, Jin et al. 2016). Laser irradiation results in local surface heating, ultimately leading to drug release. DOX release was also demonstrated to be effective on gliomas when loaded on PEGylated silica-coated G sheets (Wang, Wang et al. 2013). Carboxy-modified GO covalently linked to Thioflavin S selectively

attaches to amyloid-B fibrils (Li, Yang et al. 2012), suggesting an avenue toward the photothermal dissociation of AB fibrils and demonstrating the potential of G/GO-based materials for therapeutic application to Alzheimer's disease. Hydrazine reduction of GO at elevated temperatures increases NIR absorbance by > 6-fold relative to unreduced GO (Robinson, Tabakman et al. 2011), a function of the restoration of PI conjugation. In the most widely used state, largely due to the relative ease of production and low cost, graphene flakes exist as a semimetal with zero bandgap. More recently, the discovery that a 'nanomesh' structure can open up a bandgap in graphene (Akhavan 2010, Bai, Zhong et al. 2010) can be used to tune photothermal absorption properties. PEGylated rGO nanomesh suspension showed a much steeper temperature increase over time for NIR irradiation heating than PEGylated rGO (Akhavan and Ghaderi 2013). Although CNTs have been more widely used for photothermal therapy to date, the superior response of G (Markovic, Harhaji-Trajkovic et al. 2011) may lead to increased focus in this direction.

Laser irradiation with NIR light enables a relatively high degree of spatial precision. However, for *in vivo* applications, the ability to control release will ultimately be limited by the ability to deliver light within the brain. As such, NIR will be a useful tool for fundamental studies, as differential effects between even superficial subregions within the brain are still not well understood. Alternative triggering methods may be better suited to studies where pharmaceutical effects are elicited in deep brain regions. Electrical, magnetic, or even acoustic-based triggered release would allow such control in deeper brain regions. Layer-by-layer assembly approaches utilize protein adsorption onto substrates and subsequent capping with modified GO in either a sheet (Hong, Shah et al. 2012) or a capsule (Kurapati and Raichur 2012) format. Additional layers can be stacked together to control overall release time (Hong, Shah et al. 2012). Passive release may be sufficient for the delivery of certain drug classes, but active release allows more precise

control of treatment dose received. PAE (Choi, Kim et al. 2015) or PPy (Weaver, LaRosa et al. 2014) films can incorporate GO, resulting in a more conductive polymer matrix, whereby electrical stimulation is applied and elicits drug release. Modification of the number of GO layers and the overall areal size of the GO sheets also alters the total drug loading capability (Weaver, LaRosa et al. 2014); smaller and fewer layered sheets have increased surface area for adsorption relative to more multilayered stacks. Photothermal irradiation has also been utilized to target delivery to cytosolic locations. Although G/GO sheets can insert into membranes directly, small sized and few-layered sheets will also be taken up into the cell through endocytic processes. Ultimately these sheets will then be trafficked to endosomal compartments. rGO sheets have been used to help payload escape this fate by application of NIR irradiation to induce endosomal disruption (Kim, Lee et al. 2013).

Magnetic applications

The ability to modify the properties of G/GO, to confer magnetic sensitivity for example, will extend the utility of its applications. The presence of fluorine in the GO basal plane can induce paragmagnetic centers, making fluorinated-GO compatible with MRI applications (Romero-Aburto, Narayanan et al. 2013). Magnetic nanoparticles such as iron oxide (Fe_3O_4) can also be loaded on the surface of GO, conferring sufficient contrast enhancement to enable MRI (Yang, Hua et al. 2013). This does not disrupt the ability of G/GO to act as a drug delivery vehicle, further extending its utility.

Beyond the murine model: the use of graphene in other model systems in neuroscience

To date, most current understanding of the uses for and effects of graphene result from studies in murine models. Many of these studies are based on *in vitro* culture systems using neurons; future directions should include mechanistic characterization of the biological effects of G/GO *in vivo*. The large array of transgenic modifications possible in mice and increasingly rats have enabled the study of ever more complex behaviors in a cell-type specific manner. These new techniques have resulted in a concurrent rise in the number of studies using other model systems, which have provided fundamental insights into the function of molecules, cells, circuits, and brain regions. *Drosophila Melanogaster*, for example, is a widely used system for the study of synapses and synaptic proteins (Keshishian, Broadie et al. 1996). And historically, the sea slug *Aplysia* provided some of the earliest causal insight into the mechanisms of plasticity in the brain (Kandel 2009). We here provide a general introduction to model systems where G/GO have been used to date.

C. Elegans

The worm *C. Elegans* is a soil nematode with 302 neurons in its nervous system, whose connectome, a map of all neural connections, has been characterized (Varshney, Chen et al. 2011, Jarrell, Wang et al. 2012), leading to ongoing efforts to develop causal rules governing structure and function relationships during behavior. It lacks a blood-brain barrier, enabling screening of molecules by delivery routes not available to traditional murine models. Although graphene-based device interfaces have yet to be demonstrated in *C. Elegans*, Li et al. have demonstrated that chronic exposure to graphene elicits toxicity effects that are dosage-dependent, cell-type specific, and dependent upon the type of graphene (Li, Xu et al. 2017). Nematodes typically have a lifetime of ~ 2 weeks, and underwent a 6 day chronic exposure that resulted in graphene being distributed

throughout the digestive system. 100 mg/l graphene flakes did not significantly alter overall survival rate after 6 days, but the same concentration of GO flakes was largely lethal. Interestingly, >10 mg/l GO nanoparticles were shown to decrease expression levels of *dat-1* and *eat-4p*, fluorescent genes encoding dopaminergic and glutamatergic neurons respectively, without significant downregulation of *unc-47*, which encodes GABAergic neurons. This is in contrast to the behavior of graphite nanoplatelets, where no acute *in vivo* toxicity was observed at concentrations up to 250 mg/l (Zanni, De Bellis et al. 2012). This could be due in part to differences in surface energy between GO and graphite nanoplatelets, for example hydrophilic vs. hydrophobic wettability properties, but further investigation is warranted with more standardized concentrations between materials. As computational models and subsequent experiments have suggested that similar concentrations of graphene flakes should be destructive to the membrane, regardless of cell type (Luan, Zhou et al. 2017), it would thus be helpful for future studies interested in assessing toxicity to take into account the concentrations used in previous studies for better cross-comparison.

Zebrafish

Zebrafish represent another interesting possibility for demonstrating the utility of graphene interfaces. A developed zebrafish has ~100,000 neurons, fewer than any murine model, while still preserving many basic electrical and chemical signaling processes. This, combined with optical transparency, confers many advantages for single-cell resolution studies involving a whole population of neurons rather than the subsets that are optically accessible by even the most recent imaging approaches, for example light field microscopy in freely moving rodents (Skocek, Nöbauer et al. 2018). The availability of detailed genomic information and the relatively high

degree of homology to the human genome (~70%)(Howe, Clark et al. 2013) confer distinct advantages to their use as a model system. The relative ease of breeding and maintaining zebrafish and their short lifespan are also advantageous relative to rodents or non-human primates for reducing cost in larger scale toxicology screens (Fako and Furgeson 2009). Although a concentration of > 120 mg/L SWNT was shown to delay hatching in zebrafish (Cheng, Flahaut et al. 2007), primary sensory neurons were not developmentally effected. Further studies using GO/G to assess toxicology in zebrafish are necessary for comparison to the effects observed using SWNTs.

Future directions

The use of graphene has largely been limited in non-human primate models, due in part to lingering questions as to toxicity. However, organizations such as the European Graphene flagship have issued calls for the production of graphene electrode arrays for recording in both non-human primates and humans. This will necessitate further study of the biological effects of G and G-based devices. As new strategies are developed to handle and integrate the vast and wide-ranging data streams becoming more prevalent in modern neuroscience, non-traditional model systems will continue to play a role in helping to elucidate the brain. Thus, future research on the compatibility of graphene with other model organisms will help to clarify the utility of graphene to these systems.

Toxicity in murine systems

The extent to which G/GO become practically applicable to neuroscience will in part be determined following a systematic understanding of the long-term toxicity. As many paths toward clinical application begin with pre-clinical testing in murine models, understanding the biological

tolerance of rats and mice to G/GO represents an important first step. Here, we focus on toxicity specifically relevant to neuronal and brainwide function, for discussion of overall, environmental, or antimicrobial toxicity, which have been widely reviewed, see elsewhere (Seabra, Paula et al. 2014).

Various studies have also focused on the interaction between graphene and the cell membrane in either *in vitro* culture systems (Kitko, Hong et al. 2018) or lipid bilayer preparations. Using a 2-dimensional Langmuir-Blodgett approach, it has been suggested that the hydrophobic tail of lipids does not play a role in any bilayer interactions, but a positively charged head group would favor interactions with the carboxy-containing regions of GO (Li, Stein et al. 2013) and minimal interactions would occur between neutrally or negatively charged lipids. The size of the G/GO flakes is also a determining factor in the bilayer response. Flakes of GO that are large relative to the size of an artificial liposome cause rupture of the bilayer attached to a substrate surface (Frost, Jönsson et al. 2012). Addition of GO to supported lipid bilayers (SLBs) composed of DPPC/DOPC causes detachment of bilayer regions (Lei, Zhou et al. 2014), but as this was a function of relatively high levels of calcium used in SLB preparation, may not be viewed as representative of *in vivo* membrane damage.

Results based on computational modeling generally agree that once inside of a lipid bilayer, either via endocytic uptake or by direct membrane penetration, graphene will stably reside between phospholipid tails (Titov, Král et al. 2010, Guo, Mao et al. 2013). It is generally agreed that membrane penetration would favor an ‘edge-in’ rather than a ‘face-in’ initial contact.

Although computational models are powerful tools to provide fundamental insights into the forces governing G/GO nanomaterial and cellular interactions, these studies are often performed under different conditions than most application studies. For example, it is

computationally prohibitive to model G/GO flakes on the same size scales that are produced for experimental studies. A 'large G/GO flake' in a computational study may be on the length scale of 5 nm (Li, Yuan et al. 2013) – whereas for experimental studies the smallest reported average dimensions are on a length scale of >200 nm (Rauti, Lozano et al. 2016, Castagnola, Zhao et al. 2018). It if furthermore prohibitive to model the membrane bilayer with the full complexity of proteins, lipids, and other molecules within a neuronal bilayer. Thus, it may be difficult to draw direct parallels between toxicity claims from simulations and toxicity claims from experimental results. Study of lipid-membrane specific effects is more efficiently enabled by allowing graphene to penetrate a membrane after addition to biological media. However, many studies, even using small flakes of G/GO, deposit the material onto a glass substrate for chronic cellular interface. The membrane interactions here would be very different from G/GO located within the bilayer, further complicating arguments as to the membrane effects of G/GO.

GO was demonstrated to be toxic to gram-negative bacteria (Akhavan and Ghaderi 2010, Tu, Lv et al. 2013), yet bacteria containing more complex outer membranes are more resistant to damage. Reduction of GO increases susceptibility to membrane damage (Akhavan and Ghaderi 2010). Akhavan et al. created nanowalls of GO, which were designed such that there would be a maximal amount of direct contact between bacteria and the sharp edges of the nanomaterial. This represents a condition that would induce mechanical stress on the membrane, and indeed can result in membrane damage. Tu et al. later extended this work both through molecular dynamics simulations and experiments using *E. Coli*. Course-grained molecular dynamic simulations of relatively large few-layer graphene (FLG) sheets suggest that the most hydrophobic edge of graphene near a lipid bilayer will penetrate orthogonal to a bilayer, and then fully embed in a membrane, driven by an attraction between the graphene and lipids within the core (Li, Yuan et

al. 2013). Interestingly, this spontaneous process does not result in membrane destruction, suggesting that the degree of mechanical stress on the membrane plays a role in membrane damage when exposed to G/GO. That spontaneous membrane incorporation does cause membrane destruction is in agreement with experimental observations using cultured PC-12 cells, where 24 h exposure to few-layer G sheets did not increase lactate dehydrogenase activity or increase reactive oxygen species below 100 μg/ml treatment concentrations (Zhang, Ali et al. 2010).

Of note, these configurations, where membrane stress is likely a factor in the toxicity of G/GO, are different than most studies to date using neuronal cultures, where G/GO is more commonly used as a culture substrate. Three different mammalian cell types cultured on rGO, but not GO, for up to 5 days proliferated normally and exhibited less cytotoxicity and more outgrowth than on CNT films (Agarwal, Zhou et al. 2010). HT-29 cells also displayed increased attachment on GO-coated substrates within 6 hours compared to bare glass substrates (Ruiz, Fernando et al. 2011). Thus, studies aimed at addressing nanotoxicity should draw a distinction between scenarios where mechanical stress may be an additional factor and scenarios where spontaneous membrane incorporation alone is being studied.

The role of the biological protein corona in mediating the toxicity of G/GO

Simulations also suggest that the hydrophobicity of G/GO plays a role in its interaction with the bilayer and that the surface energy can be modified by the formation of a protein corona on the surface. For example, computational models demonstrate that the presence of a protein corona surrounding the flakes would modify the membrane response to graphene, in which case graphene would orient in parallel to and attach to the outer layer of the lipid bilayer (Li, Yuan et al. 2013). Experimental studies of protein adsorption on G/GO alone have shown that nanoflakes

can adsorb 1.6-2x their weight in BSA, largely on the timescale of minutes (Hu, Peng et al. 2011, Chong, Ge et al. 2015). A recent development, where G is exfoliated directly into a serum containing media, has given some insight into the composition of the biological corona formed. Proteomic analysis of these media-exfoliated G flakes reveals a variety of proteins and other cellular materials that make up the protein corona formed on G (Castagnola, Zhao et al. 2018): serum albumin, apolipoproteins, and vitronectin are all found on G nanoflakes in relative large abundances. Although the physicochemical interactions, kinetics, and thermodynamic processes that govern the formation and evolution of the corona that forms around nanomaterial surfaces when interfaced with a biological system is still not fully understood, general frameworks have been established as to the governing forces underlying nano-bio interactions. Because the individual environment G/GO encounter will vary widely depending upon desired neural application, the exact composition of the corona formed cannot necessarily be described *a priori* or results extended from one biological system to the next. Indeed, the chemical concentration, surface functionalization, degree of crystallinity, and surface roughness, among many properties, all play a role in the composition and evolution of biomaterials that adsorb on a nanomaterial surface (Nel, Mädler et al. 2009).

The formation of a protein corona on G/GO surfaces also differs between bacterial cultures and what would be observed in murine models *in vivo* due to differences between media compositions in cell culture or fluid composition in the extracellular space. Previous studies demonstrating membrane destruction in bacteria have suspended G flakes with *E.Coli* (Tu, Lv et al. 2013) or suspended in agar/water and dropped onto a substrate surface and later recovered (Akhavan and Ghaderi 2010). However, the presence of a protein corona (Cedervall, Lynch et al. 2007) likely plays a role in mitigating these effects. Using A549 cells, multiple reports have

demonstrated that the presence of FBS in normal culture media (Hu, Peng et al. 2011, Duan, Kang et al. 2015) or the addition of BSA (Li, Feng et al. 2014, Duan, Kang et al. 2015) result in lower cytotoxicity of GO flakes relative to serum-free media. Using a DPPC membrane, molecular dynamics simulations revealed that BSA-coating of graphene reduces the total amount of lipid removal relative to bare graphene. The coating of graphene by proteins is governed by hydrophobic interactions, van der Waals forces, and π- π interactions (Chong, Ge et al. 2015). The composition of the protein corona may vary depending upon method of introduction to the brain and the presence of any surface modifications to increase biocompatibility; this may also serve to explain the variation in effects seemingly exerted by graphene (Radic, Geitner et al. 2013). As the adsorption of proteins to GO is strong and long-lasting, this may serve as one route for the low-cost modification of GO for drug delivery application or to achieve loss or gain of function cellular control in some manner (Belling, Jackman et al. 2016).

Although many studies that attempt to evaluate the effects of G may lessen the extent to which a protein corona is involved by incubation in serum free-media (Zhang, Ali et al. 2010, Pampaloni, Lottner et al. 2018), the relatively long exposure times used may still result in the coating of nanomaterial surfaces by excreted proteins in cell culture. Indeed, proposed mechanisms for the effects underlying chronic culture on graphene have suggested that graphene still plays a large and direct mediatory role, rather than an indirect through a protein corona (Kitko, Hong et al. 2018, Pampaloni, Lottner et al. 2018). Understanding the role of cell secretion in mediating the toxicity of graphene-based materials remains an important line of future investigation.

The role of surface functionalization of G/GO in mediating toxicity

Surface functionalization has also been shown to play an important role in the toxicity of GO/G. For example, PEGylation decreases the overall cytotoxicity of GO (Li, Feng et al. 2014). And bilayer graphene functionalized with carboxyl groups showed improved viability in kidney cells relative to pristine bilayer graphene at concentrations above ~ 5 mg/l (Sasidharan, Panchakarla et al. 2011). Tu et al. modified GO with $–OCH_3$, $-NH_2$, or -PABS via PEGylated chains and cultured hippocampal neurons to 7 DIV to determine the effect of surface charge on neuronal viability and outgrowth. PEG-amine modified GO exhibited the most positive surface charge and the most neuronal outgrowth relative to other surface treatments or the native –COOH group (Tu, Pang et al. 2014), suggesting the importance of the surface in determining neuronal responses to GO. This is in line with what was observed for mouse hippocampal neurons on CVD-graphene substrates, where pristine G was shown to improve viability and connectivity up to 5 DIV, whereas disordered noncrystalline graphene did not result in any neuronal attachment (Veliev, Briançon-Marjollet et al. 2016). Thus, the crystallinity of graphene is also an important consideration in evaluating neuronal responses to graphene. Given the overall inconsistency among assessments of nanotoxicity for GO/G, it is likely that surface charge plays a role. Given the number of fabrication methods, transfer processes, and application methods for these materials, a comprehensive study of toxicity should include measurement and reporting of relevant surface characteristics (Faria, Björnmalm et al. 2018).

Distribution and trafficking of G/GO *in vivo*

Trafficking of G/GO to the brain

Mass spectrometry is a common approach to determine the bio-distribution of nanomaterials. For G/GO, most distribution studies to date have focused on overall distribution

following tail vein injection, with results indicating that very little trafficking to the brain will happen via this route. MALDI-TOF was used to determine that tail vein injection of GO results in very little accumulation in the brain after 24 h (Chen, Xiong et al. 2015), in good agreement with what was observed using radiolabeled GO for similar time periods (Zhang, Yin et al. 2011). Tail vein studies performed using rGO indicate uptake in the brain within 15 min for tail vein injection, peaking around 3 hours and decreasing by 7 days, which was corroborated by confocal microscopy (Mendonça, Soares et al. 2015). This is somewhat surprising given the relatively large sized flakes used (~340 nm), suggesting that rGO may be able to cross the blood brain barrier and may be cleared through some as yet not well understood mechanism.

In vivo assessments of trafficking and toxicity

For *in vivo* applications, further study is needed to characterize any potential brain region or cell-type specific effects. To date, most studies, such as detailed above, are performed *in vitro*. However, a few studies have characterized some of the effects of G/GO *in vivo*. Defterali et al. studied the effects of thermally reduced G on viability via stereotaxic injection into the mouse olfactory bulb. After 7 or 21 days, thermally reduced G had minimal effects on cell viability or number, and no significant increase in microglia number compared to injection only controls (Defteralı, Verdejo et al. 2016). Tail vein injection of > 250 mg/kg dextran-modified G did not show any brain toxicity after 30 days (Kanakia, Toussaint et al. 2014). However, this is not the way that graphene would encounter the brain in most intended applications, thus requiring further toxicity study *in* vivo via direct G/GO injection. Although this has not been characterized for G/GO-based materials, LDH activity has been shown to be differentially affected in a brain region specific manner in MWNTs (Bussy, Al-Jamal et al. 2015). Thus, further study is warranted to

determine if the toxicity is cell-type specific, as has been both suggested (Agarwal, Zhou et al. 2010) and argued against (Ruiz, Fernando et al. 2011).

Graphene and neurons *in vitro*

To date, even for *in vitro* systems, where there have been an array of studies using G/GO, questions remain as to toxicity. It is increasingly widely accepted that as a substrate for *in vitro* growth, graphene is a permissive surface both with and without the addition of extracellular matrix coatings. Flakes of graphene applied in culture have resulted in somewhat conflicting outcomes, but results generally support the idea that either or both high enough treatment dose or a long enough incubation times will result in cellular toxicity. Below these dosage on time thresholds, flakes of graphene also have been studied for their ability to exert biological effects. Here, we move beyond toxicity to a discussion of hypotheses as to the causal underpinnings of biological changes reported on G/GO.

Cellular growth on ECM-coated graphene

Most early studies using G/GO were conducted using a protein layer sandwiched between the substrate and neurons. For example, neural stem cells were grown on laminin-coated tissue culture polystyrene and soaked in tissue culture media overnight (Tang, Song et al. 2013). Chronic culture resulted in increases in: Ca^{2+} transient frequency, both spontaneous EPSC amplitude and frequency, and miniature EPSC frequency. These cellular changes occurred without altering overall stem cell morphology. Later versions of similar studies using neural stems cells did not observe changes in firing frequency, although were in overall agreement with increased cell signaling, here realized as increases in the percentage of cells firing action potentials during both

proliferation and differentiation stages (Guo, Zhang et al. 2016) and an increase in the density of neurites. Longer-term culture of stem cells on graphene also acts in a supportive manner by increasing overall cell count on graphene after one month (Park, Park et al. 2011). The specific effects of G/GO seem to be variable even within stem cell type, but overall results collectively suggest that graphene holds promise as a scaffold material for regenerative medicine and stem cell-based technologies.

Observations regarding the formation of synaptic connections, a fundamental unit of neuronal signaling, largely indicate that graphene is both permissive and to some extent may also enhance synaptic transmission. E18 cortical (Keshavan, Naskar et al. 2018) or E18 hippocampal (Lorenzoni, Brandi et al. 2013) neurons cultured on poly-d-lysine coated graphene 'stripes' have been used to investigate synaptogenesis, with results indicating that functional synaptic connections are formed on graphene substrates covered with an adhesion coating. P0-P1 rat (He, Zhang et al. 2016) or mouse hippocampal neurons grown on graphene coated with poly-lysine and pre-incubated in culture media demonstrated longer and more branched dendrites after 7 DIV and increased synapse number after 21 DIV (He, Zhang et al. 2016), suggesting that the enhancements observed on graphene may be the result of some sort of conserved mechanism. This collection of studies has used pre-incubation in media overnight in addition to ECM coating, as it was elsewhere demonstrated to mitigate the cytotoxicity of GO (Hu, Peng et al. 2011). The observed decrease in cytotoxicity after overnight media incubation calls raises questions regarding the complex interactions between nanomaterial surfaces, the adhesion layer, and growth factors, lipids, etc. that are contained in fetal serums. We have investigated some of the issues related to the formation of this so-called 'protein corona' on G in *Chapter 2* of this thesis.

Cellular growth on ECM-free substrates

Increasing numbers of studies are interfacing directly to G/GO, omitting the intermediate protein-coating layer. This omits confounding factors both of additional surface charges due to the complex nature of such coatings and the physical gap created between the biological material of interest and the substrate. For example, differences in surface charge been shown to alter neurite outgrowth on GO (Tu, Pang et al. 2014), with positively charged surfaces overall exhibiting increased neurite outgrowth at 7 DIV. More broadly, coatings like polylysine are polycatanionic polymers, increasing cell attachment and outgrowth – but it is unclear whether there would be coupling between the coating and G/GO, masking direct biological effects. And recent studies have begun to systematically investigate the different biological effects observed even between different classes of ECM substrate (Fischer, Zhang et al. 2018), suggesting that a single underlying mechanistic explanation of the biological effects of graphene must fully account for the composition of the substrate. The biological compatibility of G/GO substrates also does not appear to be cell-type specific, as retinal ganglion cells (Bendali, Hess et al. 2013, Fischer, Zhang et al. 2018), cortical neurons (Rauti, Lozano et al. 2016), hippocampal neurons (Veliev, Briançon-Marjollet et al. 2016, Kitko, Hong et al. 2018, Pampaloni, Lottner et al. 2018), and recently dorsal root ganglion neurons (Convertino, Luin et al. 2018) have all been cultured on bare G. However, neurite outgrowth and total number were reduced in comparison to a bare glass control for retinal ganglion cells (Bendali, Hess et al. 2013). Interestingly, this same study shows no significant enhancement on coated graphene compared to coated glass in these same properties, in contrast to much of the published literature that utilizes a protein coating layer. And later studies have made somewhat different observations, where neurons were not viable on bare glass controls but formed synaptic connections on uncoated graphene (Veliev, Briançon-Marjollet et al. 2016). This also

included comparisons to protein-coated graphene, where enhancements in neuronal surface area relative to bare graphene were observed over the duration of the study (up to 5 DIV). Although this and other studies have suggested that synaptic connections are formed on graphene, later studies were left to determine synaptic function. And the effect of extracellular matrix addition on the ability to utilize the properties of graphene for neural recordings, for example, remains to be well-characterized.

The functional effects of graphene substrates have become an increasingly important area of study for neural interfacing applications. Multiple studies have now collectively suggested both that the frequency of neuronal firing is increased on bare graphene (Kitko, Hong et al. 2018, Pampaloni, Lottner et al. 2018) and that synaptic strength is increased on bare graphene (Rauti, Lozano et al. 2016, Kitko, Hong et al. 2018), whereas high enough concentration treatment of neurons with GO flakes reduces EPSC frequency (Rauti, Lozano et al. 2016). The work presented in *Chapter 3* of this thesis further suggests that low concentrations of G flakes also acutely increase synaptic strength. However, there are somewhat conflicting explanations for the mechanisms underlying this synaptic enhancement. We hypothesize (Kitko, Hong et al. 2018) that chronic growth on graphene results in increased neuronal membrane cholesterol. This increase in cholesterol, possibly through extraction of cholesterol from a serum-containing media during the formation of a protein corona, is sufficient to explain the functional changes were observe on G. Specifically, G substrates result in an enlarged pool of synaptic vesicles and a higher vesicle release probability in neurons, and potentiated Ca^{2+} release in 3T3 cells. More recently, an alternative explanation has been proposed for the increased firing frequency on graphene (Pampaloni, Lottner et al. 2018). Pampaloni et al. hypothesize that K+ ions are depleted on bare graphene in the cleft between neurons and the substrate. This depletion of K+ ions alters neuronal signaling, increasing

EPSC frequency and altering adapting vs. tonic firing phenotypes. Computational models support this hypothesis, with the caveat that no protein deposition is present.

Graphene electrodes for in vivo imaging

Although optical technologies hold great promise for pre-clinical application, to date, electrodes remain the most widely used and sought-after new technology for neural interfacing for clinical applications. Traditionally, electrodes are designed based upon a silicon manufacturing workflow, allowing for larger scale production than is currently available for graphene – and any carbon-based – nanomaterials. Advances based upon this technology that may hold promise for a path to clinical applicability were recently demonstrated (Park, Ness et al. 2017). Graphene electrodes with over 90% transmittance have been fabricated on parylene-C or polyethylene terephthalate (PET) substrates, permitting simultaneous optogenetic stimulation (Park, Schendel et al. 2014, Liu, Lu et al. 2018), optical coherence tomography (Park, Schendel et al. 2014), deep vasculature (Thunemann, Lu et al. 2018) or Ca^{2+} imaging (Park, Ness et al. 2017, Thunemann, Lu et al. 2018) in areas where the pial surface would normally be blocked by the opacity of traditional recording materials.

An ongoing area of research will be to improve the electronic properties of graphene to better improve recording quality while, at the same time, maintaining transparency and flexibility, important for *in vivo* imaging applications. Recent data have suggested that nanoparticle doping may be an approach to meet all of these requirements. For example, platinum nanoparticles electrodeposited onto CVD G overcome the quantum capacitance limits of G electrodes alone and enable improved signal quality ECoG and EEG signals (Lu, Liu et al. 2018). These signals can be

simultaneously acquired with signals from genetically encoded indicators such as GCaMP at depths up to 250 microns using two-photon excitation.

Prospectus

The ultimate utility of graphene will be determined in part by its ability to be used in conjunction with the large array and wide variety of optical, chemical, and electrical tools commonly utilized in modern neuroscience. The ability to combine fast optical control that is tuned via real-time device-based feedback is another promising direction (Kim, Adhikari et al. 2017).

Graphene was quickly recognized as a 'wonder material' after its isolation, including recognition as the 2010 Nobel Prize in physics. The number of publications referencing graphene has jumped to several thousand per year, a quick rise from several hundred only ten years ago. Spurred on by several large initiatives, including the NIH's BRAIN and Europe's graphene flagship, which represents the European Union's largest single research initiative, new applications for graphene to broad areas of brain research should continue to be developed at a rapid pace. Yet there are still challenges remaining, including addressing the widespread utility of many graphene applications. The promises of nanomedicine are extensive; what remains to be seen is the extent to which new applications for nanomaterials deliver on the great promise so often espoused.

References

Adamala, K. P., D. A. Martin-Alarcon, K. R. Guthrie-Honea and E. S. Boyden (2016). "Engineering genetic circuit interactions within and between synthetic minimal cells." Nature Chemistry **9**: 431.

Agarwal, S., X. Zhou, F. Ye, Q. He, G. C. K. Chen, J. Soo, F. Boey, H. Zhang and P. Chen (2010). "Interfacing Live Cells with Nanocarbon Substrates." Langmuir **26**(4): 2244-2247.

Akhavan, O. (2010). "Graphene Nanomesh by ZnO Nanorod Photocatalysts." ACS Nano **4**(7): 4174-4180.

Akhavan, O. and E. Ghaderi (2010). "Toxicity of Graphene and Graphene Oxide Nanowalls Against Bacteria." ACS Nano **4**(10): 5731-5736.

Akhavan, O. and E. Ghaderi (2013). "Graphene Nanomesh Promises Extremely Efficient In Vivo Photothermal Therapy." Small **9**(21): 3593-3601.

Bae, S., H. Kim, Y. Lee, X. Xu, J.-S. Park, Y. Zheng, J. Balakrishnan, T. Lei, H. Ri Kim, Y. I. Song, Y.-J. Kim, K. S. Kim, B. Özyilmaz, J.-H. Ahn, B. H. Hong and S. Iijima (2010). "Roll-to-roll production of 30-inch graphene films for transparent electrodes." Nature Nanotechnology **5**: 574.

Bai, J., X. Zhong, S. Jiang, Y. Huang and X. Duan (2010). "Graphene nanomesh." Nature Nanotechnology **5**: 190.

Bao, H., Y. Pan, Y. Ping, N. G. Sahoo, T. Wu, L. Li, J. Li and L. H. Gan (2011). "Chitosan-Functionalized Graphene Oxide as a Nanocarrier for Drug and Gene Delivery." Small **7**(11): 1569-1578.

Barroso-Bujans, F., Á. Alegría and J. Colmenero (2010). "Kinetic Study of the Graphite Oxide Reduction: Combined Structural and Gravimetric Experiments under Isothermal and Nonisothermal Conditions." The Journal of Physical Chemistry C **114**(49): 21645-21651.

Baskin, J. M., J. A. Prescher, S. T. Laughlin, N. J. Agard, P. V. Chang, I. A. Miller, A. Lo, J. A. Codelli and C. R. Bertozzi (2007). "Copper-free click chemistry for dynamic in vivo imaging." Proceedings of the National Academy of Sciences of the United States of America **104**(43): 16793-16797.

Becerril, H. A., J. Mao, Z. Liu, R. M. Stoltenberg, Z. Bao and Y. Chen (2008). "Evaluation of Solution-Processed Reduced Graphene Oxide Films as Transparent Conductors." ACS Nano **2**(3): 463-470.

Belling, J. N., J. A. Jackman, S. Yorulmaz Avsar, J. H. Park, Y. Wang, M. G. Potroz, A. R. Ferhan, P. S. Weiss and N.-J. Cho (2016). "Stealth Immune Properties of Graphene Oxide Enabled by Surface-Bound Complement Factor H." ACS Nano **10**(11): 10161-10172.

Bendali, A., L. H. Hess, M. Seifert, V. Forster, A.-F. Stephan, J. A. Garrido and S. Picaud (2013). "Purified Neurons can Survive on Peptide-Free Graphene Layers." Advanced Healthcare Materials **2**(7): 929-933.

Brodie, B. C. (1860). "Sur le poids atomique du graphite." Annales de Chimie et de Physique **59**: 466-472.

Bussy, C., K. T. Al-Jamal, J. Boczkowski, S. Lanone, M. Prato, A. Bianco and K. Kostarelos (2015).
"Microglia Determine Brain Region-Specific Neurotoxic Responses to Chemically Functionalized Carbon Nanotubes." ACS Nano **9**(8): 7815-7830.

Cao, L., M. J. Meziani, S. Sahu and Y.-P. Sun (2013). "Photoluminescence Properties of Graphene versus Other Carbon Nanomaterials." Accounts of Chemical Research **46**(1): 171-180.

Castagnola, V., W. Zhao, L. Boselli, M. C. Lo Giudice, F. Meder, E. Polo, K. R. Paton, C. Backes, J. N. Coleman and K. A. Dawson (2018). "Biological recognition of graphene nanoflakes." Nature Communications **9**(1): 1577.

Cedervall, T., I. Lynch, S. Lindman, T. Berggård, E. Thulin, H. Nilsson, K. A. Dawson and S. Linse (2007). "Understanding the nanoparticle–protein corona using methods to quantify exchange rates and affinities of proteins for nanoparticles." Proceedings of the National Academy of Sciences **104**(7): 2050-2055.

Cellot, G., P. Lagonegro, G. Tarabella, D. Scaini, F. Fabbri, S. Iannotta, M. Prato, G. Salviati and L. Ballerini (2015). "PEDOT:PSS Interfaces Support the Development of Neuronal Synaptic Networks with Reduced Neuroglia Response In vitro." Frontiers in Neuroscience **9**: 521.

Chaudhary, U., N. Birbaumer and A. Ramos-Murguialday (2016). "Brain–computer interfaces for communication and rehabilitation." Nature Reviews Neurology **12**: 513.

Chen, F., P. W. Tillberg and E. S. Boyden (2015). "Expansion microscopy." Science **347**(6221): 543-548.

Chen, S., C. Xiong, H. Liu, Q. Wan, J. Hou, Q. He, A. Badu-Tawiah and Z. Nie (2015). "Mass spectrometry imaging reveals the sub-organ distribution of carbon nanomaterials." Nature Nanotechnology **10**: 176.

Cheng, J., E. Flahaut and S. H. Cheng (2007). "Effect of carbon nanotubes on developing zebrafish (Danio Rerio) embryos." Environmental Toxicology and Chemistry **26**(4): 708-716.

Choi, M., K.-G. Kim, J. Heo, H. Jeong, S. Y. Kim and J. Hong (2015). "Multilayered Graphene Nano-Film for Controlled Protein Delivery by Desired Electro-Stimuli." Scientific Reports **5**: 17631.

Chong, Y., C. Ge, Z. Yang, J. A. Garate, Z. Gu, J. K. Weber, J. Liu and R. Zhou (2015). "Reduced Cytotoxicity of Graphene Nanosheets Mediated by Blood-Protein Coating." ACS Nano **9**(6): 5713-5724.

Chung, K., J. Wallace, S.-Y. Kim, S. Kalyanasundaram, A. S. Andalman, T. J. Davidson, J. J. Mirzabekov, K. A. Zalocusky, J. Mattis, A. K. Denisin, S. Pak, H. Bernstein, C. Ramakrishnan, L. Grosenick, V. Gradinaru and K. Deisseroth (2013). "Structural and molecular interrogation of intact biological systems." Nature **497**: 332.

Convertino, D., S. Luin, L. Marchetti and C. Coletti (2018). "Peripheral Neuron Survival and Outgrowth on Graphene." Frontiers in Neuroscience **12**(1).

Defteralı, Ç., R. Verdejo, L. Peponi, E. D. Martín, R. Martínez-Murillo, M. Á. López-Manchado and C. Vicario-Abejón (2016). "Thermally reduced graphene is a permissive material for neurons and astrocytes and de novo neurogenesis in the adult olfactory bulb in vivo." Biomaterials **82**: 84-93.

Ding, X., H. Liu and Y. Fan (2015). "Graphene-Based Materials in Regenerative Medicine." Advanced Healthcare Materials **4**(10): 1451-1468.

Domínguez-Bajo, A., A. González-Mayorga, E. López-Dolado and M. C. Serrano (2017). "Graphene-Derived Materials Interfacing the Spinal Cord: Outstanding in Vitro and in Vivo Findings." Frontiers in Systems Neuroscience **11**(71).

Dong, H., M. Jin, Z. Liu, H. Xiong, X. Qiu, W. Zhang and Z. Guo (2016). "In vitro and in vivo brain-targeting chemo-photothermal therapy using graphene oxide conjugated with transferrin for Gliomas." Lasers in Medical Science **31**(6): 1123-1131.

Dong, H., Y. Li, J. Yu, Y. Song, X. Cai, J. Liu, J. Zhang, R. C. Ewing and D. Shi (2013). "A Versatile Multicomponent Assembly via β-cyclodextrin Host–Guest Chemistry on Graphene for Biomedical Applications." Small **9**(3): 446-456.

Donoghue, J. P., A. Nurmikko, M. Black and L. R. Hochberg (2007). "Assistive technology and robotic control using motor cortex ensemble-based neural interface systems in humans with tetraplegia." The Journal of Physiology **579**(3): 603-611.

Du, X., L. Wu, J. Cheng, S. Huang, Q. Cai, Q. Jin and J. Zhao (2015). "Graphene microelectrode arrays for neural activity detection." Journal of Biological Physics **41**(4): 339-347.

Duan, G., S.-g. Kang, X. Tian, J. A. Garate, L. Zhao, C. Ge and R. Zhou (2015). "Protein corona mitigates the cytotoxicity of graphene oxide by reducing its physical interaction with cell membrane." Nanoscale **7**(37): 15214-15224.

Eda, G., G. Fanchini and M. Chhowalla (2008). "Large-area ultrathin films of reduced graphene oxide as a transparent and flexible electronic material." Nature Nanotechnology **3**: 270.

Fako, V. E. and D. Y. Furgeson (2009). "Zebrafish as a correlative and predictive model for assessing biomaterial nanotoxicity." Advanced Drug Delivery Reviews **61**(6): 478-486.

Fang, M., J. Long, W. Zhao, L. Wang and G. Chen (2010). "pH-Responsive Chitosan-Mediated Graphene Dispersions." Langmuir **26**(22): 16771-16774.

Faria, M., M. Björnmalm, K. J. Thurecht, S. J. Kent, R. G. Parton, M. Kavallaris, A. P. R. Johnston, J. J. Gooding, S. R. Corrie, B. J. Boyd, P. Thordarson, A. K. Whittaker, M. M. Stevens, C. A. Prestidge, C. J. H. Porter, W. J. Parak, T. P. Davis, E. J. Crampin and F. Caruso (2018). "Minimum information reporting in bio–nano experimental literature." Nature Nanotechnology **13**(9): 777-785.

Fattahi, P., G. Yang, G. Kim and M. R. Abidian (2014). "A Review of Organic and Inorganic Biomaterials for Neural Interfaces." Advanced materials (Deerfield Beach, Fla.) **26**(12): 1846-1885.

Feng, L., S. Zhang and Z. Liu (2011). "Graphene based gene transfection." Nanoscale **3**(3): 1252-1257.

Fiori, G., F. Bonaccorso, G. Iannaccone, T. Palacios, D. Neumaier, A. Seabaugh, S. K. Banerjee and L. Colombo (2014). "Electronics based on two-dimensional materials." Nature Nanotechnology **9**: 768.

Fischer, R. A., Y. Zhang, M. L. Risner, D. Li, Y. Xu and R. M. Sappington (2018). "Impact of Graphene on the Efficacy of Neuron Culture Substrates." Advanced Healthcare Materials **7**(14): 1701290.

Frost, R., G. E. Jönsson, D. Chakarov, S. Svedhem and B. Kasemo (2012). "Graphene Oxide and Lipid Membranes: Interactions and Nanocomposite Structures." Nano Letters **12**(7): 3356-3362.

Geim, A. K. and K. S. Novoselov (2007). "The rise of graphene." Nature Materials **6**: 183.

Gómez-Navarro, C., R. T. Weitz, A. M. Bittner, M. Scolari, A. Mews, M. Burghard and K. Kern (2007). "Electronic Transport Properties of Individual Chemically Reduced Graphene Oxide Sheets." Nano Letters **7**(11): 3499-3503.

Gu, Y., Y. Guo, C. Wang, J. Xu, J. Wu, T. B. Kirk, D. Ma and W. Xue (2017). "A polyamidoamne dendrimer functionalized graphene oxide for DOX and MMP-9 shRNA plasmid co-delivery." Materials Science and Engineering: C **70**: 572-585.

Guo, R., J. Mao and L.-T. Yan (2013). "Computer simulation of cell entry of graphene nanosheet." Biomaterials **34**(17): 4296-4301.

Guo, R., S. Zhang, M. Xiao, F. Qian, Z. He, D. Li, X. Zhang, H. Li, X. Yang, M. Wang, R. Chai and M. Tang (2016). "Accelerating bioelectric functional development of neural stem cells by

graphene coupling: Implications for neural interfacing with conductive materials." Biomaterials **106**: 193-204.

Han, T.-H., S.-J. Kwon, N. Li, H.-K. Seo, W. Xu, K. S. Kim and T.-W. Lee (2016). "Versatile p-Type Chemical Doping to Achieve Ideal Flexible Graphene Electrodes." Angewandte Chemie International Edition **55**(21): 6197-6201.

He, Z., S. Zhang, Q. Song, W. Li, D. Liu, H. Li, M. Tang and R. Chai (2016). "The structural development of primary cultured hippocampal neurons on a graphene substrate." Colloids and Surfaces B: Biointerfaces **146**: 442-451.

Hernandez, Y., V. Nicolosi, M. Lotya, F. M. Blighe, Z. Sun, S. De, I. T. McGovern, B. Holland, M. Byrne, Y. K. Gun'Ko, J. J. Boland, P. Niraj, G. Duesberg, S. Krishnamurthy, R. Goodhue, J. Hutchison, V. Scardaci, A. C. Ferrari and J. N. Coleman (2008). "High-yield production of graphene by liquid-phase exfoliation of graphite." Nature Nanotechnology **3**: 563.

Hochberg, L. R., M. D. Serruya, G. M. Friehs, J. A. Mukand, M. Saleh, A. H. Caplan, A. Branner, D. Chen, R. D. Penn and J. P. Donoghue (2006). "Neuronal ensemble control of prosthetic devices by a human with tetraplegia." Nature **442**: 164.

Hong, J., N. J. Shah, A. C. Drake, P. C. DeMuth, J. B. Lee, J. Chen and P. T. Hammond (2012). "Graphene Multilayers as Gates for Multi-Week Sequential Release of Proteins from Surfaces." ACS Nano **6**(1): 81-88.

Howe, K., M. D. Clark, C. F. Torroja, J. Torrance, C. Berthelot, M. Muffato, J. E. Collins, S. Humphray, K. McLaren, L. Matthews, S. McLaren, I. Sealy, M. Caccamo, C. Churcher, C. Scott, J. C. Barrett, R. Koch, G.-J. Rauch, S. White, W. Chow, B. Kilian, L. T. Quintais, J. A. Guerra-Assunção, Y. Zhou, Y. Gu, J. Yen, J.-H. Vogel, T. Eyre, S. Redmond, R. Banerjee, J. Chi, B. Fu, E. Langley, S. F. Maguire, G. K. Laird, D. Lloyd, E. Kenyon, S. Donaldson, H. Sehra, J. Almeida-King, J. Loveland, S. Trevanion, M. Jones, M. Quail, D. Willey, A. Hunt, J. Burton, S. Sims, K. McLay, B. Plumb, J. Davis, C. Clee, K. Oliver, R. Clark, C. Riddle, D. Eliott, G. Threadgold, G. Harden, D. Ware, B. Mortimer, G. Kerry, P. Heath, B. Phillimore, A. Tracey, N. Corby, M. Dunn, C. Johnson, J. Wood, S. Clark, S. Pelan, G. Griffiths, M. Smith, R. Glithero, P. Howden, N. Barker, C. Stevens, J. Harley, K. Holt, G. Panagiotidis, J. Lovell, H. Beasley, C. Henderson, D. Gordon, K. Auger, D. Wright, J. Collins, C. Raisen, L. Dyer, K. Leung, L. Robertson, K. Ambridge, D. Leongamornlert, S. McGuire, R. Gilderthorp, C. Griffiths, D. Manthravadi, S. Nichol, G. Barker, S. Whitehead, M. Kay, J. Brown, C. Murnane, E. Gray, M. Humphries, N. Sycamore, D. Barker, D. Saunders, J. Wallis, A. Babbage, S. Hammond, M. Mashreghi-Mohammadi, L. Barr, S. Martin, P. Wray, A. Ellington, N. Matthews, M. Ellwood, R. Woodmansey, G. Clark, J. Cooper, A. Tromans, D. Grafham, C. Skuce, R. Pandian, R. Andrews, E. Harrison, A. Kimberley, J. Garnett, N. Fosker, R. Hall, P. Garner, D. Kelly, C. Bird, S. Palmer, I. Gehring, A. Berger, C. M. Dooley, Z. Ersan-Ürün, C. Eser, H. Geiger, M. Geisler, L. Karotki, A. Kirn, J. Konantz, M. Konantz, M. Oberländer, S. Rudolph-Geiger, M. Teucke, K. Osoegawa, B. Zhu, A. Rapp, S. Widaa, C. Langford, F. Yang, N. P. Carter, J. Harrow, Z. Ning, J. Herrero, S. M. J. Searle, A. Enright, R. Geisler, R. H. A. Plasterk, C. Lee, M. Westerfield, P. J. de Jong, L. I. Zon, J. H. Postlethwait, C. Nüsslein-Volhard, T. J. P. Hubbard, H. R. Crollius, J.

Rogers and D. L. Stemple (2013). "The zebrafish reference genome sequence and its relationship to the human genome." Nature **496**(7446): 498-503.

Hu, W., C. Peng, M. Lv, X. Li, Y. Zhang, N. Chen, C. Fan and Q. Huang (2011). "Protein Corona-Mediated Mitigation of Cytotoxicity of Graphene Oxide." ACS Nano **5**(5): 3693-3700.

Hummers, W. S. and R. E. Offeman (1958). "Preparation of Graphitic Oxide." Journal of the American Chemical Society **80**(6): 1339-1339.

Jan, E., J. L. Hendricks, V. Husaini, S. M. Richardson-Burns, A. Sereno, D. C. Martin and N. A. Kotov (2009). "Layered Carbon Nanotube-Polyelectrolyte Electrodes Outperform Traditional Neural Interface Materials." Nano Letters **9**(12): 4012-4018.

Jarrell, T. A., Y. Wang, A. E. Bloniarz, C. A. Brittin, M. Xu, J. N. Thomson, D. G. Albertson, D. H. Hall and S. W. Emmons (2012). "The Connectome of a Decision-Making Neural Network." Science **337**(6093): 437-444.

Jung, I., D. A. Field, N. J. Clark, Y. Zhu, D. Yang, R. D. Piner, S. Stankovich, D. A. Dikin, H. Geisler, C. A. Ventrice and R. S. Ruoff (2009). "Reduction Kinetics of Graphene Oxide Determined by Electrical Transport Measurements and Temperature Programmed Desorption." The Journal of Physical Chemistry C **113**(43): 18480-18486.

Kaminska, I., M. R. Das, Y. Coffinier, J. Niedziolka-Jonsson, J. Sobczak, P. Woisel, J. Lyskawa, M. Opallo, R. Boukherroub and S. Szunerits (2012). "Reduction and Functionalization of Graphene Oxide Sheets Using Biomimetic Dopamine Derivatives in One Step." ACS Applied Materials & Interfaces **4**(2): 1016-1020.

Kanakia, S., J. D. Toussaint, S. Mullick Chowdhury, T. Tembulkar, S. Lee, Y.-P. Jiang, R. Z. Lin, K. R. Shroyer, W. Moore and B. Sitharaman (2014). "Dose ranging, expanded acute toxicity and safety pharmacology studies for intravenously administered functionalized graphene nanoparticle formulations." Biomaterials **35**(25): 7022-7031.

Kandel, E. R. (2009). "The Biology of Memory: A Forty-Year Perspective." The Journal of Neuroscience **29**(41): 12748-12756.

Keshavan, S., S. Naskar, A. Diaspro, L. Cancedda and S. Dante (2018). "Developmental refinement of synaptic transmission on micropatterned single layer graphene." Acta Biomaterialia **65**: 363-375.

Keshishian, H., K. Broadie, A. Chiba and M. Bate (1996). "The Drosophila Neuromuscular Junction: A Model System for Studying Synaptic Development and Function." Annual Review of Neuroscience **19**(1): 545-575.

Kim, C. K., A. Adhikari and K. Deisseroth (2017). "Integration of optogenetics with complementary methodologies in systems neuroscience." Nature Reviews Neuroscience **18**: 222.

Kim, H., D. Lee, J. Kim, T.-i. Kim and W. J. Kim (2013). "Photothermally Triggered Cytosolic Drug Delivery via Endosome Disruption Using a Functionalized Reduced Graphene Oxide." ACS Nano **7**(8): 6735-6746.

Kitko, K. E., T. Hong, R. M. Lazarenko, D. Ying, Y.-Q. Xu and Q. Zhang (2018). "Membrane cholesterol mediates the cellular effects of monolayer graphene substrates." Nature Communications **9**(1): 796.

Kostarelos, K., A. Bianco and M. Prato (2009). "Promises, facts and challenges for carbon nanotubes in imaging and therapeutics." Nature Nanotechnology **4**: 627.

Kurapati, R. and A. M. Raichur (2012). "Graphene oxide based multilayer capsules with unique permeability properties: facile encapsulation of multiple drugs." Chemical Communications **48**(48): 6013-6015.

Kuzum, D., H. Takano, E. Shim, J. C. Reed, H. Juul, A. G. Richardson, J. de Vries, H. Bink, M. A. Dichter, T. H. Lucas, D. A. Coulter, E. Cubukcu and B. Litt (2014). "Transparent and flexible low noise graphene electrodes for simultaneous electrophysiology and neuroimaging." Nature Communications **5**: 5259.

Lee, C., X. Wei, J. W. Kysar and J. Hone (2008). "Measurement of the Elastic Properties and Intrinsic Strength of Monolayer Graphene." Science **321**(5887): 385-388.

Lei, H., X. Zhou, H. Wu, Y. Song, J. Hu, S. Guo and Y. Zhang (2014). "Morphology Change and Detachment of Lipid Bilayers from the Mica Substrate Driven by Graphene Oxide Sheets." Langmuir **30**(16): 4678-4683.

Li, D., M. B. Müller, S. Gilje, R. B. Kaner and G. G. Wallace (2008). "Processable aqueous dispersions of graphene nanosheets." Nature Nanotechnology **3**: 101.

Li, M., X. Yang, J. Ren, K. Qu and X. Qu (2012). "Using Graphene Oxide High Near-Infrared Absorbance for Photothermal Treatment of Alzheimer's Disease." Advanced Materials **24**(13): 1722-1728.

Li, P., T. Xu, S. Wu, L. Lei and D. He (2017). "Chronic exposure to graphene-based nanomaterials induces behavioral deficits and neural damage in Caenorhabditis elegans." Journal of Applied Toxicology **37**(10): 1140-1150.

Li, S., A. J. Stein, A. Kruger and R. M. Leblanc (2013). "Head Groups of Lipids Govern the Interaction and Orientation between Graphene Oxide and Lipids." The Journal of Physical Chemistry C **117**(31): 16150-16158.

Li, X., W. Cai, J. An, S. Kim, J. Nah, D. Yang, R. Piner, A. Velamakanni, I. Jung, E. Tutuc, S. K. Banerjee, L. Colombo and R. S. Ruoff (2009). "Large-Area Synthesis of High-Quality and Uniform Graphene Films on Copper Foils." Science **324**(5932): 1312-1314.

Li, X., H. Wang, J. T. Robinson, H. Sanchez, G. Diankov and H. Dai (2009). "Simultaneous Nitrogen Doping and Reduction of Graphene Oxide." Journal of the American Chemical Society **131**(43): 15939-15944.

Li, Y., L. Feng, X. Shi, X. Wang, Y. Yang, K. Yang, T. Liu, G. Yang and Z. Liu (2014). "Surface Coating-Dependent Cytotoxicity and Degradation of Graphene Derivatives: Towards the Design of Non-Toxic, Degradable Nano-Graphene." Small **10**(8): 1544-1554.

Li, Y., H. Yuan, A. von dem Bussche, M. Creighton, R. H. Hurt, A. B. Kane and H. Gao (2013). "Graphene microsheets enter cells through spontaneous membrane penetration at edge asperities and corner sites." Proceedings of the National Academy of Sciences **110**(30): 12295-12300.

Little, S., A. Pogosyan, S. Neal, B. Zavala, L. Zrinzo, M. Hariz, T. Foltynie, P. Limousin, K. Ashkan, J. FitzGerald, A. L. Green, T. Z. Aziz and P. Brown (2013). "Adaptive deep brain stimulation in advanced Parkinson disease." Annals of Neurology **74**(3): 449-457.

Liu, C.-C., J.-J. Zhao, R. Zhang, H. Li, B. Chen, L.-L. Zhang and H. Yang (2017) "Multifunctionalization of graphene and graphene oxide for controlled release and targeted delivery of anticancer drugs." American journal of translational research **9**, 5197-5219.

Liu, G., H. Shen, J. Mao, L. Zhang, Z. Jiang, T. Sun, Q. Lan and Z. Zhang (2013). "Transferrin Modified Graphene Oxide for Glioma-Targeted Drug Delivery: In Vitro and in Vivo Evaluations." ACS Applied Materials & Interfaces **5**(15): 6909-6914.

Liu, N., A. Chortos, T. Lei, L. Jin, T. R. Kim, W.-G. Bae, C. Zhu, S. Wang, R. Pfattner, X. Chen, R. Sinclair and Z. Bao (2017). "Ultratransparent and stretchable graphene electrodes." Science Advances **3**(9).

Liu, X., Y. Lu, E. Iseri, Y. Shi and D. Kuzum (2018). "A Compact Closed-Loop Optogenetics System Based on Artifact-Free Transparent Graphene Electrodes." Frontiers in Neuroscience **12**(132).

Liu, X., A. L. Miller, S. Park, B. E. Waletzki, Z. Zhou, A. Terzic and L. Lu (2017). "Functionalized Carbon Nanotube and Graphene Oxide Embedded Electrically Conductive Hydrogel Synergistically Stimulates Nerve Cell Differentiation." ACS Applied Materials & Interfaces **9**(17): 14677-14690.

Liu, Z., J. T. Robinson, X. Sun and H. Dai (2008). "PEGylated Nanographene Oxide for Delivery of Water-Insoluble Cancer Drugs." Journal of the American Chemical Society **130**(33): 10876-10877.

Liu, Z., J. T. Robinson, S. M. Tabakman, K. Yang and H. Dai (2011). "Carbon materials for drug delivery & cancer therapy." Materials Today **14**(7): 316-323.

Lorenzoni, M., F. Brandi, S. Dante, A. Giugni and B. Torre (2013). "Simple and effective graphene laser processing for neuron patterning application." Scientific Reports **3**: 1954.

Lotya, M., Y. Hernandez, P. J. King, R. J. Smith, V. Nicolosi, L. S. Karlsson, F. M. Blighe, S. De, Z. Wang, I. T. McGovern, G. S. Duesberg and J. N. Coleman (2009). "Liquid Phase Production of Graphene by Exfoliation of Graphite in Surfactant/Water Solutions." Journal of the American Chemical Society **131**(10): 3611-3620.

Lu, C.-H., C.-L. Zhu, J. Li, J.-J. Liu, X. Chen and H.-H. Yang (2010). "Using graphene to protect DNA from cleavage during cellular delivery." Chemical Communications **46**(18): 3116-3118.

Lu, Y., X. Liu, R. Hattori, C. Ren, X. Zhang, T. Komiyama and D. Kuzum (2018). "Ultralow Impedance Graphene Microelectrodes with High Optical Transparency for Simultaneous Deep Two-Photon Imaging in Transgenic Mice." Advanced Functional Materials **28**(31): 1800002.

Luan, B., S. Zhou, D. Wang and R. Zhou (2017). "Detecting Interactions between Nanomaterials and Cell Membranes by Synthetic Nanopores." ACS Nano.

Luo, X., C. L. Weaver, D. D. Zhou, R. Greenberg and X. T. Cui (2011). "Highly stable carbon nanotube doped poly(3,4-ethylenedioxythiophene) for chronic neural stimulation." Biomaterials **32**(24): 5551-5557.

Luo, Z., P. M. Vora, E. J. Mele, A. T. C. Johnson and J. M. Kikkawa (2009). "Photoluminescence and band gap modulation in graphene oxide." Applied Physics Letters **94**(11): 111909.

Markovic, Z. M., L. M. Harhaji-Trajkovic, B. M. Todorovic-Markovic, D. P. Kepić, K. M. Arsikin, S. P. Jovanović, A. C. Pantovic, M. D. Dramićanin and V. S. Trajkovic (2011). "In vitro comparison of the photothermal anticancer activity of graphene nanoparticles and carbon nanotubes." Biomaterials **32**(4): 1121-1129.

Matteini, P., F. Tatini, L. Cavigli, S. Ottaviano, G. Ghini and R. Pini (2014). "Graphene as a photothermal switch for controlled drug release." Nanoscale **6**(14): 7947-7953.

Mendonça, M. C. P., E. S. Soares, M. B. de Jesus, H. J. Ceragioli, M. S. Ferreira, R. R. Catharino and M. A. da Cruz-Höfling (2015). "Reduced graphene oxide induces transient blood–brain barrier opening: an in vivo study." Journal of Nanobiotechnology **13**(1): 78.

Moon, I. K., J. Lee, R. S. Ruoff and H. Lee (2010). "Reduced graphene oxide by chemical graphitization." Nature Communications **1**: 73.

Nel, A. E., L. Mädler, D. Velegol, T. Xia, E. M. V. Hoek, P. Somasundaran, F. Klaessig, V. Castranova and M. Thompson (2009). "Understanding biophysicochemical interactions at the nano–bio interface." Nature Materials **8**: 543.

Nicholl, R. J. T., H. J. Conley, N. V. Lavrik, I. Vlassiouk, Y. S. Puzyrev, V. P. Sreenivas, S. T. Pantelides and K. I. Bolotin (2015). "The effect of intrinsic crumpling on the mechanics of free-standing graphene." Nature Communications **6**: 8789.

Novoselov, K. S., A. K. Geim, S. V. Morozov, D. Jiang, Y. Zhang, S. V. Dubonos, I. V. Grigorieva and A. A. Firsov (2004). "Electric Field Effect in Atomically Thin Carbon Films." Science **306**(5696): 666-669.

Novoselov, K. S., D. Jiang, F. Schedin, T. J. Booth, V. V. Khotkevich, S. V. Morozov and A. K. Geim (2005). "Two-dimensional atomic crystals." Proceedings of the National Academy of Sciences of the United States of America **102**(30): 10451-10453.

Pampaloni, N. P., M. Lottner, M. Giugliano, A. Matruglio, F. D'Amico, M. Prato, J. A. Garrido, L. Ballerini and D. Scaini (2018). "Single-layer graphene modulates neuronal communication and augments membrane ion currents." Nature Nanotechnology **13**(8): 755-764.

Pang, J., R. G. Mendes, P. S. Wrobel, M. D. Wlodarski, H. Q. Ta, L. Zhao, L. Giebeler, B. Trzebicka, T. Gemming, L. Fu, Z. Liu, J. Eckert, A. Bachmatiuk and M. H. Rümmeli (2017). "Self-Terminating Confinement Approach for Large-Area Uniform Monolayer Graphene Directly over Si/SiOx by Chemical Vapor Deposition." ACS Nano **11**(2): 1946-1956.

Park, D.-W., S. K. Brodnick, J. P. Ness, F. Atry, L. Krugner-Higby, A. Sandberg, S. Mikael, T. J. Richner, J. Novello, H. Kim, D.-H. Baek, J. Bong, S. T. Frye, S. Thongpang, K. I. Swanson, W. Lake, R. Pashaie, J. C. Williams and Z. Ma (2016). "Fabrication and utility of a transparent graphene neural electrode array for electrophysiology, in vivo imaging, and optogenetics." Nature Protocols **11**: 2201.

Park, D.-W., J. P. Ness, S. K. Brodnick, C. Esquibel, J. Novello, F. Atry, D.-H. Baek, H. Kim, J. Bong, K. I. Swanson, A. J. Suminski, K. J. Otto, R. Pashaie, J. C. Williams and Z. Ma (2017). "Electrical Neural Stimulation and Simultaneous In Vivo Monitoring with Transparent Graphene Electrode Arrays Implanted in GCaMP6f mice." ACS Nano.

Park, D.-W., A. A. Schendel, S. Mikael, S. K. Brodnick, T. J. Richner, J. P. Ness, M. R. Hayat, F. Atry, S. T. Frye, R. Pashaie, S. Thongpang, Z. Ma and J. C. Williams (2014). "Graphene-based carbon-layered electrode array technology for neural imaging and optogenetic applications." Nature Communications **5**: 5258.

Park, S. and R. S. Ruoff (2009). "Chemical methods for the production of graphenes." Nature Nanotechnology **4**: 217.

Park, S. Y., J. Park, S. H. Sim, M. G. Sung, K. S. Kim, B. H. Hong and S. Hong (2011). "Enhanced Differentiation of Human Neural Stem Cells into Neurons on Graphene." Advanced Materials **23**(36): H263-H267.

Paton, K. R., E. Varrla, C. Backes, R. J. Smith, U. Khan, A. O'Neill, C. Boland, M. Lotya, O. M. Istrate, P. King, T. Higgins, S. Barwich, P. May, P. Puczkarski, I. Ahmed, M. Moebius, H. Pettersson, E. Long, J. Coelho, S. E. O'Brien, E. K. McGuire, B. M. Sanchez, G. S. Duesberg, N. McEvoy, T. J. Pennycook, C. Downing, A. Crossley, V. Nicolosi and J. N. Coleman (2014).

"Scalable production of large quantities of defect-free few-layer graphene by shear exfoliation in liquids." Nature Materials **13**: 624.

Polikov, V. S., P. A. Tresco and W. M. Reichert (2005). "Response of brain tissue to chronically implanted neural electrodes." Journal of Neuroscience Methods **148**(1): 1-18.

Qian, J., D. Wang, F.-H. Cai, W. Xi, L. Peng, Z.-F. Zhu, H. He, M.-L. Hu and S. He (2012). "Observation of Multiphoton-Induced Fluorescence from Graphene Oxide Nanoparticles and Applications in In Vivo Functional Bioimaging." Angewandte Chemie International Edition **51**(42): 10570-10575.

Quintana, M., A. Montellano, A. E. del Rio Castillo, G. V. Tendeloo, C. Bittencourt and M. Prato (2011). "Selective organic functionalization of graphene bulk or graphene edges." Chemical Communications **47**(33): 9330-9332.

Radic, S., N. K. Geitner, R. Podila, A. Käkinen, P. Chen, P. C. Ke and F. Ding (2013). "Competitive Binding of Natural Amphiphiles with Graphene Derivatives." Scientific Reports **3**: 2273.

Ramos-Murguialday, A., D. Broetz, M. Rea, L. Läer, Ö. Yilmaz, F. L. Brasil, G. Liberati, M. R. Curado, E. Garcia-Cossio, A. Vyziotis, W. Cho, M. Agostini, E. Soares, S. Soekadar, A. Caria, L. G. Cohen and N. Birbaumer (2013). "Brain–machine interface in chronic stroke rehabilitation: A controlled study." Annals of Neurology **74**(1): 100-108.

Rauti, R., N. Lozano, V. León, D. Scaini, M. Musto, I. Rago, F. P. Ulloa Severino, A. Fabbro, L. Casalis, E. Vázquez, K. Kostarelos, M. Prato and L. Ballerini (2016). "Graphene Oxide Nanosheets Reshape Synaptic Function in Cultured Brain Networks." ACS Nano **10**(4): 4459-4471.

Reina, A., X. Jia, J. Ho, D. Nezich, H. Son, V. Bulovic, M. S. Dresselhaus and J. Kong (2009). "Large Area, Few-Layer Graphene Films on Arbitrary Substrates by Chemical Vapor Deposition." Nano Letters **9**(1): 30-35.

Richardson-Burns, S. M., J. L. Hendricks, B. Foster, L. K. Povlich, D.-H. Kim and D. C. Martin (2007). "Polymerization of the conducting polymer poly(3,4-ethylenedioxythiophene) (PEDOT) around living neural cells." Biomaterials **28**(8): 1539-1552.

Rivnay, J., H. Wang, L. Fenno, K. Deisseroth and G. G. Malliaras (2017). "Next-generation probes, particles, and proteins for neural interfacing." Science Advances **3**(6).

Robinson, D. L., B. J. Venton, M. L. A. V. Heien and R. M. Wightman (2003). "Detecting Subsecond Dopamine Release with Fast-Scan Cyclic Voltammetry in Vivo." Clinical Chemistry **49**(10): 1763-1773.

Robinson, J. T., S. M. Tabakman, Y. Liang, H. Wang, H. Sanchez Casalongue, D. Vinh and H. Dai (2011). "Ultrasmall Reduced Graphene Oxide with High Near-Infrared Absorbance for Photothermal Therapy." Journal of the American Chemical Society **133**(17): 6825-6831.

Romero-Aburto, R., T. N. Narayanan, Y. Nagaoka, T. Hasumura, T. M. Mitcham, T. Fukuda, P. J. Cox, R. R. Bouchard, T. Maekawa, D. S. Kumar, S. V. Torti, S. A. Mani and P. M. Ajayan (2013). "Fluorinated Graphene Oxide; a New Multimodal Material for Biological Applications." Advanced Materials **25**(39): 5632-5637.

Rourke, J. P., P. A. Pandey, J. J. Moore, M. Bates, I. A. Kinloch, R. J. Young and N. R. Wilson (2011). "The Real Graphene Oxide Revealed: Stripping the Oxidative Debris from the Graphene-like Sheets." Angewandte Chemie International Edition **50**(14): 3173-3177.

Ruiz, O. N., K. A. S. Fernando, B. Wang, N. A. Brown, P. G. Luo, N. D. McNamara, M. Vangsness, Y.-P. Sun and C. E. Bunker (2011). "Graphene Oxide: A Nonspecific Enhancer of Cellular Growth." ACS Nano **5**(10): 8100-8107.

Sasidharan, A., L. S. Panchakarla, P. Chandran, D. Menon, S. Nair, C. N. R. Rao and M. Koyakutty (2011). "Differential nano-bio interactions and toxicity effects of pristine versus functionalized graphene." Nanoscale **3**(6): 2461-2464.

Seabra, A. B., A. J. Paula, R. de Lima, O. L. Alves and N. Durán (2014). "Nanotoxicity of Graphene and Graphene Oxide." Chemical Research in Toxicology **27**(2): 159-168.

Shih, C.-J., A. Vijayaraghavan, R. Krishnan, R. Sharma, J.-H. Han, M.-H. Ham, Z. Jin, S. Lin, G. L. C. Paulus, N. F. Reuel, Q. H. Wang, D. Blankschtein and M. S. Strano (2011). "Bi- and trilayer graphene solutions." Nature Nanotechnology **6**: 439.

Skocek, O., T. Nöbauer, L. Weilguny, F. Martínez Traub, C. N. Xia, M. I. Molodtsov, A. Grama, M. Yamagata, D. Aharoni, D. D. Cox, P. Golshani and A. Vaziri (2018). "High-speed volumetric imaging of neuronal activity in freely moving rodents." Nature Methods **15**(6): 429-432.

Stankovich, S., D. A. Dikin, R. D. Piner, K. A. Kohlhaas, A. Kleinhammes, Y. Jia, Y. Wu, S. T. Nguyen and R. S. Ruoff (2007). "Synthesis of graphene-based nanosheets via chemical reduction of exfoliated graphite oxide." Carbon **45**(7): 1558-1565.

Su, C.-Y., Y. Xu, W. Zhang, J. Zhao, X. Tang, C.-H. Tsai and L.-J. Li (2009). "Electrical and Spectroscopic Characterizations of Ultra-Large Reduced Graphene Oxide Monolayers." Chemistry of Materials **21**(23): 5674-5680.

Su, Y., X. Ping, K. J. Yu, J. W. Lee, J. A. Fan, B. Wang, M. Li, R. Li, D. V. Harburg, Y. Huang, C. Yu, S. Mao, J. Shim, Q. Yang, P.-Y. Lee, A. Armonas, K.-J. Choi, Y. Yang, U. Paik, T. Chang, T. J. Dawidczyk, Y. Huang, S. Wang and J. A. Rogers (2017). "In-Plane Deformation Mechanics for Highly Stretchable Electronics." Advanced Materials **29**(8): n/a-n/a.

Suk, J. W., A. Kitt, C. W. Magnuson, Y. Hao, S. Ahmed, J. An, A. K. Swan, B. B. Goldberg and R. S. Ruoff (2011). "Transfer of CVD-Grown Monolayer Graphene onto Arbitrary Substrates." ACS Nano **5**(9): 6916-6924.

Suk, J. W., W. H. Lee, J. Lee, H. Chou, R. D. Piner, Y. Hao, D. Akinwande and R. S. Ruoff (2013). "Enhancement of the Electrical Properties of Graphene Grown by Chemical Vapor Deposition via Controlling the Effects of Polymer Residue." Nano Letters **13**(4): 1462-1467.

Sun, X., Z. Liu, K. Welsher, J. T. Robinson, A. Goodwin, S. Zaric and H. Dai (2008). "Nano-graphene oxide for cellular imaging and drug delivery." Nano Research **1**(3): 203-212.

Tang, M., Q. Song, N. Li, Z. Jiang, R. Huang and G. Cheng (2013). "Enhancement of electrical signaling in neural networks on graphene films." Biomaterials **34**(27): 6402-6411.

Taylor, I. M., E. M. Robbins, K. A. Catt, P. A. Cody, C. L. Happe and X. T. Cui (2017). "Enhanced dopamine detection sensitivity by PEDOT/graphene oxide coating on in vivo carbon fiber electrodes." Biosensors and Bioelectronics **89**(Part 1): 400-410.

Thunemann, M., Y. Lu, X. Liu, K. Kılıç, M. Desjardins, M. Vandenberghe, S. Sadegh, P. A. Saisan, Q. Cheng, K. L. Weldy, H. Lyu, S. Djurovic, O. A. Andreassen, A. M. Dale, A. Devor and D. Kuzum (2018). "Deep 2-photon imaging and artifact-free optogenetics through transparent graphene microelectrode arrays." Nature Communications **9**(1): 2035.

Titov, A. V., P. Král and R. Pearson (2010). "Sandwiched Graphene−Membrane Superstructures." ACS Nano **4**(1): 229-234.

Tu, Q., L. Pang, Y. Chen, Y. Zhang, R. Zhang, B. Lu and J. Wang (2014). "Effects of surface charges of graphene oxide on neuronal outgrowth and branching." Analyst **139**(1): 105-115.

Tu, Y., M. Lv, P. Xiu, T. Huynh, M. Zhang, M. Castelli, Z. Liu, Q. Huang, C. Fan, H. Fang and R. Zhou (2013). "Destructive extraction of phospholipids from Escherichia coli membranes by graphene nanosheets." Nature Nanotechnology **8**: 594.

Tu, Z., V. Wycisk, C. Cheng, W. Chen, M. Adeli and R. Haag (2017). "Functionalized graphene sheets for intracellular controlled release of therapeutic agents." Nanoscale **9**(47): 18931-18939.

Varshney, L. R., B. L. Chen, E. Paniagua, D. H. Hall and D. B. Chklovskii (2011). "Structural Properties of the Caenorhabditis elegans Neuronal Network." PLOS Computational Biology **7**(2): e1001066.

Veliev, F., A. Briançon-Marjollet, V. Bouchiat and C. Delacour (2016). "Impact of crystalline quality on neuronal affinity of pristine graphene." Biomaterials **86**(Supplement C): 33-41.

Voiry, D., J. Yang, J. Kupferberg, R. Fullon, C. Lee, H. Y. Jeong, H. S. Shin and M. Chhowalla (2016). "High-quality graphene via microwave reduction of solution-exfoliated graphene oxide." Science **353**(6306): 1413.

Wang, F., B. Liu, A. C. F. Ip and J. Liu (2013). "Orthogonal Adsorption Onto Nano-Graphene Oxide Using Different Intermolecular Forces for Multiplexed Delivery." Advanced Materials **25**(30): 4087-4092.

Wang, L., M. S. H. Boutilier, P. R. Kidambi, D. Jang, N. G. Hadjiconstantinou and R. Karnik (2017). "Fundamental transport mechanisms, fabrication and potential applications of nanoporous atomically thin membranes." Nature Nanotechnology **12**: 509.

Wang, S., P. K. Ang, Z. Wang, A. L. L. Tang, J. T. L. Thong and K. P. Loh (2010). "High Mobility, Printable, and Solution-Processed Graphene Electronics." Nano Letters **10**(1): 92-98.

Wang, S., P.-J. Chia, L.-L. Chua, L.-H. Zhao, R.-Q. Png, S. Sivaramakrishnan, M. Zhou, R. G. S. Goh, R. H. Friend, A. T. S. Wee and P. K. H. Ho (2008). "Band-like Transport in Surface-Functionalized Highly Solution-Processable Graphene Nanosheets." Advanced Materials **20**(18): 3440-3446.

Wang, Y., Z. Li, D. Hu, C.-T. Lin, J. Li and Y. Lin (2010). "Aptamer/Graphene Oxide Nanocomplex for in Situ Molecular Probing in Living Cells." Journal of the American Chemical Society **132**(27): 9274-9276.

Wang, Y., K. Wang, J. Zhao, X. Liu, J. Bu, X. Yan and R. Huang (2013). "Multifunctional Mesoporous Silica-Coated Graphene Nanosheet Used for Chemo-Photothermal Synergistic Targeted Therapy of Glioma." Journal of the American Chemical Society **135**(12): 4799-4804.

Weaver, C. L., J. M. LaRosa, X. Luo and X. T. Cui (2014). "Electrically Controlled Drug Delivery from Graphene Oxide Nanocomposite Films." ACS Nano **8**(2): 1834-1843.

Welsher, K., Z. Liu, D. Daranciang and H. Dai (2008). "Selective Probing and Imaging of Cells with Single Walled Carbon Nanotubes as Near-Infrared Fluorescent Molecules." Nano Letters **8**(2): 586-590.

Wilks, S. J., S. M. Richardson-Burns, J. L. Hendricks, D. C. Martin and K. J. Otto (2009). "Poly(3,4-ethylenedioxythiophene) as a Micro-Neural Interface Material for Electrostimulation." Frontiers in Neuroengineering **2**: 7.

Won, S., Y. Hwangbo, S.-K. Lee, K.-S. Kim, K.-S. Kim, S.-M. Lee, H.-J. Lee, J.-H. Ahn, J.-H. Kim and S.-B. Lee (2014). "Double-layer CVD graphene as stretchable transparent electrodes." Nanoscale **6**(11): 6057-6064.

Xu, Y., Q. Wu, Y. Sun, H. Bai and G. Shi (2010). "Three-Dimensional Self-Assembly of Graphene Oxide and DNA into Multifunctional Hydrogels." ACS Nano **4**(12): 7358-7362.

Yang, H.-W., M.-Y. Hua, T.-L. Hwang, K.-J. Lin, C.-Y. Huang, R.-Y. Tsai, C.-C. M. Ma, P.-H. Hsu, S.-P. Wey, P.-W. Hsu, P.-Y. Chen, Y.-C. Huang, Y.-J. Lu, T.-C. Yen, L.-Y. Feng, C.-W. Lin, H.-L. Liu and K.-C. Wei (2013). "Non-Invasive Synergistic Treatment of Brain Tumors by Targeted Chemotherapeutic Delivery and Amplified Focused Ultrasound-Hyperthermia Using Magnetic Nanographene Oxide." Advanced Materials **25**(26): 3605-3611.

Yang, X., Y. Tu, L. Li, S. Shang and X.-m. Tao (2010). "Well-Dispersed Chitosan/Graphene Oxide Nanocomposites." ACS Applied Materials & Interfaces **2**(6): 1707-1713.

Yi, H., L.-Q. Wu, W. E. Bentley, R. Ghodssi, G. W. Rubloff, J. N. Culver and G. F. Payne (2005). "Biofabrication with Chitosan." Biomacromolecules **6**(6): 2881-2894.

Yu, K. J., Z. Yan, M. Han and J. A. Rogers (2017). "Inorganic semiconducting materials for flexible and stretchable electronics." npj Flexible Electronics **1**(1): 4.

Zanni, E., G. De Bellis, M. P. Bracciale, A. Broggi, M. L. Santarelli, M. S. Sarto, C. Palleschi and D. Uccelletti (2012). "Graphite Nanoplatelets and Caenorhabditis elegans: Insights from an in Vivo Model." Nano Letters **12**(6): 2740-2744.

Zhang, S., K. Yang, L. Feng and Z. Liu (2011). "In vitro and in vivo behaviors of dextran functionalized graphene." Carbon **49**(12): 4040-4049.

Zhang, X., J. Yin, C. Peng, W. Hu, Z. Zhu, W. Li, C. Fan and Q. Huang (2011). "Distribution and biocompatibility studies of graphene oxide in mice after intravenous administration." Carbon **49**(3): 986-995.

Zhang, Y., S. F. Ali, E. Dervishi, Y. Xu, Z. Li, D. Casciano and A. S. Biris (2010). "Cytotoxicity Effects of Graphene and Single-Wall Carbon Nanotubes in Neural Phaeochromocytoma-Derived PC12 Cells." ACS Nano **4**(6): 3181-3186.

Chapter 2

Membrane cholesterol mediates the cellular effects of monolayer graphene substrates

Abstract

Graphene possesses extraordinary properties which promise great potential in biomedicine. However, fully leveraging these properties requires close contact with the cell surface, raising the concern of unexpected biological consequences. Computational models have demonstrated that graphene preferentially interacts with cholesterol, a multifunctional lipid unique to eukaryotic membranes. Here, we demonstrate an interaction between graphene and cholesterol. We find that graphene increases cell membrane cholesterol and potentiates neurotransmission, which is mediated by increases in the number, release probability, and recycling rate of synaptic vesicles. In fibroblasts grown on graphene, we also find an increase in cholesterol, which promotes the activation of P2Y receptors, a family of receptor regulated by cholesterol. In both cases, direct manipulation of cholesterol levels elucidates that a graphene-induced cholesterol increase underlies the observed potentiation of each cell signaling pathway. These findings identify cholesterol as a mediator of graphene's cellular effects, providing insight into the biological impact of graphene.

Introduction

Graphene is a two-dimensional material composed of a single-layer of hexagonal sp^2-hybridized carbon atoms (Geim 2009). A consequence of its unique atomic structure, graphene possesses a myriad of attractive chemical and physical properties: exceptionally high electron mobility, thermal conductivity, optical transmittance, mechanical strength, chemical stability, and surface area-to-volume ratio (Geim 2009, Novoselov, Fal′ko et al. 2012). This combination of features has made graphene a promising material for a broad range of biomedical applications, including drug delivery, tissue engineering, biosensing, and neuroprosthetics (Zhang, Nayak et al. 2012, Bitounis, Ali-Boucetta et al. 2013, Mao, Laurent et al. 2013). Furthermore, its superior carrier mobility enables graphene-based electrodes to detect electrochemical changes associated with a variety of cellular activities or to deliver optical or electrical stimuli. For example, graphene electrodes have been used as voltage sensors to measure membrane potential changes at the single cell level and to record electrical activity in neuronal networks *in vitro* and *in vivo* (Kuzum, Takano et al. 2014, Zhang, Dodson et al. 2016). However, a significant drawback to the use of graphene-based devices remains, in that detection efficiency exponentially decreases as the distance from the cells or tissue increases. Therefore, graphene needs to be close to cell or tissue surfaces (Zhang, Dodson et al. 2016) in order to maximize its utility in bioapplications. This then raises a fundamental question: how graphene affects the plasma membrane and related cellular functions.

Prior studies have documented that graphene flakes are destructive to gram-negative bacteria such as *Escherichia coli* through the disruption of plasma membrane integrity (Akhavan and Ghaderi 2010, Hu, Peng et al. 2010, Liu, Zeng et al. 2011). Computational modeling and electron microscopy have suggested that this is the result of nanoscale graphene flakes penetrating the bacterial plasma membrane and dispersing phospholipids (Li, Yuan et al. 2013), which leads

to membrane disintegration and cell death (Tu, Lv et al. 2013). Interestingly, no such cytotoxicity has been reported in eukaryotic cells. Instead, cell proliferation (Nayak, Andersen et al. 2011), differentiation (Wang, Lee et al. 2012), and morphogenesis (Li, Zhang et al. 2011) were improved when graphene with traditional tissue culture coatings was used as a culture substrate. For mouse neurons grown on bare graphene, Veliev *et al* demonstrated that the crystallinity of graphene promotes cell adhesion and neurite outgrowth (Veliev, Briancon-Marjollet et al. 2016), suggesting the significance of close contact between graphene and the cell surface in mediating graphene's effects. Aggregated graphene flakes used as a substrate or applied acutely to mature neuronal cultures resulted in few developmental or morphological changes (Bendali, Hess et al. 2013, Fabbro, Scaini et al. 2016, Rauti, Lozano et al. 2016). Aggregated graphene flakes, however, have very different surface characteristics and physicochemical properties from monolayer graphene substrates (Bo, Zhou et al. 2016). Given the variation in experimental outcomes and the increasing interest in bioapplications of graphene, it remains important to understand how graphene interacts with the eukaryotic plasma membrane and how its diverse cellular effects are realized.

We reasoned that since the plasma membrane is the initial point via which any downstream cellular responses to graphene would be realized, membrane-associated molecule(s) were responsible for the variation of cellular effects in response to graphene. We hypothesized that cholesterol was involved for two reasons: it is unique to and abundant in the eukaryotic plasma membrane but absent from prokaryotic membranes, and it is related to many cellular processes, realized through both direct and indirect interactions with other lipids and proteins (Ikonen 2008). For example, cholesterol influences membrane fluidity (Korade and Kenworthy 2008), facilitates exo-/endocytosis (Subtil, Gaidarov et al. 1999), regulates integral membrane proteins like G

protein-coupled receptors (GPCRs) (Cherezov, Rosenbaum et al. 2007), and organizes cytoskeletal attachment as well as cell adhesion (Head, Patel et al. 2014). The distribution of cholesterol within the cell membrane is highly heterogeneous and dynamic (Ikonen 2008), with trafficking between surface and intracellular membranes helping to maintain overall cholesterol homeostasis. Intriguingly, it has been empirically demonstrated that the planar tetracyclic ring structure of cholesterol may permit it to stack on the graphene surface (Gburski, Górny et al. 2010, Gburski, Gorny et al. 2011, Hibino and Tsuchiya 2014, Zhang and Wang 2015, Zhang, Xu et al. 2016). We thus sought to investigate if and how the cellular effects of monolayer graphene are related to the cell membrane, membrane cholesterol, and associated cellular processes.

Here, we use liquid-phase exfoliation (LPE) of graphene powder to produce suspended graphene flakes (GFs), which enables solution-based measurements to investigate a graphene-cholesterol interaction. GFs extract cholesterol from cholesterol-containing culture media and effectively quench a fluorescent cholesterol analog, suggesting an interaction between graphene and cholesterol. For cell-based studies, we grew both neurons and fibroblast cells on large-area monolayer graphene sheets. In neurons on graphene, we find increased cell membrane cholesterol and significant increases in the number, the release probability, and the turnover rate of synaptic vesicles - all of which are modulated by membrane cholesterol (Chang, Kim et al. 2009, Dason, Smith et al. 2010, Puchkov and Haucke 2013, Yue and Xu 2015). Bidirectional manipulations of membrane cholesterol demonstrate that a graphene-induced membrane cholesterol increase is an underlying mechanism for the potentiated neurotransmitter release. Furthermore, we demonstrate that graphene substrates allosterically enhance the Ca^{2+}-responses of P2Y receptors to ATP

stimulation in a cholesterol-dependent manner. Our findings collectively reveal that cholesterol is a key mediator of graphene's biological effects on eukaryotic cells.

Methods

Graphene production

To produce GFs, we used liquid exfoliation of graphite powder (ASBURY CARBONS, Grade: 2299) in the presence of 2 wt% PVP (molecular weight: 1,300,000 g mol^{-1}, from Sigma) water solution and sonicated for 9 h in a bath sonicator. The uniform GF suspension was then centrifuged with a Thermo Scientific Fiberlite F15-6 X 100y rotor at 4000 r.p.m. and at room temperature for 1 h to sediment large graphite aggregates. The upper 50% of supernatant was carefully decanted, resulting in PVP-functionalized GF suspension (Hernandez 2008) . The transmission characterization of GF suspension was carried out on a Varian Cary 5000 UV-VIS-NIR spectrophotometer. The concentration of GF was estimated with an absorption coefficient of 2460 L/g/m at 660 nm (Hernandez 2008), which is typically 26 mg L^{-1} for freshly made GF suspension. The suspension is stored at 4 °C and remains stable for >3 years. Single-layer graphene sheets were synthesized by CVD on a copper foil with 100 sccm (standard cubic centimeter per minute) hydrogen and 10 sccm methane as the feed gases (Li 2009). A layer of poly(methyl methacrylate) (PMMA) was then spin-coated onto the graphene film that was grown on the copper foil, which was later removed through wet etching in ferric chloride solution. Subsequently, the graphene film was transferred onto glass coverslips, and the PMMA support was dissolved in acetone.

Raman spectroscopic characterization of graphene

The quality of graphene sheets was examined by a DXR Raman Microscope (Thermo Scientific). A 532-nm laser (~5 mW power) was expanded and focused to a diffraction-limited laser spot (<1 μm) through a 50× Olympus objective. The intensity features of graphene Raman spectra could be found at ~1590 and ~2680 cm^{-1}, corresponding to the G and 2D modes, respectively. The high 2D-to-G intensity ratio (>1) and symmetric shape of the 2D peak indicate that the graphene is monolayer. For Raman mapping, the samples were moved by a motorized microscope stage at a step of 1 μm for both *x* and *y* axis. A Raman spectrum was recorded at each position, and the intensities of the G and 2D modes were plotted to form spatially resolved images.

Cholesterol assay

An enzymatic assay (Amplex Red Cholesterol Assay Kit, Life Technologies) was used to quantify free cholesterol concentrations according to the manufacturer's instructions (Amundson and Zhou 1999). Briefly, a serial dilution of cholesterol standard (0, 2, 5, 10, 15 and 20 μM) was used to generate a calibration curve. One-milliliter aliquots of media were incubated as prepared or with the addition of 0.002 wt% PVP in phosphate-buffered saline (PBS), or 260 ng mL^{-1} graphene nanoflakes (GFs) with 0.002 wt% PVP in PBS at 37 °C and 5% CO_2 for 24 h. Graphene fractions were separated from media using Amicon centrifugal filters (100 kDa, Millipore) and resuspended in 1 mL of fresh media. The flow-through media was also collected for the graphene fraction. Media alone, media incubated with PVP, GNFs separated from media, and flow-through media were assayed. The fluorescence intensities of all enzymatic reaction products were measured using a spectrofluorometer (FluoroMax-4, Horiba). Excitation and emission slit widths were set at 5 nm for all measurements. Samples were excited at 570 nm, and emission was measured at 590 nm. For each group, four different batches of media were used, and four

independent measurements were performed for each media sample. Cholesterol concentrations were then calculated using the standard curve.

Spectrofluorometer measurements

TFC (Avanti) or BODIPY (Thermo Fisher) were diluted in water at a final concentration of 1.3 μM and incubated at room temperature for all time points. All fluorescence emission measurements were performed using a FluoroMax-4 spectrofluorometer (Horiba). Excitation and emission slit widths were set at 5 nm for all measurements. Samples were excited at 400 nm to avoid spectral bleed-through and non-specific excitation in mixed solutions. Emission spectra were collected from 500 to 650 nm. Three replicates were scanned three times each for every sample and the result averaged. Subsequently, averaged intensities were corrected for the broadband absorbance of either graphene or PVP across the emission spectra, as defined by:

$$F_{TFC,\lambda}+(1-T)F_{TFC,\lambda}F_{TFC,\lambda}+(1\text{-}T)F_{TFC,\lambda},$$

where F is the fluorescence emission value at a wavelength for TFC and T is the transmittance value at that same wavelength for graphene or PVP calculated from the Beer–Lambert relationship. Data smoothing was performed using a nine-point Savitzky–Golay filter in Matlab.

Cell culture

All animal procedures and all experimental procedures were approved by the Vanderbilt University Animal Care and Use Committee (VUACUC, #M1500052) and were performed in accordance with the VUACUC approved guidelines and regulations. Rat hippocampal cultures were prepared as previously described. Hippocampal neurons (CA1–CA3) derived from postnatal

(P0/P1) Sprague–Dawley rats of both sexes were used. Neurons were dissociated to a single-cell suspension, recovered by centrifugation, and resuspended in plating media composed of Minimal Essential Medium (MEM, Life Technologies) containing (in mM) 27 glucose, 2.4 $NaHCO_3$, 0.00125 transferrin, 2 L-glutamine, 0.0043 insulin, and 10%/vol fetal bovine serum (FBS, Omega). Because of the addition of FBS, all neuronal media contained cholesterol. Cell resuspension was deposited on round 12 mm coverslips at a density of ~200,000 cells/mL for two different surface conditions: bare glass or graphene-coated glass. After 2 h, 1 mL of culture media was added, a 1:1 mixture of plating and 4-Arac-containing media: MEM containing (in mM) 27 glucose, 2.4 $NaHCO_3$, 0.00125 transferrin, 1.25 L-glutamine, 0.0022 insulin, 2 Ara-C, 1 %/vol B27 supplement (Life Technologies), and 7.5 %/vol FBS. Ara-C mimimized astroglia proliferation. For cell attachment studies, coverslips were washed three times with Hank's solution and cells remaining in randomly selected fields of view were counted. Sister cultures supplying conditioned media were prepared in the same manner, except that 1 mL of plating media was added 4 h after plating to allow glial cell proliferation. After the confluence of glial cells (~2 DIV), 1 mL of 4-Arac media was added. For cells growing on graphene and glass, after 2 DIV, 1 mL of culture media was replaced with an equal volume of conditioned media from sister cultures. Experiments were performed on cultures at 3 and 7 DIV for developmental studies and between 13 and 17 DIV for all other studies using neurons.

NIH-3T3 cells were grown at 37 °C with 5% CO_2 in Dulbecco's modified Eagle's medium containing 4.5 g L^{-1} glucose and l-glutamine supplemented with 10% FBS, 100 units/mL penicillin, and 100 μg mL^{-1}streptomycin. Because of the addition of FBS, this media also contains cholesterol. Cells were regularly passaged to maintain adequate growth and were passaged at least five times before trypsinization and plating on either graphene-coated or bare glass coverslips

(25 μL or ~2×10^6cells per coverslip). Cells were grown to 50–80% confluence for 24 h on coverslips prior to imaging.

Filipin staining and image analysis

Cells were fixed in PBS containing 4% paraformaldehyde for 30 min, washed, and incubated with filipin (1:500 in PBS, Sigma-Aldrich) for 2 h at room temperature. Fluorescence imaging was performed on an Olympus IX-81 inverted microscope using a Nikon Intensilight illuminator, a Nikon Plan Apo VC 20× objective (N.A. 0.75) and a fluorescence filter set (Ex 390/40, DiC T425LPXR, Em 460/50, Semrock). Images were acquired with a CoolSnap K4 CCD camera (Photometrics) via Micro-manager with the same acquisition settings (exposure time = 300 ms and gain = 1) across each experimental group. For analysis, three independent batches of cultures were analyzed ($n > 9$ different coverslips). The total number of neurites or cells analyzed are reported (see figure legends). For the analysis of neurons, we manually selected ROIs covering neurites (Figs. 3 and 8) of morphologically identified neurons. Neurite selections were drawn to be approximately the same length for each ROI. For analysis of 3T3 cells, we used a threshold-based approach in ImageJ with a common threshold setting for all images in all experimental groups to select ROIs corresponding to cells. Average ROI intensity was measured in ImageJ. For every field of view (FOV), at least three ROIs from cell-free regions were manually selected, and their mean fluorescence intensities were calculated in the same manner. For background subtraction, the mean intensity value of every cell-containing ROI was subtracted by the average intensity of the three background ROIs in the same image.

Immunocytochemistry and image analysis

For immunostaining after electrophysiological recordings, coverslips containing recorded cells were fixed in PBS containing 4% paraformaldehyde, washed, blocked for 1 h with PBS containing 1% BSA, and incubated overnight at 4 °C with diluted primary antibodies (TuJ1—1:500, Synaptophysin—1:2000, and Streptavidin—1:500, all from Synaptic Systems). Secondary antibodies with distinct fluorophores (Alexa 488, 568 and 647, 1: 500 dilution for all, Biotium) were then incubated at room temperature for 2 h. Fluorescence imaging was performed on an Olympus IX-51 inverted microscope with a 60× UPlanFL (N.A. = 1.25) objective and a Flash 4.0 sCMOS camera (Hamamatsu). The optical filter sets (Chroma and Semrock) for Alexa 488, 568, and 647 fluorescence were, respectively: Ex 470/20 DiC 510LP 535/25, Ex 565/25 DiC 585LP Em 630/90, and Ex 630/60 DiC 660LP Em 695/100. For each fluorescence channel, images were taken with the same acquisition settings (excitation light intensity and exposure time: 500 ms for Alexa 488 anti-mouse, 500 ms for CF568 Streptavidin, 50 ms for Alexa 647 anti-guinea pig). Biocytin-positive neurons were positioned approximately in the center of the fields of view for imaging. Not all electrophysiologically recorded neurons were identified and imaged, as some were damaged during Biocytin infusion.

For Syp intensity analysis, a set of overlapping masks were used to restrict analysis to synapses on the processes of cells that were recorded (biocytin+). Binary masks of biocytin+ cells were generated by intensity-based global thresholding in ImageJ using a common threshold setting for the minimum value. Syp images corresponding to the same FOV were also thresholded to generate a second binary mask. Using the Boolean logic function in ImageJ, a new mask was generated from the intersection of the Syn+ and biocytin+ masks (AND function). This mask was then subjected to minimum particle size restrictions and ROI sets were generated for each FOV. These ROI sets were applied to the original Syp image and mean intensities were measured. For

cluster analysis, the standard deviation of the values obtained from the Syp intensity measurement were used. Background subtraction was performed on intensity values measured from each FOV by subtraction of the average of at least three different manually selected ROIs from cell-free areas of the Syp channel. Data were pooled for analysis, and the total number of synapses analyzed for each condition are reported in the figure legends.

Sholl analysis

Using the immunolabeled streptavidin-filled neurons from above, Sholl analysis was performed on images taken on an Olympus IX-51 inverted microscope with a 60× UPlanFL (N.A. = 1.25) objective and a Flash 4.0 sCMOS camera (Hamamatsu). The center of the filled soma was marked as the starting point and concentric circles spaced equidistantly were drawn. At each distance, the number of intersections was manually counted. Manual counting was taken as the best ground truth to exclude possible artifacts from image thresholding and further to ensure that all counted projections originated from the cell of interest. Error bars represent the S.E.M. of the pooled intersections from all cells in a treatment group at each distance.

Electrophysiology

At least three coverslips from five batches of neuronal culture were selected for recording, using at least one neuron per coverslip. Whole-cell voltage clamp recordings were performed on 13–17-DIV neurons using a Multi-Clamp 700B amplifier, digitized through a Digidata 1440 A, and interfaced via pCLAMP 10 (all from Molecular Devices). All recordings were performed at room temperature. Cells were voltage clamped at −70 mV for all experiments. Patch pipettes were pulled from borosilicate glass capillaries with resistances ranging from 3 to 6 MΩ when filled with

pipette solution. The bath solution (Tyrode's saline) contained (in mM): 150 NaCl, 4 KCl, 2 $MgCl_2$, 2 $CaCl_2$, 10 N-2 hydroxyethyl piperazine-n-2 ethanesulphonic acid (HEPES), 10 glucose, pH 7.35. The pipette solution contained (in mM): 120 Cesium Methanesulfonate, 8 CsCl, 1 $MgCl_2$, 10 HEPES, 0.4 ethylene glycol-bis-(aminoethyl ethane)-*N*,*N*,*N*',*N*'-tetraacetic acid (EGTA), 2 MgATP, 0.3 GTP-Tris, 10 phosphocreatine, QX-314 (50 μM), 5 biocytin (Tocris), pH 7.2. For the recordings of mEPSCs, bath solution was supplied with 1 μM tetrodotoxin (TTX, Abcam). The last 50 mEPSCs at the end of 5 min recordings in the presence of TTX were collected and analyzed using template-based event detection. The template was generated from our own representative data. To measure AMPA receptor currents, 20 μM D-(-)-2-Amino-5-phosphonopentanoic acid (D-AP5, Abcam), an NMDA receptor antagonist, was added to the bath solution. NMDA receptor currents were recorded in the presence of 10 μM 2,3-dihydroxy-6-nitro-7-sulfamoylbenzo[f]quinoxaline-2,3-dione (NBQX, Abcam), an AMPA receptor antagonist, in 0 mM [Mg^{2+}]/3 mM [Ca^{2+}] bath solution at −70 mV holding potential. Isolated AMPA and NMDA EPSCs were recorded from the same neurons sequentially by first applying D-AP5 then completely replacing it with NBQX. The NMDA/AMPA ratio for every neuron was calculated from the average amplitudes of the last 10 NMDA and AMPA events during 5 min D-AP5 or subsequent NBQX application. No postsynaptic currents were detected if D-AP5 and NBQX were applied together. All signals were digitized at 20 kHz, filtered at 2 kHz, and analyzed offline in Clampfit (Molecular Devices).

Live cell fluorescence imaging and image analysis

Live cell imaging was performed with 13–17 DIV cells using an Olympus BX-51WI microscope equipped with a 60× LUMPPlanFl water-immersion objective (N.A. 0.9), a Sutter

Instrument MP-78 xyz motorized stage, a Solamere laser combiner and launcher (405, 480, 561, and 640 nm lasers), a Yokogawa CSU-X1 spinning disk confocal head, and an Evolve 512 EMCCD (Photometrics). For TFC, GP, and Ca^{2+}imaging, cells growing on bare or graphene-covered glass coverslips were pre-incubated with TFC (20 min, 1 μM, Avanti), C-laurdan (1 h, 1 μM, TP Probes), or Rhod-2 AM ester (30 min, 1 μM, Biotium) at 37 °C with 5% CO_2. After dye loading, coverslips were washed and mounted in an RC-26G imaging chamber (Warner Instruments) bottom-sealed with a 24 × 40 mm^2 size 0 cover glass (Fisher Scientific). The chamber was fixed in a PH-1 platform (Warner Instruments) fixed on the MP-78 stage and bath solutions were applied via gravity perfusion with a constant rate of ~50 μL/s. All perfusion lines were merged into an SHM-6 in-line solution heater (Warner Instruments). The temperatures of both the imaging chamber and the perfusion solution were maintained at 34 °C by a temperature controller (TC344B, Warner Instruments). For FM dye or Quantum dot (Qdot) loading of the evoked pool of synaptic vesicles, mounted coverslips were incubated with 10 μM FM1-43, 10 μM FM4-64, or 100 or 0.8 nM Qdots (Qdot 605, Thermo Fisher) for 2 min in high K^+bath solution containing (in mM): 64 NaCl, 90 KCl, 2 $MgCl_2$, 2 $CaCl_2$, 10 N-2 hydroxyethyl piperazine-n-2 ethanesulphonic acid (HEPES), 10 glucose, 1 μM TTX, pH 7.35. For Qdot loading of the spontaneous pool of synaptic vesicles, cells were incubated with 100 nM Qdots for 15 min in normal Tyrode's solution. The Qdots used here had a hydrodynamic diameter of ~15 nm, limiting loading to one per synaptic vesicle (~25 nm luminal diameter) (Zhang, Cao et al. 2007, Zhang, Li et al. 2009). After FM or Qdot loading, cells were washed with normal Tyrode's solution containing 10 μM NBQX and 20 μM D-AP5 for 5 or 10 min, respectively, to remove surface dye/Qdots. Electric field stimulation (10 Hz, 70 V) was triggered by a 5-V 2-ms TTL pulse generated by the Clampex software 30 s after imaging began and delivered via a pair of platinum wires attached to both sides of the imaging

chamber by a Grass SD9 stimulator. Synchronization of perfusion with image acquisition was via a VC-6 valve system (Warner Instruments) and controlled in Clampex.

For TFC imaging, a 100 mW 480-nm laser (20% power) and a filter combination of DiC 500LX and Em 520/20 were used. Exposure time was 100 ms and the EM gain was 250 for all images. For every FOV, 10 repeated images were taken and averaged. For FM1-43 imaging, laser and filter sets were the same as those for TFC. Exposure time was 50 ms, the EM gain was 300, and the acquisition rate was 1 Hz. For GP imaging using C-laurdan, a 405-nm laser (40% power) and a filter combination of a DiC 409LP and an Em 440/40 or 483/32 (for blue or green channels, respectively) were usually used. For TFC pretreated cells, we used an arc lamp (LUMen 200, Prior) and a D350x excitation filter (Chroma) to avoid spectral cross-excitation of TFC. The exposure time was 50 ms with an EM gain of 900 for all images. For every FOV and each fluorescence channel, 10 repeated images were taken and averaged. For Ca^{2+} imaging, a 100 mW 561-nm laser (20% power) and a filter combination of DiC 580LPXR and Em 605/52 were used. The exposure time was 150 ms, the EM gain was 500 for all images, and the acquisition rate was 1 Hz. For Qdot imaging, a 480-nm laser (80% power) and a filter combination of DiC 510LX and Em 605/10 were used. The exposure time was 200 ms, the EM gain was 250 for all images, and the acquisition rate was 5 Hz. For FM4-64 imaging, a 50-mW 640-nm laser (30% power) and a filter combination of DiC 660LX and Em 710/50 were used. The exposure time was 50 ms, the EM gain was 500 for all images, and the acquisition rate was 1 Hz. For static images, 10-frame stacks were averaged. All images were taken with the same acquisition settings between sample groups (laser intensity, exposure time, and EM gain).

Image analyses were performed in ImageJ. Four rectangular ROIs were drawn in cell-free regions in every FOV and their intensities averaged. For fluorescence imaging of TFC, C-laurdan

(blue channel), FM1-43 (first 10 frames), FM4-64 (first 10 frames), and Rhod-2 AM, we pooled all background ROIs regardless of treatment differences in order to calculate the mean and standard deviation of the background intensity. Again, a masked threshold approach was applied in ImageJ, and the mean intensity plus two standard deviations was used as the common threshold for all images or image stacks. For every FOV, ROIs were generated by particle analysis based on a binary threshold mask. For TFC loading, watershed segmentation was used to generate ROIs. For FM1-43 and FM4-64, watershed segmentation and particle size limits (0.3–3 μm) were applied in ImageJ to isolate ROIs for synaptic boutons (~1 μm). ΔFM4-64 is defined here as the difference of FM4-64 fluorescence intensity before and after four rounds of exhaustive stimulation.

For Rhod-2, FM1-43, and FM4-64 time-lapse data, the average intensity from four background ROIs was subtracted from the average intensity of each individual ROI in the same FOV. Normalization was performed using the average intensity of the first 10 frames. For C-laurdan images, ROIs generated from blue channel images were used to analyze both channels. GP value was calculated as $I_{GP} = (I_{blue} - G \times I_{green})/(I_{blue} + G \times I_{green})$, in which G is the sensitivity correction factor between the two channels. G was empirically determined by imaging 1 μM C-laurdan diluted in dimethyl sulfoxide (DMSO) using the prescribed protocol. Given $GP_{DMSO} = 0.006$, the G value of our imaging setup was calculated using the following formula: $G = (I_{blue} \times (1 - GP_{DMSO}))/(I_{green} \times (1 + GP_{DMSO}))$. For Qdot images, FM4-64-defined ROIs were applied and the mean Qdot photoluminescence intensity in each ROI was calculated. Quantal analysis for single Qdots was performed as described previously (Zhang, Cao et al. 2007, Zhang, Li et al. 2009). Briefly, maximum likelihood estimates were used to fit Qdot counts to a distribution of intensities. Qdot intensities were binned every 30 a.u. without background subtraction. The estimated threshold based on the mean background signal plus two standard

deviations was near 3000 a.u. by which we set the cut-off for a single Qdot. To analyze the behavior of vesicles labeled by single Qdots, we selected ROIs having only one Qdot. Time-dependent Qdot photoluminescence traces were extracted with a five-frame moving window.

Statistical analysis

All experiments were carried out blindly and repeated in at least three different batches of cultures ($N \geq 3$). All imaging experiments were repeated with at least three randomly selected coverslips per batch with one randomly chosen FOV per coverslip. No statistical methods were used to predetermine sample size. All values presented are mean ± S.E.M. All fluorescence intensity values are background corrected except in Figure S5a. For two-group comparison of average values, data were first assessed for normality using the Lillefors test. Unpaired two-tailed *t*-tests or the Wilcoxin rank-sum test were used for two-group comparison of average values. Cumulative distribution functions (FM dye and Qdot imaging) or histograms (GP imaging) were used for two-group comparison of pooled values. Cumulative distributions are an accepted measure to provide an overview of intensity distributions from synapses (Thiagarajan, Lindskog et al. 2005) and more clearly demonstrate the overall trend of the individual data points than an average measure. For GP imaging data, all individual pixels from each FOV were pooled from each treatment condition as the GP distributions for the generation of test statistics. Kolmogorov–Smirnov tests were used to compare distributions. For Sholl analysis datasets, statistics were calculated using two-way analysis of variance (ANOVA) with repeated measures followed by the Bonferroni multiple comparisons test. ω^2 values were calculated as effect-size metrics for relevant ANOVA data. A one-way ANOVA and the Tukey–Kramer method as post-hoc analysis was used for three or more groups. Fisher *z*-tests were used to compare correlation coefficients. Because the

sample sizes of several reported values are large and thus may overestimate true significance (Sullivan and Feinn 2012), Cohen's *d*-statistic (Hentschke and Stuttgen 2011) was also reported for some datasets.

Characterizing an interaction between graphene and cholesterol

To test graphene's ability to attract cholesterol, we produced GFs from graphite powder using a well-established LPE protocol (Hernandez, Nicolosi et al. 2008). GFs were suspended in 2 wt% polyvinylpyrrolidone (PVP) at 260 ng/mL to prevent aggregation. We mixed this suspension with serum-containing neuronal culture media and incubated for 24 hours to mimic chronic exposure during culture. Serum in our culture media contains cholesterol (see result below and Methods), which enabled us to measure cholesterol adsorption onto the graphene surface. GFs were separated out by size-dependent filtration and subjected to an enzymatic cholesterol assay (Amundson and Zhou 1999). The remaining fraction, untreated fresh media, and media mixed with PVP (as a vehicle control) were assayed in the same manner.

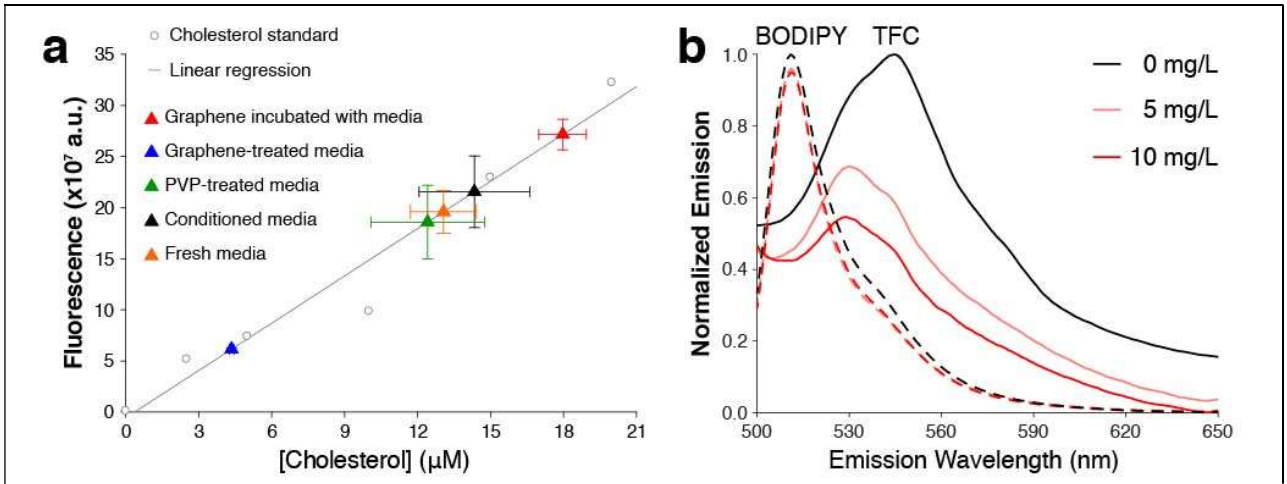

Figure 2.1 **Graphene interacts with cholesterol. (a)** Cholesterol concentrations (based on the working curve generated from cholesterol standards, gray circles and line) in fresh serum-

containing (orange triangle), untreated (black triangle), PVP-treated (green triangle), graphene-treated media (blue triangle), and graphene incubated with media (red triangle). n = 4 samples per batch, N = 4 total batches. Error bars are S.E.M. **(b)** Spectrofluorometer measurements of BODIPY (dashed line) and TFC (solid line) emission after 1-hour incubation with graphene (light or dark red), adjusted for the concentration-dependent broadband absorbance of graphene (**Fig. 2.2**) and normalized to the maximum value of 0 mg/L graphene and minimum value of 10 mg/L graphene at each measured wavelength for both dyes.

After calibration by a cholesterol standard, we determined that cholesterol concentrations in the PVP-treated media (12.4 ± 2.3 μM) and untreated fresh media (12.3 ± 0.9 μM) were similar. The GFs fraction (graphene incubated with media) showed a significantly higher cholesterol concentration (18.0 ± 1.0 μM), while there was a correspondingly lower concentration (4.3 ± 0.1 μM) in the remaining fraction (graphene-treated media) (**Figure 2.1a**), suggesting that GFs extract cholesterol from culture media. To verify that this was due to an interaction between graphene and cholesterol rather than the non-specific adsorption of proteins that cholesterol is complexed with, we used a fluorescent cholesterol analog, TopFluor Cholesterol (TFC, a.k.a. BODIPY-cholesterol). TFC is biophysically similar to cholesterol and thus can be used to study cell membrane cholesterol in live cells (Hölttä-Vuori, Uronen et al. 2008, Holtta-Vuori, Sezgin et al. 2016, Sezgin, Can et al. 2016). Since graphene is a highly efficient acceptor in Förster resonance energy transfer (Kasry, Ardakani et al. 2012), we reasoned that TFC fluorescence would be quenched if an interaction stabilized cholesterol on the GFs surface. In line with this prediction, spectrofluorometry measurements demonstrated that GFs significantly reduced TFC fluorescence in a concentration- and time-dependent manner (**Figure 2.1b** and **Figure 2.2**).

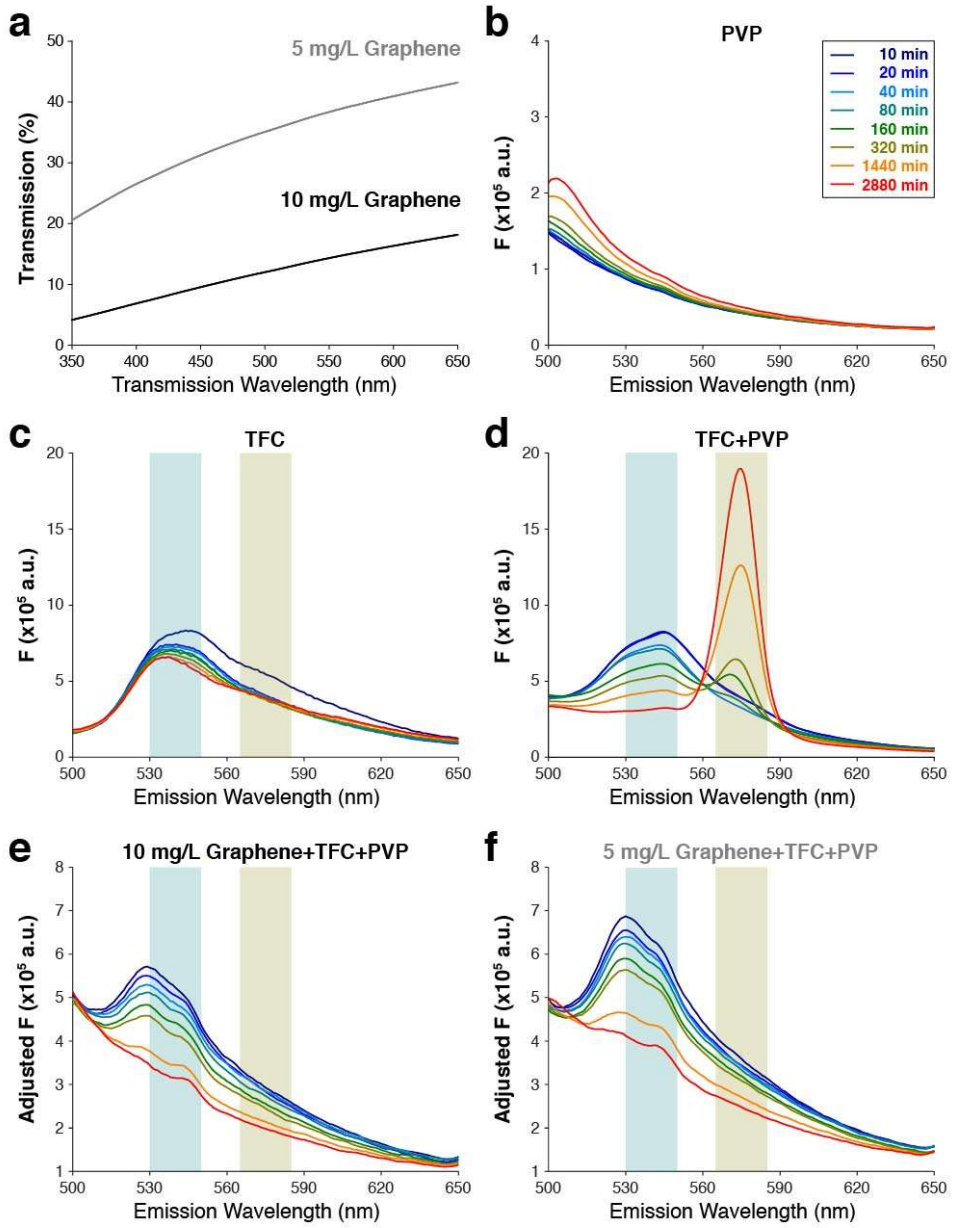

Figure 2.2 **Spectrofluorometry demonstrates an interaction between TFC and graphene. (a)** Transmission spectra of 5 and 10 mg/L graphene (gray and black, respectively) in H_2O with 2 wt% PVP show a concentration-dependent broadband graphene absorbance. **(b)** Time-lapse emission spectra of 2 wt% PVP in H_2O. **(c)** 1.3 μM TFC in H_2O shows a time-dependent fluorescence decay in the 530-549 nm range (cyan box, the peak of TFC fluorescence in H_2O) and the 565-584 nm range (beige box). **(d)** Addition of 2 wt% PVP to 1.3 μM TFC in H_2O. **(e)** Time-lapse emission spectra of 1.3 μM TFC in H_2O containing 2 wt% PVP and 10 mg/L graphene, adjusted by the absorbance of 10 mg/L graphene. **(f)** Time-lapse emission spectra of 1.3 μM TFC in H_2O containing 2 wt% PVP and 5 mg/L graphene, adjusted by the corresponding absorbance of 5 mg/L graphene.

Furthermore, GFs had little effect on BODIPY fluorescence (**Figure 2.1b**), suggesting the interaction between GFs and TFC is specific to the cholesterol group.

Production and characterization of graphene substrates

Having demonstrated an interaction between GFs and cholesterol, we set out to test if this interaction plays a role in mediating graphene's cellular effects. We produced large films of planar graphene via chemical vapor deposition (CVD), which were solution transferred to bare glass coverslips to be used as culture substrates (**Figure 2.3a**).

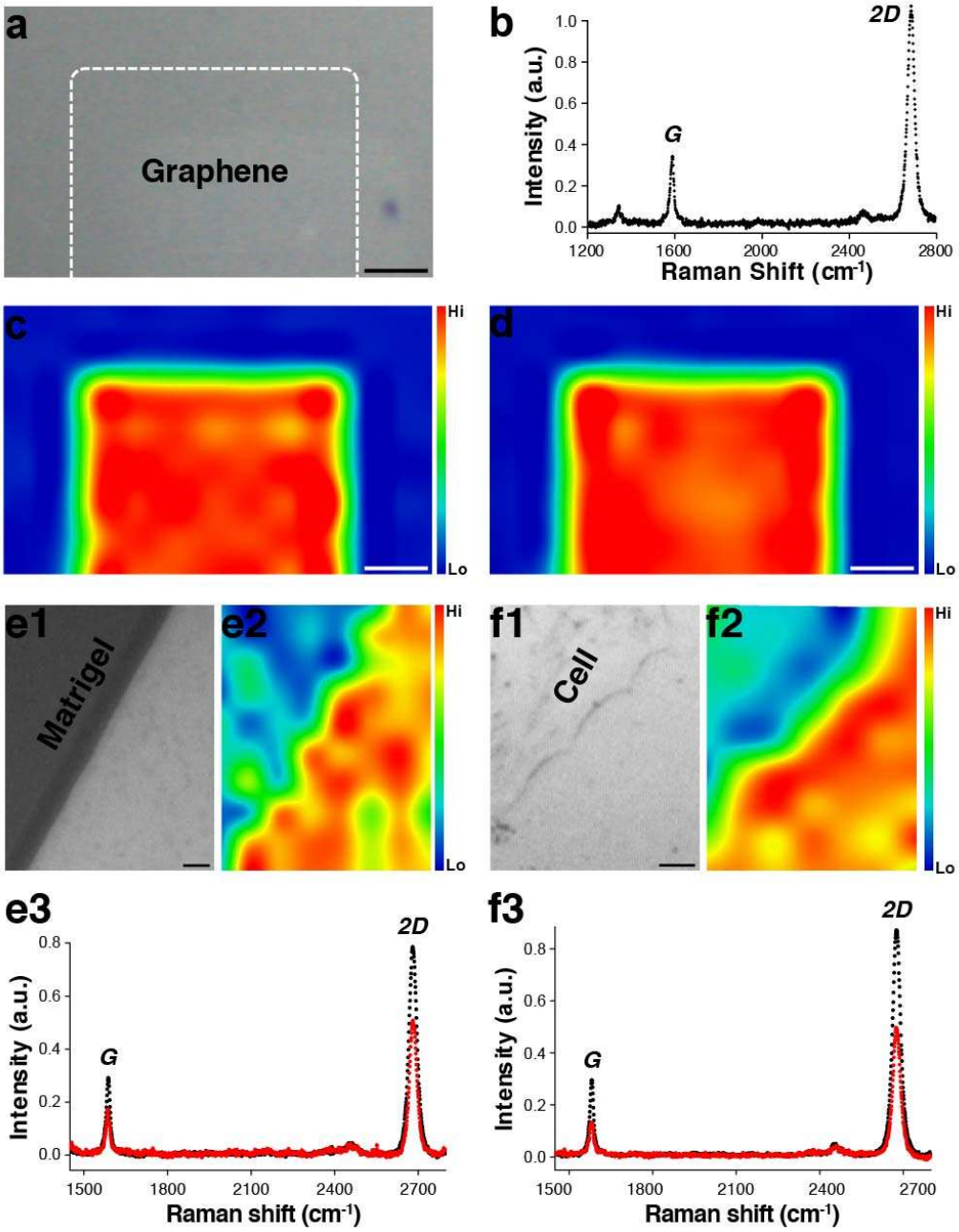

Figure 2.3 **Characterization of graphene films. (a)** Bright field image shows the field of view. Scale bar, 1 mm. **(b)** Raman spectrum at the graphene covered area shows characteristic G and 2D peaks. The high 2D *vs.* G ratio and a symmetric 2D peak are consistent with those of monolayer graphene. Corresponding spatially-resolved map of **(c)** Raman G-peak intensity and **(d)** 2D-peak intensity from the same field of view. Scale bar, 1 mm. **(e)** Bright field image shows the edge of a Matrigel droplet (upper-left) on a graphene-coated glass coverslip. **(f)** Corresponding Raman 2D-peak intensity map. Scale bar, 5 μm. **(g)** Raman spectrum of the bare graphene area (black) shows a high 2D *vs.* G ratio and a symmetric 2D peak, indicating monolayer graphene. At the Matrigel-coated graphene area (red), there is a strong reduction of intensity of both the G and 2D peaks. **(h)**

Bright field image shows the edge of a cell (upper-left) growing on a graphene-coated glass coverslip. **(i)** Corresponding Raman 2D-peak intensity map. Scale bar, 5 μm. **(j)** Raman spectrum at the cell-covered graphene area (red) also exhibits an intensity reduction for both G and 2D peaks in comparison to that at the bare graphene area (black).

The quality of the CVD graphene was examined by Raman spectroscopy. The characteristic 2D and G peaks as well as the large ratio between them (Li, Cai et al. 2009, Lee, Lee et al. 2014) suggest that the graphene films are monolayer (**Figure 2.3b**). Spatially-resolved Raman intensity maps of the G and 2D peaks further demonstrate their uniformity (**Figure 2.3c&d**). Because previous reports have demonstrated that neurons remain viable on uncoated graphene during long-term culture (Bendali, Hess et al. 2013, Fabbro, Scaini et al. 2016, Veliev, Briancon-Marjollet et al. 2016), we omitted Matrigel, an extracellular substrate commonly used for hippocampal cultures (see Methods), and plated dissociated neurons directly on pristine graphene. Conventional hippocampal cultures contain a considerable number of astrocytes (Liu and Tsien 1995), which if allowed to proliferate over the length of the culture period would have covered the substrate surfaces, further limiting the exposure of neurons to graphene. To minimize potential effects from the astrocyte layer, we applied a mitotic inhibitor (Ara-C) immediately after cell plating, which blocks astrocyte proliferation without any effect on non-proliferative cells (i.e. neurons) (Liu and Tsien 1995). However, astrocytes play important developmental and functional roles for neurons, so to compensate for the lack of astrocytes, we routinely supplied cultures with conditioned media (see Methods) harvested from conventional hippocampal cultures prepared in parallel. As a negative control, the same astrocyte-deprived hippocampal cultures were grown on bare glass coverslips and maintained in the same manner.

It is well-established that nanomaterial surfaces will be covered by a variety of biomolecules (i.e. a protein corona) after introduction to any biological system. Although we

omitted a much thicker artificial protein-coating layer (Matrigel) in plating our cultures, we cannot exclude the likelihood of the formation of a protein corona on the graphene surface. However, our cell-free assays demonstrate that cholesterol enrichment on graphene still occurs even in the likely presence of a protein corona after 24-hour incubation (**Figure 2.1a**). We performed Raman spectroscopy on neurons grown on graphene and found that the intensity of both 2D and G peaks were suppressed in cell-containing regions (**Figure 2.3h-j**), similar to what was observed in Matrigel-coated areas (**Figure 2.3e-g**), suggesting that plated neurons change graphene's Raman spectra in the same manner that Matrigel does.

Increased cholesterol in neurons on graphene substrates

Computational studies predict that graphene oriented parallel to the cell surface can induce a local enrichment of cholesterol (Gburski, Gorny et al. 2011, Zhang, Xu et al. 2016). To experimentally investigate possible changes in cholesterol after chronic growth on graphene, we first performed Filipin staining, a conventional method for labeling cholesterol in fixed cells (Maxfield and Wustner 2012).

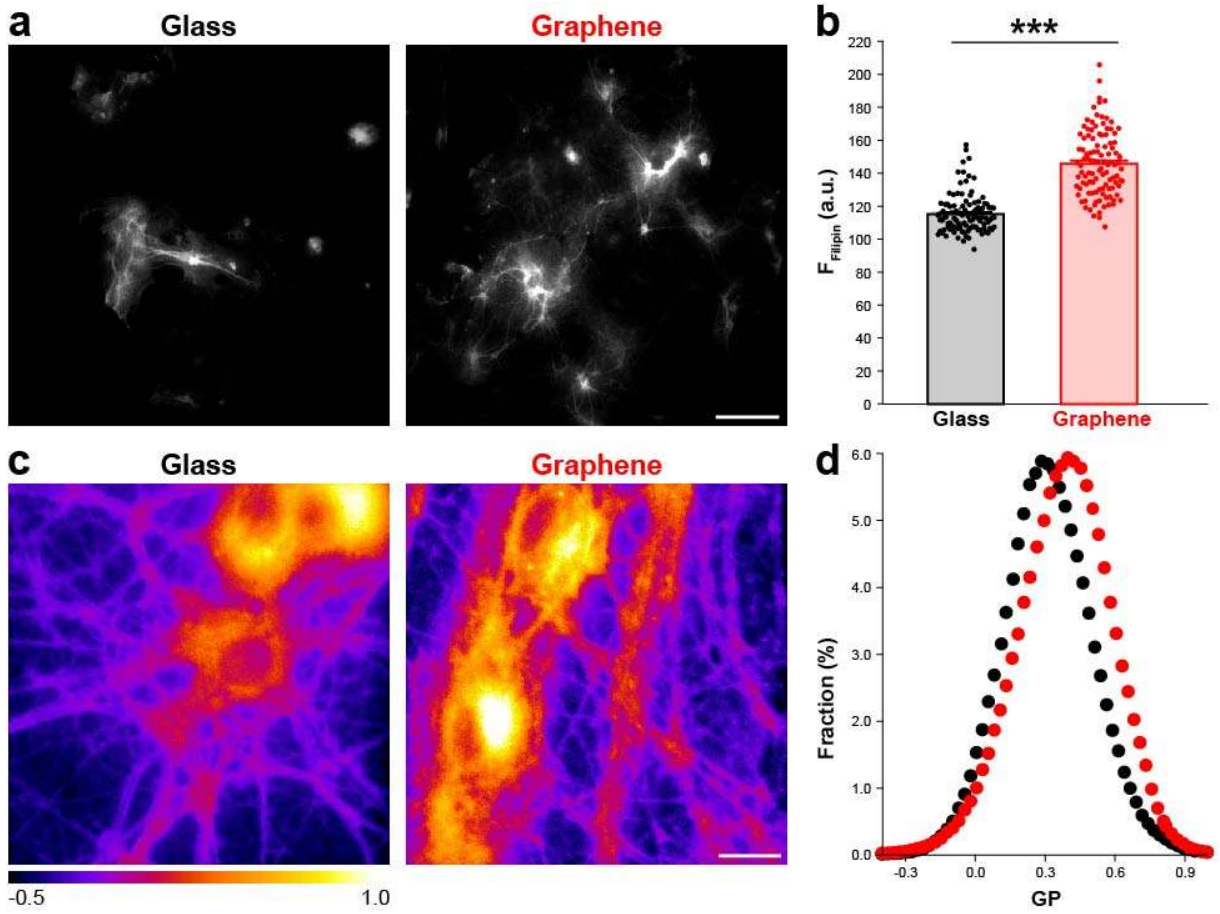

Figure 2.4 **Graphene increases cell membrane cholesterol. (a)** Sample images of Filipin staining. Scale bar, 100 μm. **(b)** Filipin fluorescence intensity in neuronal neurites (n_{glass} = 118 and $n_{graphene}$ = 112 neurites, N = 3 batches, ***, $p < 0.001$, Wilcoxin rank-sum test, Cohen's d = 1.89). (**c**) Sample generalized polarization (GP) images. Scale bar, 20 μm. (**d**) distributions of GP values over individual image pixels (n = 7 FOVs, N = 3 batches for each group; $p < 0.05$, Kolmogorov-Smirnov test of the distributions of GP values, see data analysis section of the methods). Error bars are S.E.M.

We found a 27% increase in Filipin staining intensity in the neurites of neurons cultured on graphene (**Figure 2.4a&b**), suggesting that graphene indeed increased cholesterol in neurites. To determine if a cholesterol increase occurred in live neurons, we turned to generalized polarization (GP) imaging, which uses a ratiometric reporter based on a fluorescent dye sensitive to membrane fluidity. Since membrane fluidity is in turn inversely correlated to membrane cholesterol concentration, GP imaging is commonly used to indirectly measure cholesterol

changes in the cell membrane (Gaus, Zech et al. 2006). We used C-laurdan, a more sensitive and photostable derivative of the commonly used Laurdan (Kim, Choo et al. 2007). GP value was calculated as $(I_{blue}-G\times I_{green})/(I_{blue}+ G\times I_{green})$, in which G is a correction factor and I_{blue} and I_{green} are fluorescence intensity values (Gaus, Zech et al. 2006). We found that C-laurdan fluorescence exhibited a blue-shift on graphene, which translated to an overall shift toward increased GP values, indicating increased plasma membrane cholesterol on graphene substrates (**Figure 2.4c&d**).

Given that TFC has been demonstrated to behave similarly to endogenous cholesterol in membrane incorporation and phase partitioning (Hölttä-Vuori, Uronen et al. 2008, Holtta-Vuori, Sezgin et al. 2016, Sezgin, Can et al. 2016), we used TFC to mimic the membrane distribution of endogenous cholesterol and thus to examine graphene's effect on cell membrane cholesterol. Because of reported differences between TFC and cholesterol in intracellular transportation and lysosomal accumulation (Holtta-Vuori, Sezgin et al. 2016, Sezgin, Can et al. 2016) we used a shorter loading time (1 hour) and lower concentration (1 μM) of TFC; this should largely result in TFC incorporation into the plasma membrane. However, we cannot exclude the possibility that membrane turnover will also result in some intracellular membrane labelling.

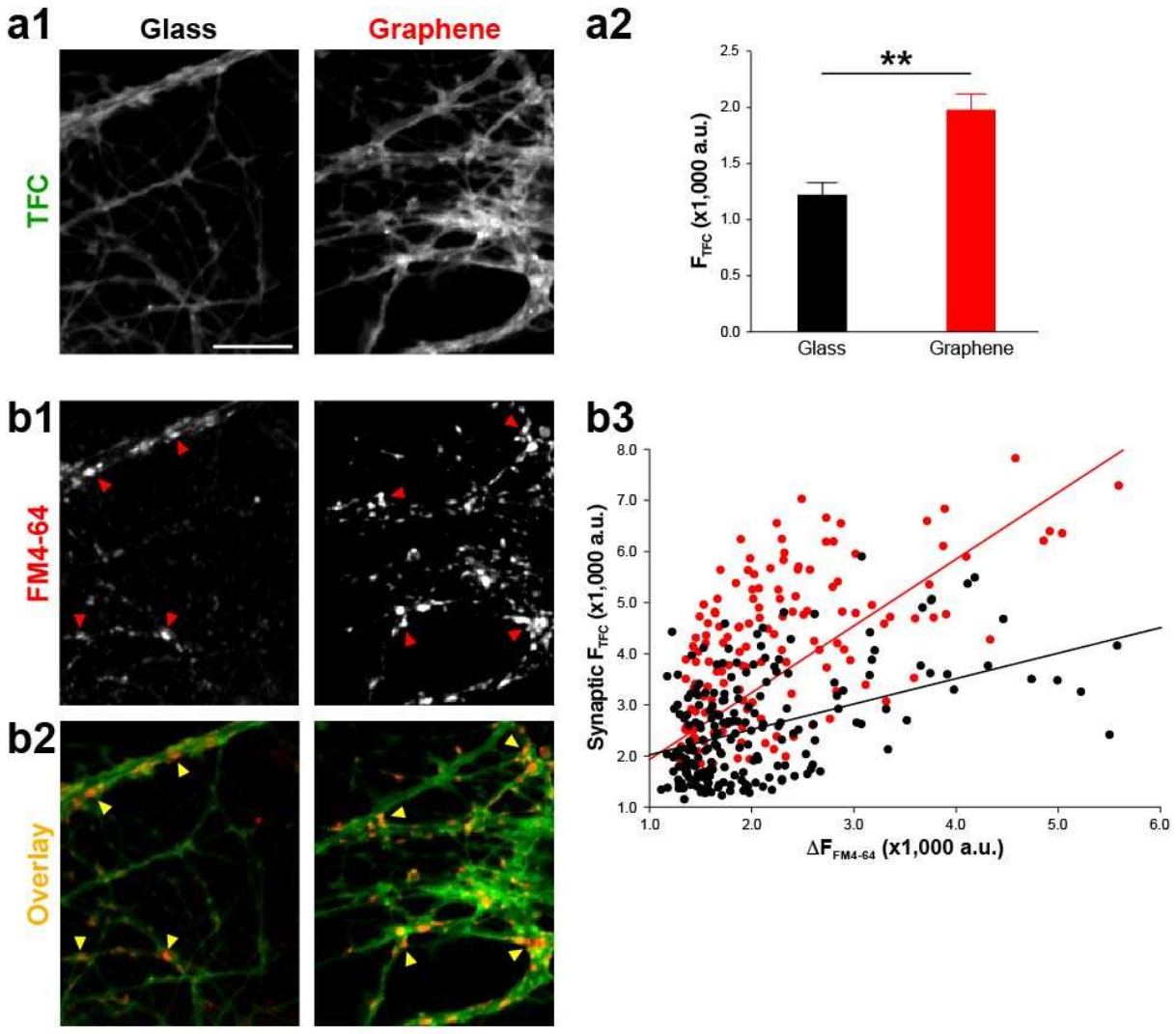

Figure 2.5 **Graphene increases synaptic membrane cholesterol. (a)** Sample images of TopFluor-Cholesterol (TFC) staining of neurons. Scale bar, 10 μm. **(b)** Average TFC staining intensity of threshold defined ROIs (n = 9 FOVs, N = 3 batches for each group, **, $p < 0.01$, two-tailed *t*-test). **(c)** Sample images of FM4-64 staining of neurons. Same scale bar as **a**. Arrowheads indicate examples of synaptic boutons defined by FM4-64 labelling. **(d)** Overlay of **a** and **b**, arrowheads from **b**. **(e)** ΔFM 4-64 fluorescence intensity (see Methods) *vs.* TFC intensity in FM4-64 defined synaptic boutons (both n = 9 FOVs, N = 3 batches for each group; $p < 0.05$, two-tailed *t*-test). Linear regression fittings indicate correlation for graphene ($F_{TFC} = 1.2083 \times F_{FM4-64} - 253.29$ a.u., Pearson correlation coefficient = 0.6629, red solid line) and glass ($F_{TFC} = 0.6273 \times F_{FM4-64} + 837.85$ a.u., Pearson correlation coefficient = 0.5698, black solid line). Error bars are S.E.M.

We found that TFC is distributed throughout neurites (**Figure 2.5a**). Intriguingly, neurons

on graphene showed significantly increased TFC labeling (**Figure 2.5b**). As synaptic boutons generally have a higher cholesterol concentration than other parts of the neuronal membrane (Takamori, Holt et al. 2006, Wilhelm, Mandad et al. 2014) which might thus limit the ability of the membrane to incorporate cholesterol analogue, we then asked if graphene could also increase TFC's membrane insertion within synaptic boutons. To this end, we measured TFC intensity in areas defined by FM4-64 labeling (i.e. synaptic boutons) (**Figure 2.5c&d**, arrow heads), a far-red fluorescent dye which preferentially labels synaptic vesicles (Rouze and Schwartz 1998). Since an increase of synaptic vesicles can increase the total presynaptic membrane area and consequently TFC staining, we examined the relationship between TFC staining and FM4-64 staining (**Figure 2.5e**, scatter plots and regression fits). The overall increase of TFC intensity relative to increases in FM4-64 intensity was higher on graphene (**Figure 2.5e**), suggesting that graphene increases membrane cholesterol regardless of possible changes in synaptic vesicle numbers at synaptic boutons.

Physiological properties of neurons on graphene

To probe if an increase in cholesterol elicited functional effects, we recorded synaptically connected neurons on graphene or glass between 13 and 17 DIV (days *in vitro*) (**Figure 2.6a**).

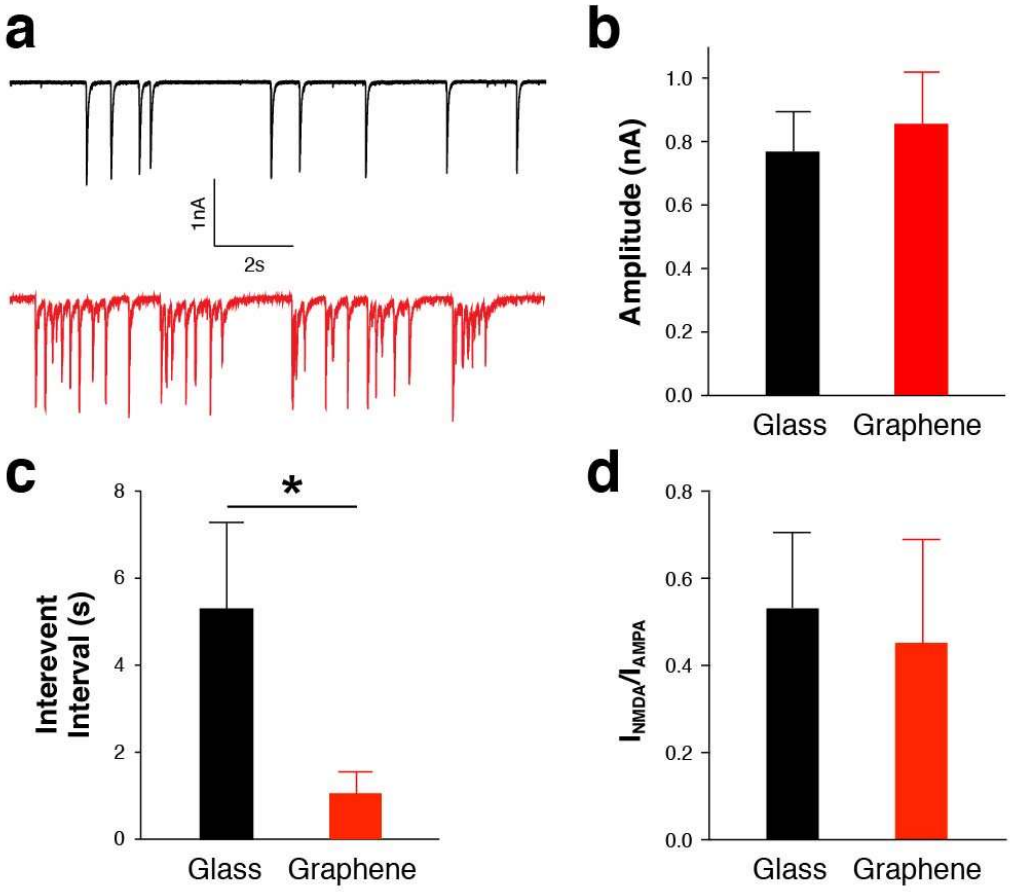

Figure 2.6 **Graphene increases spontaneous firing frequency in neurons. (a)** Sample traces from neurons on glass (black) or graphene (red). **(b)** Mean sEPSC amplitudes (n_{glass} = 13 cells, $n_{graphene}$ = 15 cells, N > 4 batches; p > 0.1, two-tailed t-test, Cohen's d = 0.10). **(c)** Mean sEPSC inter-event intervals (n_{glass} = 13 cells, $n_{graphene}$ = 15 cells, N > 4 batches, *, p < 0.05, two-tailed t-test, Cohen's d = 1.30). **(d)** I_{NMDAR}/I_{AMPAR} (n_{glass} = 10 cells, $n_{graphene}$ = 9 cells, N > 3 batches; p > 0.1, two-tailed t-test, Cohen's d = 0.27). Error bars are S.E.M.

The amplitude of spontaneous excitatory postsynaptic currents (sEPSCs) was slightly but not significantly larger in neurons on graphene (**Figure 2.6b**), while sEPSC frequency was significantly higher (i.e. a shorter inter-event interval) (**Figure 2.6c**). Glutamate is the major excitatory neurotransmitter in our culture configuration and sEPSCs are largely mediated by two ionotropic glutamate receptors: α-amino-3-hydroxy-5-methyl-4-isoxazolepropionic acid receptors (AMPARs) and *N*-methyl-D-aspartate receptors (NMDARs), which have distinct activation and decay kinetics (**Figure 2.7**).

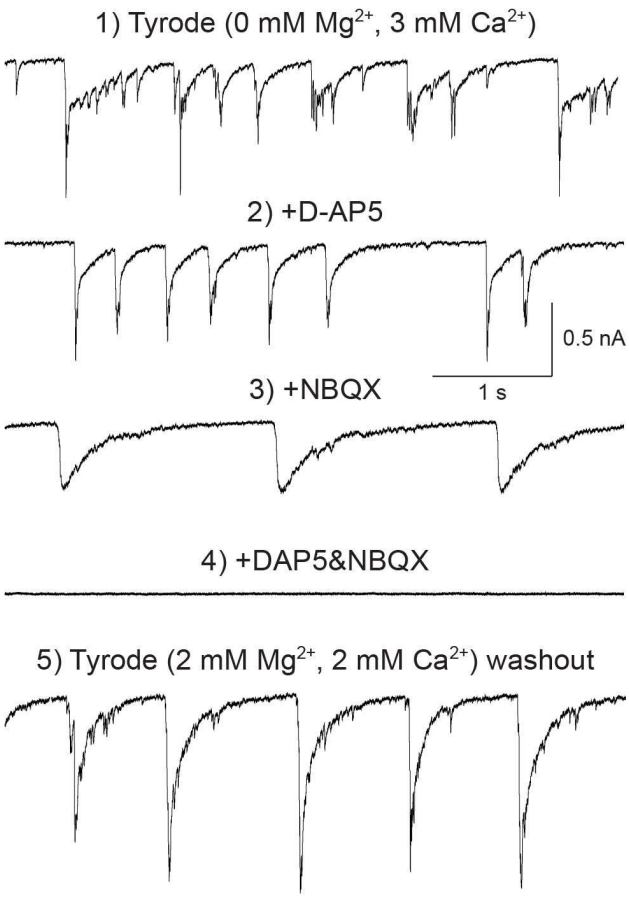

Figure 2.7 **Sequential recording of AMPA and NMDA receptor-mediated EPSCs from the same neurons**. 0 mM Mg^{2+} Tyrode releases the voltage gating of NMDARs and thus results in readily distinguishable AMPAR and NMDAR contributions to the sEPSC records. Addition of the NMDAR antagonist D-AP5 isolates the fast AMPAR component. Addition of the AMPAR antagonist NBQX after wash off of D-AP5 allows the isolation of the slow NMDAR component. Addition of both D-AP5 and NBQX completely eliminates sEPSCs, and washout with 2 mM Mg^{2+} Tyrode's solution recovers sEPSCs that are largely mediated by fast AMPAR components which can also be seen in the traces in (1). 0 mM Mg^{2+}, as shown in (1), also acts to remove the NMDA receptor blockade that exists in normal physiological solution [1]. Thus, the contribution of NMDA-receptor mediated currents are more readily visible in (1) than in (5).

Because changes in sEPSC frequency could be modulated through changes in presynaptic neurotransmitter release or by changes in the postsynaptic composition of NMDARs and AMPARs (measured as the I_{NMDAR} vs. I_{AMPAR} ratio (Malinow and Malenka 2002)), to determine if the increased sEPSC frequency on graphene was driven by postsynaptic mechanisms, we measured

I_{NMDAR}/I_{AMPAR}. Here we observed a small but non-significant decrease in this ratio (**Figure 2.6d**). Taken together with a small but non-significant increase in sEPSC amplitude, this suggested that the effects of graphene are presynaptic.

Morphological characterization of neurons on graphene

To understand the cellular basis of our observed electrophysiological changes, we performed immunofluorescence labeling using antibodies against a selective synaptic vesicle marker, Synaptophysin (Syp), and a neurite-specific marker, β-III Tubulin (Tuj1). Recorded neurons were retrospectively identified by biocytin infused through the patch electrodes (**Figure 2.8a**).

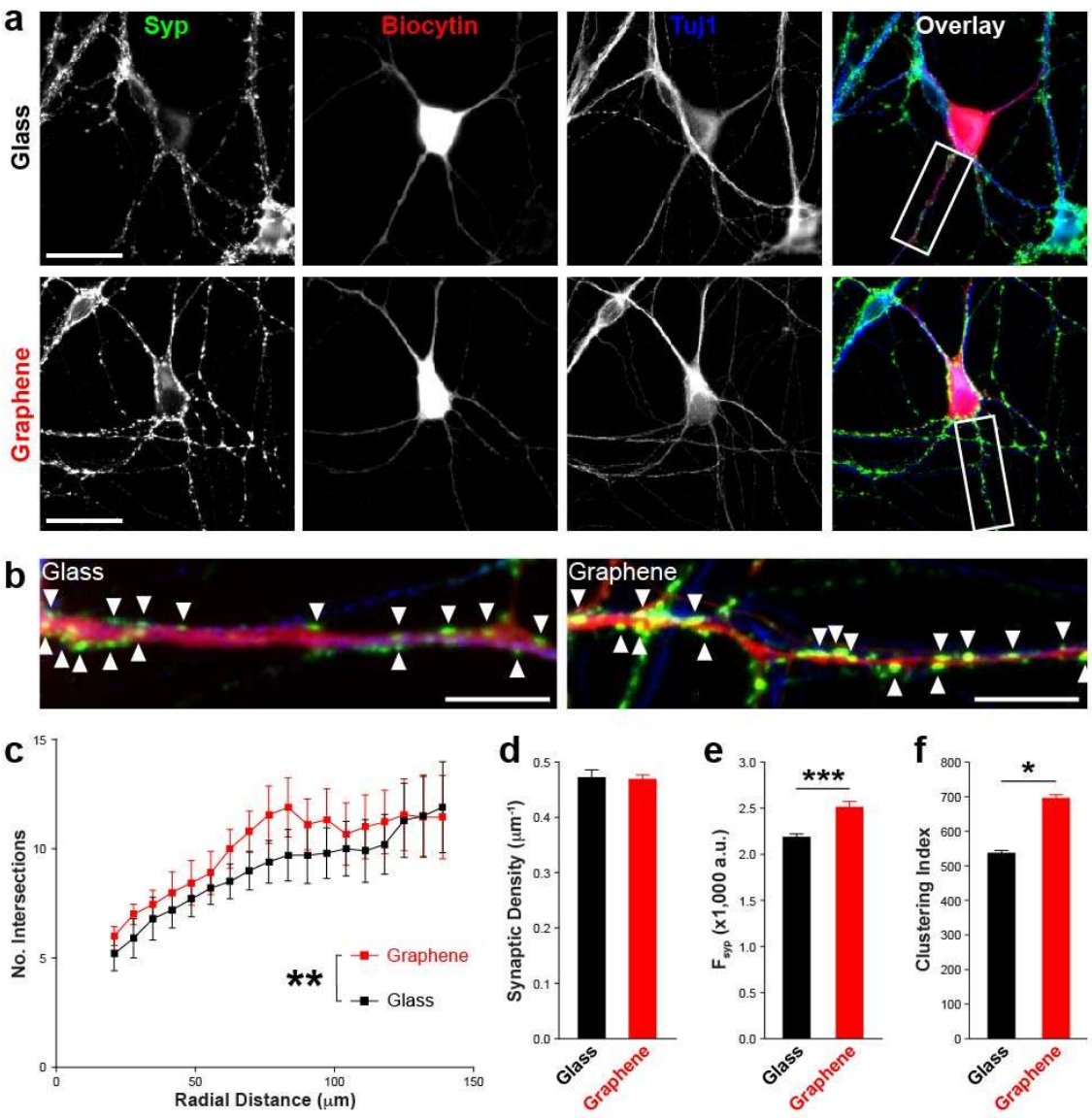

Figure 2.8 **Morphological comparison of neurons on glass or graphene**. **(a)** Sample images of immunofluorescence staining for the synaptic vesicle marker, Synaptophysin (Syp, green), and neuron-specific class III β-tubulin (TuJ1, blue) in recorded cells (biocytin filled, red). Scale bar, 30 μm. **(b)** Inset regions from the sample images are indicated by white boxes. Scale bar, 15 μm. Arrowheads indicate examples of Syp puncta. **(c)** Sholl analysis (** $p = 0.01$, $F(1,323) = 6.7$, Two-Way ANOVA with repeated measures followed by a Bonferroni multiple comparisons test, $\omega^2 = 0.017$, $n_{glass} = 12$ cells, $n_{graphene} = 11$ cells, $N > 4$ batches). **(d)** Lateral density of Syp puncta along the neurites of recorded neurons (Tuj1-positive and biocytin-positive) ($n_{glass} = 12$ cells, $n_{graphene} = 11$ cells, $N > 4$ batches; $p > 0.1$, two-tailed *t*-test). **(e)** Average Syp immunostaining ($n > 10{,}000$ synapses analyzed, $N > 3$ batches, *** $p < 0.001$, two-tailed *t*-test, Cohen's $d = 0.500$). **(f)** Average Syp clustering within individual synaptic boutons ($n \geq 3$ FOVs, $N = 3$ batches; * $p < 0.05$, two-tailed *t*-test, Cohen's $d = 0.65$). Error bars are S.E.M.

We first examined neurite complexity, as complexity is correlated to synaptic connectivity (Missaire and Hindges 2015). It is generally established that increased neurite complexity is associated with more synaptic connections between neurons, and more synaptic connections in turn lead to more synaptic inputs (i.e. higher sEPSC frequency) (Citri and Malenka 2008). We performed Sholl analysis to quantify arborization, which counts the number of neurite intersections at concentric circles of increasing radius originating at the neuronal soma (Sholl 1953).

Although there was an overall increase in neurite complexity on graphene between 12-18 DIV (**Figure 2.8c** and **Table 2.1**), the effect was small (see **Figure 2.8c** legend) and furthermore not significant at any distance.

Table 2.1 Summary Sholl analysis at 12-18 DIV.

	Graphene	**Glass**	***p* - value (one-way ANOVA)**
Critical Value	78.89	98.57	0.5567
Dendrite Maximum	17.56	20.43	0.0721
Schoenen Ramification Index	3.6582	5.1643	0.0490
Regression Coefficient	0.0439	0.0522	0.1568

However, we did note a non-significant increase on graphene at 68 μm. To determine if the overall increase was a result of early developmental changes, we performed Sholl analysis on neurons at 3 or 7 DIV.

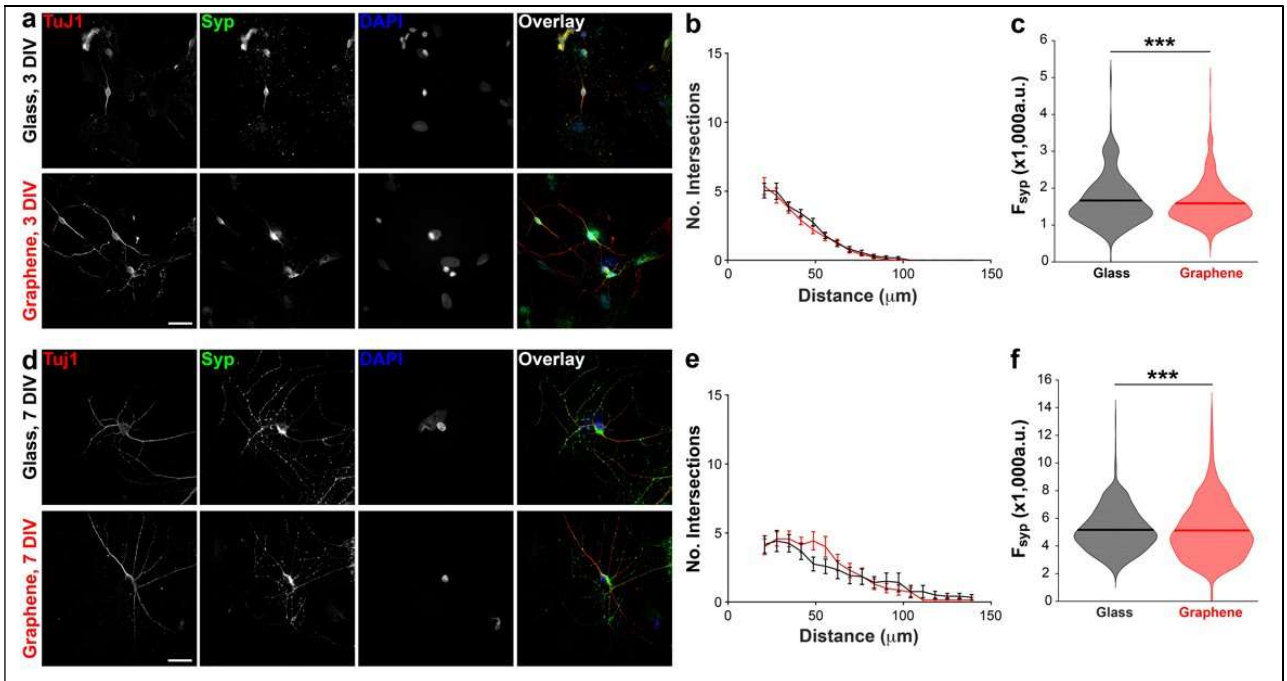

Figure 2.9 **Graphene does not substantially alter early synaptic development. (a)** Sample images of fluorescence immunostaining for the synaptic vesicle marker Synaptophysin (Syp, green), neuron-specific class III β-tubulin (TuJ1, red) and nuclear marker DAPI (blue) at 3 DIV. Scale bar, 50 μm. **(b)** Sholl analysis at 3 DIV ($p > 0.05$, Two-Way ANOVA with repeated measures, $n_{glass} = 17$ cells and $n_{graphene} = 22$ cells). **(c)** Intensity of Syp staining in TuJ1(+) processes at 3 DIV ($n_{glass} = 1524$ synapse sand $n_{graphene} = 1715$ synapses, *** $p < 0.001$, two-tailed *t*-test, Cohen's $d = 0.188$) Solid lines indicate mean value. **(d)** Sample images of fluorescence immunostaining for Syp (green), TuJ1 (red) and DAPI (blue) at 7 DIV. Scale bar, 50 μm. **(e)** Sholl analysis at 7 DIV ($p > 0.05$, Two-Way ANOVA with repeated measures, $n_{glass} = 17$ cells and $n_{graphene} = 11$ cells). **(f)** Intensity of Syp staining in TuJ1(+) processes at 7 DIV ($n_{glass} = 4381$ synapses and $n_{graphene} = 3990$ synapses, *** $p < 0.001$, two-tailed *t*-test, Cohen's $d = 0.146$). Solid lines indicate mean value. All error bars are the S.E.M. of the number of intersections from each FOV.

Here we found no differences in overall complexity (i.e. number of intersections); there were also only very small increases in Syp staining intensity (**Figure 2.9**). Collectively, our analysis of neurite complexity throughout development suggests that graphene does not substantially alter early outgrowth (up to 7 DIV), but does slightly increase the overall dendritic arbor during late phase development (7-12 DIV). To determine if neurons on graphene had more synaptic connections per neurite, we measured the lateral density of synaptic boutons along

neurites (the number of Syp-positive puncta in a unitary length of Tuj1- and biocytin-positive process) (**Figure 2.8b**). The lateral density of boutons was not altered on graphene (**Figure 2.8d**), in line with the idea that developmental changes on graphene are limited and do not act to alter synaptic connectivity in mature neurons.

Given that our functional data documented synaptic potentiation on graphene (**Figure 2.6c**), we next examined Syp immunostaining. Syp is highly localized to within synaptic vesicles (Granseth, Odermatt et al. 2006), thus differences in Syp staining intensity are positively correlated to differences in the number of vesicles within presynaptic terminals. We found that the mean fluorescence of Syp-positive puncta was ~21% greater in the graphene group (**Figure 2.8e**). We also analyzed the standard deviation of the pixel intensity (i.e. clustering index) within individual Syp-positive puncta. Within an individual ROI (see Methods), distributed vesicles would lead to a more uniform overall intensity, thus a lower standard deviation – i.e. a lower clustering index. Conversely, more clustered vesicles would be less uniform, resulting in a larger clustering index within individual boutons (Wilhelm, Mandad et al. 2014). We found a significantly increased average clustering index across all ROIs on graphene (**Figure 2.8f**), suggesting that synaptic vesicles are more tightly clustered in individual presynaptic terminals.

Graphene substrates potentiate neurotransmitter release

Our electrophysiological and immunolabeling results collectively suggested synaptic vesicle changes in presynaptic terminals. Because cholesterol is essential for synaptic vesicle origination, distribution, and turnover (Pfrieger 2003), we turned our attention to changes in synaptic vesicles on graphene substrates. To study synaptic vesicles, we used FM1-43, a styryl dye

with better kinetic properties than FM4-64 (Betz and Bewick 1992).

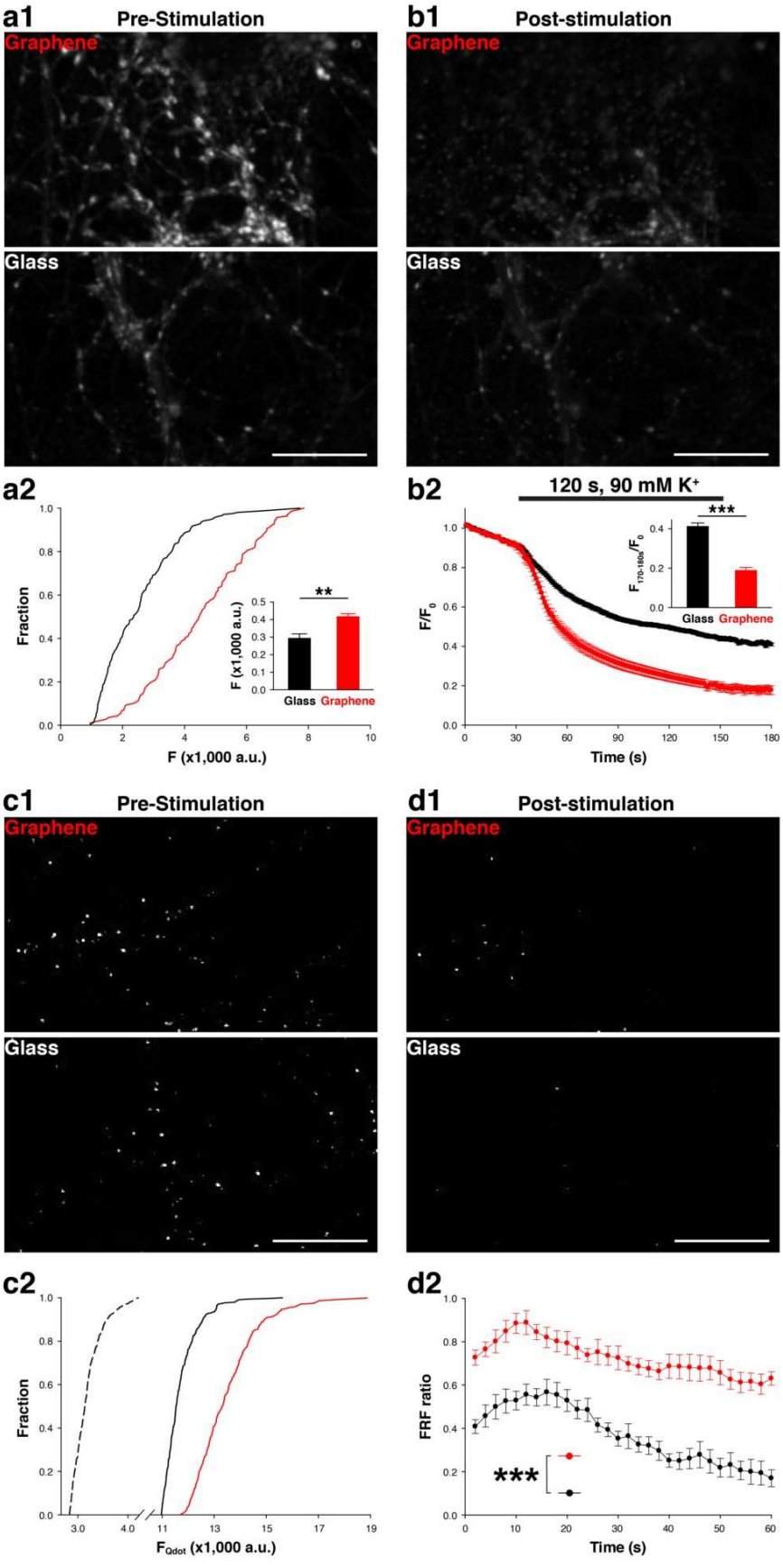
a1
Pre-Stimulation
Graphene
Glass
b1
Post-stimulation
Graphene
Glass
a2
Fraction
F (x1,000 a.u.)
**
F (x1,000 a.u.)
Glass
Graphene
b2
120 s, 90 mM K+
***
F/F0
Time (s)
Glass
Graphene
c1
Pre-Stimulation
Graphene
Glass
d1
Post-stimulation
Graphene
Glass
c2
Fraction
FQdot (x1,000 a.u.)
d2
FRF ratio
***
Time (s)

Figure 2.10 **Graphene induces presynaptic potentiation. (a)** Sample images of FM1-43 labeling. Scale bar, 30 μm. **(b)** Cumulative distributions of FM1-43 intensities at synaptic boutons (black, glass; red, graphene, same color coding hereafter). n_{glass} = 207 ROIs, $n_{graphene}$ = 139 ROIs, N = 3; * $p < 0.05$, Kolmogorov-Smirnov test). Inset. Average FM1-43 fluorescence. ** $p < 0.01$, 2-tailed *t*-test. (**c**) Sample images of FM1-43 labeling after destaining. Scale bar, 30 μm. (**d**) FM1-43 fluorescence during destaining. Inset is average fluorescence from 170-180s (n_{glass} = 207 ROIs, $n_{graphene}$ = 139 ROIs, N = 3; *** $p < 0.001$, two-tailed *t*-test). **(e)** Sample images of single Qdot loading. Scale bar, 30 μm. **(f)** Cumulative distributions of Qdot intensity after background subtraction in ROIs defined by retrospective FM4-64 labeling (single Qdot loading, dotted line; total recycling pool loading, solid lines). The average single Qdot intensity after background subtraction is 378±41 a.u.. The average total Qdot intensities after background subtraction are 8,787 ± 156 a.u. for glass and 11,050 ± 224 a.u. for graphene (n_{glass} = 187 ROIs, $n_{graphene}$ = 211 ROIs, N = 4; *** $p < 0.001$, Kolmogorov-Smirnov test). The estimated average numbers of total recycling vesicles are 23.2 for glass and 29.2 for graphene. **(g)** Sample images of single Qdot labeling after stimulation. Scale bar, 30 μm. **(h)** Fast-and-reversible fusion (FRF) ratio (out of all fusion events) during 1-min 10-Hz field stimulation (n_{glass} = 174 ROIs, $n_{graphene}$ = 181 ROIs, N = 3; *** $p < 0.001$, two-tailed *t*-test on the average FRF values from a 5-frame window at the end of each time course). Error bars are S.E.M.

The amount of FM1-43 uptake reflects the number of the releasable synaptic vesicles (Betz and Bewick 1992). In good agreement with FM4-64 loading (**Figure 2.5e**) and Syp staining (**Figure 2.8e**), there was significantly more FM1-43 uptake (~27%) by neurons on graphene (**Figure 2.10a&b and 2.10b inset**), suggesting an increase in releasable vesicles. Subsequent high-K^+ stimulation with a dye-free external solution causes FM1-43 loss from synaptic vesicles as they undergo evoked exocytosis. The amount and the rate of dye loss reflect synaptic vesicle release probability (Betz and Bewick 1992). We observed a ~30% increase in total dye loss in neurons on graphene (**Figure 2.10c&d and 2.10d inset**) and an increase in the rate of dye loss (**Figure 2.11**), indicating an increased pool of releasable vesicles and an increase in their release probability.

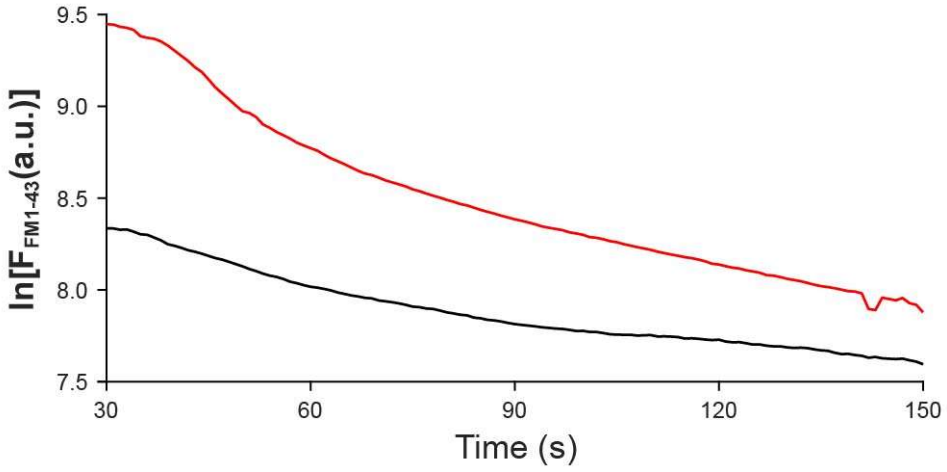

Figure 2.11 **FM1-43 destaining rate suggests increased vesicle release probability in neurons on graphene.** Raw FM1-43 fluorescence intensity values for graphene (red solid line) or glass (black solid line) during the stimulation period.

Together, our results suggest that graphene leads to an increase of releasable vesicles, which acts to potentiate neurotransmission.

To further elucidate the mechanisms underlying this presynaptic potentiation, we performed single vesicle imaging using quantum dots (Qdots), an approach which provides a more precise estimate of releasable synaptic vesicle amounts and their release probability. We began by loading Qdots into all releasable vesicles (the total releasable pool, TRP) using a combination of a high concentration of Qdots (100 nM) and strong stimulation (2-minute 90 mM-K^+) (Zhang, Cao et al. 2007, Zhang, Li et al. 2009) (**Figure 2.10e**). Based on the unitary photoluminescence of a single Qdot (see supplementary discussion), we estimated that the average numbers of total releasable pool vesicles per synapse were 23.2 ± 0.4 on glass and 29.2 ± 0.6 on graphene, a ~26% increase (**Figure 2.10f**). We next applied Qdots at a low concentration (0.8 nM) to randomly load single vesicles across the total releasable pool (**Figure 2.10g**). Quantal analysis of Qdot photoluminescence (Zhang, Cao et al. 2007, Zhang, Li et al. 2009) in FM4-64 defined synaptic

boutons confirmed that a large fraction of terminals were loaded with single Qdots inside individual synaptic vesicles (**Figure 2.12**).

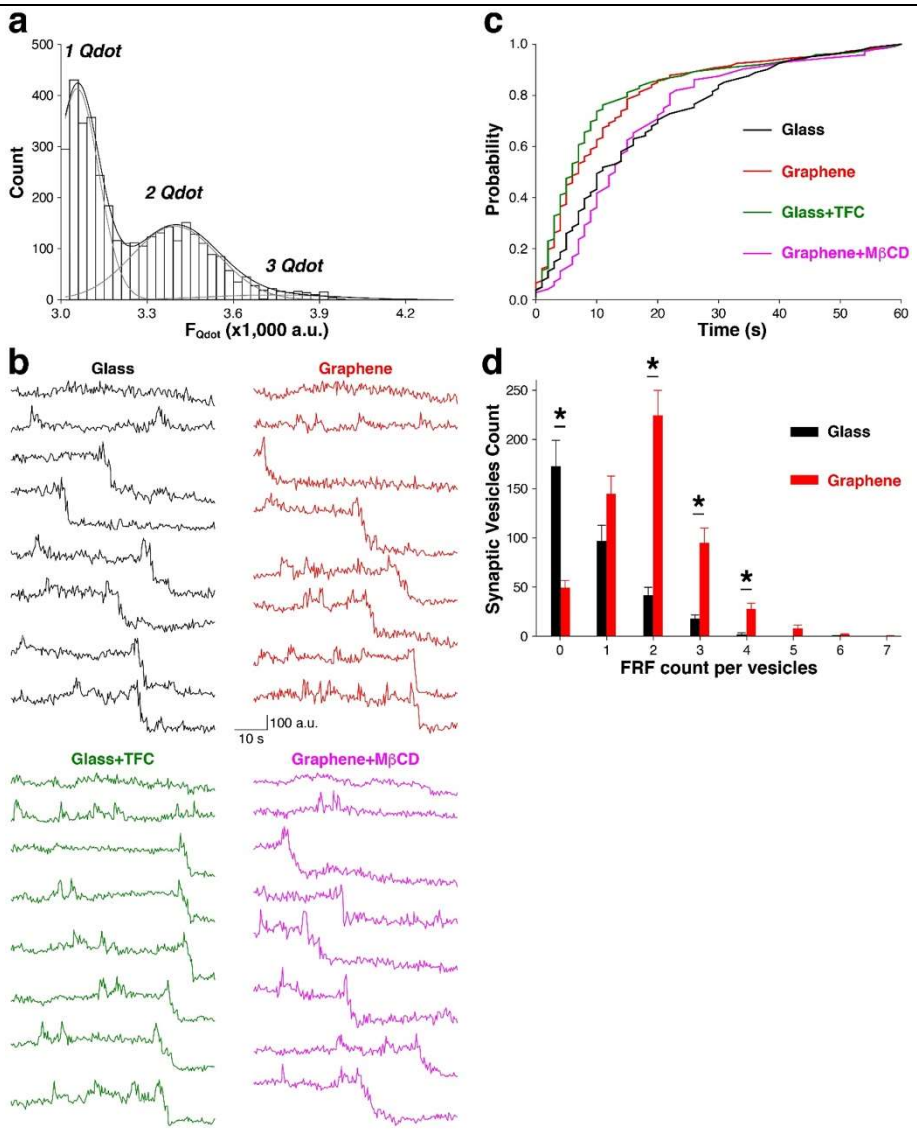

Figure 2.12 **Single Qdot imaging to measure single vesicle turnover. (a)** The distribution of mean intensity values (without background correction) in individual synaptic boutons defined by retrospective FM4-64 staining. The intensity distribution was fit with Gaussians of equal offset (i.e. mean and variance increase in folds). Quantal analysis (black and gray lines, Gaussian fits based on a maximal likelihood estimate) indicates that the mean intensity representing the unitary Qdot photoluminescence is 378 ± 41 a.u. with an average background intensity of 2719 ± 54 a.u. **(b)** Sample traces showing prototypical photoluminescence traces of single Qdots for the four different treatments: neurons on glass without (black) or with TFC pretreatment (green) and

neurons on graphene without (red) or with MβCD pretreatment (purple). A small and transient increase in Qdot fluorescence (uptick) represents fast-and-reversible fusion (FRF), and a large and unitary decrease following an uptick represents full-collapse fusion (FCF). **(c)** Vesicle release probability (measured as the first fusion events of individual Qdot-loaded synaptic vesicles) is significantly higher in neurons on graphene (red) than on glass (black) ($p < 0.05$) but is significantly reduced by MβCD pretreatment (purple) ($n_{graphene} = 231$, $n_{graphene+M\beta CD} = 214$, $n_{glass} = 183$, $n_{glass+TFC} = 225$ Qdots, N = 3 for every group; $p < 0.05$, two-tailed *t*-test). In contrast, the release probability on glass (black) is significantly increased by TFC pretreatment (green) ($p < 0.05$, two-tailed *t*-test). (**d**) Number of synaptic vesicles (y-axis) conducting the specified numbers of FRF events during the stimulation (x-axis) in neurons on graphene (red) or glass (black) (n = 3 FOVs from N = 3 for each group *, $p < 0.05$, two-tailed *t*-test). Error bars are the S.E.M. from each FOV.

We stimulated neurons for 1-minute with high-K^+ solution and imaged Qdot release from synaptic vesicles. The size and inherent pH-sensitivity of Qdots allows for discrimination between recycling modes via patterns of photoluminescence changes (**Figure 2.12**): a small and transient increase in Qdot photoluminescence alone indicates fast and reversible fusion (FRF), while such an increase immediately followed by a unitary Qdot loss indicates full-collapse fusion (FCF) (Zhang, Li et al. 2009). In neurons on graphene, individual synaptic vesicles conducted more FRF (**Figure 2.12**) and, correspondingly, a significantly larger fraction of FRF out of all vesicle release events (**Figure 2.10h**), which would be expected for a cholesterol increase in the plasma and vesicular membranes of presynaptic terminals (Chang, Kim et al. 2009, Dason, Smith et al. 2010, Puchkov and Haucke 2013, Yue and Xu 2015). Thus, we concluded that graphene promotes fast synaptic vesicle turnover in addition to increases in vesicle number and their release probability.

Synaptic potentiation on graphene is cholesterol dependent

To further investigate the extent to which membrane cholesterol levels mediate presynaptic potentiation on graphene, we sought to directly manipulate cell membrane cholesterol levels. We first increased membrane cholesterol levels in neurons grown on glass by the addition of TFC as

an exogenous cholesterol supply (Lund, Lomholt et al. 2012). Neurons were treated with 1 μM TFC for 1 hour, which was sufficient to allow incorporation into the plasma membrane.

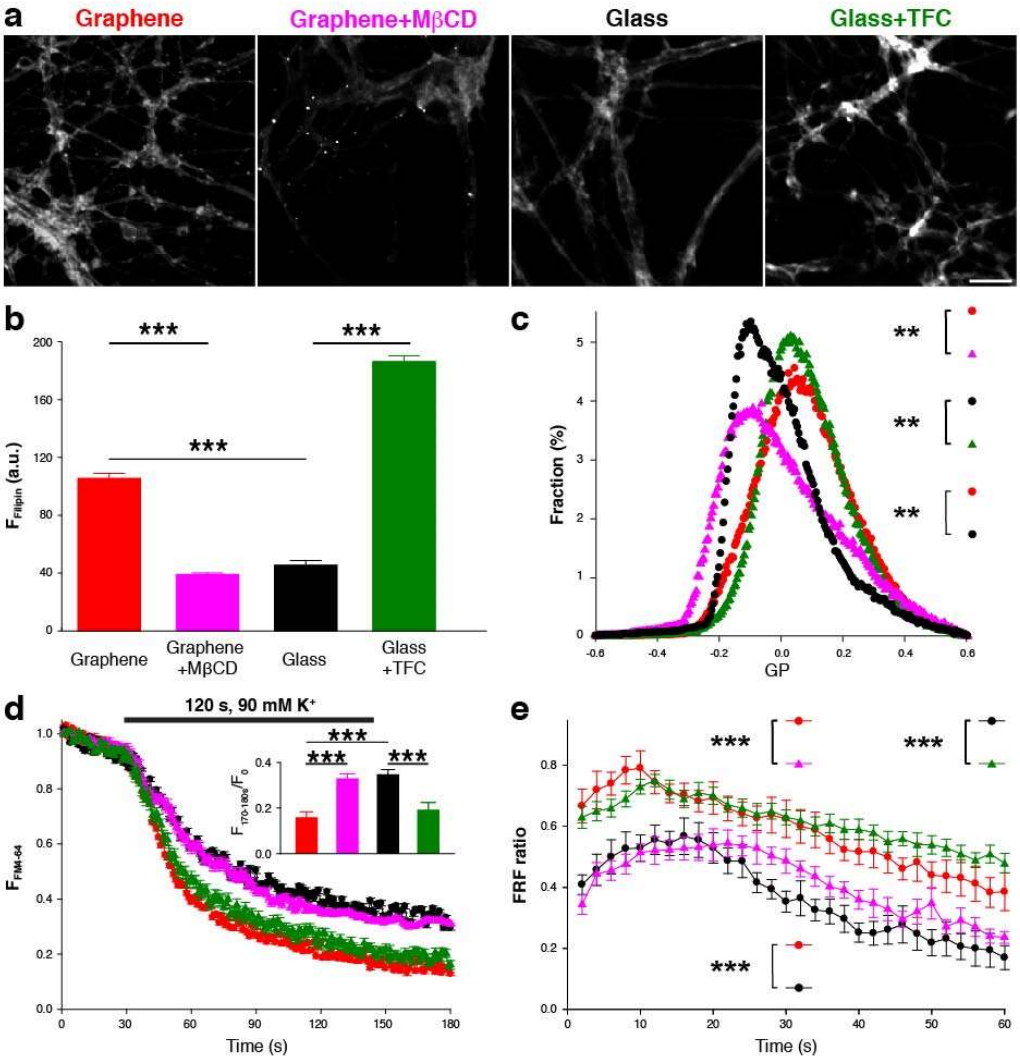

Figure 2.13 **Cholesterol mediates graphene-induced presynaptic changes. (a)** Sample Filipin staining images of neurites on graphene with (purple) or without (red) MβCD treatment and on glass with (green) or without (black) TFC loading. Scale bar, 50 μm. Same color coding hereafter. **(b)** Average Filipin staining intensities in neurites ($n_{graphene}$ = 107 neurites, $n_{graphene+M\beta CD}$ = 151 neurites, n_{glass} = 188 neurites, $n_{glass+TFC}$ = 152 neurites, N = 3 batches for every group; for graphene *vs.* graphene + MβCD, graphene *vs.* glass, and glass *vs.* glass + TFC, *** $p < 0.001$, all Wilcoxin rank-sum tests). **(c)** Distributions of GP values over individual image pixels (n = 6 FOVs, N = 3 batches for every group; for graphene *vs.* graphene + MβCD and glass *vs.* glass + TFC, both $p < 0.05$, for graphene *vs.* glass + TFC, $p = 0.073$, Kolmogorov-Smirnov test of the distributions of

GP values, see data analysis section of the Methods). **(d)** FM 4-64 fluorescence changes before and during 2-min 90-mM K^+ and (inset) average fluorescence decrease using a 5-frame window at the end of the stimulation period (n = 6 FOVs, N = 3 batches per group; for graphene *vs.* graphene + MβCD, graphene *vs*. glass, and glass *vs.* glass + TFC, *** $p < 0.001$, for graphene vs. glass + TFC and graphene + MβCD *vs*. glass, N.S. $p > 0.05$, all two-tailed *t*-tests). **(e)** FRF ratios during 1- min 30-Hz electrical stimulation (n = 3 FOVs, N = 3 batches for every group; for graphene *vs.* graphene + MβCD and glass *vs.* glass + TFC, both $p < 0.05$, two-tailed *t*-tests on the average of a 5-frame window at the end of the stimulation period). Error bars are S.E.M.

We used two independent measurements to assess Cholesterol levels: Filipin staining (again measured in neurites) (**Figure 2.13a&b**) of fixed neurons and GP imaging (**Figure 2.13c**) of live neurons. To avoid the cross-excitation of TFC when imaging C-laurdan, all GP imaging experiments involving the manipulation of membrane cholesterol levels were performed using a different optical configuration (see Methods and **Figure 2.14**).

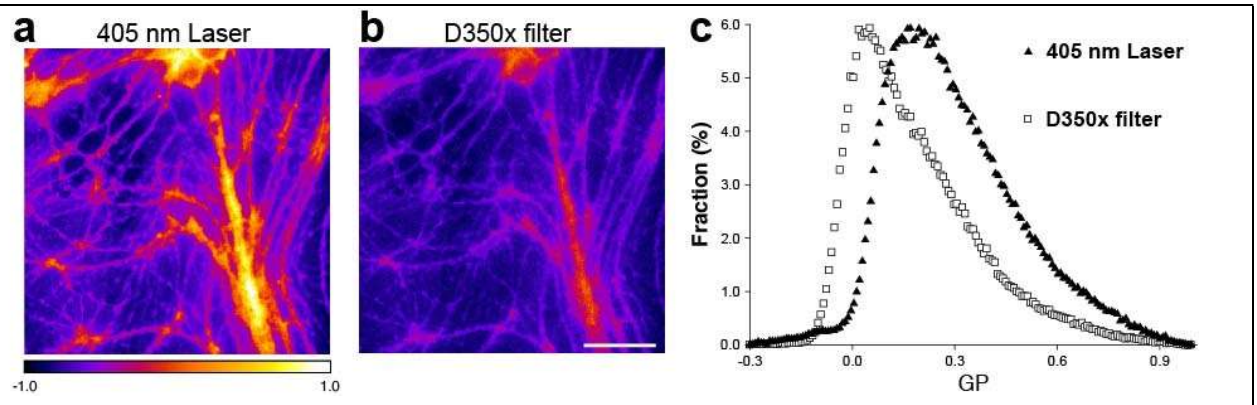

Figure 2.14 **GP values with two different excitation settings.** (**a & b**) Sample GP images with a 405 nm laser (**a**) or Prior 200 light source and D350x filter (**b**)(Chroma). Scale bar, 20 μm. (**c**) The distribution of GP pixel values for both conditions.

Notably, although Filipin staining intensity was greater for the acute addition of TFC than for chronic growth on graphene, the similarity in GP distributions suggests that cholesterol levels within the plasma membrane were similar between graphene and TFC-treated glass samples. TFC

treatment of neurons on glass increased the FM4-64 destaining rate, increased the FRF ratio, and also increased release probability (**Figure 2.13d-e** and **Figure 2.14b&c**), similar to the effects we observed on graphene. We next used methyl-β-cyclodextrin (MβCD), a cholesterol-binding compound (Zidovetzki and Levitan 2007), to decrease cholesterol levels in neurons on graphene. To limit its effect to the cell membrane, we applied a low concentration (0.5 mM) of MβCD for a short time (10 minutes). 10 μM D-AP5 and 5 μM NBQX were co-applied to prevent the activity-induced exposure of intracellular membrane cholesterol. Again, independent assessment of cholesterol levels by both Filipin staining in fixed neurites (**Figure 2.13a&b**), and GP imaging of live neurons (**Figure 2.13c and Figure 2.15**) confirmed a reduction of cholesterol levels.

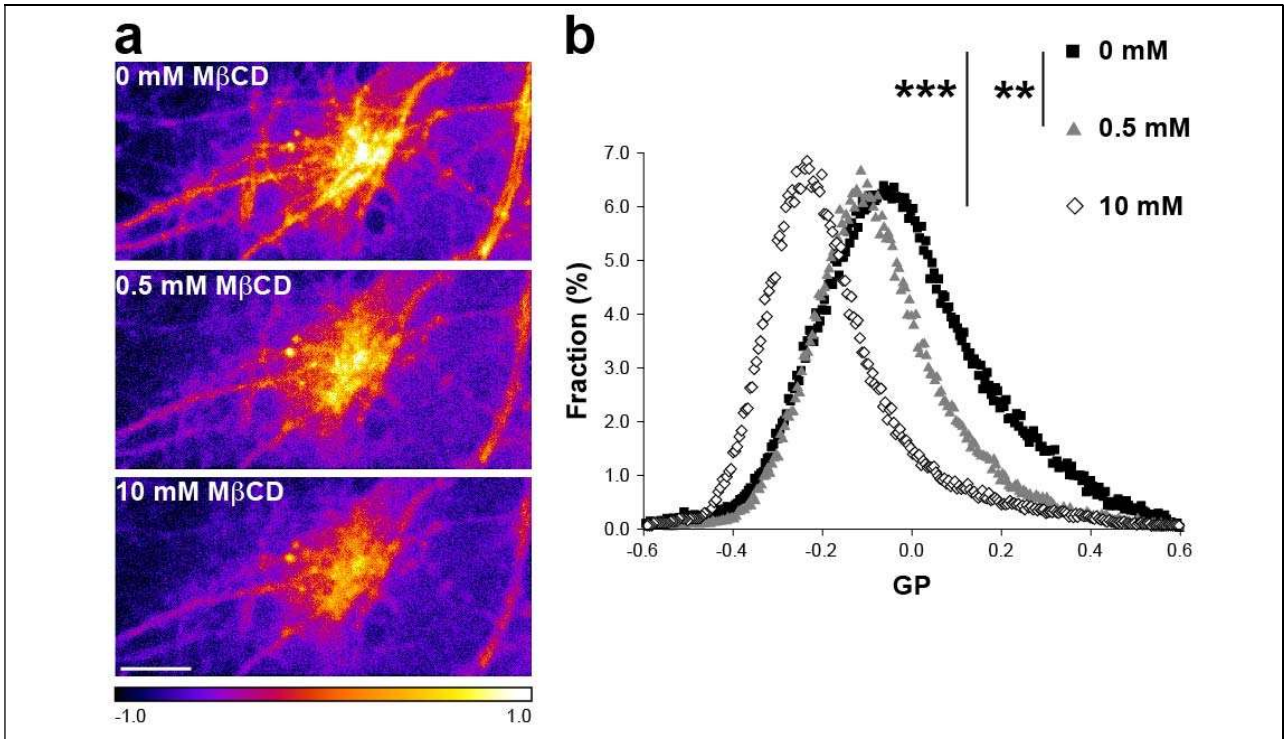

Figure 2.15 **Cholesterol depletion after MβCD treatment reduces GP values.** (**a**) Sample images of the same field of view after treatment with 0, 0.5-mM 5-min, or 10-mM 30-min MβCD. Scale bar, 20 μm. (**b**) Distributions of GP values over individual image pixels (n = 3 FOVs, N = 3 batches for every treatment; for 0.5 and 10 mM in comparison to 0 mM, $p < 0.01$

and < 0.001 respectively, *Kolmogorov-Smirnov* test of the distributions of GP values, see data analysis section of the methods).

We then imaged FM4-64 and Qdots unloading during high-K^+ stimulation. MβCD treatment decreased the rate of FM4-64 loss, the amount of fast vesicle fusion, and the vesicle release probability (**Figure 2.13d&e**) of neurons on graphene, demonstrating that reversing the graphene-induced cholesterol increase via MβCD application also reverses graphene's effect on synaptic vesicles. Our data collectively demonstrate that cholesterol, most likely in the plasma membrane, is an important mediator of graphene's ability to potentiate neurotransmission.

Cholesterol dependent potentiation of P2YR signaling on graphene

As membrane cholesterol plays an integral role in the binding and regulation of many transmembrane proteins (Song, Kenworthy et al. 2014), we asked if and how cholesterol enrichment on graphene substrates could affect transmembrane proteins and the signaling pathways they mediate. Using the same approach that was used for our neuronal culture configuration, mouse fibroblast cells (NIH 3T3) were plated directly on graphene or glass. Filipin staining demonstrated a ~49% increase of fluorescence intensity in 3T3 cells on graphene (**Figure 2.16a&b**), a much greater increase than what was observed in neurons, possibly due to lower homeostatic concentrations of plasma membrane cholesterol in 3T3 cells (Pankov, Markovska et al. 2006) than in neurons (Calderon, Attema et al. 1995).

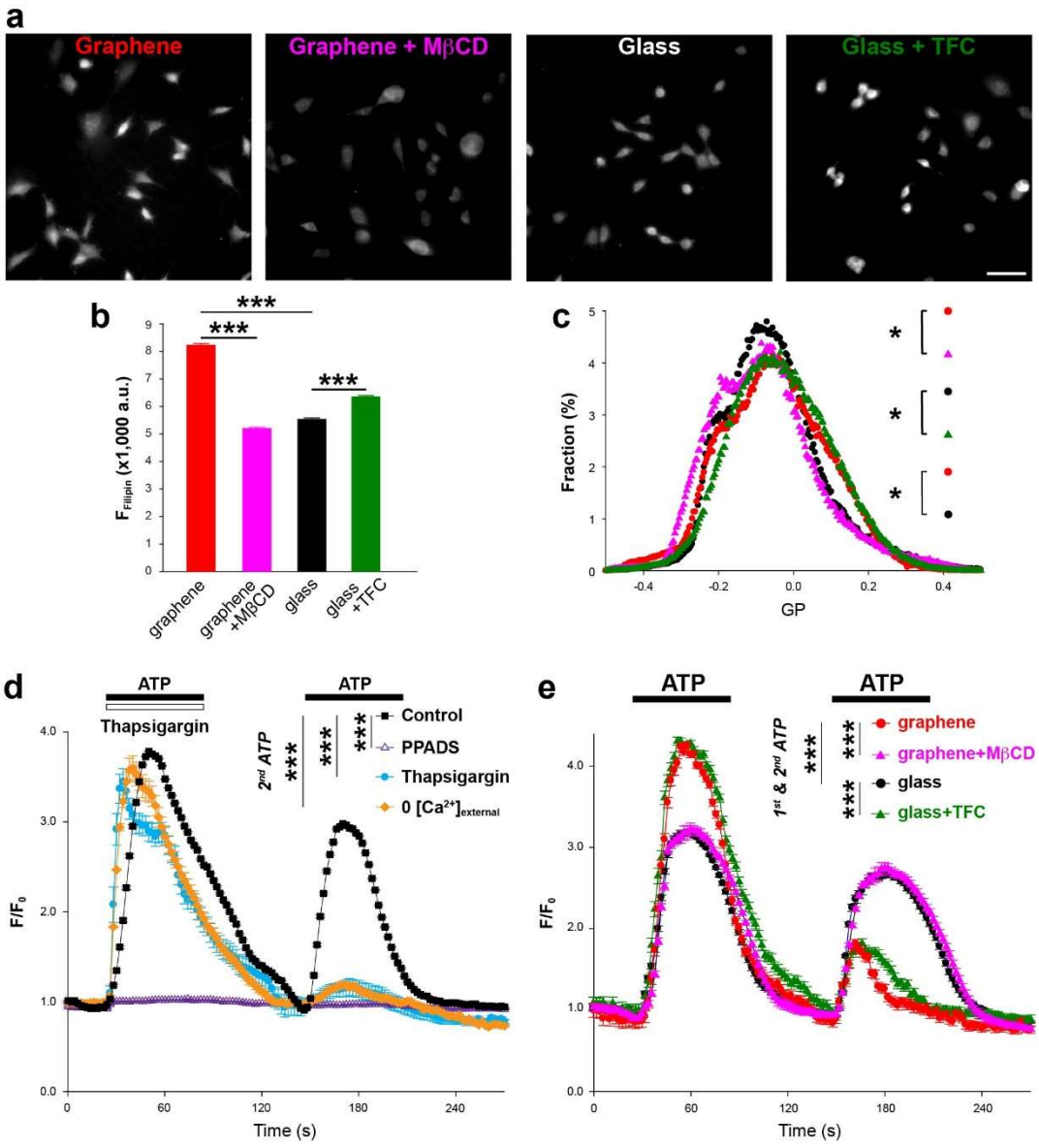

Figure 2.16 **Graphene enhances P2Y receptor-mediated Ca^{2+}-responses. (a)** Sample images of Filipin staining of 3T3 cells on graphene with (purple) or without (red) MβCD treatment and on glass with (green) or without (black) TFC loading. Same color coding hereafter. Scale bar, 50 μm. **(b)** Average intensities of Filipin staining ($n_{graphene}$ = 1536 cells, $n_{graphene + MBCD}$ = 2286 cells, n_{glass} = 1317 cells, $n_{glass + TFC}$ = 1487 cells, N = 3 batches for every group; for graphene *vs.* graphene + MβCD, graphene *vs.* glass, and glass *vs.* glass + TFC, ***, $p < 0.001$, all Wilcoxin rank-sum tests). **(c)** Distributions of GP values over individual image pixels (n = 6 FOVs, N = 3 batches for every group; for graphene *vs.* graphene + MβCD and glass *vs.* glass + TFC, both $p < 0.05$, for graphene *vs.* glass +TFC, $p > 0.05$, Kolmogorov-Smirnov test of the distributions of GP values, see data analysis in the method section). **(d)** Two consecutive 100-μM ATP applications elicited the release of Ca^{2+} from internal Ca^{2+}-stores (n = 6 FOVs, N = 3 batches for every condition). The 2nd Ca^{2+}-response was smaller than the 1st with a 1 min interval between. Both Ca^{2+}-responses were blocked by 50 μM PPADS (pyridoxalphosphate-6-azophenyl-2',4'-disulphonic acid), a P2YR inhibitor

(white triangles). 1 μM Thapsigargin (blue dots) elicited a similar Ca^{2+}-response as ATP, but significantly reduced the 2nd response by exhausting internal Ca^{2+}-stores. In the absence of extracellular Ca^{2+} (the source for refilling internal Ca^{2+}-stores) (orange diamonds), the 2nd response was also significantly reduced (n = 6 FOVs, N = 3 batches for every condition). **(e)** ATP-elicited Ca^{2+} release from internal stores was facilitated by graphene or TFC pretreatment and reduced by MβCD (n = 6 FOVs, N = 3 batches for every group; for graphene *vs.* graphene + MβCD, graphene *vs*. glass, and glass *vs.* glass + TFC, *** $p < 0.001$, two-tailed *t*-tests). Error bars are S.E.M.

GP imaging suggested a modest reduction of lipid membrane fluidity on graphene (**Figure 2.16c**). Among many cholesterol-sensitive transmembrane proteins, we chose therapeutically valuable P2Y receptors (P2YRs) (Wu, Holstein et al. 2007), a class of GPCR. GPCRs are one of the largest protein families in the human genome (Fredriksson, Lagerstrom et al. 2003), and represent about half of all modern pharmaceutical targets (Fabbrizio, Le Cam et al. 1999). Structural models have elucidated that membrane cholesterol allosterically promotes GPCR activity by binding to the transmembrane domain (Cherezov, Rosenbaum et al. 2007). In 3T3 cells, P2YRs mediate a fast Ca^{2+}-response to extracellular ATP (Fabbrizio, Le Cam et al. 1999), which can be quantitatively measured at high spatiotemporal resolution via Ca^{2+}-imaging. We applied two ATP stimuli at a 1-minute interval and observed that the second Ca^{2+}-response was significantly diminished (**Figure 2.16d)**. This is consistent with P2YR-mediated Ca^{2+} release from internal stores, which require longer than 1 minute to refill**.** We then pharmacologically isolated relevant components in the transmembrane signaling pathway. Application of PPADS (a selective P2YR antagonist) inhibited Ca^{2+}-responses, confirming P2YRs as the ATP receptor (**Figure 2.16d**). Both Tharpsigargin (an agonist for Ca^{2+}-release from internal stores) and Ca^{2+}-free bath solution (preventing the refilling of internal Ca^{2+} stores) reduced the 2nd Ca^{2+}-response, collectively confirming internal stores as the Ca^{2+} source (**Figure 2.16d**).

We observed a significantly larger Ca^{2+}-response to the 1st ATP stimulus and, subsequently, a smaller response to the 2nd stimulus in 3T3 cells on graphene relative those on glass (**Figure 2.16e**), demonstrating that P2YR-mediated Ca^{2+}-responses are enhanced. Since ATP stimulation was still required for Ca^{2+}-release, the facilitation we observed in cells on graphene was likely allosteric. In the same manner as the studies we performed using neurons, we next manipulated cholesterol to study its role in the enhanced Ca^{2+} responses we observed on graphene. 3T3 cells growing on graphene or glass were pretreated with MβCD or TFC, respectively, using the same protocols we used for neurons. TFC pretreatment increased Filipin staining intensity in 3T3 cells on glass (~15%, **Figure 2.16a&b**), although not to the levels observed on graphene, and membrane fluidity was moderately reduced (**Figure 2.16c**). Conversely, MβCD treatment of 3T3 cells on graphene reduced Filipin staining intensity (**Figure 2.16a&b**) and increased membrane fluidity (**Figure 2.16c**). Although we did observe differences in Filipin intensity when comparing non-treatment vs. treatment conditions, our GP data demonstrate that our treatments were consistent in altering plasma membrane cholesterol in that MβCD application resulted in GP distributions similar to glass (**Figure 2.16c**) and TFC application resulted in GP distributions similar to those on graphene. Our data are consistent with the idea that membrane cholesterol levels are increased within a certain physiological range, but over the length of our 3T3 cell culture, additional cholesterol may be trafficked to and distributed homogeneously in intracellular membrane areas. Again, our bidirectional manipulations of cholesterol resulted in functional outcomes similar to what we observed for neurons on glass or graphene (**Figure 2.16e**). Enhanced Ca^{2+}-responses on graphene were significantly diminished by MβCD treatment, and Ca^{2+}-responses on glass were significantly potentiated by TFC application (**Figure 2.16e**). Together, these results suggest that a graphene-induced cholesterol increase is capable of potentiating cell

signaling pathways via transmembrane proteins whose activities are allosterically regulated by cholesterol.

Discussion

Here, we show that pristine monolayer graphene, when in chronic contact with the cell membrane, can modify cellular processes via increased cholesterol. In cell-free systems, we observed that graphene extracts cholesterol from cell culture media and quenches a fluorescent cholesterol analog, consistent with prior predictions of a graphene-cholesterol interaction. Cell-based measurements cooperatively revealed that graphene increased plasma membrane cholesterol. In neurons, this results in a presynaptic potentiation of neurotransmission, realized by increases in synaptic vesicle number, release probability, and turnover rate. Notably, all of these are regulated by membrane cholesterol (Pfrieger 2003, Chang, Kim et al. 2009, Dason, Smith et al. 2010, Puchkov and Haucke 2013, Yue and Xu 2015). Manipulation of membrane cholesterol levels validated the correlation between graphene-induced membrane cholesterol increase and changes in synaptic vesicle number and behavior. We extended our findings by studying graphene's impact on integral membrane receptors that are known to be affected by cholesterol concentration and observe enhanced P2YR-mediated Ca^{2+}-responses in fibroblast cells on graphene. Congruent with our findings in neurons, we demonstrate that this potentiation is facilitated by cholesterol.

Both LPE and CVD produce single- and few-layer graphene with similar surface characteristics (Hernandez, Nicolosi et al. 2008, Geim 2009, Li, Cai et al. 2009, Lee, Lee et al. 2014). Thus, the interaction demonstrated using LPE graphene flakes should remain valid for the

CVD graphene films used in our cell-based studies. The nature of this interaction likely involves both a hydrophobic interaction and stacking between cholesterol's planar tetracyclic ring group and graphene's hexagonal lattice (Gburski, Górny et al. 2010, Gburski, Gorny et al. 2011, Hibino and Tsuchiya 2014, Zhang and Wang 2015, Zhang, Xu et al. 2016). Our spectral data (**Figure 2.1b** and **Figure 2.2**) suggest that the interaction may be more complex than a simple hydrophobic interaction. Further work, including both empirical studies and computational modeling, will aid in elucidating the mechanisms of this interaction within complex membranes which contain many types of molecules. This will clarify the relative selectivity of cholesterol in comparison to other types of biomolecules, including phospholipids, peptides, and carbohydrates, which are common constituents of culture media and also located on the cell surface.

Given the importance of minimizing the distance between graphene and cells, we chose an approach similar to previous studies (Fabbro, Scaini et al. 2016, Veliev, Briancon-Marjollet et al. 2016) - cells were plated directly on bare CVD graphene films without a Matrigel (e.g.) coating. Because it gels upon incubation at physiological temperatures, Matrigel acts as an effective interlayer between the substrate and the cell membrane in traditional culture configurations. We reasoned that removal of this layer would better resemble scenarios where graphene is used as a biosensor. However, this approach does not prevent biomolecule deposition from our culture media onto the graphene surface. A protein corona is likely formed over the length of our culture period. Hu et al. recently demonstrated that within minutes of exposure to serum-containing media a stable protein corona will form on graphene oxide (Hu, Peng et al. 2011), which has a more favorable surface for protein adsorption than graphene. We have found a similar time course for dissociated neurons to attach to bare glass surfaces (**Figure 2.17**).

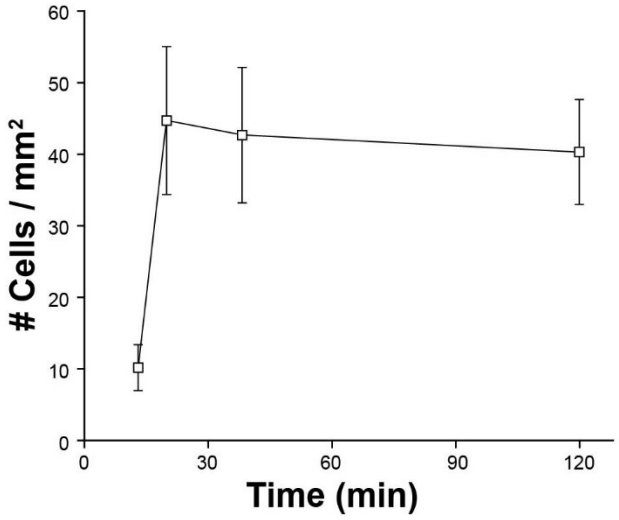

Figure 2.17 **Cell adhesion after plating.** Dissociated hippocampal neurons were plated on bare glass coverslips and incubated in plating media for designated periods of time before washing with Hank's solution. Cells in randomly chosen FOVs were counted to calculate cell densities. Error bars are S.E.M for each time point.

This suggests that as cells are adhering to graphene there may still be areas where protein adsorption does not completely cover the surface, which would allow for contact between graphene and the cell membrane. Intriguingly, when neurons were cultured in conditioned media, previous reports have demonstrated that the crystallinity of the graphene surface is a determinant of axon outgrowth, suggesting that even with biomolecule deposition, graphene still acts to alter cell function (Veliev, Briancon-Marjollet et al. 2016). This is in line with the findings of our cholesterol assay (**Figure 2.1a**), where chronic exposure resulted in cholesterol enrichment on the graphene surface. The development of biocompatible surface modification strategies to minimize fouling on carbon nanomaterials remains an important issue for improving biosensor lifetime, but our results demonstrate that even in the presence of a biomolecular corona, cholesterol is a mediator of graphene's functional effects.

We employed two independent approaches to evaluate changes in cellular cholesterol levels on graphene substrates: Filipin staining and generalized polarization imaging. Filipin fluoresces upon cholesterol binding and is a well-accepted qualitative reporter for cellular cholesterol in fixed cells. It permeabilizes the cell membrane and binds intracellular cholesterol as well as other lipids (Maxfield and Wustner 2012). This may explain the inconsistency in the absolute difference between graphene and glass (**Figure 2.3b** vs. **Figure 2.8b**); notably the overall increase on graphene was substantial across experiments. To obtain an additional measure of cholesterol that would not disturb the membrane, we employed GP imaging in live cells. The magnitudes of GP distribution shifts across different experiment sets were consistent (~0.15). Although much smaller than the relative changes we observed for Filipin staining, such changes are in line with what has been observed previously for GP value at different cholesterol amounts (Weber, Wagner et al. 2010): modest absolute changes correlate to much larger differences in overall cholesterol content. To empirically demonstrate how GP shifts represent differences in neuronal membrane cholesterol, we performed GP imaging on neurons after weak or strong cholesterol depletion by MβCD (**Figure 2.15**) (Zidovetzki and Levitan 2007). Because the GP changes we observed on graphene or after bidirectional manipulations (~ 0.15) lie between the shifts we observed for weak (~0.089) and strong (~0.191) MβCD treatment, we conclude that the membrane cholesterol changes were moderate. Broadly, both GP and Filipin were qualitatively consistent with the observation that cells on graphene had increased TFC labeling (**Figure 2.4**), all of which support our conclusion that graphene increases cholesterol. However, because TFC acts as an exogenous source of cholesterol and was applied acutely, quantitative comparison of TFC labeling to Filipin staining or GP shift is challenging.

After the addition or removal of cholesterol from neurons on glass or graphene respectively, Filipin staining seemingly reported large changes in cellular cholesterol (**Figure 2.13b**) whereas neither neuronal membrane rigidity (**Figure 2.13c**) nor synaptic vesicle release (**Figure 2.13d&e**) reported changes exceeding those on glass or graphene. We speculate that although cholesterol levels can be increased, there are additional factors which place some limit on cholesterol's ability to modulate cellular function. For example, membrane rigidity also requires the involvement of saturated or unsaturated fatty acids to maintain or modify lipid phase order. And for synaptic vesicles, changes in number were likely confined by the sizes of the different vesicle pools. As only a subpopulation of synaptic vesicles is releasable, this may explain why Syp staining, which labels all vesicles, exhibited a smaller increase (~21%) in the graphene group than FM or Qdot loading, which only label releasable vesicles (~26-30%). Furthermore, the ability of excess cholesterol to be incorporated into fusion machinery as well as the limited number of release sites may help to set bounds beyond which overall homeostasis would be irreparably disrupted. We also cannot exclude the possibility that Filipin labels intracellular cholesterol, which may be affected by our manipulations but is not accounted for in GP or FM/Qdot imaging.

After bidirectional manipulation of cholesterol levels, we observed that the resulting changes in cellular cholesterol and membrane rigidity were larger in neurons than 3T3 cells (**Figure 2.13b** vs. **2.16b and Figure 2.13c** vs. **2.16c**). This discrepancy may be due to metabolic and homeostatic differences in membrane cholesterol between neurons and 3T3 cells (Calderon, Attema et al. 1995, Pankov, Markovska et al. 2006, Lange, Ye et al. 2014). Moreover, neurons have higher levels of plasma membrane cholesterol (Calderon, Attema et al. 1995) than 3T3 cells

(Pankov, Markovska et al. 2006) and cells may respond differently to MβCD or TFC depending upon both concentration and treatment time.

We have demonstrated that neurons grow and form functional synapses on both glass and monolayer graphene substrates without significant developmental or gross morphological defects. This is seemingly different from a recent report (Veliev, Briancon-Marjollet et al. 2016) which focused on neuronal development and noted that neurons were unable to grow normally on bare glass. There are several technical differences that may explain this discrepancy, including species and age of cells at plating. The use of serum in our culture media serves as a rich source of cholesterol in comparison to the reported study (Veliev, Briancon-Marjollet et al. 2016) where serum-free conditioned media was used. Our culture media contains approximately 12-14 μM cholesterol (**Figure 2.1a**), whereas astrocyte conditioning only further increases this concentration by 2 μM (**Figure 2.1a**). The additional growth and attachment factors present in serum likely help to mitigate any deficits in neuronal adhesion and development. Functionally, we observe no difference in neuronal membrane conductance (similar sEPSC amplitudes, **Figure 2.6**) and no Ca^{2+} leakage in 3T3 cells (stable basal cytosolic Ca^{2+} concentration without stimulation or after P2YR inhibition, **Figure 2.16d**) on graphene, extending the findings of previous studies which have demonstrated that graphene substrates do not damage the eukaryotic membrane (Akhavan and Ghaderi 2010, Hu, Peng et al. 2010, Liu, Zeng et al. 2011). TFC and FM dye labeling further indicate that membrane integrity and trafficking are uncompromised, as labeling would have appeared atypical with significant membrane degradation.

There are two scenarios that explain the enrichment of cholesterol we observe. Chronic

contact between graphene and cells may attract cholesterol to areas nearest to the graphene surface, reducing cholesterol in other membrane compartments such as the endoplasmic reticulum (where cholesterol sensors reside (Goldstein and Brown 2015)). Consequently, cholesterol synthesis and/or uptake is upregulated, resulting in a total cholesterol increase over time (**Figure 2.4, 2.13a&2.16a**). An alternative scenario seems equally possible: that graphene adsorbs cholesterol from the culture media onto its surface (**Figure 2.1a**), providing an enriched local cholesterol supply to the neighboring plasma membrane. Membrane cholesterol levels are elevated and over time excess cholesterol is trafficked to internal membranes (**Figure 2.16a-c**). This is in line with evidence demonstrating that the uptake of exogenous cholesterol is critical for mature neuronal function (Pfrieger 2003). Differentiating between these two scenarios will require the acute application of graphene and the ability to monitor cholesterol trafficking in live cells at adequate spatiotemporal resolution.

Although graphene has been documented to damage bacterial cell membranes (Tu, Lv et al. 2013), it has seemingly few adverse effects on eukaryotic cells based on our own and others' previous observations (Bendali, Hess et al. 2013, Fabbro, Scaini et al. 2015, Veliev, Briancon-Marjollet et al. 2016). This difference between cell types can be explained in part by our cell culture configuration and in part by the presence or absence of membrane cholesterol. Prokaryotic membrane destruction was caused by nanometer-sized graphene flakes that pierced through the bacterial membrane causing lipids to disperse (Tu, Lv et al. 2013). In our and an additional study(Veliev, Briancon-Marjollet et al. 2016), large CVD graphene films are essentially fixed on a surface (**Figure 2.3**). The extremely high in-plane strength of graphene effectively prohibits small flakes from breaking off of the glass surface and inserting into the cell membrane. Therefore,

graphene remained parallel to the cell membrane during culture and was unlikely to cause membrane disruption in the same manner as previously described. Fully distinguishing the role cholesterol plays in the cellular responses to different types of graphene will require further study using both graphene flakes applied to eukaryotic cells and chronic growth on graphene of prokaryotic cells.

Cholesterol modulates many membrane-associated proteins and other cellular functions in addition to its role in the structural integrity of the eukaryotic plasma membrane. Thus, it would be interesting to further study graphene's impact on other signaling pathways regulated by cholesterol. For example, it helps to define the fluidity of the lipid bilayer, which in turn regulates the dynamics and subcellular distribution of many transmembrane proteins (Subtil, Gaidarov et al. 1999). Cholesterol is also essential for the activity of various disease-associated membrane proteins like γ-secretase, an amyloidogenic enzyme thought to be an important therapeutic target in Alzheimer's disease. In addition, cholesterol is a key constituent of membrane nanodomains (a.k.a. lipid rafts), which are believed to act as the nexus for transmembrane protein complexes, mediating signal transduction across the plasma membrane, carrying out receptor-mediated endocytosis and more (Simons and Toomre 2000). Therefore, further study is warranted for a comprehensive view of graphene's effect on the organization and trafficking of eukaryotic cell membranes as well as membrane protein distribution and mobility.

For the majority of graphene-based bioapplications, especially those seeking to harness its unique electrical properties, cells or tissue need to be directly interfaced with the surface to maximize detection efficiency. Given our findings, these applications should further consider the

involvement of the cell membrane when evaluating the effect of the material on any biological system. The effects we observe may also occur in other carbon allotropes, for example carbon nanotubes. It is possible that the variation of atomic structure among different allotropes may uniquely influence their cholesterol affinity; thus investigating the shared or unique effects of other carbon allotropes on the plasma membrane and whether cholesterol is involved in these effects will be highly informative. New advances in the ability to modify carbon nanomaterials without compromising their electrical properties may help to tailor interactions with cholesterol or other biomolecules. Since cholesterol is a precursor for many steroids, which also contain the same tetracyclic ring, graphene could potentially be utilized to detect, deliver, or manipulate steroids *in vitro* and *in vivo*. This opens future directions for graphene in biomedicine, but also demands further structural and mechanistic investigation of the membrane interaction between graphene and diverse biomolecules.

Experiments and data from Chapter 2 have been published in:

Kitko, K. E., T. Hong, R. M. Lazarenko, D. Ying, Y. Q. Xu and Q. Zhang (2018). "Membrane cholesterol mediates the cellular effects of monolayer graphene substrates." Nat Commun **9**(1): 796.

References

Akhavan, O. and E. Ghaderi (2010). "Toxicity of graphene and graphene oxide nanowalls against bacteria." ACS Nano **4**(10): 5731-5736.

Amundson, D. M. and M. Zhou (1999). "Fluorometric method for the enzymatic determination of cholesterol." J Biochem Biophys Methods **38**(1): 43-52.

Amundson, D. M. and M. Zhou (1999). "Fluorometric method for the enzymatic determination of cholesterol." J. Biochem. Biophys. Methods **38**.

Bendali, A., L. H. Hess, M. Seifert, V. Forster, A.-F. Stephan, J. A. Garrido and S. Picaud (2013). "Purified Neurons can Survive on Peptide-Free Graphene Layers." Advanced Healthcare Materials **2**(7): 929-933.

Betz, W. J. and G. S. Bewick (1992). "Optical Analysis of Synaptic Vesicle Recycling at the Frog Neuromuscular Junction." Science **255**(5041): 200.

Bitounis, D., H. Ali-Boucetta, B. H. Hong, D. H. Min and K. Kostarelos (2013). "Prospects and challenges of graphene in biomedical applications." Adv Mater **25**(16): 2258-2268.

Bo, X., M. Zhou and L. Guo (2016). "Electrochemical sensors and biosensors based on less aggregated graphene." Biosens Bioelectron.

Calderon, R. O., B. Attema and G. H. DeVries (1995). "Lipid composition of neuronal cell bodies and neurites from cultured dorsal root ganglia." J Neurochem **64**(1): 424-429.

Chang, J., S. A. Kim, X. Lu, Z. Su, S. K. Kim and Y. K. Shin (2009). "Fusion step-specific influence of cholesterol on SNARE-mediated membrane fusion." Biophys J **96**(5): 1839-1846.

Cherezov, V., D. M. Rosenbaum, M. A. Hanson, S. G. Rasmussen, F. S. Thian, T. S. Kobilka, H. J. Choi, P. Kuhn, W. I. Weis, B. K. Kobilka and R. C. Stevens (2007). "High-resolution crystal structure of an engineered human beta2-adrenergic G protein-coupled receptor." Science **318**(5854): 1258-1265.

Citri, A. and R. Malenka (2008). "Synaptic plasticity: multiple forms, functions, and mechanisms." Neuropsychopharmacology **33**: 18 - 41.
Dason, J. S., A. J. Smith, L. Marin and M. P. Charlton (2010). "Vesicular sterols are essential for synaptic vesicle cycling." J Neurosci **30**(47): 15856-15865.

Fabbrizio, E., L. Le Cam, J. Polanowska, M. Kaczorek, N. Lamb, R. Brent and C. Sardet (1999). "Inhibition of mammalian cell proliferation by genetically selected peptide aptamers that functionally antagonize E2F activity." Oncogene **18**(30): 4357-4363.

Fabbro, A., D. Scaini, V. Leon, E. Vazquez, G. Cellot, G. Privitera, L. Lombardi, F. Torrisi, F. Tomarchio, F. Bonaccorso, S. Bosi, A. C. Ferrari, L. Ballerini and M. Prato (2016). "Graphene-Based Interfaces Do Not Alter Target Nerve Cells." ACS Nano **10**(1): 615-623.

Fredriksson, R., M. C. Lagerstrom, L. G. Lundin and H. B. Schioth (2003). "The G-protein-coupled receptors in the human genome form five main families. Phylogenetic analysis, paralogon groups, and fingerprints." Mol Pharmacol **63**(6): 1256-1272.

Gaus, K., T. Zech and T. Harder (2006). "Visualizing membrane microdomains by Laurdan 2-photon microscopy." Mol Membr Biol **23**(1): 41-48.

Gburski, Z., K. Górny and P. Raczyński (2010). "The impact of a carbon nanotube on the cholesterol domain localized on a protein surface." Solid State Communications **150**(9–10): 415-418.

Geim, A. K. (2009). "Graphene: status and prospects." Science **324**.

Goldstein, J. L. and M. S. Brown (2015). "A century of cholesterol and coronaries: from plaques to genes to statins." Cell **161**(1): 161-172.

Granseth, B., B. Odermatt, S. J. Royle and L. Lagnado (2006). "Clathrin-mediated endocytosis is the dominant mechanism of vesicle retrieval at hippocampal synapses." Neuron **51**(6): 773-786.

Head, B. P., H. H. Patel and P. A. Insel (2014). "Interaction of membrane/lipid rafts with the cytoskeleton: impact on signaling and function: membrane/lipid rafts, mediators of cytoskeletal arrangement and cell signaling." Biochim Biophys Acta **1838**(2): 532-545.

Hentschke, H. and M. C. Stuttgen (2011). "Computation of measures of effect size for neuroscience data sets." Eur. J. Neurosci. **34**.

Hernandez, Y., V. Nicolosi, M. Lotya, F. M. Blighe, Z. Sun, S. De, I. T. McGovern, B. Holland, M. Byrne, Y. K. Gun'Ko, J. J. Boland, P. Niraj, G. Duesberg, S. Krishnamurthy, R. Goodhue, J. Hutchison, V. Scardaci, A. C. Ferrari and J. N. Coleman (2008). "High-yield production of graphene by liquid-phase exfoliation of graphite." Nat Nanotechnol **3**(9): 563-568.

Hibino, M. and H. Tsuchiya (2014). "Self-assembled monolayers of cholesterol and cholesteryl esters on graphite." Langmuir **30**(23): 6852-6857.

Holtta-Vuori, M., E. Sezgin, C. Eggeling and E. Ikonen (2016). "Use of BODIPY-Cholesterol (TF-Chol) for Visualizing Lysosomal Cholesterol Accumulation." Traffic **17**(9): 1054-1057.

Hölttä-Vuori, M., R.-L. Uronen, J. Repakova, E. Salonen, I. Vattulainen, P. Panula, Z. Li, R. Bittman and E. Ikonen (2008). "BODIPY-Cholesterol: A New Tool to Visualize Sterol Trafficking in Living Cells and Organisms." Traffic **9**(11): 1839-1849.

Hu, W., C. Peng, W. Luo, M. Lv, X. Li, D. Li, Q. Huang and C. Fan (2010). "Graphene-based antibacterial paper." ACS Nano **4**(7): 4317-4323.

Hu, W., C. Peng, M. Lv, X. Li, Y. Zhang, N. Chen, C. Fan and Q. Huang (2011). "Protein corona-mediated mitigation of cytotoxicity of graphene oxide." ACS Nano **5**(5): 3693-3700.

Ikonen, E. (2008). "Cellular cholesterol trafficking and compartmentalization." Nat Rev Mol Cell Biol **9**(2): 125-138.

Kasry, A., A. A. Ardakani, G. S. Tulevski, B. Menges, M. Copel and L. Vyklicky (2012). "Highly Efficient Fluorescence Quenching with Graphene." The Journal of Physical Chemistry C **116**(4): 2858-2862.

Kim, H. M., H. J. Choo, S. Y. Jung, Y. G. Ko, W. H. Park, S. J. Jeon, C. H. Kim, T. Joo and B. R. Cho (2007). "A two-photon fluorescent probe for lipid raft imaging: C-laurdan." Chembiochem **8**(5): 553-559.

Korade, Z. and A. K. Kenworthy (2008). "Lipid rafts, cholesterol, and the brain." Neuropharmacology **55**(8): 1265-1273.

Kuzum, D., H. Takano, E. Shim, J. C. Reed, H. Juul, A. G. Richardson, J. de Vries, H. Bink, M. A. Dichter, T. H. Lucas, D. A. Coulter, E. Cubukcu and B. Litt (2014). "Transparent and flexible low noise graphene electrodes for simultaneous electrophysiology and neuroimaging." Nat Commun **5**: 5259.

Lange, Y., J. Ye and T. L. Steck (2014). "Essentially all excess fibroblast cholesterol moves from plasma membranes to intracellular compartments." PLoS One **9**(7): e98482.

Lee, J. H., E. K. Lee, W. J. Joo, Y. Jang, B. S. Kim, J. Y. Lim, S. H. Choi, S. J. Ahn, J. R. Ahn, M. H. Park, C. W. Yang, B. L. Choi, S. W. Hwang and D. Whang (2014). "Wafer-scale growth of single-crystal monolayer graphene on reusable hydrogen-terminated germanium." Science **344**(6181): 286-289.

Li, N., X. Zhang, Q. Song, R. Su, Q. Zhang, T. Kong, L. Liu, G. Jin, M. Tang and G. Cheng (2011). "The promotion of neurite sprouting and outgrowth of mouse hippocampal cells in culture by graphene substrates." Biomaterials **32**(35): 9374-9382.

Li, X. (2009). "Large-area synthesis of high-quality and uniform graphene films on copper foils." Science **324**.

Li, X., W. Cai, J. An, S. Kim, J. Nah, D. Yang, R. Piner, A. Velamakanni, I. Jung, E. Tutuc, S. K. Banerjee, L. Colombo and R. S. Ruoff (2009). "Large-Area Synthesis of High-Quality and Uniform Graphene Films on Copper Foils." Science **324**(5932): 1312-1314.

Li, Y., H. Yuan, A. von dem Bussche, M. Creighton, R. H. Hurt, A. B. Kane and H. Gao (2013). "Graphene microsheets enter cells through spontaneous membrane penetration at edge asperities and corner sites." Proc Natl Acad Sci U S A **110**(30): 12295-12300.

Liu, G. and R. W. Tsien (1995). "Synaptic transmission at single visualized hippocampal boutons." Neuropharmacology **34**(11): 1407-1421.

Liu, S., T. H. Zeng, M. Hofmann, E. Burcombe, J. Wei, R. Jiang, J. Kong and Y. Chen (2011). "Antibacterial activity of graphite, graphite oxide, graphene oxide, and reduced graphene oxide: membrane and oxidative stress." ACS Nano **5**(9): 6971-6980.

Lund, F., M. Lomholt, L. Solanko, R. Bittman and D. Wustner (2012). "Two-photon time-lapse microscopy of BODIPY-cholesterol reveals anomalous sterol diffusion in chinese hamster ovary cells." BMC Biophysics **5**(1): 20.

Malinow, R. and R. C. Malenka (2002). "AMPA receptor trafficking and synaptic plasticity." Annu Rev Neurosci **25**: 103-126.

Mao, H. Y., S. Laurent, W. Chen, O. Akhavan, M. Imani, A. A. Ashkarran and M. Mahmoudi (2013). "Graphene: Promises, Facts, Opportunities, and Challenges in Nanomedicine." Chemical Reviews **113**(5): 3407-3424.

Maxfield, F. R. and D. Wustner (2012). "Analysis of cholesterol trafficking with fluorescent probes." Methods Cell Biol **108**: 367-393.

Missaire, M. and R. Hindges (2015). "The role of cell adhesion molecules in visual circuit formation: from neurite outgrowth to maps and synaptic specificity." Dev Neurobiol **75**(6): 569-583.

Nayak, T. R., H. Andersen, V. S. Makam, C. Khaw, S. Bae, X. Xu, P.-L. R. Ee, J.-H. Ahn, B. H. Hong, G. Pastorin and B. Özyilmaz (2011). "Graphene for Controlled and Accelerated Osteogenic Differentiation of Human Mesenchymal Stem Cells." ACS Nano **5**(6): 4670-4678.

Novoselov, K. S., V. I. Fal′ko, L. Colombo, P. R. Gellert, M. G. Schwab and K. Kim (2012). "A roadmap for graphene." Nature **490**(7419): 192-200.

Novoselov, K. S., A. K. Geim, S. V. Morozov, D. Jiang, Y. Zhang, S. V. Dubonos, I. V. Grigorieva and A. A. Firsov (2004). "Electric field effect in atomically thin carbon films." Science **306**(5296): 666-669.

Pankov, R., T. Markovska, P. Antonov, L. Ivanova and A. Momchilova (2006). "The plasma membrane lipid composition affects fusion between cells and model membranes." Chem Biol Interact **164**(3): 167-173.

Pfrieger, F. W. (2003). "Role of cholesterol in synapse formation and function." Biochim Biophys Acta **1610**(2): 271-280.

Puchkov, D. and V. Haucke (2013). "Greasing the synaptic vesicle cycle by membrane lipids." Trends Cell Biol **23**(10): 493-503.

Rauti, R., N. Lozano, V. Leon, D. Scaini, M. Musto, I. Rago, F. P. Ulloa Severino, A. Fabbro, L. Casalis, E. Vazquez, K. Kostarelos, M. Prato and L. Ballerini (2016). "Graphene Oxide Nanosheets Reshape Synaptic Function in Cultured Brain Networks." ACS Nano **10**(4): 4459-4471.

Rouze, N. C. and E. A. Schwartz (1998). "Continuous and Transient Vesicle Cycling at a Ribbon Synapse." The Journal of Neuroscience **18**(21): 8614.

Sezgin, E., F. B. Can, F. Schneider, M. P. Clausen, S. Galiani, T. A. Stanly, D. Waithe, A. Colaco, A. Honigmann, D. Wustner, F. Platt and C. Eggeling (2016). "A comparative study on fluorescent cholesterol analogs as versatile cellular reporters." J Lipid Res **57**(2): 299-309.

Sholl, D. A. (1953). "Dendritic organization in the neurons of the visual and motor cortices of the cat." Journal of Anatomy **87**(Pt 4): 387-406.381.

Simons, K. and D. Toomre (2000). "Lipid rafts and signal transduction." Nat Rev Mol Cell Biol **1**(1): 31-39.

Song, Y., A. K. Kenworthy and C. R. Sanders (2014). "Cholesterol as a co-solvent and a ligand for membrane proteins." Protein Sci **23**(1): 1-22.

Subtil, A., I. Gaidarov, K. Kobylarz, M. A. Lampson, J. H. Keen and T. E. McGraw (1999). "Acute cholesterol depletion inhibits clathrin-coated pit budding." Proc Natl Acad Sci U S A **96**(12): 6775-6780.

Sullivan, G. M. and R. Feinn (2012). "Using effect size-or why the P value is not enough." J. Grad. Med. Educ. **4**.

Takamori, S., M. Holt, K. Stenius, E. A. Lemke, M. Grønborg, D. Riedel, H. Urlaub, S. Schenck, B. Brügger, P. Ringler, S. A. Müller, B. Rammner, F. Gräter, J. S. Hub, B. L. De Groot, G. Mieskes, Y. Moriyama, J. Klingauf, H. Grubmüller, J. Heuser, F. Wieland and R. Jahn (2006). "Molecular Anatomy of a Trafficking Organelle." Cell **127**(4): 831-846.

Thiagarajan, T. C., M. Lindskog and R. W. Tsien (2005). "Adaptation to synaptic inactivity in hippocampal neurons." Neuron **47**.

Tu, Y., M. Lv, P. Xiu, T. Huynh, M. Zhang, M. Castelli, Z. Liu, Q. Huang, C. Fan, H. Fang and R. Zhou (2013). "Destructive extraction of phospholipids from Escherichia coli membranes by graphene nanosheets." Nat Nanotechnol **8**(8): 594-601.

Veliev, F., A. Briancon-Marjollet, V. Bouchiat and C. Delacour (2016). "Impact of crystalline quality on neuronal affinity of pristine graphene." Biomaterials **86**: 33-41.

Wang, Y., W. C. Lee, K. K. Manga, P. K. Ang, J. Lu, Y. P. Liu, C. T. Lim and K. P. Loh (2012). "Fluorinated Graphene for Promoting Neuro-Induction of Stem Cells." Advanced Materials **24**(31): 4285-4290.

Weber, P., M. Wagner and H. Schneckenburger (2010). "Fluorescence imaging of membrane dynamics in living cells." J Biomed Opt **15**(4): 046017.

Wilhelm, B. G., S. Mandad, S. Truckenbrodt, K. Krohnert, C. Schafer, B. Rammner, S. J. Koo, G. A. Classen, M. Krauss, V. Haucke, H. Urlaub and S. O. Rizzoli (2014). "Composition of isolated synaptic boutons reveals the amounts of vesicle trafficking proteins." Science **344**(6187): 1023-1028.

Wu, J., J. D. Holstein, G. Upadhyay, D. T. Lin, S. Conway, E. Muller and J. D. Lechleiter (2007). "Purinergic receptor-stimulated IP3-mediated Ca2+ release enhances neuroprotection by increasing astrocyte mitochondrial metabolism during aging." J Neurosci **27**(24): 6510-6520.

Yue, H. Y. and J. Xu (2015). "Cholesterol regulates multiple forms of vesicle endocytosis at a mammalian central synapse." J Neurochem **134**(2): 247-260.

Zhang, L. and X. Wang (2015). "Mechanisms of graphyne-enabled cholesterol extraction from protein clusters." RSC Advances **5**(16): 11776-11785.

Zhang, L., B. Xu and X. Wang (2016). "Cholesterol Extraction from Cell Membrane by Graphene Nanosheets: A Computational Study." The Journal of Physical Chemistry B.

Zhang, Q., Y.-Q. Cao and R. W. Tsien (2007). "Quantum dots provide an optical signal specific to full collapse fusion of synaptic vesicles." Proceedings of the National Academy of Sciences **104**(45): 17843-17848.

Zhang, Q., Y. Li and R. W. Tsien (2009). "The Dynamic Control of Kiss-And-Run and Vesicular Reuse Probed with Single Nanoparticles." Science **323**(5920): 1448-1453.

Zhang, Y., K. H. Dodson, R. Fischer, R. Wang, D. Li, R. M. Sappington and Y. Q. Xu (2016). "Probing electrical signals in the retina via graphene-integrated microfluidic platforms." Nanoscale **8**(45): 19043-19049.

Zhang, Y., T. R. Nayak, H. Hong and W. Cai (2012). "Graphene: a versatile nanoplatform for biomedical applications." Nanoscale **4**(13): 3833-3842.

Zidovetzki, R. and I. Levitan (2007). "Use of cyclodextrins to manipulate plasma membrane cholesterol content: evidence, misconceptions and control strategies." Biochim Biophys Acta **1768**(6): 1311-1324.

Chapter 3

Graphene nanoflakes acutely modify cell signaling via lipid packing

Abstract

Graphene-based nanomaterials are increasingly used as interfaces with biological systems, yet there still remains controversy as to the structural and functional effects of graphene on cells. In cell membranes, cholesterol is structurally essential within the lipid bilayer and functionally influential for transmembrane signaling. Here, we report that graphene nanoflakes (GNFs) have a preferential affinity to cholesterol. We further demonstrate that GNFs acutely alter the biophysical properties of the cell membrane. As secretory vesicles and receptors are major mediators for membrane signal output and input respectively, we demonstrate using two representative systems, synaptic vesicles and G protein-coupled receptors, the utility of GNFs for modulating transmembrane signaling via plasma membrane packing. In cultured hippocampal neurons, GNFs promote neurotransmitter release, leading to presynaptic potentiation. In fibroblasts, GNFs enhance ATP-induced Ca^{2+}-responses by enhancing P2Y receptor activity in a membrane-packing dependent manner. Together, our results provide a framework for cell membrane-associated bioapplications of graphene-based nanomaterials.

Introduction

In eukaryotic cells, the plasma membrane acts as the sole interface between cells and the environment. Recent work has demonstrated that cells growing on graphene, a single-layer carbon crystal (Novoselov, Geim et al. 2004), exhibit elevated membrane cholesterol, resulting in

cholesterol-associated functional changes (Kitko, Hong et al. 2018). This and similar studies have further demonstrated that graphene substrates are largely biocompatible and in fact serve to strengthen neuronal synapses (Bendali, Hess et al. 2013, Fabbro, Scaini et al. 2016, Rauti, Lozano et al. 2016, Veliev, Briancon-Marjollet et al. 2016, Pampaloni, Lottner et al. 2018). However, other results suggest that nanometer-scale graphene flakes are toxic to cells. Results from both computational modeling and electron microscopy studies have indicated that single- or few-layer graphene nanoflakes (GNFs), with their sharp edges and hydrophobic surfaces, can insert into the lipid bilayer, extracting phospholipids and thus disrupting the integrity of the prokaryotic plasma membrane (Li, Yuan et al. 2013, Tu, Lv et al. 2013). However, eukaryotic cells exposed to graphene are seemingly resistant to such membrane disruption (Li, Zhang et al. 2011, Nayak, Andersen et al. 2011, Wang, Lee et al. 2012). Intriguingly, computational simulations have suggested that cholesterol, unique to eukaryotic membranes, tightly surrounds inserted GNFs (Zhang, Xu et al. 2016), which may prevent cell membrane destruction. This motivated us to understand the specificity of a potential graphene-cholesterol interaction. As we uncover that the interaction between GNFs and cholesterol is relatively specific, we then explored the utility of GNFs for manipulation of membrane organization and function in live cells, which led to the discovery that GNFs can acutely increase lipid packing and modify transmembrane signaling pathways.

Methods

Preparation and characterization of graphene nanoflakes (GNFs) suspensions

GNFs suspension was prepared by liquid exfoliation of graphite powder. Graphite powder was purchased from ASBURY CARBONS (Grade: 2299). Polyvinylpyrrolidone (PVP, MW: 1,300,000 g/mol) was purchased from Sigma. Hydrophobic graphite powder was added into 2 wt% PVP or 1 wt% SDS (sodium dodecyl sulfate) water solution and sonicated for 9 h in a bath sonicator (Wajid, Das et al. 2012). The uniform GNFs suspension was then centrifuged with a Thermo Scientific Fiberlite F15-6 X 100y rotor at 4,000 rpm and at room temperature for 1 h to sediment large graphite aggregates. The upper 50% of supernatant was carefully decanted, resulting in PVP-functionalized GNFs suspension (O'Connell, Bachilo et al. 2002, Hernandez, Nicolosi et al. 2008). The transmission characterization of GNFs suspension was carried out on a Varian Cary 5000 UV-VIS-NIR spectrophotometer. The concentration of GNFs was estimated with an absorption coefficient of 2460 L g^{-1} m^{-1} at 660 nm (Hernandez, Nicolosi et al. 2008), which is typically 26 mg/L for freshly-made GNFs suspension. The suspension is stored at 4 ºC and remains stable for more than a year. As shown in Figure 3.1, a one-year old GNFs suspension (*left*) shows no precipitation and is as evenly-distributed as a freshly-prepared sample (*right*).

Characterization of GNFs

GNFs suspension was characterized using transmission electron microscopy (TEM). TEM samples were prepared by drop casting a small volume (~ 2 μl) of GNFs suspension onto carbon grids (300 mesh size, Ted Pella). Samples were air dried for 2 h, and then rinsed with DI water to remove excessive solvent. Bright field TEM images of representative GNFs were taken by an Osiris TEM (FEI) at an accelerating voltage of 200 kV. Raman spectroscopy was also employed to characterize the quality of the GNFs. GNFs were drop-casted onto an Si/SiO_2 wafer (300 nm

SiO_2) and then washed with DI water to remove excess suspension agents. Raman spectra were taken by a DXR Raman microscope (Thermo Scientific) with 532 nm laser excitation. The size and thickness of GNFs were further investigated by a Nanoscope III atomic force microscope (AFM). GNFs suspension was spin-coated onto a Si wafer with 300 nm SiO_2, and washed with DI water to remove solvent residue. The AFM was operated in tapping mode with a typical image size of 2-5 μm.

Cell culture

Murine procedures and all relevant experimental protocols were approved by the Vanderbilt University Animal Care and Use Committee. Rat postnatal hippocampal cultures were prepared as previously described (Liu and Tsien 1995), with modifications. Rat hippocampi (CA1-CA3) from both hemispheres were dissected from P0-1 Sprague-Dawley rats and dissociated into a single-cell suspension. Dissociated cells were recovered by centrifugation (x 200 g, 5 minutes) at 4 °C and re-suspended in plating media composed of Minimal Essential Medium (MEM, Life Technologies) with (in mM) 27 glucose, 2.4 $NaHCO_3$, 0.00125 transferrin, 2 L-glutamine, 0.0043 insulin and 10%/vol fetal bovine serum (FBS, Omega). 100 μl of cell suspension was added onto round 12mm-∅ glass coverslips (200-300 cells/mm^2). 100 μl of Matrigel (BD Biosciences, 1:50 dilution) was deposited on the coverslips and incubated at 37°C with 5% CO_2 for ~ 2 h, then aspirated before cells were plated. Cells were allowed to settle on the coverslip surfaces for 4 h before the addition of 1 mL culture media made of MEM containing (in mM) 27 glucose, 2.4 $NaHCO_3$, 0.00125 transferrin, 1.25 L-glutamine, 0.0022 insulin, 1 %/vol B27 supplement (Life Technologies) and 7.5 %/vol FBS. 1 to 2 days after plating, 2% Ara-C was introduced with another

1 mL of culture media, which efficiently prevented astroglia proliferation. All experiments were performed using cultures between 12-18 DIV.

NIH 3T3 cells were grown at 37°C with 5% CO_2 in Dulbecco's modified Eagle's medium containing 4.5 g/L glucose and L-glutamine supplemented with 10% fetal bovine serum, 100 units mL^{-1} penicillin, and 100 μg mL^{-1} streptomycin. Cells were regularly passaged to maintain adequate growth and were passaged at least 5 times before trypsinization and plating on Matrigel-coated round 12mm-∅ glass coverslips (75 μL of 1-3 x 10^6 cell solution per coverslip). Cells were grown to 50-80% confluency for 24 h on coverslips prior to experiments.

Fluorescence lifetime measurements

Fluorescence lifetime images were acquired using a custom-built multiphoton fluorescence system (Bruker) built on an inverted microscope (Nikon Ti-E). For bulk solution measurements, 500 μL sample volumes were illuminated using a 40x oil-immersion objective (N.A. 1.3). TFC (TopFluor Cholesterol, Avanti), TFSM (TopFluor Sphingomyelin, Avanti), TFPC (TopFluor Phosphotidylcholine, Avanti), or BODIPY (boron-dipyrromethene, Thermo Fisher Scientific) were added to suspended GNFs (26 ng/mL) or 0.002 wt% PVP in H_2O at a final concentration of 1 μM for 1 h prior to imaging. NIH-3T3 cell samples were illuminated using a 100x oil-immersion objective (N.A. 1.45). For cell membrane loading experiments, GNFs suspension was added to cells at a final concentration of 260 μg/L in normal Tyrode for 10 min before TFC was added at a final concentration of 1 μM. Samples were excited with a Ti:Sapphire laser (Coherent, Inc.) tuned to 960 nm, passed through a 550/100 emission filter, and detected using a GaAsP photomultiplier tube (H7422P-40, Hamamatsu). Pixel dwell time was 4.8 μs and the acquired

images were 256x256 pixels with a 60 s acquisition time at an average incident power of approximately 10 mW. Fluorescence lifetime images were acquired using time-correlated single photon counting electronics (SPC-150; Becker & Hickl). The instrument response function (IRF) was generated by measuring the second harmonic generation of urea crystals excited at 900 nm. The full width at half maximum of the IRF was 244 ps. Fluorescence lifetime was validated before each experiment by imaging a fluorescent bead standard (Polysciences, Inc.). The measured lifetime of this bead was 2.1 ± 0.005 ns (n=3), in good agreement with published values (Bird, Yan et al. 2005). Phasor analysis was performed as described previously (Digman, Caiolfa et al. 2008), using custom-written Matlab algorithms based on a previously published phasor analysis software (Stefl, James et al. 2011).

Giant plasma membrane vesicle preparation

NIH-3T3 cells at greater than 85% confluency were washed 3 times with PBS and labeled at 5 μg/ml for 10 min at 37°C with 1,1'-Dilinoleyl-3,3,3',3'-tetramethylindocarbocyanine,4-chlorobenzenesulfonate (FAST-DiI, C-18, Life Technologies). GPMV isolation was performed as previously described(Sezgin, Kaiser et al. 2012). Cells were blebbed in deionized water containing, in mM: 10 HEPES, 150 NaCl, 2 $CaCl_2$, pH 7.4, with 25 mM PFA and 2mM DTT at 37°C for 2-3 h. PVP or GNFs treatments (final concentration 260 μg/L of either 0.002 wt% PVP or GNFs suspension) were performed either prior to or following GPMV isolation (see figure legends). For treatments prior to GPMV isolation, the supernatant, containing GPMVs, was collected and allowed to settle for at least 1 hour at 4°C prior to imaging. Three independent GPMV

preparations were performed for each treatment group and a minimum of 60 GPMVs were imaged at each individual temperature point.

GPMV fluorescence imaging and lipid phase separation

Lipid phase separation was achieved using a commercial liquid-nitrogen cooled temperature stage equipped with two heating elements (GS350, Linkam Scientific Instruments). Thermal grease (Linkam) was applied to stage surfaces for each sample to minimize thermal contact resistance and maximize conductive heat transfer. 60 uL of GPMV solution was added to the center of a 20x40 mm size 0 coverslip, which was top-sealed with another coverslip of the same size using vacuum grease. Samples were allowed to equilibrate for 1 min at each temperature point prior to image acquisition. Images were acquired with a 60X LUMP PlanFl Olympus water-immersion objective (N.A. 0.9) on a customized spinning disk confocal setup built on an Olympus BX-51WI microscope with a CSU-X1 (Yokogawa) spinning disk head and an Evolve 512 EMCCD (Photometrics). Samples were visualized with a 561 nm laser (Coherent) and an Em 605/52 filter set. All data collected for quantitative comparisons were collected with identical imaging parameters. Images stacks were analyzed manually to determine phase separated vs. non-separated fractions. L_d fraction was quantified by manually drawing arc lengths on GPMVs in ImageJ.

Folch extraction

500 µL and 250 µL of 5% HCl were added to cells and to 250 µL of media, respectively. 750 µL of Folch solution (2:1, $CHCl_3$:MeOH with 17 mg/L BHT, butylated hydroxytoluene) was utilized for extraction and 10 µL of 1.25 mg/mL 5β-cholestan-3α-ol was added as an internal standard for cholesterol quantitation. The Folch solution was vortexed and centrifuged briefly to allow distinct organic and aqueous layers to separate. The organic layer was then used for cholesterol identification and quantification (GC-FID, Gas chromatography – Flame ionization detector, and GC-MS, Gas chromatography – Mass spectrometry).

Cholesterol derivatization

Folch extractions from both cells and media were dried down and reconstituted in 40 µL of bistrimethylsilyltrifluoroacetamide (BSTFA) kit solution (Sigma-Aldrich) for at least 2 h with internal standard to account for extraction and derivatization efficiencies.

Gas chromatography – flame ionization detector (GC-FID)

Cholesterol quantification was carried out in duplicates for all biological replicates with a GC-6890 gas chromatograph (Hewlett-Packard) equipped with a DB-5 (30 mm × 0.32 mm × 0.25 mm) fused silica column (Sigma Aldrich). Briefly, sterols were separated using a temperature program as follows: samples were heated from 220 to 275 °C at 15 °C/min, then further heated to 280 °C at 1 °C/min and maintained for 2 min, followed by heating to 290 °C at 5 °C/min rate and holding for 10 min.

Determination of total protein content

Proteins separated during Folch extraction were MeOH washed, pelleted, and dried before re-suspension in 2% SDS (Sigma Aldrich). A Pierce BCA assay (Life Technologies) was performed according to manufacturer specifications using 25 µL of protein sample per microwell. Sample absorption was measured at 560 nm using a Glomax Discover (Promega) 96-well microplate reader.

Filipin staining and image analysis

Cells were fixed in PBS containing 4% paraformaldehyde for 30 min, washed, and incubated with filipin (1:500 in PBS, Sigma-Aldrich) for 2 h at room temperature. Fluorescence imaging was performed on an Olympus IX-81 inverted microscope using a Nikon Intensilight illuminator, a Nikon Plan Apo VC 20X objective (N.A. 0.75) and a fluorescence filter set (Ex 390/40, DiC T425LPXR, Em 460/50, Semrock). Images were acquired with an EMCCD (Andor) via Micro-manager with the same acquisition settings across each experimental group. For analysis, three independent batches of cultures were analyzed ($n > 9$ different coverslips). The total number of cells analyzed are reported (see figure legends). For the analysis of 3T3 cells, we manually selected ROIs covering cell-containing regions. ROIs corresponding to out of focus cells were manually excluded. Average ROI intensity was measured in ImageJ. For every field of view, at least three ROIs from cell-free regions were manually selected and their mean fluorescence intensities were calculated in the same manner. For background subtraction, the mean intensity

value of every cell-containing ROI was subtracted by the average intensity of the three background ROIs in the same image.

Live cell fluorescence imaging and analysis

All live cell imaging except generalized polarization imaging was performed using the spinning disk confocal setup used for GPMV imaging. For generalized polarization imaging(Kim, Choo et al. 2007), cells were pre-incubated with culture media containing 1 μM C-laurdan (TP Probes) at 37°C and 5% CO_2 for 1 h. For TFC imaging, cells were pre-incubated in culture media containing 1 μM TFC at 37° C with 5% CO_2 for 20 min. For DiO imaging, cells were pre-loaded with 10 μM DiO (Invitrogen) in culture media at 37°C with 5% CO_2 for 15 min. For voltage imaging, the DiO containing solution was replaced with 20 mM DPA (dipicrylamine) in normal Tyrode. For Ca^{2+} imaging, cells were pre-incubated with culture media containing 10 μM XRhod-1AM (Life Technologies) at 37°C with 5% CO_2 for 30 min. For FM dye or Quantum dot (Qdot) loading of the evoked pool of synaptic vesicles, cells were incubated with 10 μM FM1-43 or FM4-64, or 100 or 0.8 nM Qdots (Qdot 605, Life Technologies) for 2 min in high K^+ bath solution containing (in mM): 64 NaCl, 90 KCl, 2 $MgCl_2$, 2 $CaCl_2$, 10 N-2 hydroxyethyl piperazine-n-2 ethanesulphonic acid (HEPES), 10 glucose, 1 μM TTX, pH 7.35. After loading, cells were washed with normal bath solution containing 10 μM NBQX (2,3-dihydroxy-6-nitro-7-sulfamoylbenzo[f]quinoxaline-2,3-dione) and 20 μM D-AP5 (D-(-)-2-Amino-5-phosphonopentanoic acid) for at least 10 min prior to imaging. Coverslips were mounted in an RC-26G imaging chamber (Warner Instruments) bottom-sealed with a 24X40 mm size 0 cover glass (Fisher Scientific). The chamber was fixed in a PH-1 platform (Warner Instruments) placed on the

microscope stage. Gravity perfusion was controlled by a VC-6 valve control system (Warner Instruments) with a constant rate of ~50 μL/sec. All perfusion lines were combined into an SHM-6 in-line solution heater (Warner Instruments). The temperatures of both the imaging chamber and the perfusion solution were maintained at 34°C by a temperature controller (TC344B, Warner Instruments). Image acquisition and synchronized perfusion were controlled via Micro-manager software.

For generalized polarization imaging, C-Laurdan loaded cells were imaged using a Nikon Ti-E equipped with an iX897 EMCCD (Andor) and a 100X ApoVC objective (N.A. 1.40). A filter combination of D350x for excitation and a DiC 409LP with an Em 440/40 or 483/32 (for blue or green channels, respectively) were used. The acquisition rate was 0.5 Hz. For TFC, FM1-43, and DiO/DPA imaging, a 480-nm laser (Coherent) and a filter combination of DiC 500LX and Em 520/20 were used. The acquisition rate was 1 Hz for all imaging. For Ca^{2+} imaging, a 561-nm laser (Coherent) and a filter combination of DiC 580LPXR and Em 605/52 were used. The acquisition rate was 1 Hz. For Qdot imaging, a 480-nm laser and a filter combination of DiC 510LX and Em 605/10 were used. The acquisition rate was 5 Hz. For FM4-64 imaging, a 561-nm laser (Coherent) and a filter combination of DiC 600LX and Em 620/20 were used. The acquisition rate was 1 Hz. For static images, ten-frame stacks were averaged. All images were taken with the same acquisition settings among different treatment groups (laser intensity, exposure time, and EM gain). For each dye, images were taken with the same acquisition settings (excitation light intensity, spinning disk speed, exposure time, and EM gain) for all samples.

All image analyses were performed in ImageJ as described previously (Zhang, Li et al. 2009). Four rectangular ROIs were drawn in cell-free regions in every FOV and their intensities averaged for background correction. For every type of fluorescence imaging, we pooled all

background ROIs regardless of treatment differences. Again, a masked threshold approach was applied in ImageJ, and the mean intensity plus two standard deviations was used as the common threshold for all images or image stacks. For every FOV, ROIs were generated by particle analysis based on the binary threshold mask image. For FM1-43 and FM4-64, watershed segmentation and particle size limits (0.3 – 3 μm) were applied in ImageJ to isolate ROIs for synaptic boutons (~1 μm). Background correction was performed by subtracting the average of four rectangular ROIs from the average intensity of each individual ROI in the same FOV. Normalization was performed using the average intensity of the first 10 frames. For C-laurdan images, ROIs generated from blue channel images were used to analyze both channels. For generalized polarization images, ROIs generated from blue channel images were used to analyze both channels. GP value was calculated using the following formula: $I_{GP}=(I_{blue}-G\times I_{green})/(I_{blue}+G\times I_{green})$, in which G is the sensitivity correction factor between the two channels (Hansen and Helix-Nielsen 2011). G was empirically determined by imaging 1 μM C-laurdan diluted in DMSO using the standard protocol. Given GP_{DMSO} = 0.006, the G value of our imaging setup was calculated using the following formula: $G=(I_{blue}\times(1-GP_{DMSO}))/(I_{green}\times(1+GP_{DMSO}))$. For Qdot images, FM4-64-defined ROIs were applied and the mean Qdot photoluminescence intensity in each ROI was calculated. Quantal analysis for single Qdots was performed as described previously(Zhang, Cao et al. 2007, Zhang, Li et al. 2009). Briefly, maximum likelihood estimates were used to fit Qdot numbers to a distribution of intensities. Qdot intensities were binned every 30 a.u. without background subtraction. The estimated threshold based on the mean background signal plus two standard deviations was near 3,000 a.u., by which we set the cut-off threshold for a single Qdot. To analyze the behavior of vesicles labeled by single Qdots, we selected ROIs having only one Qdot. Time-dependent Qdot photoluminescence changes were extracted with a 5-frame moving window.

Electrophysiology

Whole-cell voltage clamp recordings were performed on neurons from 12 - 18 DIV cultures using a Multi-Clamp 700B amplifier, digitized through a Digidata 1440A, and interfaced via pCLAMP 10 software (all from Molecular Devices). All recordings were performed at room temperature. Cells were voltage clamped at -70 mV for all experiments. Patch pipettes were pulled from borosilicate glass capillaries with resistances ranging from 3 - 6 MΩ when filled with pipette solution. The bath solution (Tyrode's saline) contained (in mM): 150 NaCl, 4 KCl, 2 $MgCl_2$, 2 $CaCl_2$, 10 HEPES, 10 glucose, pH 7.35. The pipette solution contained (in mM): 120 Cesium Methanesulfonate, 8 CsCl, 1 $MgCl_2$, 10 HEPES, 0.4 EGTA, 2 MgATP, 0.3 GTP-Tris, 10 phosphocreatine, QX-314 (50 □M), 5 biocytin (Tocris), pH 7.2. For tmEPSC recordings, bath solution was supplied with 1 μM tetrodotoxin (TTX, Abcam). The last 50 mEPSCs at the end of 5 min recordings with TTX were collected and analyzed using template based event detection. The template was generated from our own representative data. To measure AMPA receptor currents, D-AP5 (Abcam), an NMDA receptor antagonist, was added to the bath solution. NMDA receptor currents were recorded in the presence of 10 μM NBQX (Abcam), an AMPA receptor antagonist, in 0 mM [Mg^{2+}] / 3 mM [Ca^{2+}] bath solution at -70 mV holding potential. Isolated AMPA and NMDA EPSCs were recorded from the same neurons sequentially, by first applying D-AP5 then completely replacing it with NBQX. The I_{NMDAR}/I_{AMPAR} ratio for every neuron was calculated from the average amplitudes of the last 10 NMDA and AMPA events during 5 min D-AP5 or subsequent NBQX application. No postsynaptic currents were detected if D-AP5 and NBQX were applied together. All signals were digitized at 20 kHz, filtered at 2 kHz, and analyzed offline with Clampfit software (Molecular Devices).

Statistical analysis

No statistical methods were used to predetermine sample size. All experiments were repeated in at least three different batches of cells to ensure reproducibility and adequate sample power. Values presented are mean ± s.e.m. For calculating statistics, Lillefors tests were first used to assess the normality of all data. The Student's *t*-test was used for 2-group comparison of average values when data were distributed normally, otherwise Wilcoxin rank-sum tests were used. Fisher *z*-tests were used to compare correlation coefficients. 2-sided *Kolmogorov-Smirnov* tests were used to test for equivalent distributions.

Production and characterization of GNFs

To obtain high quality GNFs, we used liquid-phase exfoliation (LPE) of graphite powder, which produces single- and few-layer GNFs in a scalable fashion (Hernandez, Nicolosi et al. 2008, Geim 2009). We suspended GNFs uniformly in H_2O containing 2 wt% polyvinylpyrrolidone (PVP), which effectively prevented GNFs aggregation (**Fig. 3.1a**).

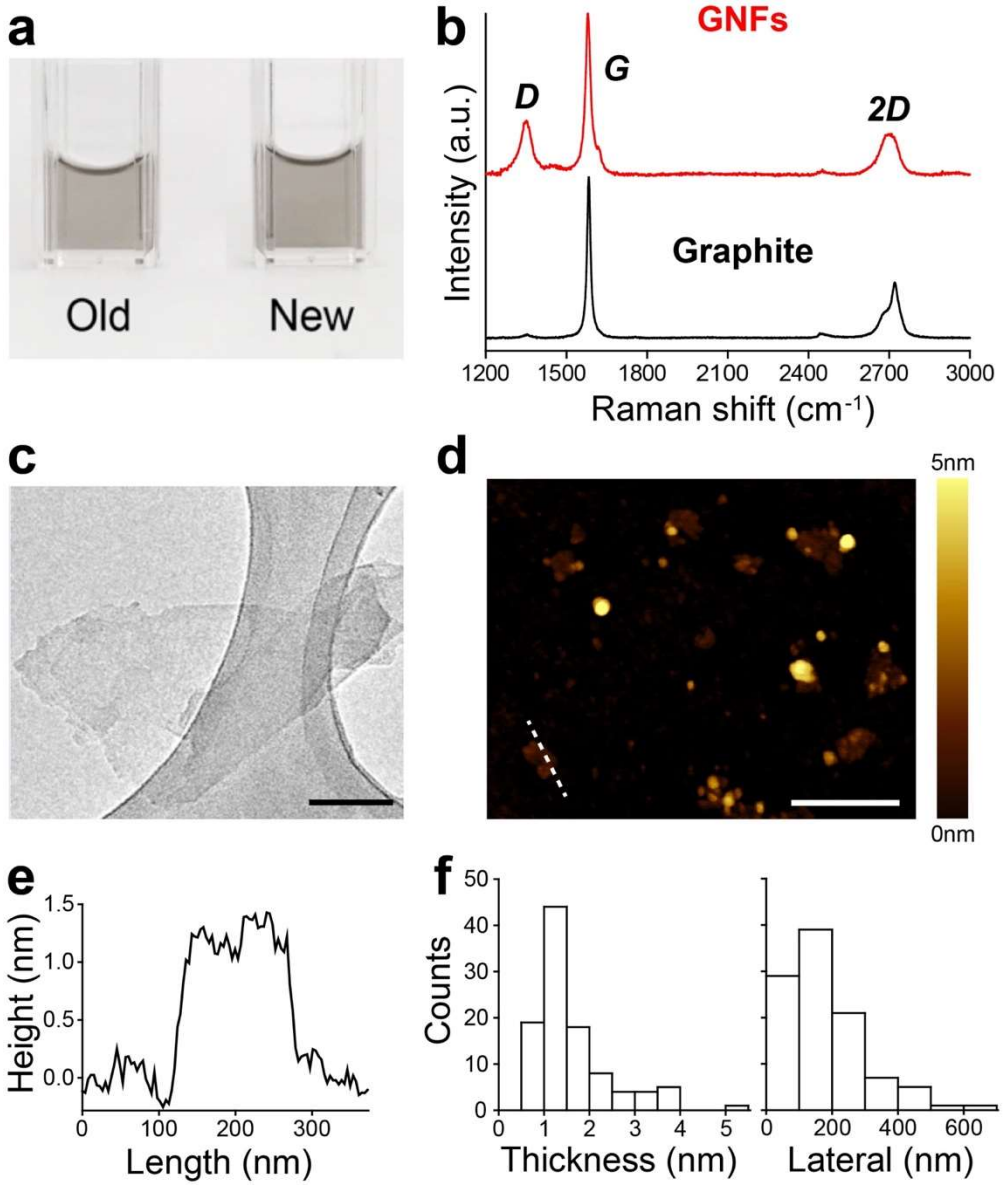

Figure 3.1 **Characterization of graphene nanoflakes.** (**a**) Samples of GNFs suspension. The left is one-year old and the right is freshly prepared. Both contain 26 mg/L GNFs. (**b**) Raman spectra for GNFs suspended in 2 wt% PVP (red) and bulk graphite (black), respectively. (**c**) Sample TEM image of a GNF. Scale bar, 100 nm. (**d**) Sample AFM image of dispersed GNFs from the suspension. Scale bar, 500 nm. (**e**) Line profile of a GNF along the white dashed line in (**d**). (**f**) The distributions of GNFs thickness (left) and lateral dimension (right) obtained from AFM images (N = 37 FOVs).

Notably, over more than two years, we did not observe any aggregation in the prepared suspensions. We estimated that our suspended GNFs concentration is ~26 mg/L, based on an

absorption coefficient at 660nm (Hernandez, Nicolosi et al. 2008). We characterized the GNFs using Raman spectroscopy (**Fig. 3.1b**). At 532 nm excitation, GNFs suspensions exhibited characteristic G peaks (~1,580 cm^{-1}) and 2D peaks (~2,700 cm^{-1}) similar to bulk graphite (Hernandez, Nicolosi et al. 2008). However, unlike graphite, Raman D peaks (~1,350 cm^{-1}) were larger in the GNFs suspensions, matching the strong edge effects of nanometer-size GNFs (Ferrari, Meyer et al. 2006). To better estimate the size distributions within our suspensions, we performed both transmission electron microscopy (TEM) and atomic force microscopy (AFM) to estimate GNFs lateral dimension and thickness. As shown in **Figure 3.1c**, representative TEM micrographs suggest that GNFs have smooth planar structures and uniform flake edges, supporting an estimate of one to few layers. We then quantified AFM measurements to obtain a better estimate of average GNFs size and thickness (**Fig. 3.1d**). Our analysis of AFM data demonstrates that the majority of the flakes are 1-2 nm thick with lateral dimensions of a few hundred nanometers (**Fig. 3.1e&f**). This is expected for single- or few-layer GNFs because of the tendency for aggregation during AFM sample preparation (Lotya, Hernandez et al. 2009) and the presence of PVP on the GNFs surface (Hernandez, Nicolosi et al. 2008). Importantly, median GNFs thickness (~ 1.3 nm) and size (~ 180 nm) (**Fig. 3.1f)** were consistent with previous reports (Hernandez, Nicolosi et al. 2008).

Preferential interaction between GNFs and cholesterol

Previous work has suggested that GNFs can extract cholesterol from culture media containing serum. However, the relative selectivity of cholesterol compared to other major membrane components is less understood. To better understand the selectivity of GNFs to cholesterol, we employed fluorescence lifetime imaging microscopy (FLIM) (Bastiaens and

Squire 1999) to measure proximity-dependent Förster resonance energy transfer (FRET) (Kasry, Ardakani et al. 2012) between GNFs and fluorophore conjugated cholesterol, TFC (cholesterol tagged with boron-dipyrromethene, a. k. a BODIPY) (Hölttä-Vuori, Uronen et al. 2008), or other membrane lipids. BODIPY is relatively nonpolar and electrically neutral, minimizing the dye-induced perturbation of conjugated lipids (Hölttä-Vuori, Uronen et al. 2008). Because graphene is an acceptor in energy transfer exchanges (Kasry, Ardakani et al. 2012), we reasoned that the degree of interaction between GNFs and lipid molecules would correlate to shorter fluorescence lifetimes of BODIPY (the donor fluorophore). FRET-FLIM is less affected by fluorophore concentration than intensity-based approaches.

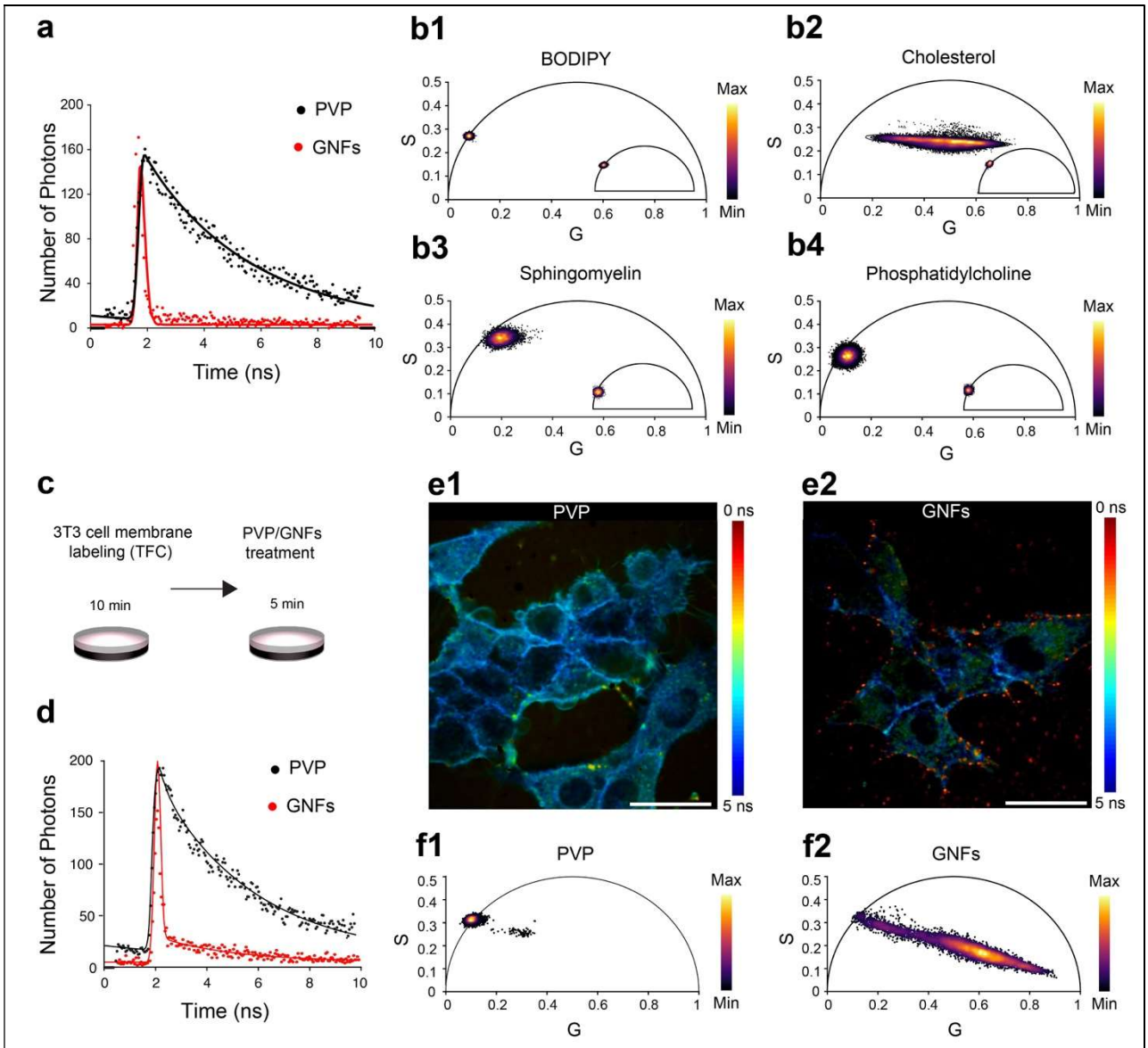

Figure 3.2 **GNFs preferentially shorten the fluorescence lifetime of a cholesterol analog.** (**a**) Representative fluorescence lifetime decays (circles) and corresponding fits (lines). The data are best fit by 1 or 2-component exponential decays (for the decay constants in ns, $\tau_{TFC\&PVP} = 3.36$, $\tau_{BODIPY\&GNFs} = 4.47$, and $\tau_{TFC\&GNFs(1)} = 0.15$ and $\tau_{TFC\&GNFs(2)} = 3.19$; N = 3). (**b1-b4**) Representative phasor plots of BODIPY-labelled cholesterol and other major membrane lipid classes (see methods). G components were calculated as Mcos(ϕ) and S components were calculated as Msin(ϕ) (see methods). Insets represent the lipid dye in PVP-containing solution. (**c**) 3T3 cell membrane loading of TFC and treatments. (**d**) Representative fluorescence lifetime decays (circles) and corresponding fits (lines). The data are best fit by 1 or 2-component decays (in ns, $\tau_{GNFs(1)} = 0.165$ and $\tau_{GNFs(2)} = 3.41$, $\tau_{PVP} = 3.79$). **(e1&e2)** Representative pseudocolor FLIM images of treated 3T3 cells. Scale bars, 20 μm. **(f1&f2)** Corresponding phasor plots from the same FOV. G components were calculated as Mcos(ϕ) and S components were calculated as Msin(ϕ) (see methods).

1 μM TFC mixed with 260 μg/L GNFs in 0.02 wt% PVP exhibited a shortened fluorescence lifetime relative to TFC mixed with PVP at the same concentrations (**Fig. 3.2a**). For a data representation that was unbiased to fit parameters, we used phasor analysis, which transforms a fluorescence decay at every pixel to a data point in a phasor plot (Digman, Caiolfa et al. 2008). In the absence of FRET, for a fluorophore with a single component fluorescence lifetime decay, data points are concentrated at a spot on the semicircle, representing uniformly single-exponential decays of fluorescence lifetime; when FRET interactions occur, data points are shifted towards the inside of the semicircle. BODIPY phasors were almost identical between the presence of GNFs (**Fig. 3.2b1**) and PVP (**Fig. 3.2b1 inset**), i.e. >99% of points in each clustered on the semicircle, suggesting GNFs do not change the lifetime of BODIPY. In contrast, GNFs dispersed the TFC phasor to inside the semicircle in comparison to PVP (**Fig. 3.2b2** and **inset**), reflecting FRET between GNFs and TFC and thus suggesting an interaction between GNFs and cholesterol. If the mechanism for the reduction in lifetime was nonspecific among membrane lipids, for example a hydrophobic interaction, similar changes in phasor distributions in the presence of GNFs should be expected for other lipids. To test this, we repeated FRET-FLIM measurements of GNFs and PVP (insets) using BODIPY-conjugated sphingomyelin (TFSM) and phosphocholine (TFPC), which are among the most abundant lipids in the plasma membrane. GNFs had little effect on the fluorescence lifetimes of TFPC or TFSM, as most data points remained close to the semicircle (**Fig. 3.2b3-4** and **insets**). To address if GNFs shorten the fluorescence lifetime of TFC in the plasma membrane of live cells, we labeled the membranes of 3T3 cells, a fibroblast cell line, with TFC and performed FRET-FLIM (**Fig. 3.2c**). GNFs shortened TFC fluorescence lifetime relative to PVP controls (**Fig. 3.2d&e**), and dispersed phasor data towards a shorter lifetime

location (**Fig. 3.2f**). Interestingly, spatially resolved lifetime maps suggest that FRET of TFC in the presence of GNFs occurs in patches across the cell surface (**Fig.3. 2e**).

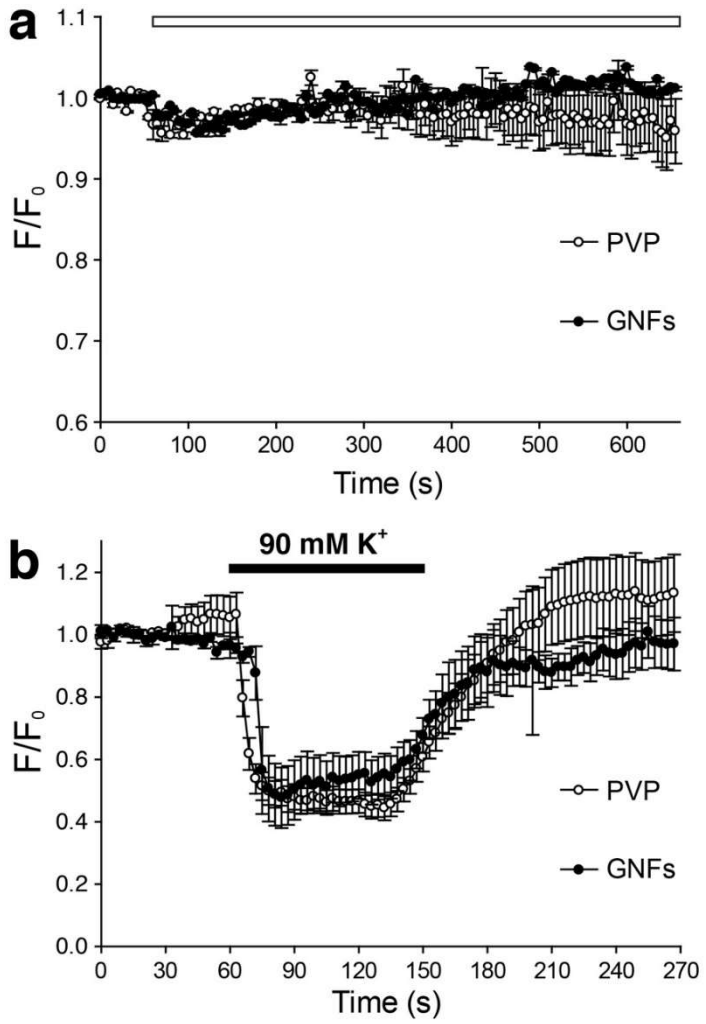

Figure 3.3 **Acute application of GNFs does not affect DiO fluorescence or its voltage sensing capabilities. (a)** Effect of PVP or 260 $ngml^{-1}$GNFs (white bar, starting at 60s and lasting 600s) on DiO fluorescence (both N = 5 coverslips). **(b)** DiO fluorescence (when paired with DPA) in response to 90 mM K^+ after a 5 min treatment with PVP or GNFs (both N = 5 coverslips).

Furthermore, GNFs do not quench membrane-embedded DiO (a common lipophilic fluorescent dye), even after a longer incubation (**Fig. 3.3**).

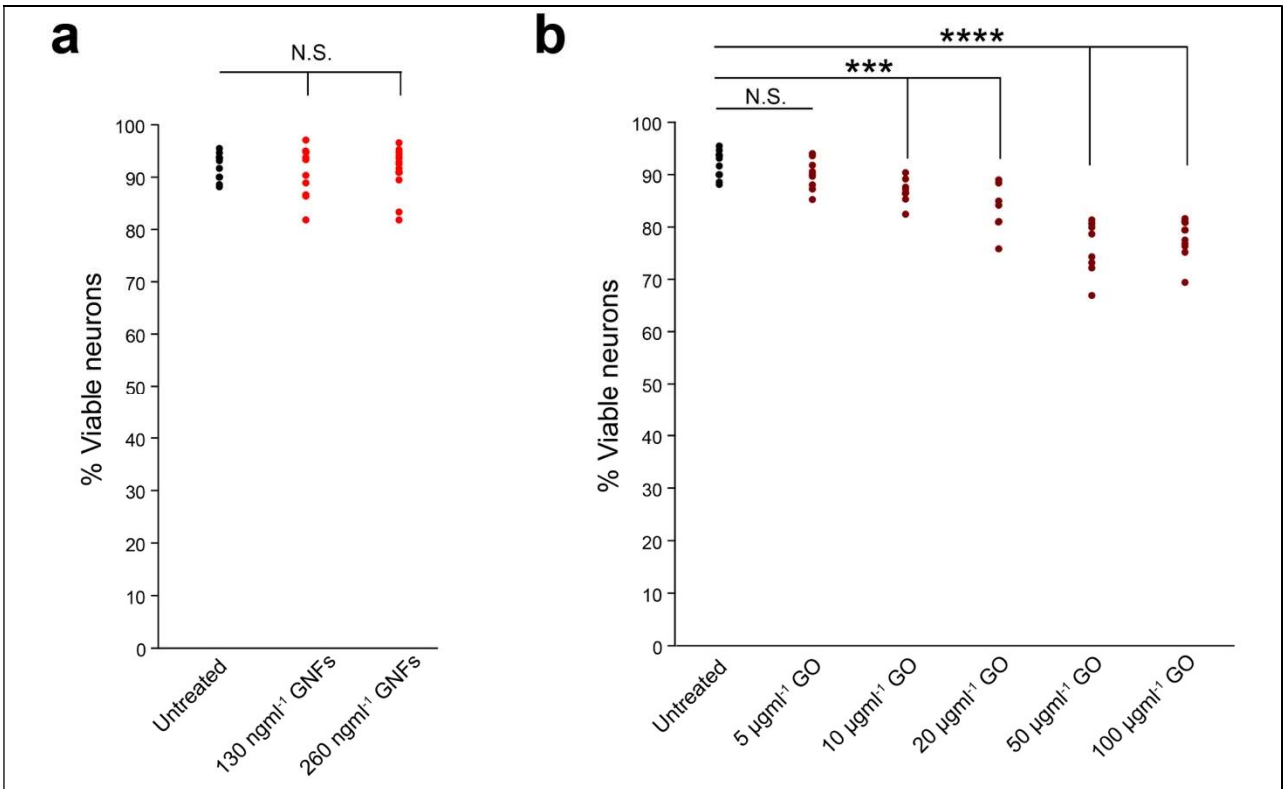

Figure 3.4 **Effect of 1-hour GNFs or graphene oxide flake treatment on cell viability.** Neurons were treated with (**a**) GNFs or (**b**) graphene oxide nanoflakes for 1-hour and viability was assessed using Trypan Blue staining (for paired comparisons to untreated: 130 nmgl^{-1} GNFs = 0.8267, 260 ngml^{-1} GNFs = 0.4423, 5 µgml^{-1} GO = 0.1750, 10 µgml^{-1} GO = .0015, 20 µgml^{-1} GO = 0.001, 50 µgml^{-1} GO = 1.7e-4, 100 µgml^{-1} GO = 1.9e-4. n > 6, N > 3, Wilcoxin rank-sum test). *** $p <$ 0.001, **** $p < 0.0001$.

We also did not observe significant cell death after treatment with GNFs or for low concentrations of graphene oxide nanoflakes (**Fig. 3.4**).

Taken together, our results support a relatively selective interaction between GNFs and cholesterol in solution and in the plasma membrane of live cells.

GNFs increase membrane lipid packing

The selective affinity to cholesterol prompted us to ask if and how GNFs treatment would change cellular cholesterol. Filipin staining, a histochemical marker for cholesterol, revealed that cell membrane cholesterol was increased by GNFs (**Fig. 3.5**).

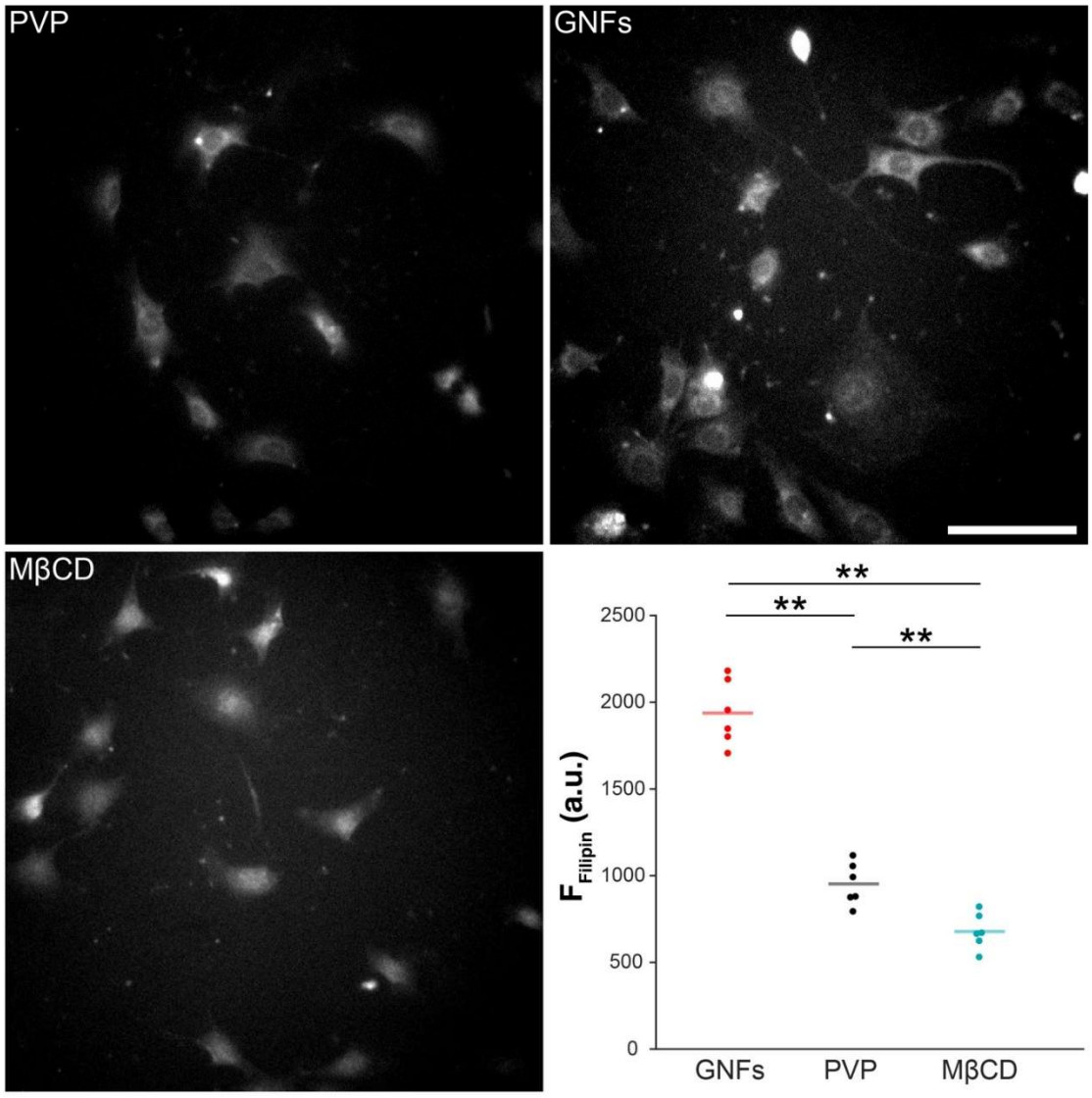

Figure 3.5 **Filipin staining demonstrates a GNFs-induced cell surface cholesterol increase.** 3T3 cells were treated for 1 hour with either PVP, 260 ngml^{-1} GNFs or MβCD. Scale bar, 100 μm; N = 6. Data points are individual coverslips; solid bars are mean values. For paired comparisons, GNFs vs. PVP, p = 0.0022, GNFs vs. MβCD, p = 0.0019, PVP vs. MβCD, p = 0.0048, Wilcoxin rank-sum tests. ** $p < 0.01$.

Because Filipin staining is only a semi-quantitative measure of cholesterol, we also performed Gas chromatography coupled with a flame ionization detector mass spectroscopy (GC-FID) to quantitatively assess whole cell cholesterol levels, and found no significant increases in total cellular cholesterol, even after 24-hour GNFs treatment (**Fig. 3.6**).

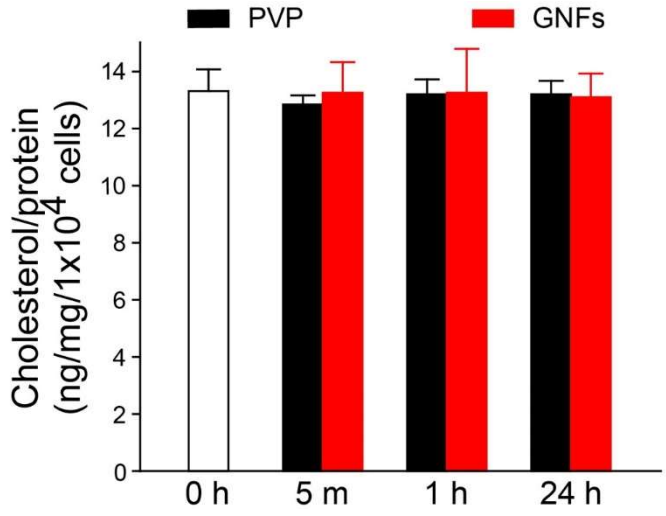

Figure 3.6 **GNFs treatment does not change total cellular cholesterol.** Total cellular cholesterol quantifications by gas chromatography coupled with a flame ionization detector after specified periods of incubation with PVP or 260 $ngml^{-1}$ GNFs (all n = 3, N = 3; all $p > 0.05$ for either paired comparisons or comparison to sham treatment, Wilcoxin rank-sum tests). Error bars are S.E.M..

Together, these results suggest that GNFs induce redistribution of cholesterol towards the plasma membrane rather than upregulating cell-wide cholesterol metabolism.

Because cholesterol governs lipid packing and membrane fluidity (Yeagle 1985, Baumgart, Hammond et al. 2007), we asked if GNFs alter plasma membrane biophysics. We began with cell-derived giant plasma-membrane vesicles (GPMVs), whose molecular composition and biophysical properties resemble those of the plasma membrane (Sezgin, Kaiser et al. 2012). GPMVs exhibit a temperature-dependent separation into micron-sized lipid ordered (L_o) and disordered (L_d) phases (Levental, Byfield et al. 2009) (**Fig. 3.7a**). The temperature at which 50% of GPMVs contain co-existing L_o and L_d domains is defined as the average miscibility temperature, T_{misc}.

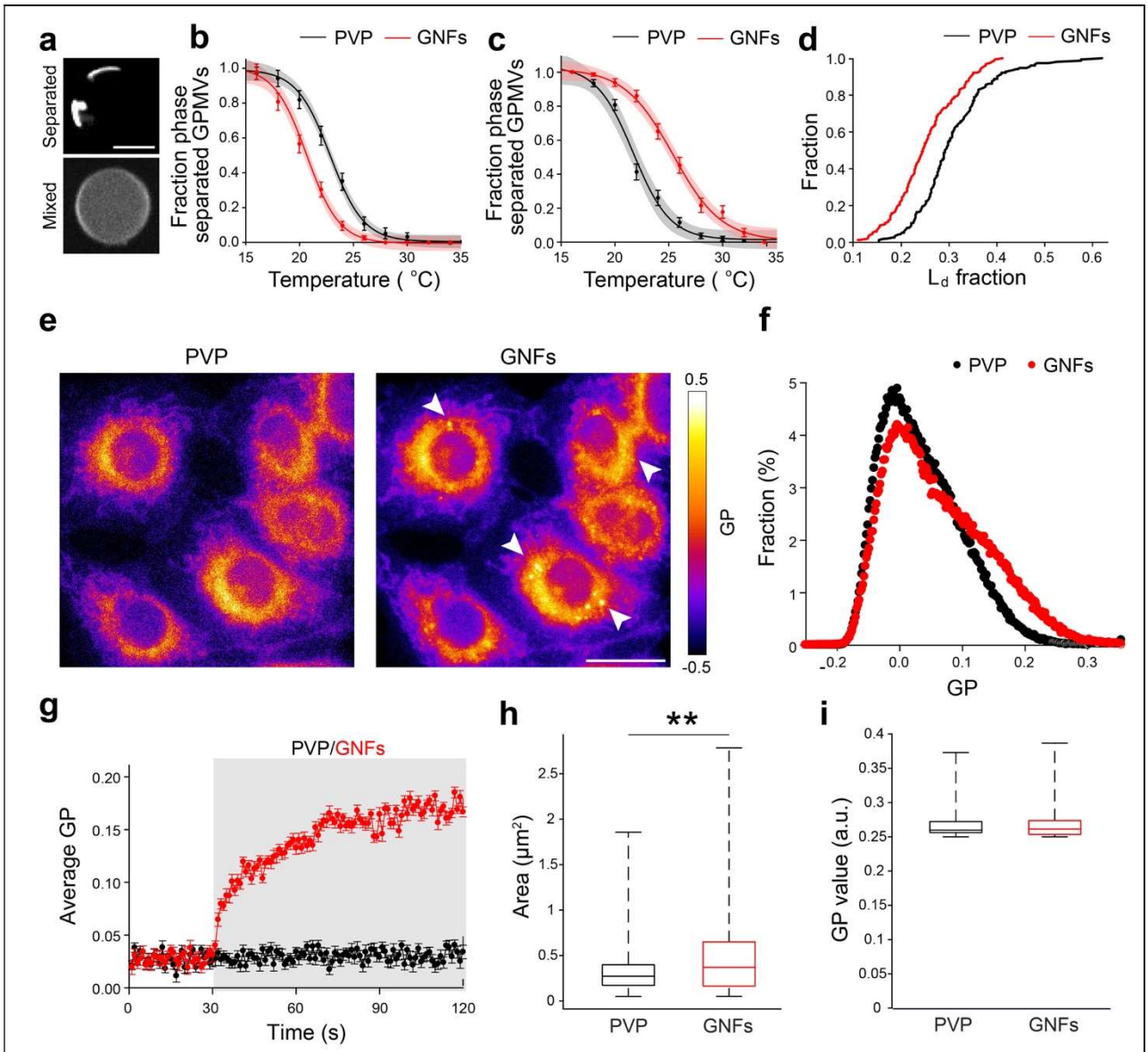

Figure 3.7 **Graphene nanoflakes increase membrane lipid packing.** (**a**) Temperature-dependent lipid phase separation of GPMVs. Scale bar, 5 μm. (**b**) T_{misc} of GPMVs isolated from 3T3 cells after 1-hour pretreatment. Phase separated fraction was calculated from the numbers of phase-separated and non-separated GPMVs. Area of light shading shows the 95% CI on the sigmoidal fit function. For each temperature point, n > 70 GPMVs imaged. **(c)** T_{misc} of GPMVs isolated from 3T3 cells that were then treated for 1-hour. For each temperature point, n > 70 GPMVs imaged; N = 3. (**d**) Cumulative distribution of L_d fractions of GPMVs in (**c**) at 15 ºC. (**e**) GP imaging of 3T3 cells after a 5 minute treatment. White arrowheads indicate puncta with high GP values. Scale bar, 10 μm. (**f**) Pixel GP value distributions after 5-minute treatment (n = 6 FOVs; $p < 0.05$, K-S test). (**g**) Time-resolved average GP values in 3T3 cells in response to treatment. Both n = 6 FOVs. (**h&i**) Box plots. Solid center lines represent the median value, boxed areas extend from the 25th to 75th percentiles, dashed whiskers represent full data range. (**h**) Area values ($p = 0.006$, Wilcoxin Rank-Sum test. (**i**) GP values ($p = 0.08$, Wilcoxin Rank-Sum test). * $p < 0.05$, ** $p < 0.01$.

Pretreatment of 3T3-cells with GNFs or PVP for 1 hour and then subsequent formation of GPMVs results in an average T_{misc} decrease from 27.8 °C in PVP-treated controls to 25.2 °C with GNFs (**Fig. 3.7b** and **Fig. 3.8**), a change correlated to an increase in membrane cholesterol (Levental, Byfield et al. 2009).

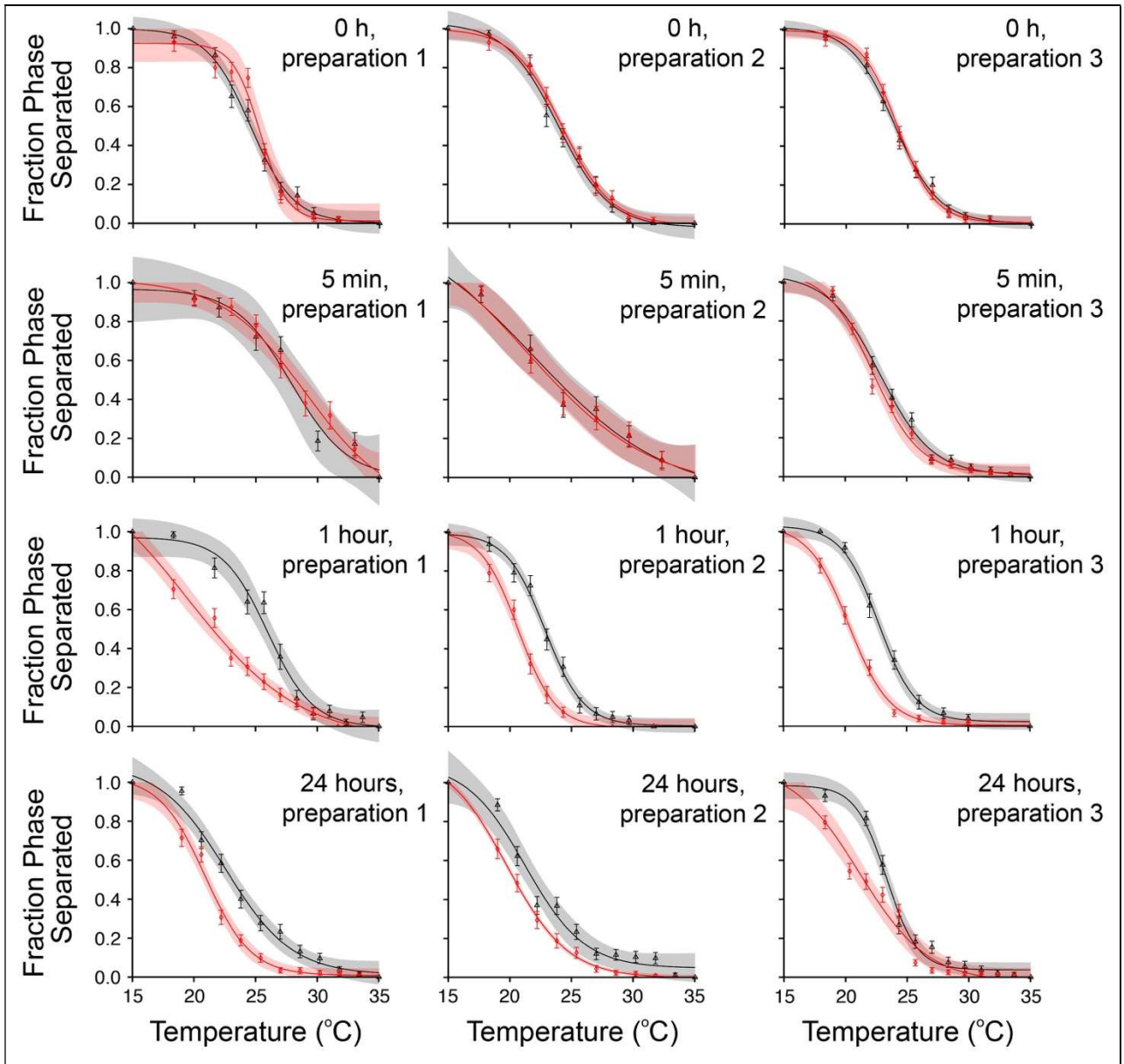

Figure 3.8 **Application of GNFs prior to GPMV isolation reduces miscibility temperature .** Phase separation of 3T3 cells pre-incubated with media containing either PVP (black) or 260 $ngml^{-1}$ GNFs (red). Phase separated fractions were calculated from the total numbers of phase-separated and non-separated GPMVs at each temperature point. Areas of light shading show the 95%

confidence interval on the sigmoidal fit function, defined as: $f(x) = A + B * \left(1 - \frac{1}{1+e^{-\frac{x-C}{D}}}\right)$. Each plot represents an independent preparation. Error bars are S.E.M..

Given that GPMVs, once vesiculated, are cut off from intracellular cholesterol supplies, we next isolated GPMVs and then treated with GNFs or PVP to determine if GNFs would stabilize cholesterol-rich L_o domains (Baumgart, Hammond et al. 2007, Gray, Karslake et al. 2013). We indeed found that in GPMVs isolated prior to treatment, GNFs application increased T_{misc} (**Fig. 3.7c** and **3.9**) and L_o fraction (**Fig. 3.7d**). Taken together, these results suggest that GNFs alter membrane lipid packing.

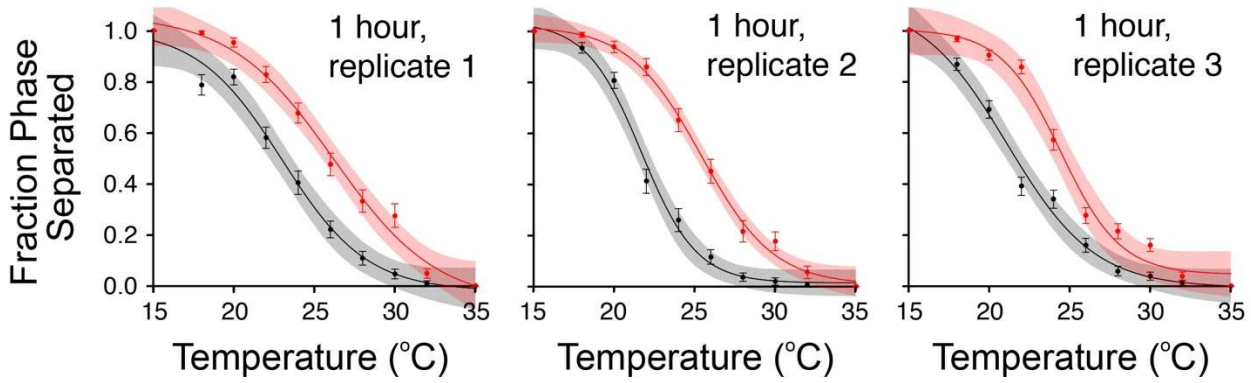

Figure 3.9 **1-hour application of GNFs after GPMV isolation increases miscibility temperature.** Phase separation of isolated GPMVs treated with either PVP (black) or 260 $ngml^{-1}$ GNFs (red) for 1 h. Phase separated fractions were calculated from the total numbers of phase-separated and non-separated GPMVs at each temperature point. Areas of light shading show the 95% confidence interval on the sigmoidal fit function, defined as: $f(x) = A + B * \left(1 - \frac{1}{1+e^{-\frac{x-C}{D}}}\right)$.

Next, we examined the biophysical impact of GNFs on the plasma membranes of live cells. For this, we performed generalized polarization (GP) imaging, a ratiometric approach based on

fluorescent reporters like Laurdan which are sensitive to membrane lipid polarity and packing (Barrantes, Antollini et al. 1999). We loaded 3T3 cells with C-Laurdan, a derivative of Laurdan with higher photostability and better correlation to membrane polarity (Kim, Choo et al. 2007). During continuous GP imaging, we sequentially applied 0.02 wt% PVP followed by 260 μg/L GNFs, and observed that GNFs increased GP value (**Fig. 3.7e**) in a time-dependent manner (**Fig. 3.7g**). Within 90s of application, GNFs skewed the distribution of pixel GP values to the right (**Fig. 3.7f**), consistent with the idea that GNFs acutely increased lipid membrane packing in live cells. Intriguingly, bright GP puncta started to emerge or enlarge (**Fig. 3.7e,** white arrowheads). Since GP is a membrane-specific reporter, this suggests the emergence of membrane 'hotspots' due to GNFs. Analysis of puncta with a minimum intensity threshold (mean pixel GP value > 0.25) revealed that GNFs significantly increased average area (**Fig. 3.7h**) (from 0.31 ± 0.02 μm^2 to 0.46 ± 0.03 μm^2 before and after GNFs application, respectively; $p = 0.006$, Wilcoxin Rank-Sum test) without a corresponding increase in average mean pixel GP value (**Fig. 3.7i**) (0.26 ± 0.02 vs. 0.27 ± 0.03 before and after GNFs application, respectively; $p = 0.08$, Wilcoxin Rank-Sum test). Taken together, FLIM, GPMV, and GP imaging results collectively demonstrate that GNFs favorably interact with cell membrane cholesterol and increase membrane lipid packing on a timescale of seconds to minutes.

GNFs induce highly-packed membrane subareas in the plasma membrane

GP puncta that appeared after GNFs application (**Fig. 3.7e**) led us to ask if GNFs could induce highly-packed subareas in the plasma membrane. This is best investigated in live cells, as fixation methods may artificially change membrane packing. Visualization of GNFs via optical

methods is challenging, as they are both sub-diffraction limit and optically transparent. Given the relative specificity of the TFC-GNFs interaction (**Fig. 3.2**), we reasoned that TFC could be used to fluorescently label GNFs. To prepare TFC-coated GNFs complexes, we mixed PVP-suspended GNFs (2.6 mg/L) with TFC (100 μM) and sonicated for 12 hours, similar to the preparation of DNA-coated GNFs (Liu, Li et al. 2010, Lv, Guo et al. 2010). Subsequently, we concentrated the product via size-dependent filtration and resuspended it in solution (see methods).

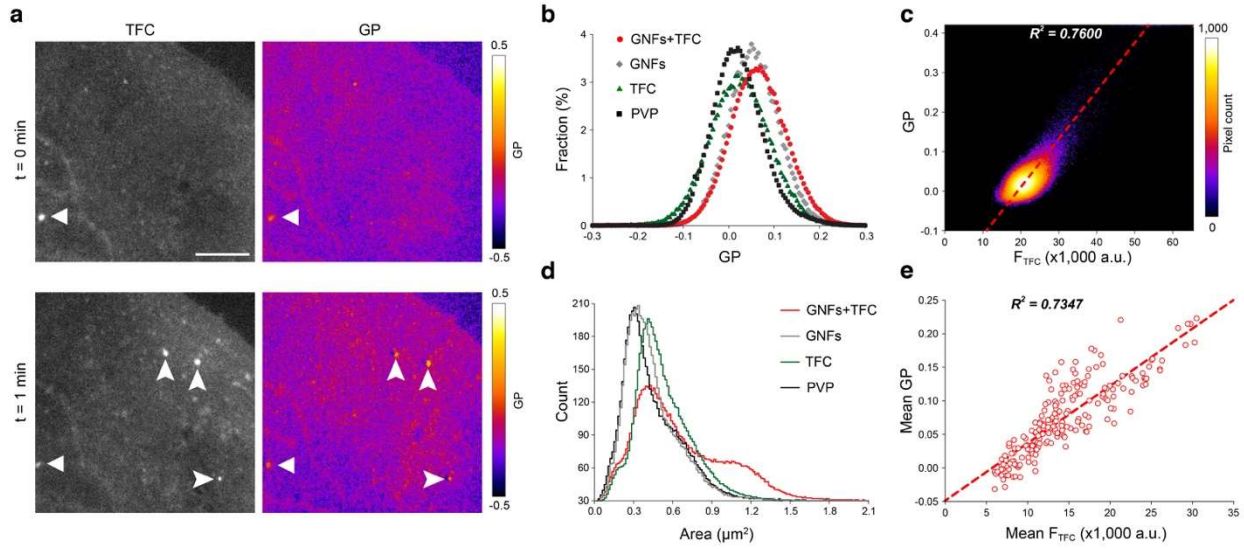

Figure 3.10 **GNFs induce acute and local membrane packing increases.** (**a**) Sample images of the same FOV 1 minute before and 1 minute after the application of TFC-coated GNFs. White triangles indicate pre-existing puncta; white arrowheads indicate puncta appearing after TFC-coated GNFs application. Scale bar, 10 μm. (**b**) Pixel GP value distributions after a 1 minute treatment (N = 6 FOVs; all $p < 0.05$ for pairwise comparisons to PVP, K-S test on the distribution of raw values). (**c**) 2D histogram of TFC fluorescence vs. GP value from thresholded ROIs (GP > -0.1 and F_{TFC} > 10,000 a.u.). Dashed line is a linear regression fitting. Slope $(1.11 \pm 0.24) \times 10^{-5}$. Pearson's R= 0.7600, N = 6 FOVs. (**d**) Size distributions of TFC puncta (GNFs vs. PVP, p = 0.0078, K-S test; TFC vs. PVP, p = 0.0003, K-S test; TFC-labeled GNFs, p = 0.000087, K-S test). All N = 6 FOVs. (**e**) Average TFC fluorescence (background subtracted) vs. GP values from the same ROIs in (**d**). Linear regression fitting (dashed line). Slope $(8.91 \pm 2.73) \times 10^{-6}$. Pearson's R= 0.7347, p = 0.0002, n = 202 ROIs, N = 6 FOVs.

We preloaded cultured neurons with a low-concentration of TFC (10 nM) and C-Laurdan (1 μM) to visualize the plasma membrane and membrane fluidity, respectively. In both TFC and GP images, we observed a low number of spatially co-localized puncta (**Fig. 3.10a**) with an average size of 0.36 ± 0.04 μm^2. This is unlikely an artifact of spectral bleed-through based on blank controls for single dye loading (**Fig. 3.11**).

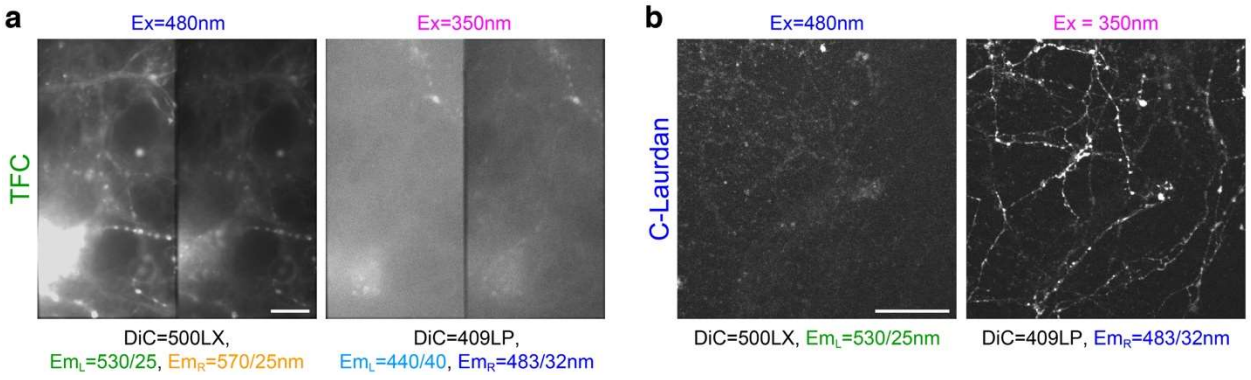

Figure 3.11 **Spectral separation of TFC and C-Laurdan. (a)** TFC-loaded neurons imaged using an OptoSplitII (simultaneous dual-channel) with a filter combination optimized for TFC (left) or C-Laurdan (right). Signals in the right image are likely autofluorescence. TFC also emits weak orange fluorescence, making it detectable using a 570/25nm emission filter. Scale bar, 10 μm. **(b)** C-Laurdan-loaded neurons imaged with a filter combination optimized for TFC (left) or C-Laurdan green fluorescence emission (right). Scale bar, 20 μm.

Importantly, we observed the appearance of additional GP and TFC puncta after the application of TFC-coated GNFs (**Fig. 3.10a**), suggesting that GNFs were integrated into the membrane architecture. Application of GNFs alone or TFC alone also increased GP value – although to a lesser extent than TFC-coated GNFs (**Fig. 3.10b**). Differences in the average GP value between TFC-coated GNFs and GNFs are likely due to an additive effect of GNFs being complexed with TFC or the more hydrophilic nature of TFC-coated GNFs compared to GNFs. Pixel-based analysis (Costes, Daelemans et al. 2004) confirmed a correlation between TFC fluorescence intensity and GP value (**Fig. 3.10c**, R = 0.7600). Furthermore, comparison of the size of TFC puncta in all four conditions demonstrates the bimodal nature of the size distribution for

TFC-coated GNFs, with one subpopulation significantly larger than PVP controls (0.29 ± 0.18 for PVP and 0.42 ± 0.26 μm^2 for TFC-coated GNFs) and another even larger subpopulation (1.12 ± 0.35 μm^2) unique to TFC-coated GNFs (**Fig. 3.10d**). Puncta in the larger subpopulation mostly emerged after the application of TFC-coated GNFs, and TFC fluorescence intensities were correlated to GP value (**Fig. 3.10e**), suggesting a relationship between GNFs' cell membrane deposition and an increase of membrane lipid packing. Average puncta sizes also increased after TFC (0.46 ± 0.28 μm^2) or GNFs (0.31 ± 0.20 μm^2) treatment (**Fig. 3.10d**) (Hölttä-Vuori, Uronen et al. 2008). Additionally, co-localized TFC and GP puncta appeared in neurites within 20 minutes after application of TFC-coated GNFs, whereas longer TFC treatment failed to further increase puncta size (**Fig. 3.12a** *vs.* **3.12b**).

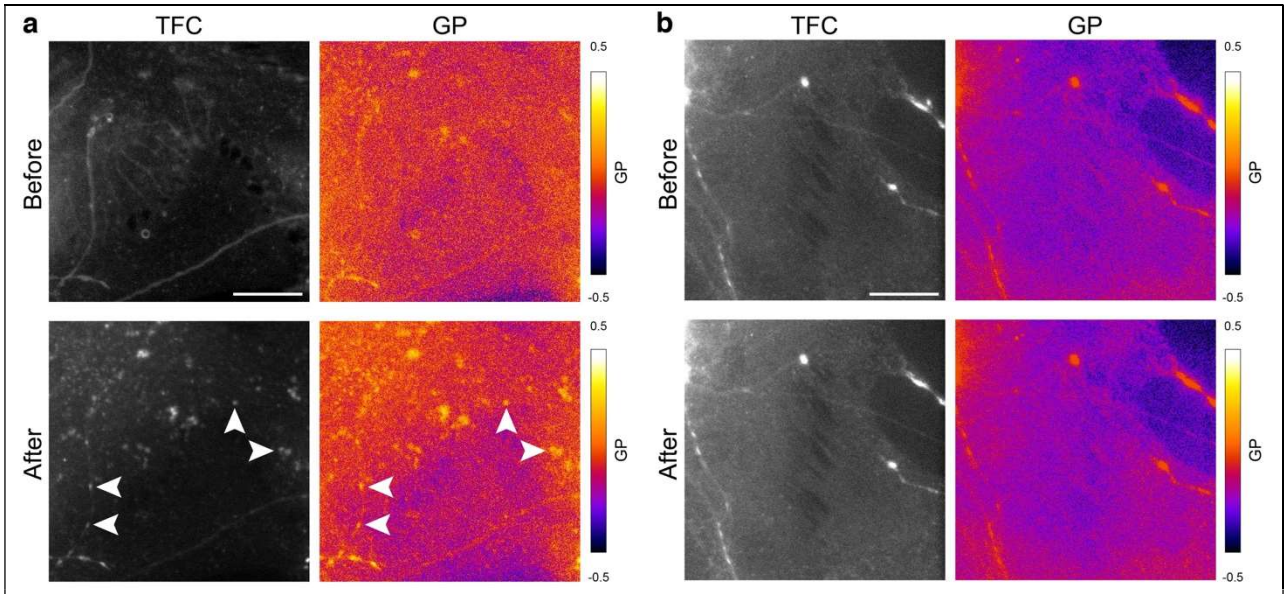

Figure 3.12 **Effect of GNFs on neurite membranes after 20 minutes of incubation. (a)** For GNFs-TFC complexes. Scale bar, 10 μm. **(b)** For TFC alone. Scale bar, 10 μm.

Our data indicate that TFC-coating allows visualization of the cell surface deposition of GNFs and suggest that GNFs focally promote lipid packing in the plasma membrane of live cells.

GNFs acutely potentiate neurotransmitter release

Cholesterol is not only an indispensable structural component of the plasma membrane, but also modulates a number of transmembrane signaling pathways. The ability of GNFs to modify membrane packing, likely via cholesterol, led us to explore GNFs' potential in modulating transmembrane signaling. Generally, intercellular communication involves the release of signaling molecules and subsequent binding or uptake by specific receptors, both of which are affected by membrane cholesterol and lipid packing. Neurotransmitter release from synaptic vesicles (SVs) at axon terminals is a representative example. It has been documented that cholesterol is essential for the origination and maintenance of vesicle pools (Mauch, Nägler et al. 2001, Dason, Smith et al. 2014), the distribution and function of release machinery (Lang 2007, Enrich, Rentero et al. 2015, Yang, Kreutzberger et al. 2016), and membrane fusion/fission during exo-/endocytosis (Chang, Kim et al. 2009, Kreutzberger, Kiessling et al. 2015). Therefore, we asked if and how GNFs could be used to modulate neurotransmitter release.

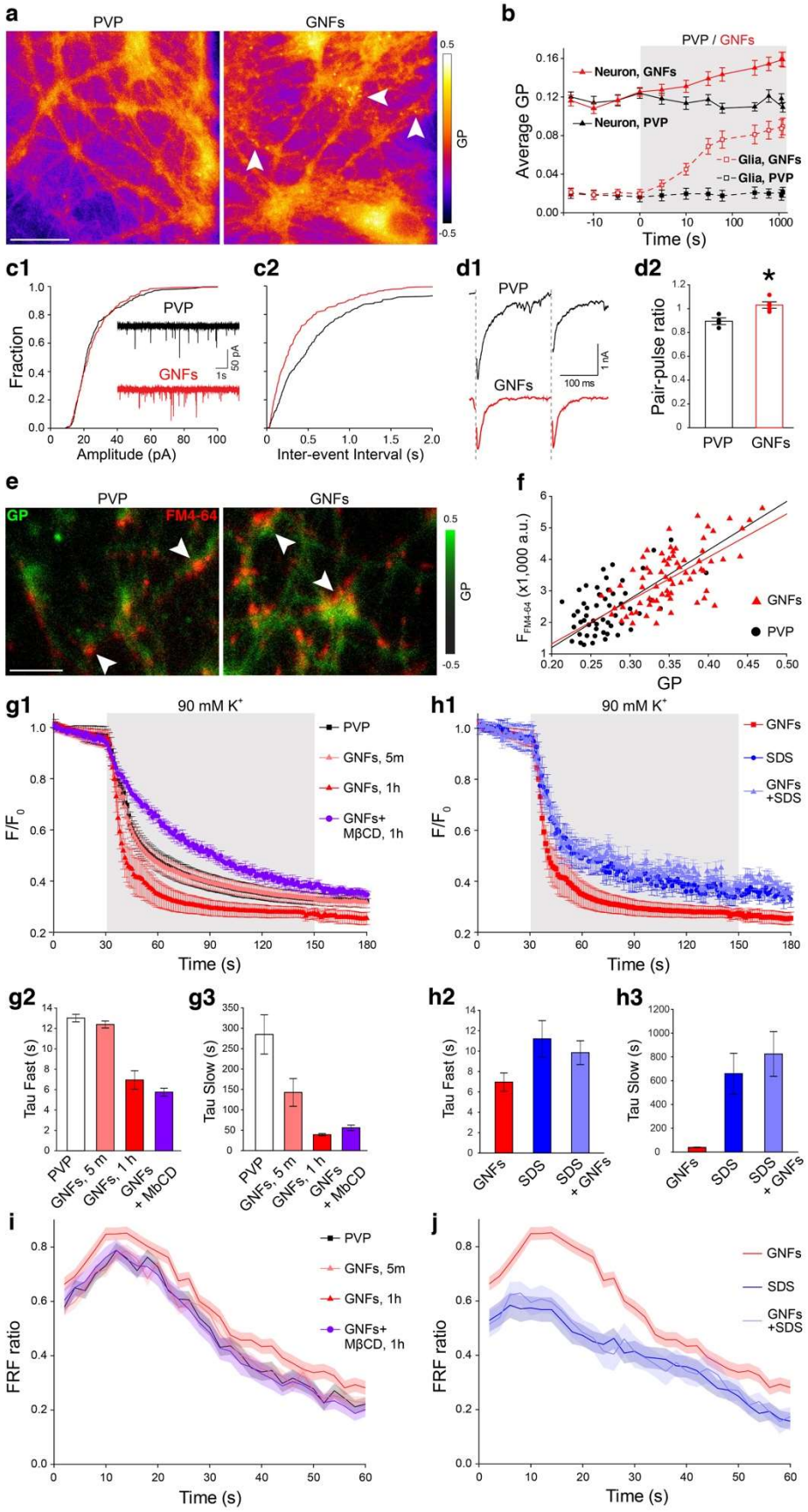
a
PVP
GNFs
GP
b
PVP / GNFs
Neuron, GNFs
Neuron, PVP
Glia, GNFs
Glia, PVP
Average GP
Time (s)
c1
PVP
GNFs
Fraction
Amplitude (pA)
c2
Inter-event Interval (s)
d1
PVP
GNFs
d2
Pair-pulse ratio
e
GP
FM4-64
f
GNFs
PVP
GP
g1
90 mM K+
PVP
GNFs, 5m
GNFs, 1h
GNFs+ MβCD, 1h
F/F0
Time (s)
h1
GNFs
SDS
GNFs +SDS
g2
Tau Fast (s)
g3
Tau Slow (s)
h2
h3
i
FRF ratio
j

Figure 3.13 **GNFs acutely potentiate lipid packing and modulate neurotransmission.** (**a**) Representative GP images of neurons after 1-hour treatment. White arrowheads indicate areas with high GP values. Scale bar, 20 μm. (**b**) Average GP values after PVP (black bars) or GNFs (red bars) application ($n_{neuron, PVP} = 46$, $n_{neuron, GNFs} = 53$; $n_{glia, PVP} = 111$, $n_{glia, GNFs} = 95$). Data plotted as mean ± s.e.m.. (**c1**) Cumulative distribution of amplitudes. Inset are representative sample traces. $p = 0.0934$, *K-S* test. (**c2**) Cumulative distribution of inter-event intervals. $p = 0.0001$, *K-S* test. (**d1**) Representative PPR traces and (**d2**) Average PPR ($N_{PVP} = 4$, $N_{GNFs} = 5$, $p = 0.0159$, Wilcoxin rank-sum test). Data plotted as mean ± s.e.m.. (**e**) Representative GP (green) images of neurons after 1-hour treatment superimposed with FM4-64 (red) images from the same FOV. Arrowheads indicate overlapping puncta of GP and FM4-64. Scale bar, 10 μm. (**f**) FM4-64 intensity vs. GP value. Linear regression fits: for PVP, $F_{FM4-64} = 11{,}024.45 \times GP + 1{,}202.42$, $R = 0.5620$; For GNFs, $F_{FM4-64} = 10{,}538.30 \times GP + 1{,}307.99$, $R = 0.7344$. (**g1**) FM4-64 destaining during 90 mM K^+. (all n = 6 FOVs; all at 180-s time point, for average values: PVP *vs.* GNFs(5m), $p = 0.5142$; PVP *vs.* GNFs(1h), $p = 0.021$; for PVP *vs.* GNFs+MβCD, $p = 0.0062$; unpaired two-tailed *t*-tests). Decay curves were fit with 2-component exponential decays, representing fast (**g2**) and slow (**g3**) decay curve contributions. Data plotted as mean ± s.e.m.. (**h1**) FM 4-64 destaining after 1-hour treatment with SDS. (all n = 50, N = 6; at the 180-s time point: GNFs vs. SDS, $p = 0.33$; GNFs vs. SDS-GNFs, $p = 0.019$, unpaired two-tailed *t*-tests). Decay curves were fit with 2-component exponentials, representing fast (**h2**) and slow (**h3**) decay curve contributions. (**i**) Qdot-based measurement of fusion modes during 1-minute 10-Hz electric field stimulation, reported as the ratio of FRF vs. all fusion events (all n = 20, N = 6). Data are plotted as mean (solid line) ± s.e.m. (shaded regions). (**j**) Qdot-based measurement of fusion modes during 1-minute 10-Hz electric field stimulation, reported as the ratio of FRF vs. all fusion events (all n = 20, N = 6). Data plotted as mean (solid line) ± s.e.m. (shaded regions). * $p < 0.05$.

Because we previously demonstrated that GNFs treatment acutely increases membrane packing in 3T3 cells, we first asked if GNFs would also increase membrane packing in neurons. In comparison to PVP, 1-hour GNFs treatment increased GP value (**Fig. 3.13a**), and interestingly, time-lapse GP imaging showed that the relative increase in neurons was slower and smaller than in neighboring astrocytes (**Fig. 3.13b**). To measure the functional impact, we performed whole-cell patch clamp recordings and measured miniature evoked postsynaptic currents (mEPSCs). 1-hour GNFs treatment had no effect on mEPSC amplitude, whereas inter-event interval was significantly reduced after GNFs treatment (**Fig. 3.13c**). This suggests a possibly presynaptic mechanism, in line with a previous report (Kitko, Hong et al. 2018). To corroborate synaptic mechanisms, we also measured the paired-pulse ratio of evoked postsynaptic currents. This ratio was higher in GNFs-treated neurons than in PVP controls, suggesting synaptic alterations in

response to GNFs treatment (**Fig. 3.13d**). To confirm that GNFs did not change membrane conductance (i.e. by perforating the plasma membrane (Tu, Lv et al. 2013) or altering extracellular K^+ concentration (Pampaloni, Lottner et al. 2018)), we measured current-voltage relationships of neurons following 1-hour treatment.

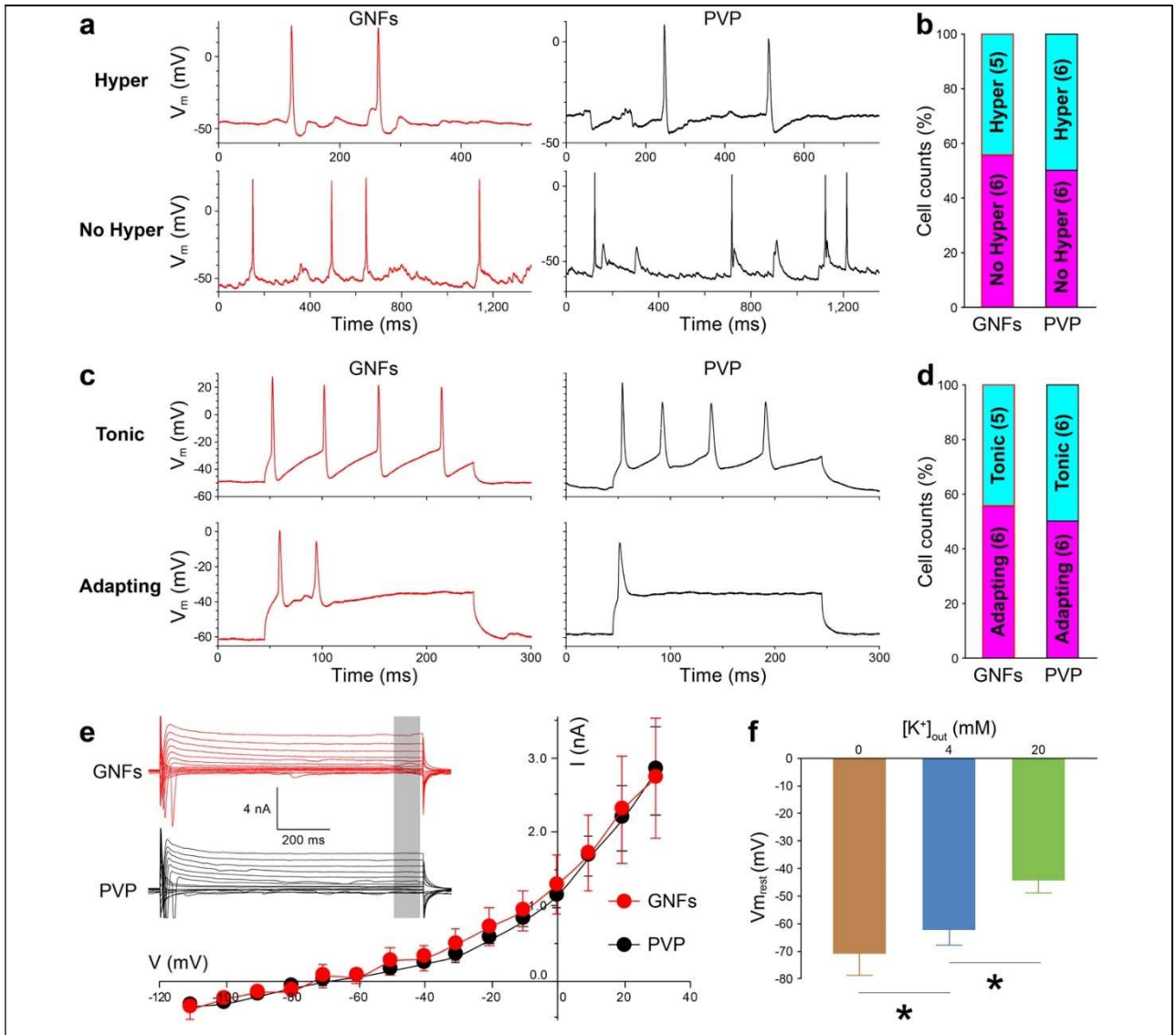

Figure 3.14 **1-hour GNFs treatment does not change neuronal activity via extracellular K^+.** (**a**) Representative traces of spontaneous firing with or without hyperpolarization in GNFs or PVP-treated neurons. (**b**) Proportions of neurons with or without hyperpolarization. (**c**) Representative traces of evoked firing with tonic or adapting patterns in GNFs or PVP-treated neurons. (**d**) Proportions of neurons with tonic or adapting patterns. (**e**) I/V curves for 1-hour PVP or GNFs treatment. Inset are representative records for both groups and the gray box indicates the (100 ms)

interval for average measurement at steady-state. (**f**) Resting membrane potentials in response to 0, 4, and 20 mM extracellular K^+ in neurons after 1-hour GNFs treatment. n = 5, 6, and 5 neurons for 0, 4, and 20 mM K^+, respectively; between 0 and 4 mM K^+, $p = 0.049$, unpaired two-tailed t-test; between 4 and 20 mM K^+, $p = 0.024$, unpaired two-tailed t-test.

There was no difference between treatments (**Fig. 3.14a&b**), suggesting that GNFs do not compromise membrane integrity – in good agreement with viability data. Furthermore, resting membrane potential, firing pattern, and hyperpolarization after action potential were also unchanged (**Fig. 3.14c-f**), indicating unaltered extracellular K^+ concentration.

To verify that electrophysiological changes were presynaptic, we used FM dyes, whose loading and unloading are used to estimate the number of releasable vesicles and their release probability ($P_{r,v}$), respectively (Betz and Bewick, 1992). We chose FM4-64 to minimize spectral overlap with both C-Laurdan and TFC. 1-hour GNFs treatment increased FM4-64 uptake (**Fig. 3.13e**), suggesting an enlarged pool of releasable SVs. This SV pool enlargement may explain PPR increase described previously (Hanse and Gustafsson, 2001). FM4-64 loading is correlated to GP value at synaptic boutons (**Fig. 3.13f**), suggesting a relationship between membrane packing and releasable SVs at synaptic boutons. During subsequent stimulation to induce vesicle turnover, the rate of FM4-64 destaining and the total amount of destaining were both greater following 1-hour, but not 5 minute, GNFs treatment (**Fig. 3.13g**), indicating a higher release probability ($P_{r,v}$) and/or a larger fraction of releasable synaptic vesicles. Membrane cholesterol reduction by the co-application of 0.5 mM Methyl-β-cyclodextrin (MβCD) significantly decreased FM4-64 destaining amount (**Fig. 3.13g**). Because PVP-coating generally results in limited surface coverage, potentially leaving portions of the GNFs surface unexposed, we tested if GNFs surface exposure was required to increase $P_{r,v}$. In the same manner that carbon nanotubes have previously been prepared (O'Connell, Bachilo et al. 2002), exfoliation of GNFs in 1% w/v SDS results in complete

surface coverage (SDS-GNFs hereafter) without causing GNFs aggregation (Hsieh, Korkut et al. 2013, Hsieh, Punckt et al. 2013). 1-hour treatment with SDS-GNFs failed to alter destaining rate or amount in comparison to SDS or GNFs controls (**Fig. 3.13h**), demonstrating the importance of the graphene surface in inducing changes in neurotransmitter release.

To further illustrate kinetic changes in SV turnover, we performed quantum dot (Qdot) enabled single vesicle imaging (Zhang, Li et al. 2009). The hydrodynamic diameter of the Qdots (~15 nm) is smaller than the luminal diameter of SVs (~25 nm) but much larger than the estimated fusion pore size (~1-3 nm). This leads to the loading of only one Qdot per SV (Zhang, Cao et al. 2007) (**Fig. 3.15a**), and allows for an accurate estimate of the total releasable pool (TRP) of vesicles at every synaptic bouton.

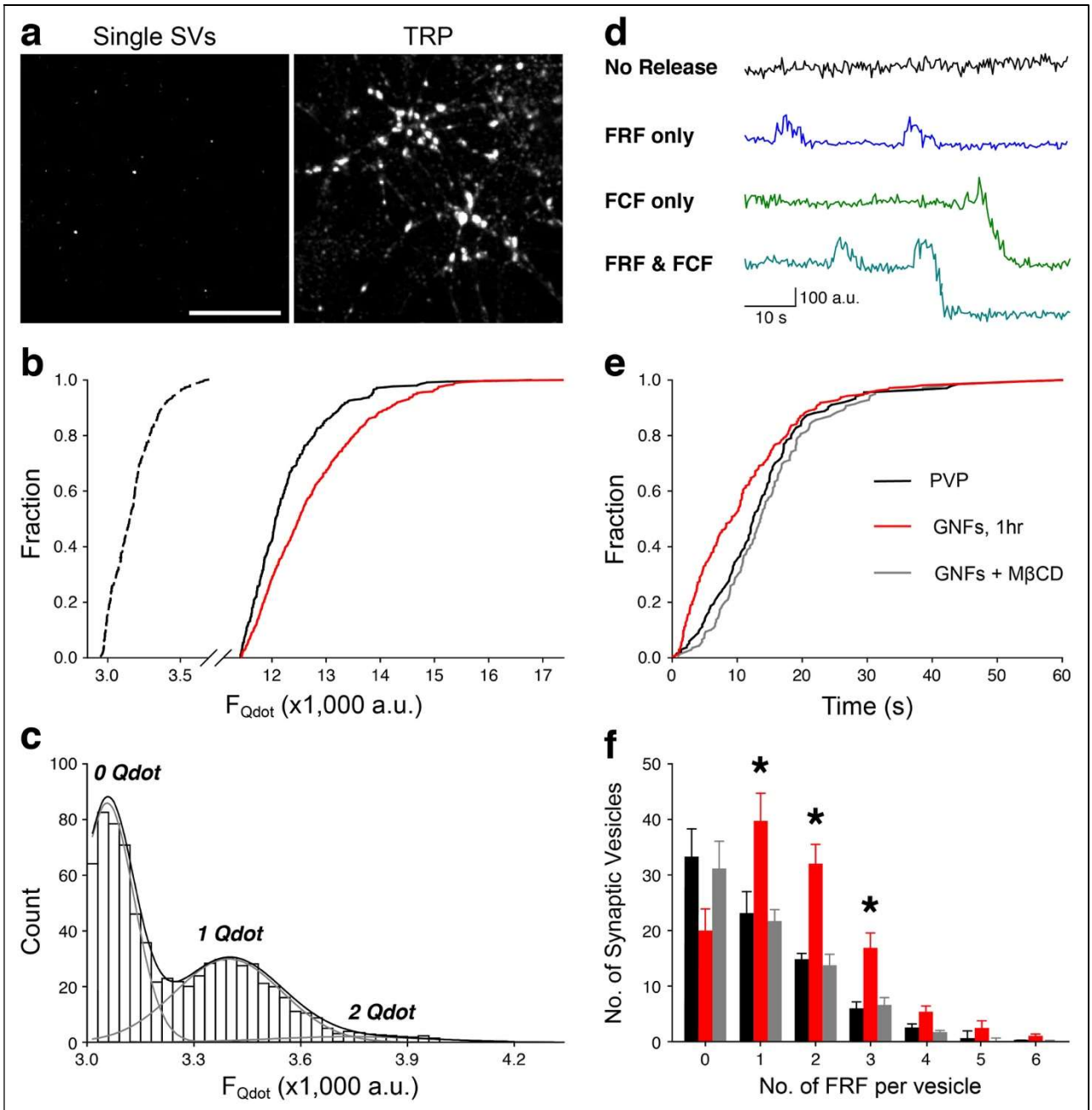

Figure 3.15 **Single Qdot imaging reports single vesicle fusion kinetics.** (**a**) Sample images of single synaptic vesicle loading for releasable pool (0.8 nM Qdot) or TRP loading (100 nM Qdot). (**b**) Synaptic Qdot photoluminescence intensities from single vesicle and TRP loading were measured with the same settings and plotted on the same scale. The background intensity was 2,784 ± 96 a.u. and the detection threshold was set at 2,900 a.u.. Under single vesicle loading, the mean Qdot photoluminescence intensity was 402 ± 43 a.u.. Under total recycling pool loading, the mean Qdot photoluminescence intensities were 8,913 ± 144 a.u. for neurons treated with PVP and 9,980 ± 185 a.u. for neurons treated with graphene, which is significantly higher ($p < 0.05$). Based on these intensity values, we estimated that the average numbers of total recycling vesicles are 23.4 for neurons on glass and 26.2 for those on graphene. (**c**) The distribution of mean Qdot

photoluminescence in individual synaptic boutons defined by retrospective FM4-64 staining. Quantal analysis (black and gray lines) indicates that the mean photoluminescence intensity of loaded single Qdots was 388 ± 71 a.u. after background subtraction. (**d**) Sample photoluminescence traces of single Qdots for four different types of synaptic vesicle release behaviors. (**e**) Synaptic vesicle release probability (measured as the first fusion event of Qdot-loaded synaptic vesicles) in neurons treated with PVP, GNFs or GNFs+MβCD (GNFs 1 hr,* $p < 0.05$). (**f**) Distribution of individual synaptic vesicles conducting different rounds of FRF. *$p < 0.05$. Error bars represent the S.E.M.

We calculated the total number of Qdots taken up after maximal loading — i.e. strong stimulation (2 minutes, 90 mM K^+) with a high concentration of Qdots (100 nM) (Zhang, Li et al. 2009). In agreement with FM4-64 destaining, 1-hour treatment, on average, resulted in a 12% increase of the releasable SV pool size (measured as mean Qdot photoluminescence at synaptic boutons; F_{PVP} = 8,913 ± 144 a.u. and F_{GNFs} = 9,980 ± 185 a.u.; $p < 0.0001$, *Kolmogorov-Smirnov* test) (**Fig. 3.15b**). Using single-Qdot imaging, we analyzed the kinetics of SV turnover. We applied the same stimulation but used a much lower concentration of Qdots (0.8 nM) to randomly label SVs across the TRP (Zhang, Li et al. 2009). Quantal analysis of Qdot photoluminescence in FM4-64 defined individual synaptic boutons (Zhang, Li et al. 2009) confirmed single SV loading (**Fig. 3.15c**). Deconvolution of Qdot photoluminescence changes resulting from SV exo-/endocytosis during a 10-Hz 60-s stimulation (see methods) allowed us to distinguish between two different modes of SV turnover, the classical full-collapse fusion (FCF), or fast and reversible fusion (FRF): a small increase immediately followed by the complete loss of unitary Qdot photoluminescence or a small increase alone, respectively (Zhang, Li et al. 2009) (**Fig. 3.15d**). 1-hour GNFs treatment increased SV release probability, measured as the latency of first fusion events of Qdot-labeled SVs (**Fig. 3.15e**) and the number of FRF events by individual SVs (**Fig. 3.15f**), cooperatively leading to a higher FRF ratio (**Fig. 3.13i**). To address the role of membrane cholesterol and lipid packing in the presence of GNFs, we co-applied MβCD, which offset

increases by GNFs. As expected, there was no increase in FRF ratio (**Fig. 3.13i**). To confirm the importance of the GNFs surface interaction with the plasma membrane, we again used SDS-GNFs. 1-hour SDS-GNFs application failed to modulate FRF ratio in the same manner as PVP-suspended GNFs (**Fig. 3.13j**). Taken together, these results suggest that, within 1-hour, GNFs enhance membrane lipid packing, enlarge the releasable SV pool, and increase SV release probability. Collectively, these changes result in an overall presynaptic potentiation of synaptic transmission.

GNFs Acutely and Allosterically Modulate Transmembrane Receptors

Much of signal input into and across the plasma membrane is mediated through transmembrane proteins such as receptors. Increasing evidence demonstrates that, within the plasma membrane, such proteins are sensitive to the local microenvironment (Groves and Kuriyan 2010, Chabanon, Stachowiak et al. 2017); thus lipid packing directly or indirectly regulates membrane protein-mediated signaling pathways (Lingwood and Simons 2010, Oates and Watts 2011, Yeagle 2014). For this reason, we set out to explore the utility of GNFs in manipulating receptor-mediated transmembrane signaling. We examined ubiquitously expressed and therapeutically important P2Y receptors (P2YRs), a class of GPCR preferentially localized within cholesterol-enriched nanodomains (N and Volonte 2013). We reasoned that modulation of membrane packing in the presence of GNFs would alter the activity of P2YRs on the plasma membrane. Extracellular ATP application activates P2YRs and subsequently triggers Ca^{2+}-release from internal stores, which can be measured using fluorescent Ca^{2+}-indicators (Zhang, Pangrsic et al. 2004). Pharmacological isolation of components of this process confirmed that P2YRs predominantly mediate ATP-induced Ca^{2+}-responses in 3T3 cells (**Fig. 3.16**).

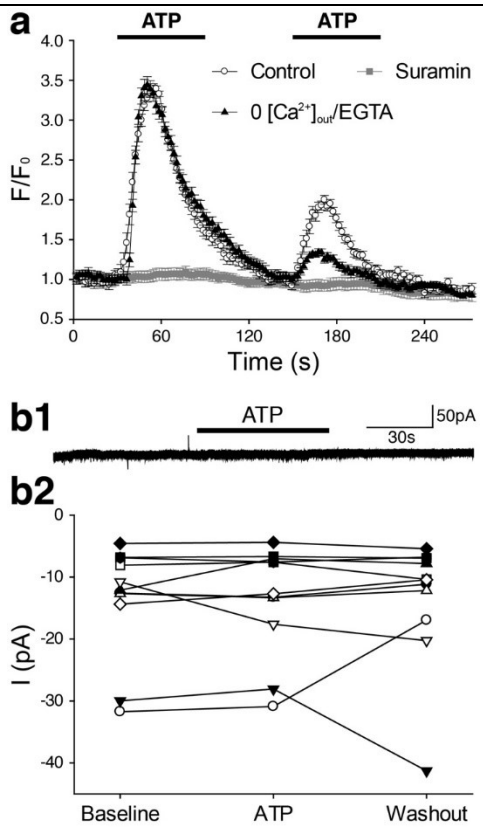

Figure 3.16 **P2YRs mediate ATP-induced Ca^{2+}-release from internal Ca^{2+}-stores. (a)** Average Ca^{2+}-response to 100 μM ATP application in Tyrode's solution or Tyrode's containing Suramin (100 μM) or 0 Ca^{2+}/EGTA (2 mM). **(b1)** Representative record of a 3T3 cell before, during, and after 100 μM ATP application. **(b2)** Average currents within the 10 s period before, during, and after 100 μM ATP application (n = 11 cells; $p > 0.05$ for baseline vs. ATP, ATP vs. washout, and baseline vs. ATP, paired t-tests).

Membrane conductance also remained unchanged after either 5 minute or 1-hour GNFs treatment, again demonstrating that GNFs do not compromise membrane integrity (data not shown).

To measure P2YR responses, we applied two consecutive ATP stimuli at a 1-minute interval, which is insufficient to replenish internal Ca^{2+} stores. Because the amount of internal Ca^{2+} available for release is thus limited, enhanced P2YR activity should increase the first response and decrease the second. We quantified the ratio of 2^{nd} vs. 1^{st} peak Ca^{2+}-responses as this would be

less affected by the number of cell surface P2YRs and the capacity of internal Ca^{2+} stores, both of which can be variable among cells. Interestingly, 5-minute GNFs treatment potentiated the first response and reduced the second (**Fig. 3.17a1**), resulting in a smaller 2nd vs. 1st response ratio (**Fig. 3.17a2**).

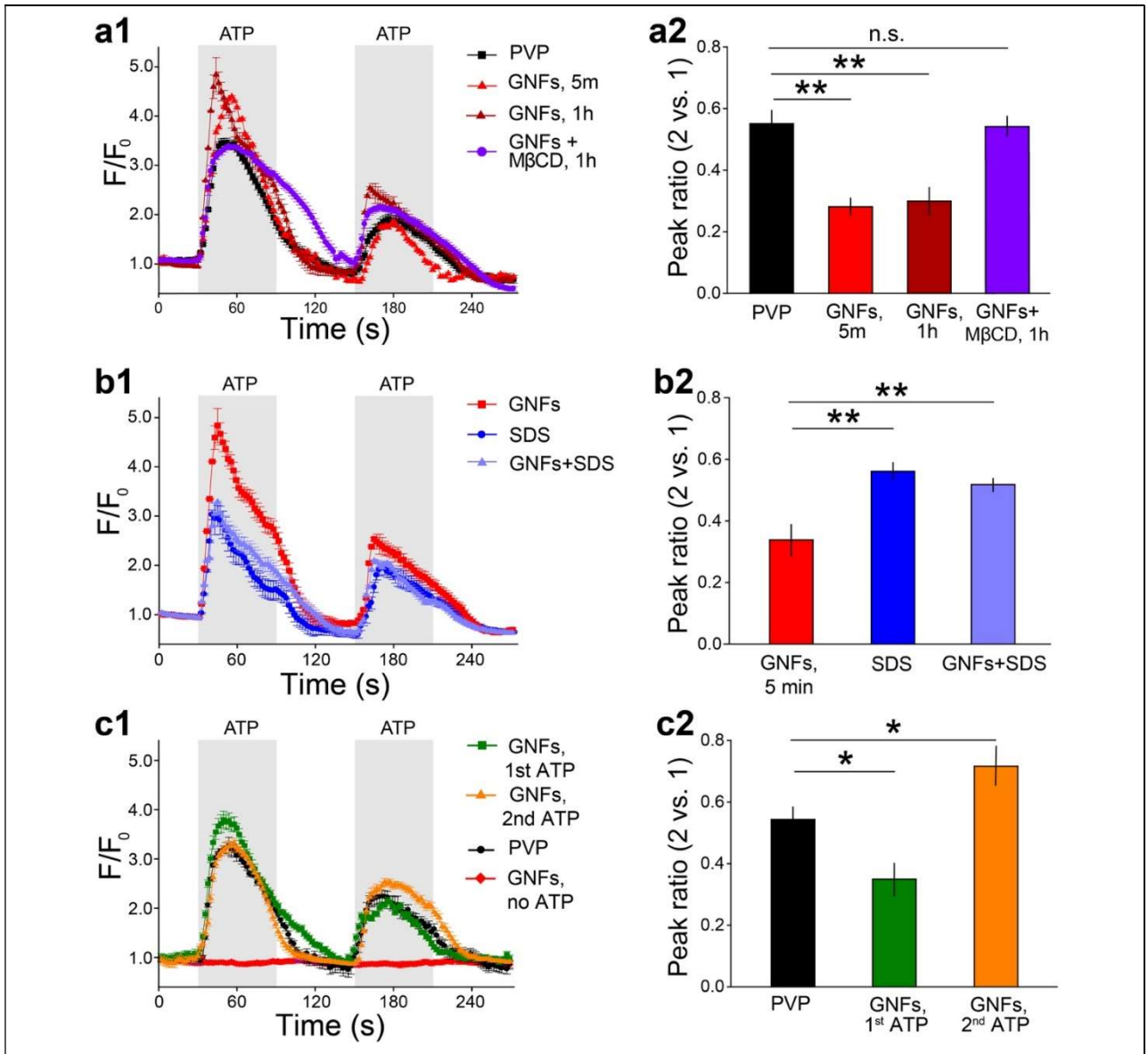

Figure 3.17 **GNFs acutely potentiate P2YR signaling in 3T3 cells.** (**a1**) Ca^{2+}-responses to 100 μM ATP. (**a2**) Ratios of 2nd to 1st peak amplitude (n_{PVP} = 131, $n_{GNFs,\ 5m}$ = 119, $n_{GNFs,\ 1h}$ = 146, $n_{GNFs+M\beta CD}$ = 120 cells; **, p = 0.0057 for PVP vs. 5-min GNFs and p = 0.0072 for PVP vs. 1-hr GNFs, n.s., p = 0.293 for PVP vs. GNFs+MβCD, unpaired two-tailed t-tests). (**b1**) Effect of SDS coating on ATP-induced Ca^{2+}-responses. (**b2**) Ratios of 2nd to 1st peak amplitude (n_{GNFs} = 146,

n_{SDS} = 133, $n_{GNFs+SDS}$ = 119 cells; **, $p < 0.01$, unpaired two-tailed t-tests). (**c1**) Effect of co-application of GNFs with either the 1st or 2nd ATP application. (**c2**) Ratios of 2nd to 1st peak amplitude (n_{PVP} = 130, $n_{GNFs,1st\ ATP}$ = 153, $n_{GNFs,2nd\ ATP}$ = 127 cells; *, $p = 0.029$, unpaired two-tailed t-test). ** $p < 0.01$, * $p < 0.05$.

1-hour treatment also led to a smaller ratio, although the 2nd response was slightly larger than that of controls (**Fig. 3.17a1**). The increase in 2nd ATP response following 1-hour GNFs treatment could result from changes in intracellular membrane cholesterol distribution, which reportedly promote the refilling of internal Ca^{2+}-stores (Dionisio, Galan et al. 2011, Gwozdz, Dutko-Gwozdz et al. 2012). To confirm the involvement of membrane cholesterol, we again treated 3T3 cells with 0.5 mM MβCD co-applied with GNFs. 1-hour MβCD treatment reversed GNFs-induced enhancement of Ca^{2+}-responses (**Fig. 3.17a1&2**). And to confirm the importance of the GNFs' surface for the observed P2YR enhancement, we again employed SDS-GNFs. 1-hour SDS-GNFs treatment did not potentiate ATP-induced Ca^{2+}-responses in the same manner as PVP-GNFs (**Fig. 3.17b**). Importantly, GNFs alone did not elicit a Ca^{2+}-response (**Fig. 3.17c**), suggesting that any potentiation in Ca^{2+} responses by GNFs is allosteric.

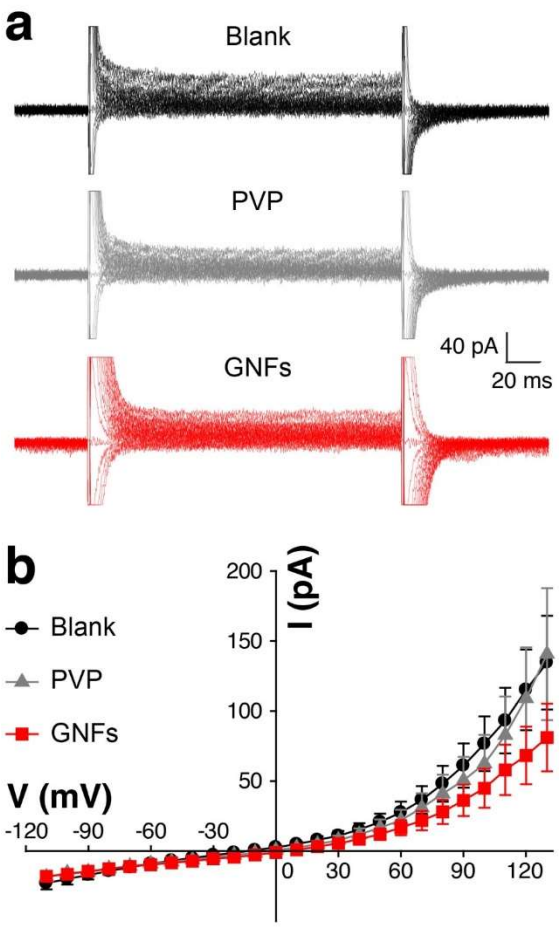

Figure 3.18 **Acute application of GNFs does not alter current-voltage characteristics in 3T3 cells. (a)** Trace overlays for a 3T3 cell in Tyrode or Tyrode containing either PVP or 260 $ngml^{-1}$ GNFs. **(b)** Average I-V curves of the same 3T3 cells (n = 5 cells; for blank control vs. PVP, PVP vs. GNFs, blank control vs. GNFs, $p > 0.05$, unpaired two-tailed t-tests). Values presented are mean ± S.E.M.

Furthermore, GNFs did not alter cell membrane permeability (**Fig. 3.18**), arguing against the idea that Ca^{2+}-responses were Ca^{2+} influx through membrane punctures created by GNFs. To further confirm whether GNFs act on P2YRs orthosterically or allosterically, we added ATP and GNFs simultaneously or separately. Only addition of GNFs simultaneously with either the 1st or 2nd ATP increased the corresponding Ca^{2+}-response (**Fig. 3.17c1**). These results suggest that GNFs act allosterically and acutely alter receptor activity.

Discussion

The biological impact and associated cytotoxicity of nanomaterials remains a key issue moving toward clinical translation. Graphene has been hypothesized to be cytotoxic due to its nanometer size and sharp edges (Seabra, Paula et al. 2014), yet a framework explaining its toxicity to some systems and not others has yet to be established. Experimental studies of prokaryotic cells and computational simulations of phospholipid bilayers suggest graphene is destructive, especially to the cell membrane (Li, Yuan et al. 2013, Tu, Lv et al. 2013). However, studies using graphene as a substrate for eukaryotic cell growth have found increases in synaptic strength (Kitko, Hong et al. 2018), neuronal connectivity (Veliev, Briancon-Marjollet et al. 2016), and stem cell proliferation (Nayak, Andersen et al. 2011) and differentiation (Wang, Lee et al. 2012). These seemingly contradictory findings led us to the idea that distinct eukaryotic membrane moieties mediate graphene's cellular effects. Consistent with previous reports, eukaryotic membranes were undamaged by low concentrations of GNFs, supporting that idea. We discovered a preferential interaction between GNFs and cholesterol, which is unique to and abundant in the eukaryotic plasma membrane. This preference over other lipid molecules indicates that the interaction between GNFs and cholesterol is more complex than a hydrophobic interaction alone, involving weak interactions such as stacking or Van der Waals forces. Given the diversity of biomolecules within the plasma membrane, likely more unique interactions remain to be explored. Improvements in computational techniques, for example more biophysically realistic membrane models, will provide a better understanding of the underlying physics governing the interaction between graphene and diverse biomolecules including proteins, lipids, and carbohydrates. And

new technologies that enable quantitative study of membrane properties in live cells may allow more precise evaluation of nanomaterial – membrane interactions.

Here, we present multiple lines of evidence that cholesterol mediates GNFs' biological effects (Filipin staining, GC-FID, miscibility temperatures in GPMVs and GP imaging with C-Laurdan) through increased cell membrane cholesterol and thus increased membrane packing. Using TFC-coated GNFs and co-imaging of TFC and C-Laurdan, we further demonstrate that GNFs heterogeneously increase lipid packing in submicron areas of the plasma membrane, morphologically resembling stable membrane microdomains. GNFs may cause the focal clustering of cholesterol at membrane deposition points, forming or stabilizing microdomains. As current methods to selectively modify cholesterol distribution in subareas of the plasma membrane lack spatial precision, GNFs may be engineered to acutely and focally manipulate membrane packing, opening new doors to understanding the role of cholesterol and membrane packing in cell membrane organization and dynamics.

As the interface between intracellular and extracellular environments, the plasma membrane plays an important and multifunctional role in a variety of cellular processes including signal transduction. Here, we illustrate the functional effects of GNFs on transmembrane signaling pathways using two representative systems: the secretion of neurotransmitters from axon terminals as signal output, and the activation of P2Y receptors by extracellular ATP as signal input. For the former, GNFs potentiate secretion by promoting vesicle origination, recycling, and membrane fusion/fission, processes regulated by membrane cholesterol (Mauch, Nägler et al. 2001, Chang, Kim et al. 2009, Dason, Smith et al. 2014, Kreutzberger, Kiessling et al. 2015). For the latter, GNFs allosterically promote P2YR activity, likely through cholesterol and other membrane lipids' role in receptor localization, trafficking, stability, and dimerization (Cherezov, Rosenbaum et al.

2007, Hanson, Cherezov et al. 2008, N and Volonte 2013). The time course for GNFs' effects varied by more than an order of magnitude between P2Y receptor activation (**Fig. 3.17a1&2**) and SV release (**Fig. 3.13g&i**). This may be due to differences in the role that cholesterol and membrane packing play in each system. Receptor conformations, for example, may be much more sensitive to perturbations in local lipid environment. Given that cholesterol modulates many lipid and protein complexes in the cell membrane and is pathologically linked to many disorders (Maxfield and Tabas 2005), biofunctionalization of graphene may open new venues for the investigation of membrane-related diseases.

References

Barrantes, F. J., S. Antollini and R. Massol (1999). "Fluorescence studies of the nicotinic acetylcholine receptor in its membrane environment." Biosci Rep **19**(5): 335-344.

Bastiaens, P. I. H. and A. Squire (1999). "Fluorescence lifetime imaging microscopy: spatial resolution of biochemical processes in the cell." Trends in Cell Biology **9**(2): 48-52.

Baumgart, T., A. T. Hammond, P. Sengupta, S. T. Hess, D. A. Holowka, B. A. Baird and W. W. Webb (2007). "Large-scale fluid/fluid phase separation of proteins and lipids in giant plasma membrane vesicles." Proc Natl Acad Sci U S A **104**(9): 3165-3170.

Bendali, A., L. H. Hess, M. Seifert, V. Forster, A.-F. Stephan, J. A. Garrido and S. Picaud (2013). "Purified Neurons can Survive on Peptide-Free Graphene Layers." Advanced Healthcare Materials **2**(7): 929-933.

Betz, W. J. and G. S. Bewick (1992). "Optical Analysis of Synaptic Vesicle Recycling at the Frog Neuromuscular Junction." Science **255**(5041): 200.

Bird, D. K., L. Yan, K. M. Vrotsos, K. W. Eliceiri, E. M. Vaughan, P. J. Keely, J. G. White and N. Ramanujam (2005). "Metabolic mapping of MCF10A human breast cells via multiphoton fluorescence lifetime imaging of the coenzyme NADH." Cancer Res **65**(19): 8766-8773.

Chabanon, M., J. C. Stachowiak and P. Rangamani (2017). "Systems biology of cellular membranes: a convergence with biophysics." Wiley Interdiscip Rev Syst Biol Med **9**(5).

Chang, J., S. A. Kim, X. Lu, Z. Su, S. K. Kim and Y. K. Shin (2009). "Fusion step-specific influence of cholesterol on SNARE-mediated membrane fusion." Biophys J **96**(5): 1839-1846.

Cherezov, V., D. M. Rosenbaum, M. A. Hanson, S. G. Rasmussen, F. S. Thian, T. S. Kobilka, H. J. Choi, P. Kuhn, W. I. Weis, B. K. Kobilka and R. C. Stevens (2007). "High-resolution crystal structure of an engineered human beta2-adrenergic G protein-coupled receptor." Science **318**(5854): 1258-1265.

Costes, S. V., D. Daelemans, E. H. Cho, Z. Dobbin, G. Pavlakis and S. Lockett (2004). "Automatic and quantitative measurement of protein-protein colocalization in live cells." Biophys J **86**(6): 3993-4003.

Dason, J. S., A. J. Smith, L. Marin and M. P. Charlton (2014). "Cholesterol and F-actin are required for clustering of recycling synaptic vesicle proteins in the presynaptic plasma membrane." J Physiol **592**(Pt 4): 621-633.

Digman, M. A., V. R. Caiolfa, M. Zamai and E. Gratton (2008). "The phasor approach to fluorescence lifetime imaging analysis." Biophys J **94**(2): L14-16.

Dionisio, N., C. Galan, I. Jardin, G. M. Salido and J. A. Rosado (2011). "Lipid rafts are essential for the regulation of SOCE by plasma membrane resident STIM1 in human platelets." Biochim Biophys Acta **1813**(3): 431-437.

Enrich, C., C. Rentero, A. Hierro and T. Grewal (2015). "Role of cholesterol in SNARE-mediated trafficking on intracellular membranes." J Cell Sci **128**(6): 1071-1081.

Fabbro, A., D. Scaini, V. Leon, E. Vazquez, G. Cellot, G. Privitera, L. Lombardi, F. Torrisi, F. Tomarchio, F. Bonaccorso, S. Bosi, A. C. Ferrari, L. Ballerini and M. Prato (2016). "Graphene-Based Interfaces Do Not Alter Target Nerve Cells." ACS Nano **10**(1): 615-623.

Ferrari, A. C., J. C. Meyer, V. Scardaci, C. Casiraghi, M. Lazzeri, F. Mauri, S. Piscanec, D. Jiang, K. S. Novoselov, S. Roth and A. K. Geim (2006). "Raman spectrum of graphene and graphene layers." Phys Rev Lett **97**(18): 187401.

Geim, A. K. (2009). "Graphene: Status and Prospects." Science **324**(5934): 1530-1534.

Gray, E., J. Karslake, B. B. Machta and S. L. Veatch (2013). "Liquid general anesthetics lower critical temperatures in plasma membrane vesicles." Biophys J **105**(12): 2751-2759.

Groves, J. T. and J. Kuriyan (2010). "Molecular mechanisms in signal transduction at the membrane." Nat Struct Mol Biol **17**(6): 659-665.

Gwozdz, T., J. Dutko-Gwozdz, C. Schafer and V. M. Bolotina (2012). "Overexpression of Orai1 and STIM1 proteins alters regulation of store-operated Ca2+ entry by endogenous mediators." J Biol Chem **287**(27): 22865-22872.

Hanse, E. and B. Gustafsson (2001). "Paired-pulse plasticity at the single release site level: an experimental and computational study." J Neurosci **21**(21): 8362-8369.

Hansen, J. S. and C. Helix-Nielsen (2011). "An epifluorescence microscopy method for generalized polarization imaging." Biochem Biophys Res Commun **415**(4): 686-690.

Hanson, M. A., V. Cherezov, M. T. Griffith, C. B. Roth, V. P. Jaakola, E. Y. Chien, J. Velasquez, P. Kuhn and R. C. Stevens (2008). "A specific cholesterol binding site is established by the 2.8 A structure of the human beta2-adrenergic receptor." Structure **16**(6): 897-905.

Hernandez, Y., V. Nicolosi, M. Lotya, F. M. Blighe, Z. Sun, S. De, I. T. McGovern, B. Holland, M. Byrne, Y. K. Gun'Ko, J. J. Boland, P. Niraj, G. Duesberg, S. Krishnamurthy, R. Goodhue, J. Hutchison, V. Scardaci, A. C. Ferrari and J. N. Coleman (2008). "High-yield production of graphene by liquid-phase exfoliation of graphite." Nat Nanotechnol **3**(9): 563-568.

Hölttä-Vuori, M., R.-L. Uronen, J. Repakova, E. Salonen, I. Vattulainen, P. Panula, Z. Li, R. Bittman and E. Ikonen (2008). "BODIPY-Cholesterol: A New Tool to Visualize Sterol Trafficking in Living Cells and Organisms." Traffic **9**(11): 1839-1849.

Hsieh, A. G., S. Korkut, C. Punckt and I. A. Aksay (2013). "Dispersion stability of functionalized graphene in aqueous sodium dodecyl sulfate solutions." Langmuir **29**(48): 14831-14838.

Hsieh, A. G., C. Punckt, S. Korkut and I. A. Aksay (2013). "Adsorption of sodium dodecyl sulfate on functionalized graphene measured by conductometric titration." J Phys Chem B **117**(26): 7950-7958.

Kasry, A., A. A. Ardakani, G. S. Tulevski, B. Menges, M. Copel and L. Vyklicky (2012). "Highly Efficient Fluorescence Quenching with Graphene." The Journal of Physical Chemistry C **116**(4): 2858-2862.

Kim, H. M., H. J. Choo, S. Y. Jung, Y. G. Ko, W. H. Park, S. J. Jeon, C. H. Kim, T. Joo and B. R. Cho (2007). "A two-photon fluorescent probe for lipid raft imaging: C-laurdan." Chembiochem **8**(5): 553-559.

Kitko, K. E., T. Hong, R. M. Lazarenko, D. Ying, Y. Q. Xu and Q. Zhang (2018). "Membrane cholesterol mediates the cellular effects of monolayer graphene substrates." Nat Commun **9**(1): 796.

Kreutzberger, Alex J. B., V. Kiessling and Lukas K. Tamm (2015). "High Cholesterol Obviates a Prolonged Hemifusion Intermediate in Fast SNARE-Mediated Membrane Fusion." Biophysical Journal **109**(2): 319-329.

Lang, T. (2007). "SNARE proteins and 'membrane rafts'." J Physiol **585**(Pt 3): 693-698.

Levental, I., F. J. Byfield, P. Chowdhury, F. Gai, T. Baumgart and P. A. Janmey (2009). "Cholesterol-dependent phase separation in cell-derived giant plasma-membrane vesicles." Biochem J **424**(2): 163-167.

Li, N., X. Zhang, Q. Song, R. Su, Q. Zhang, T. Kong, L. Liu, G. Jin, M. Tang and G. Cheng (2011). "The promotion of neurite sprouting and outgrowth of mouse hippocampal cells in culture by graphene substrates." Biomaterials **32**(35): 9374-9382.

Li, Y., H. Yuan, A. von dem Bussche, M. Creighton, R. H. Hurt, A. B. Kane and H. Gao (2013). "Graphene microsheets enter cells through spontaneous membrane penetration at edge asperities and corner sites." Proc Natl Acad Sci U S A **110**(30): 12295-12300.

Lingwood, D. and K. Simons (2010). "Lipid rafts as a membrane-organizing principle." Science **327**(5961): 46-50.

Liu, G. and R. W. Tsien (1995). "Synaptic transmission at single visualized hippocampal boutons." Neuropharmacology **34**(11): 1407-1421.

Liu, J., Y. Li, Y. Li, J. Li and Z. Deng (2010). "Noncovalent DNA decorations of graphene oxide and reduced graphene oxide toward water-soluble metal–carbon hybrid nanostructures via self-assembly." Journal of Materials Chemistry **20**(5): 900-906.

Lotya, M., Y. Hernandez, P. J. King, R. J. Smith, V. Nicolosi, L. S. Karlsson, F. M. Blighe, S. De, Z. Wang, I. T. McGovern, G. S. Duesberg and J. N. Coleman (2009). "Liquid phase production of graphene by exfoliation of graphite in surfactant/water solutions." J Am Chem Soc **131**(10): 3611-3620.

Lv, W., M. Guo, M.-H. Liang, F.-M. Jin, L. Cui, L. Zhi and Q.-H. Yang (2010). "Graphene-DNA hybrids: self-assembly and electrochemical detection performance." Journal of Materials Chemistry **20**(32): 6668-6673.

Mauch, D. H., K. Nägler, S. Schumacher, C. Göritz, E.-C. Müller, A. Otto and F. W. Pfrieger (2001). "CNS Synaptogenesis Promoted by Glia-Derived Cholesterol." Science **294**(5545): 1354-1357.

Maxfield, F. R. and I. Tabas (2005). "Role of cholesterol and lipid organization in disease." Nature **438**(7068): 612-621.

N, D. A. and C. Volonte (2013). "Metabotropic purinergic receptors in lipid membrane microdomains." Curr Med Chem **20**(1): 56-63.

Nayak, T. R., H. Andersen, V. S. Makam, C. Khaw, S. Bae, X. Xu, P.-L. R. Ee, J.-H. Ahn, B. H. Hong, G. Pastorin and B. Özyilmaz (2011). "Graphene for Controlled and Accelerated Osteogenic Differentiation of Human Mesenchymal Stem Cells." ACS Nano **5**(6): 4670-4678.

Novoselov, K. S., A. K. Geim, S. V. Morozov, D. Jiang, Y. Zhang, S. V. Dubonos, I. V. Grigorieva and A. A. Firsov (2004). "Electric field effect in atomically thin carbon films." Science **306**(5296): 666-669.

O'Connell, M. J., S. M. Bachilo, C. B. Huffman, V. C. Moore, M. S. Strano, E. H. Haroz, K. L. Rialon, P. J. Boul, W. H. Noon, C. Kittrell, J. Ma, R. H. Hauge, R. B. Weisman and R. E. Smalley (2002). "Band gap fluorescence from individual single-walled carbon nanotubes." Science **297**(5581): 593-596.

Oates, J. and A. Watts (2011). "Uncovering the intimate relationship between lipids, cholesterol and GPCR activation." Curr Opin Struct Biol **21**(6): 802-807.

Pampaloni, N. P., M. Lottner, M. Giugliano, A. Matruglio, F. D'Amico, M. Prato, J. A. Garrido, L. Ballerini and D. Scaini (2018). "Single-layer graphene modulates neuronal communication and augments membrane ion currents." Nat Nanotechnol.

Rauti, R., N. Lozano, V. Leon, D. Scaini, M. Musto, I. Rago, F. P. Ulloa Severino, A. Fabbro, L. Casalis, E. Vazquez, K. Kostarelos, M. Prato and L. Ballerini (2016). "Graphene Oxide

Nanosheets Reshape Synaptic Function in Cultured Brain Networks." ACS Nano **10**(4): 4459-4471.

Seabra, A. B., A. J. Paula, R. de Lima, O. L. Alves and N. Duran (2014). "Nanotoxicity of graphene and graphene oxide." Chem Res Toxicol **27**(2): 159-168.

Sezgin, E., H.-J. Kaiser, T. Baumgart, P. Schwille, K. Simons and I. Levental (2012). "Elucidating membrane structure and protein behavior using giant plasma membrane vesicles." Nat. Protocols **7**(6): 1042-1051.

Stefl, M., N. G. James, J. A. Ross and D. M. Jameson (2011). "Applications of phasors to in vitro time-resolved fluorescence measurements." Anal Biochem **410**(1): 62-69.

Tu, Y., M. Lv, P. Xiu, T. Huynh, M. Zhang, M. Castelli, Z. Liu, Q. Huang, C. Fan, H. Fang and R. Zhou (2013). "Destructive extraction of phospholipids from Escherichia coli membranes by graphene nanosheets." Nat Nanotechnol **8**(8): 594-601.

Veliev, F., A. Briancon-Marjollet, V. Bouchiat and C. Delacour (2016). "Impact of crystalline quality on neuronal affinity of pristine graphene." Biomaterials **86**: 33-41.

Wajid, A. S., S. Das, F. Irin, H. S. T. Ahmed, J. L. Shelburne, D. Parviz, R. J. Fullerton, A. F. Jankowski, R. C. Hedden and M. J. Green (2012). "Polymer-stabilized graphene dispersions at high concentrations in organic solvents for composite production." Carbon **50**(2): 526-534.

Wang, Y., W. C. Lee, K. K. Manga, P. K. Ang, J. Lu, Y. P. Liu, C. T. Lim and K. P. Loh (2012). "Fluorinated Graphene for Promoting Neuro-Induction of Stem Cells." Advanced Materials **24**(31): 4285-4290.

Yang, S. T., A. J. B. Kreutzberger, J. Lee, V. Kiessling and L. K. Tamm (2016). "The role of cholesterol in membrane fusion." Chem Phys Lipids **199**: 136-143.

Yeagle, P. L. (1985). "Cholesterol and the cell membrane." Biochimica et Biophysica Acta (BBA) - Reviews on Biomembranes **822**(3): 267-287.

Yeagle, P. L. (2014). "Non-covalent binding of membrane lipids to membrane proteins." Biochimica et Biophysica Acta (BBA) - Biomembranes **1838**(6): 1548-1559.

Zhang, L., B. Xu and X. Wang (2016). "Cholesterol Extraction from Cell Membrane by Graphene Nanosheets: A Computational Study." The Journal of Physical Chemistry B.

Zhang, Q., Y.-Q. Cao and R. W. Tsien (2007). "Quantum dots provide an optical signal specific to full collapse fusion of synaptic vesicles." Proceedings of the National Academy of Sciences **104**(45): 17843-17848.

Zhang, Q., Y. Li and R. W. Tsien (2009). "The Dynamic Control of Kiss-And-Run and Vesicular Reuse Probed with Single Nanoparticles." Science **323**(5920): 1448-1453.

Zhang, Q., T. Pangrsic, M. Kreft, M. Krzan, N. Z. Li, J. Y. Sul, M. Halassa, E. Van Bockstaele, R. Zorec and P. G. Haydon (2004). "Fusion-related release of glutamate from astrocytes." Journal of Biological Chemistry **279**(13): 12724-12733.

Chapter 4

Monovalent quantum dot-aptamer conjugates for single particle tracking of synaptic vesicles

Background

The term 'quantum dot', coined in the 1980s (Reed, Bate et al. 1986), encompasses an array of core/shell combinations, but to date the majority of biological applications for these small nanocrystals have utilized CdSe core structures. The motivation behind the use of 'dot' is not structure related, but rather the result of quantum confinement effects. Quantum dots (Qdots) are ordered nanocrystals - either zincblende or wurtzite in crystal structure (Subila, Kishore Kumar et al. 2013). A widely exploited feature across both biological and engineering applications of semiconductor nanocrystals is their size-dependent properties. For example, Qdots exhibit a large shift in photoluminescence emission as a function of size (Alivisatos 1996). Unlike conventional fluorophores, where particle tracking has only recently been extended to a length scale of ~ 7 min with the addition of a cocktail of chemicals designed to minimize triplet state transitions through consecutive redox reactions (Tsunoyama, Watanabe et al. 2018), Qdots may potentially be tracked inside of biological tissue for a time period of up to ~ hours (Michalet, Pinaud et al. 2005). The 'blinking' of Qdots is increasingly understood in terms of underlying physics (Efros and Nesbitt 2016), and has been an area of investigation, although controversial at times, for either control of blinking frequency or suppression of blinking (Chen, Vela et al. 2008, Mahler, Spinicelli et al. 2008). However, for single particle tracking applications, blinking is often advantageous, as it allows for the discrimination of single versus multiple labeling of a target. Furthermore, for a single excitation wavelength, the narrow emission spectra of Qdots enables greater multiplexing

capabilities than with either organic dyes or fluorescent proteins, which are generally limited to two color-labeling due to broad emission spectra tails. To date, simultaneous 5-6 color labeling has been demonstrated using Qdots, although sample preparations have been largely limited to immunolabeled fixed cell - and not live-cell - samples (Giepmans, Deerinck et al. 2005, Liu, Lau et al. 2010, Zrazhevskiy and Gao 2013). The recent growth in molecular recorders (Shipman, Nivala et al. 2017, Farzadfard and Lu 2018) and barcode-based connectomics (Peikon, Kebschull et al. 2017, Han, Kebschull et al. 2018, Kalhor, Kalhor et al. 2018) suggests that combinatorial mixtures of Qdots may someday find application in greatly increasing the number of molecular species simultaneously detectable with traditional optical techniques (Han, Gao et al. 2001).

The specific biological applications of Qdots encompass a variety of methods across neuroscience. Many such applications predate, yet are complementary to, an array of more recent neuroscience techniques that allow optical manipulation or readout in genetically defined cell populations, such as optogenetics (Boyden, Zhang et al. 2005) or calcium imaging (Chen, Wardill et al. 2013). The engineering of new shell chemistries aimed at enhancing photoluminescence stability (Dabbousi, Rodriguez-Viejo et al. 1997) has enabled high signal to noise ratio single particle tracking at fast frame rates (Dahan, Lévi et al. 2003, Geng, Qian et al. 2008, Lévi, Schweizer et al. 2008, Mikasova, Groc et al. 2008, Chang, Tomlinson et al. 2012, Park, Li et al. 2012). A different subset of applications has exploited the pH-sensitivity of Qdots to allow different modes of synaptic vesicle fusion to be distinguished (Zhang, Cao et al. 2007, Zhang, Li et al. 2009, Kitko, Hong et al. 2018). Lastly, the energy spectra of Qdots is advantageous for donor-receptor pair interactions, where Qdots act as donors when paired with organic dyes (Medintz, Clapp et al. 2003, Clapp, Medintz et al. 2004, Mandal, Zhou et al. 2018) or fluorescent proteins (Boeneman, Delehanty et al. 2012, Dennis, Rhee et al. 2012) for Förster resonance energy transfer

studies. Recently, there has been increasing interest in incorporating Qdots in applications where labelling targets with small numbers of fluorophores results in insufficient signal brightness or where resistance to photobleaching would be advantageous, for example in-situ hybridization in hydrogel composites (Chen, Wassie et al. 2016, Sylwestrak, Rajasethupathy et al. 2016). Sequencing applications are of interest for connectomics, allowing molecular identification of RNAs of interest in cell populations. Although recent progress in optical measurement of neuronal activity – via calcium or voltage imaging – has greatly increased the number of neurons whose activity can be recorded simultaneously *in vivo*, for non-invasive deep-brain imaging these tools are limited to largely depth-limited superficial brain regions. It has recently been proposed that by embedding Qdots within the lipid bilayer, sufficient fluorescence changes during action potential firing may enable optical voltage sensing at high spatial resolution (Efros, Delehanty et al. 2018), potentially enabling direct deep-brain readout of membrane depolarization events. The proposed mechanism for this is via electric field changes during neuronal depolarization, which would result in a red-shift of Qdot photoluminescence (Miller, Chemla et al. 1984). To date, however, the focus for most applications of Qdots remains largely on single particle tracking. Future applications, for example *in vivo* single particle tracking used in combination with optogenetic perturbation or calcium/voltage imaging, will greatly enhance the understanding of how protein trafficking acts in concert with cellular activity, but will require improvements in the ability to target Qdots to small and confined cell membrane regions.

Materials and methods

Reagents

All reagents were from Sigma-Aldrich unless otherwise noted. Organic phase quantum dots were purchased from Thermo Fisher (Em 605, CdSe/ZnS ITK, Q21701MP and Em 545, CdSe/ZnS ITK, Q21791MP) or Ocean Nanotech (Em 600, CdSe/ZnS, QSP-600-0010). Steptavidin-conjugated quantum dots were purchased from Thermo Fisher (Em 605, Strepatividin Conjugate, Q10101MP). Secondary antibody quantum dots were purchased from Thermo Fisher (Em 605, F(ab')2-Goat anti-Mouse IgG (H+L) Secondary Antibody, Q-11001MP). Gold nanoparticles were purchased from Nanocs (Streptavidin Nanoparticles 5 nm, GNA5). 2,5,8,11,14,17,20-heptaoxadocosane-22-thiol was purchased from Polypure (mPEG thiol, molecular weight (MW) 356.5 g/mol, 95% purity). HS-(CH2)11-(OCH2CH2)6-OCH2CO2H was purchased from ProChimia (HSC11EG6CO2H). Sodium borate buffer was purchased from Alfa Aesar.

Oligonucleotide sequences

All DNA or RNA sequences were purchased from IDT or Midland Scientific and stored at -20 ºC until immediately prior to usage.

Phase transfer of organic Qdots

Quantum dots were phase transferred as previously described (Farlow et al. 2013), with modifications. Organic phase quantum dots first underwent three successive washes in methanol, followed by precipitation by centrifugation, to clean the Qdots surface. 1.5 mL of organic Qdots were diluted 1:1 with an equal volume of chloroform. 2.0 mL of 0.3 M TBAB and 100 uL of mPEG thiol were added to the dilute Qdots from the previous step. This mixture was added to a shaker and allowed to shake at room temperature for up to 24 hours. After shaking, 4.0 mL 0.2 M

NaOH was added dropwise while stirring. The aqueous phase was recovered and additional volumes of NaOH were added in the same manner until Qdots were largely recovered. Recovered Qdots were then concentrated in a centrifugal filter (30 kDa, Amicon) to a volume of 1-1.5 mL and solution exchanged into 1-1.5 mL of 10 mM Tris containing 30 mM NaCl (pH 8.0) buffer with a desalting column (NAP 10, GE Healthcare). Concentration was estimated by absorption measurement at 350 nm.

ptDNA wrapping of Qdots

ptDNA addition was performed as previously described (Farlow et al. 2013). 200 µL of 200 nM ptDNA was added dropwise to 200 nM Qdots while stirring. The ptDNA-Qdot mixture was allowed to stir at 4 ºC overnight before assessment of stoichiometry via gel electrophoresis. Samples of unreacted Qdots and ptDNA-wrapped Qdots were loaded onto gels following 2:1 dilution into a 70% glycerol solution. 0.8% agarose gels were prepared using 200 nM sodium borate buffer both for the gel and for the running solution and run at 8 V/cm for 17 min. Additional ptDNA was titrated in if Qdots remained in well locations that corresponded to the locations of bare Qdots. The mPEG thiol surface ligand should result in a neutrally charged Qdot, thus unreacted Qdots should remain in wells. To limit the effects of DNA degradation, once ptDNA wrapping was performed, Qdots were used immediately for aptamer conjugation or were stored at 4 ºC and used within a few days. 10 µL of 10 mM carboxy PEG6 alkane thiol $(CO_2H)CH_2O(CH_2CH_2O)_6C_{11}H_{23}SH$ in the same Tris buffer used for buffer exchange were added to 100 µL of ptDNA-wrapped Qdots while stirring and stirred for 10 min. Qdots were then run through NAP5 desalt column (GE Healthcare) to remove excess alkane thiol ligands. At this step,

Qdots were used within 24 hours, as the alkane thiol ligand may displace the ptDNA on the Qdots surface.

RNA aptamer hybridization

RNAse inhibitor was used in all solutions after the addition of the RNA aptamer at a dilution of 100 units/mL. 200 µL ptDNA-wrapped Qdots were mixed with 30 µL GFP aptamer in the presence of 10 µL RNAse inhibitor for 15 min in the dark at 4 ºC. The mixture was then heated to 55 ºC for 10 min to break any secondary structures, and then placed on ice to cool.

Transmission electron microscopy

Following RNA hybridization, Qdots were used immediately to complex with Au NPs. Aptamer-Qdots were treated with 2 equivalents of Streptavidin-Au NPs that had previously been incubated for 1 hour at 4 ºC with 1 nM of a biotinylated anti-GFP antibody (Abcam). The Streptavidin-Au NPs complexes were then incubated overnight with 1 nM recombinant GFP (Abcam) prior to treatment with aptamer Qdots. Qdot-Au complexes were mixed for 30 min at 4 ºC then drop cast onto ultrathin carbon TEM grids (Ted Pella), let dry overnight, and imaged on an Osiris TEM (FEI). All micrograph analysis was performed manually except for centroid distances, which were calculated manually using ImageJ line functions.

Neuronal culture

Rodent procedures and all relevant experimental protocols were approved by the Vanderbilt University Animal Care and Use Committee. Rat hippocampi (CA1-CA3) from both hemispheres were dissected from P0-1 Sprague-Dawley rats and dissociated into a single-cell

suspension. Dissociated cells were recovered by centrifugation (x 200 g, 5 minutes) at 4 °C and re-suspended in plating media composed of Minimal Essential Medium (MEM, Life Technologies) with (in mM) 27 glucose, 2.4 $NaHCO_3$, 0.00125 transferrin, 2 L-glutamine, 0.0043 insulin and 10%/vol fetal bovine serum (FBS, Omega). 100 µl of cell suspension was added onto round 12mm-∅ glass coverslips (200-300 cells/mm^2). 100 µl of Matrigel (BD Biosciences, 1:50 dilution) was deposited on the coverslips and incubated at 37°C with 5% CO_2 for ~ 2 h, then aspirated before cells were plated. Cells were allowed to settle on the coverslip surfaces for 4 h before the addition of 1 mL culture media made of MEM containing (in mM) 27 glucose, 2.4 $NaHCO_3$, 0.00125 transferrin, 1.25 L-glutamine, 0.0022 insulin, 1 %/vol B27 supplement (Life Technologies) and 7.5 %/vol FBS. 1 to 2 days after plating, 2% Ara-C was introduced with another 1 mL of culture media, which efficiently prevented astroglia proliferation. All experiments were performed using cultures between 12-18 DIV.

Plasmid transfection

Neurons were transfected using a calcium phosphate method at 7-10 DIV. pcDNA3.1/Puro-CAG-ASAP1 was a gift from Michael Lin (Addgene plasmid # 52519). SV2a-pHluorin was a gift from Ed Chapman (University of Wisconsin, Madison). CMV::SypHy A4 was a gift from Leon Lagnado (Addgene plasmid # 24478). SNAP-CB1R was purchased from Cisbio (Cobolet, France).

Fluorescence microscopy

Fluorescence imaging was performed on a custom-microscope built on an Olympus IX-81 base using either wide-field illumination (Nikon Intensilight) or a resonance scanning confocal

system (ThorLabs) at 100x with a Nikon oil immersion objective (1.45NA Plan Apo VC). Fluorescent protein fields of view were acquired with a 488 nm laser line at 15% power output. Qdot fields of view were acquired using wide-field illumination with a 400 nm (400/25, Semrock) excitation filter and a 600 nm (600/75, Chroma) emission filter. All tracking experiments were performed at 34 °C using a sample heater (PH-1, Warner Instruments) on a ThorLabs motorized stage. Image acquisition was controlled using Micro-Manager. Qdot images were acquired on an Andor EMCCD (iXon 897) at a 10 Hz frame rate, gain = 75. Fields of view were the same for both channels and selected based on the fluorescent protein channel. All live cell imaging was performed using cells that were bathed in a 4 mM K^+ Tyrode solution. The bath solution composition for all cell-based experiments was (in mM): 150 NaCl, 4 KCl, 2 $MgCl_2$, 2 $CaCl_2$, 10 N-2 hydroxyethyl piperazine-n-2 ethanesulphonic acid (HEPES), 10 glucose, pH 7.35.

Qdots immobilization

Aptamer-Qdots or Streptavidin-Qdots were diluted to 5 pM in Tris containing HCl and mixed with a 1% agarose in sodium borate buffer solution immediately after heating to dissolve agarose. Prior to cooling, a thin layer of agarose-containing Qdots was spread on glass coverslips and imaged at 100x with a Nikon oil immersion objective (1.45NA Plan Apo VC). Immobilized Qdots were imaged on an Olympus IX-81 based with a Nikon Intensilight shutter and a 400 nm (400/25, Semrock) excitation filter and a 600 nm (600/75, Chroma) emission filter. Image acquisition was controlled using Micro-Manager. Qdot images were acquired on an Andor EMCCD (iXon 897) at a 10 Hz frame rate, gain = 75. Image stacks were analyzed in Matlab using custom algorithms.

Trypan blue viability

Neurons were treated for 1 hour with either 10 µL/mL RNAse inhibitor in Fluorobrite or Fluorobrite (Thermo Fisher). Pre-warmed 4K Tyrode solution was diluted 1:1 with Trypan Blue (0.4%, Sigma) and neurons were incubated at room temperature for 2 min. Viability was assessed on an inverted microscope with a 10x objective (0.25 NA, Nikon) and a CCD camera (Photometrics CoolSNAP K4).

Calcium imaging

Neurons were treated for 1 hour with either 10 µL/mL RNAse inhibitor in Fluorobrite or Fluorobrite and then stained with 5 µM Fluo-4 in Fluorobrite and incubated for 10 min at 37 °C and 5% CO_2. Fluorescence imaging was performed on a custom-built Olympus IX-81 microscope using an mCherry filter cube combination (Semrock) and a 10x objective (0.25 NA, Nikon). Image acquisition was controlled using Micro-Manager. All calcium imaging experiments were performed at 34 °C using a sample heater (PH-1, Warner Instruments) on a ThorLabs motorized stage. Images were acquired on an Andor EMCCD (iXon 897) with a 25 ms exposure time, gain = 15. Field stimulation was controlled via a Grass stimulator using custom-written protocols and triggered through Micro-Manager. Image analysis was performed using custom written algorithms in Matlab.

Single particle tracking and analysis

Quantum dot tracking videos were analyzed using the u-track function in Matlab based on published analyses from Jaqaman et al. (Jaqaman et al. 2008). Centroid positions (x_i,y_i) were determined for each time t and custom algorithms were used to calculate the mean squared

displacement (MSD) versus time (τ) curves for each particle trajectory, which were fit to a model of anomalous diffusion to give a diffusion coefficient (D). Tracks shorter than 25 frames were discarded.

Statistical analysis

Lillefors tests were used to determine appropriateness of 2-group comparison test. Either unpaired two-tailed *t*-tests or Wilcoxin rank-sum tests were used for two-group comparisons.

Results

Single-particle tracking applications where a large number of possible targets may be accessible for binding within a confined space, for example proteins with multiple copy numbers present at the luminal surface of synaptic vesicles, still largely employ traditional biotin-streptavidin conjugates. However, in these scenarios a monovalent tag would be advantageous to ensure better estimates of the true underlying dynamics of the system of interest by excluding the possibility of a single Qdot being conjugated to multiple binding sites, which would result in an underestimation of the true dynamics of the biological entity of interest. To achieve this for synaptic vesicles, we set out to modify and extend a previously established method to generate monovalent Qdots (Farlow, Seo et al. 2013). This approach generates monovalent Qdots based on the proposed mechanism that biomolecules or other conjugates attached to a Qdot surface will create steric effects that can be exploited to result in largely monovalent surface conjugation. Farlow et al. previously determined that phosphorothioate DNA containing a 50-Adenosine sequence generated the most favorable surface interaction with Qdots after transfer to an aqueous phase, where the 50-A DNA bases wrap around the thiol-rich Qdot surface. Using this approach,

commercially available Qdots (Qdot ITK, Life Technologies) are first ligand exchanged in the presence of mPEG thiols, TBAB, and NaOH to an aqueous solution. The resulting surface is enriched in mPEG thiols, which was previously demonstrated to result in the most stable ptDNA wrapping (Farlow, Seo et al. 2013). Modifications to the previous approach increase the phase transfer yield for VIVID Qdots and also result in fewer failed phase transfers than for commercially available core/shell Qdots tested, which are stabilized in the organic phase by octadecylamine (ODA) surface ligands (e.g., Ocean Nanotech). Farlow et al. previously observed relatively poor phase transfer yields for VIVID Qdots, but following modification of the ligand exchange procedure, we used these Qdots in all further experiments due to the relatively poor phase transfer we observed for ODA-surface capped Qdots. Thus, phase transfer parameters may be optimized based upon the surface ligand present on the Qdot in the organic phase. Of note, we also found that phase transfer yield was greatly increased by modifying the NaOH addition process to achieve phase transfer: NaOH addition was performed while stirring rather than by static addition followed by vortexing (see Methods). We reasoned that this approach would be less disruptive to the relatively weak surface interactions between the Qdots and mPEG thiols, while still allowing sufficient mixing to encourage phase exchange. Following NaOH addition, Qdots continued to stir for 1 min before removal and collection of the aqueous phase. Repeating this step several times resulted in increased yields of stably ligand exchanged Qdots. Excess solvent was then removed by centrifugal filtration followed by buffer exchanging Qdots through a desalt column (**Figure 4.1a**). ptDNA was then titrated in to Qdots as described previously (Farlow, Seo et al. 2013).

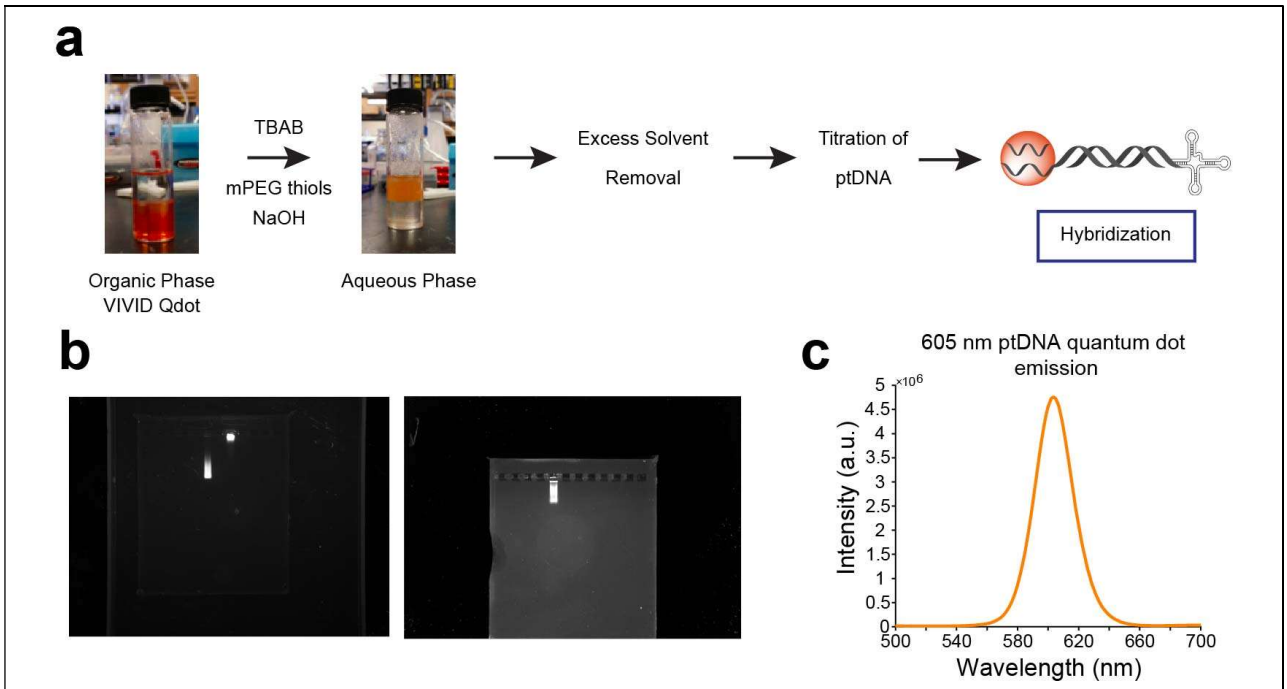

Figure 4.1 **Production of monovalent Qdots.** (**a**) Production steps for monovalent Qdots. (**b**) Electrophoretic separation to assess overall wrapping. Gel on the left shows both wrapped Qdots (*left*) and neutrally charged bare Qdots after thiol addition (*right*). Gel on the right shows Qdots where sufficient ptDNA has not been added and a continuous band is observed. (**c**) 605 nm ptDNA emission spectra before the final aptamer hybridization step.

After sufficient ptDNA addition, ptDNA-wrapped and bare Qdots were electrophoresed to grossly assess overall surface charge (**Figure 4.1b**): Qdots with mPEG thiols on the surface are relatively neutrally charged, thus should not migrate a large distance from the loading wells, while ptDNA wrapping imparts a net negative charge and causes Qdots migration. Prior to proceeding to aptamer hybridization, electrophoresis was repeated each time titration of ptDNA was performed, and addition was halted when ptDNA-wrapped Qdots collapsed onto a largely single and defined band (**Figure 4.1b**). Aptamer hybridization was performed prior to the addition of the alkane thiol PEG as described previously (Farlow, Seo et al. 2013). Notably, significant peak broadening was not observed for Qdots emission spectra following phase transfer and ptDNA

addition (**Figure 4.1c**), suggesting that the ability to multiplex Qdots is preserved and thus monovalency may be achieved for a combination of distinct Qdot sizes.

To extend the utility of monovalent Qdots, we chose a hybridization procedure that confers several distinct advantages. Antibody or nanobody conjugation to biotin followed by conjugation to Streptavidin-Qdots remains the most common strategy for target-of-interest linkage to either organic dyes or Qdots for single particle tracking. However, as much previous effort has focused on improvements in tracking algorithms, for example by the incorporation of Bayesian statistics into the estimation of particle trajectories, or the generation of compact Qdots for more accurate representations of true protein or vesicle mobility, alternative strategies designed to reduce the size of the targeting group would be beneficial. To this end, the small size of aptamers is advantageous. After ptDNA wrapping, a number of different biomolecules can be attached via complementary DNA pairing. Here, we chose to take an aptamer-based approach to take advantage of the small size and the possibility of easily generating large libraries of aptamers using SELEX-based screening. Thus, we designed a hybrid DNA/RNA aptamer, whose RNA sequence results in a structure that binds GFP with nanomolar affinity (Shui, Ozer et al. 2012). The overall hybrid structure is 72 base pairs of RNA with an additional 12 base pairs of DNA that enable two-step hybridization between the ptDNA-wrapped Qdots and the RNA aptamer. Prior to hybridization, the DNA/RNA aptamer was heated to 55 ºC and then rapidly cooled to room temperature to break any secondary structures and allow the proper conformations necessary for RNA binding to form.

After hybridization of the DNA/RNA aptamer to ptDNA-wrapped Qdots, we first assessed the effect of the incorporation of the RNA aptamer on Qdots monovalency. For an approach that allowed a more direct examination of Qdot binding than gel electrophoresis, we prepared complexes to be used for visualization via transmission electron microscopy (TEM). To quantify

binding valencies, an additional electron dense material was required that was readily distinguishable from CdSe/ZnS nanocrystals. For this we used commercially available streptavidin-conjugated Au nanoparticles (NPs) with an ~5 nm diameter. Although the size distributions between Qdots and Au NPs are thus relatively similar, differing electron densities allowed facile discrimination between Au NPs and Qdots.

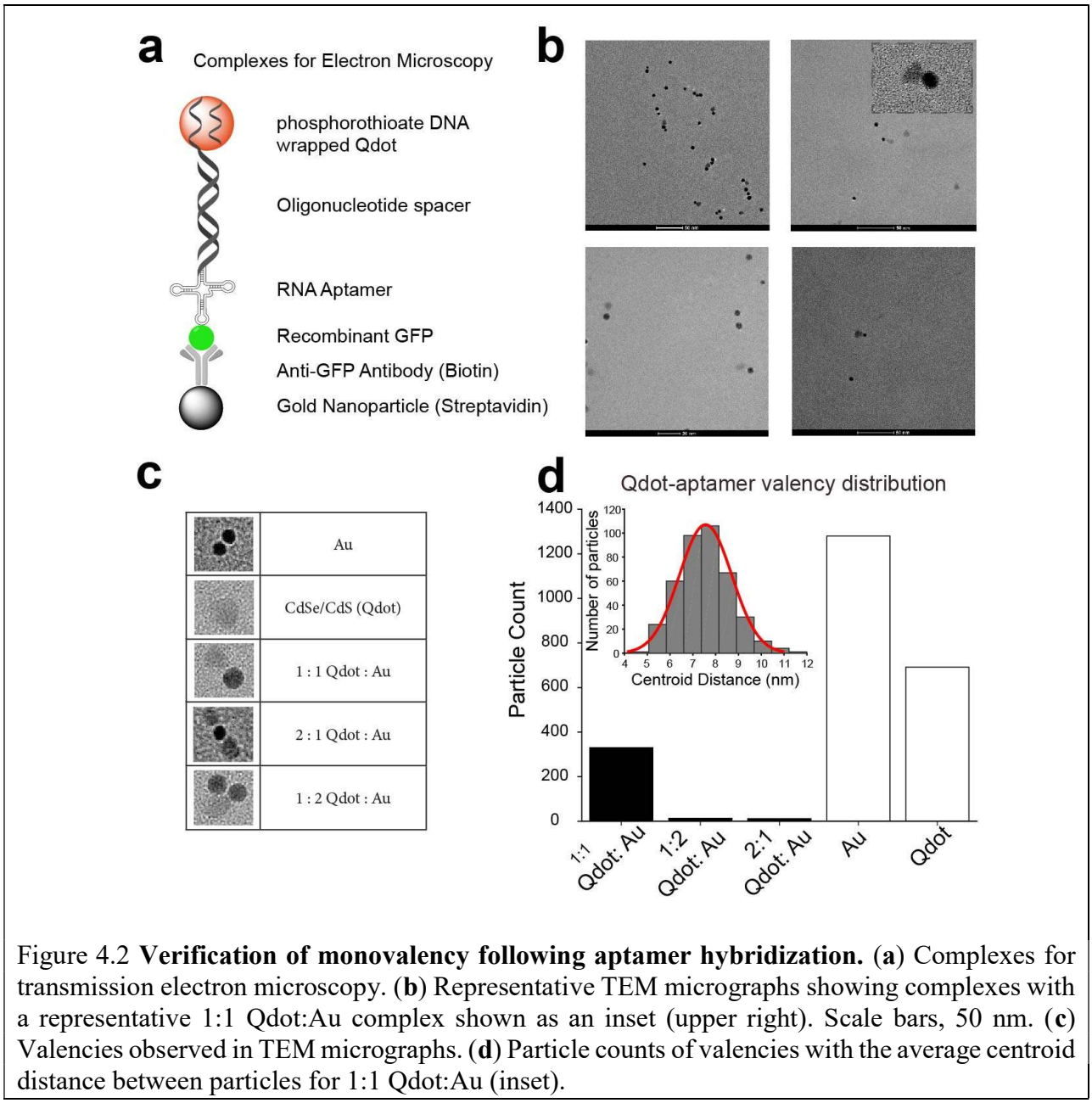

Figure 4.2 **Verification of monovalency following aptamer hybridization.** (**a**) Complexes for transmission electron microscopy. (**b**) Representative TEM micrographs showing complexes with a representative 1:1 Qdot:Au complex shown as an inset (upper right). Scale bars, 50 nm. (**c**) Valencies observed in TEM micrographs. (**d**) Particle counts of valencies with the average centroid distance between particles for 1:1 Qdot:Au (inset).

Complex formation was achieved as follows: recombinant GFP was first bound to DNA/RNA aptamer-conjugated Qdots. The complex was then conjugated to a biotinylated monoclonal anti-GFP antibody, where the biotin group binds to SAv-Au NPs and the antibody binds to the recombinant GFP-aptamer Qdots (**Figure 4.2a**). We observed these particles under TEM (**Figure 4.2b&c**) and noted that, although there were large populations of unbound Qdots or Au NPs, likely since we did not purify our complexes by electrophoresis prior to deposition on TEM grids, the majority of complexes (~95%) that bound were monovalent (**Figure 4.2d**). We further quantified the centroid distances for all 1:1 bound particles, which were normally distributed around a ~7.6 nm spacing (**Figure 4.2d**).

One challenge to the widespread adoption of RNA aptamers for live cell applications has been RNA stability (Mayer 2009). As synthesized, the GFP-binding aptamer validated in Shui et al. does not incorporate modifications such as fluorine modified oligonucleotides, which enhance stability by preventing nuclease degradation (Kawasaki, Casper et al. 1993). Thus, to determine the length of time our RNA aptamer was stable in conventional live cell imaging solutions (see Methods), we ran a series of RNA gels. We determined that within 5 minutes, incubation in either serum-containing or serum-free imaging media resulted in almost complete RNA degradation. To circumvent rapid RNA degradation without the additional rounds of SELEX screening required when balancing RNA binding strength with the time required to select through many more screening rounds, we included RNAse inhibitor in all of our hybridization steps and imaging solutions. We again ran RNA gels to assess RNA degradation, and determined that the addition of RNAse inhibitor resulted in aptamer stability over a time window of ~2 hours.

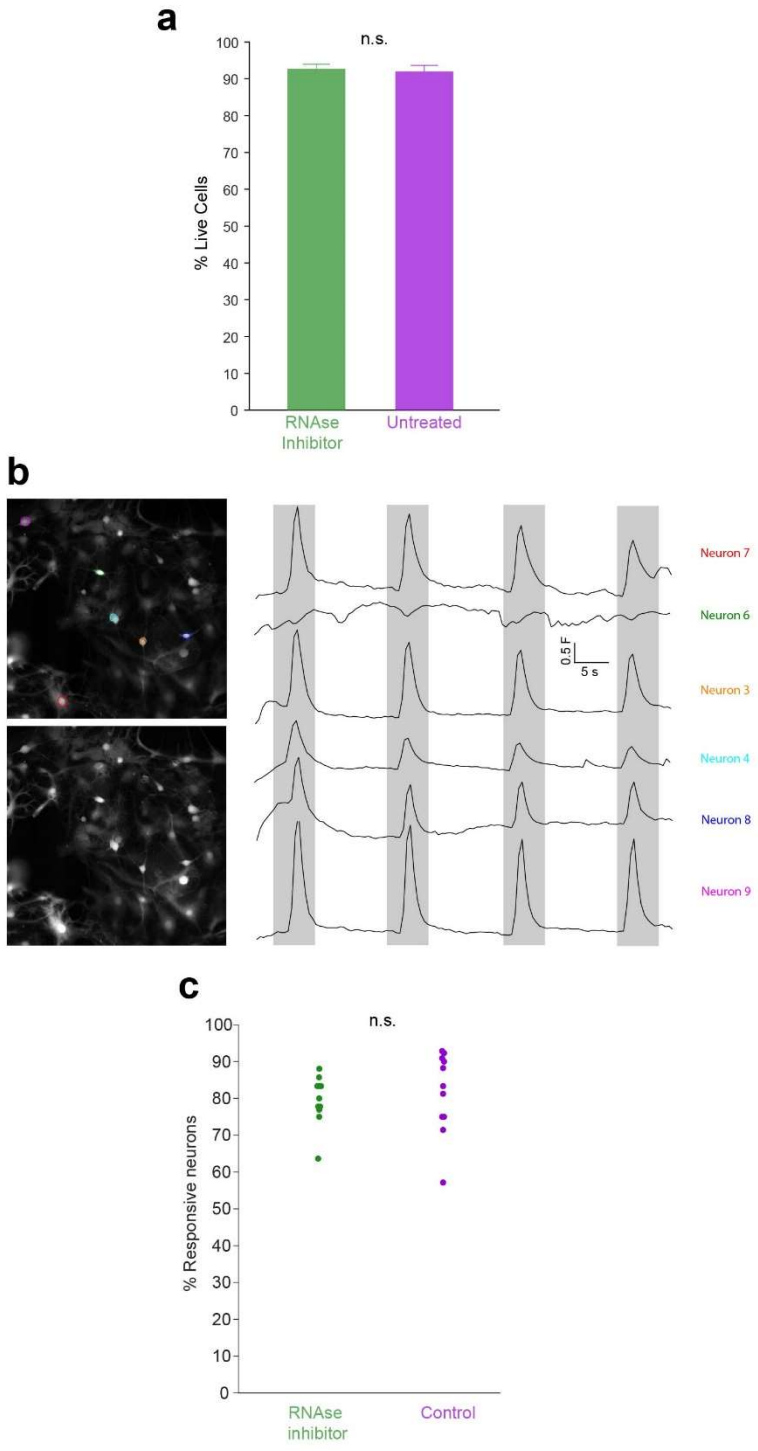

Figure 4.3 **Effects of RNAse inhibitor addition on neuronal viability and excitability.** (**a**) Trypan blue viability following 1-hour treatment with RNAse inhibitor. N = 6 coverslips. (**b**) Calcium imaging following 1-hour treatment with RNAse inhibitor. Individual neurons are shown as color coded, and (**c**) the percent responsiveness to 4 rounds of electrical stimulation are quantified for N = 9 (RNAse inhibitor) or N = 10 (untreated blank control) coverslips.

RNAse inhibitor is widely used in RNA-based experimental methods, for example RNA isolation, however, how it effects neuronal viability and function is less understood. To determine the effect of RNAse inhibitor addition on neurons, we measured both neuronal viability and responsiveness to multiple rounds of electrical stimulation. Neuronal viability was determined after a 1-hour incubation with RNAse inhibitor in concentrations matched to those used during Qdots incubation. To assess viability, we used Trypan blue staining of cultured hippocampal neurons, a traditional assay for quantitation of the number of live/dead cells (Strober 1997). We observed no significant differences in neuronal viability compared to blank controls (**Figure 4.3a**), suggesting that RNAse inhibitor is not toxic to neurons for the concentrations and incubation times used in Qdots labelling. To further address the possibility that neuronal signaling was grossly altered due to the presence of RNAse inhibitor, we performed calcium imaging. Neurons were treated for 1 hour with RNAse inhibitor and pre-loaded with Fluo-4 for 10 min in a serum-free solution before imaging (**Figure 4.3b**). To assess overall neuronal responsiveness to electrical stimulation, we designed a stimulation paradigm where both frequency and intensity were such that control neurons would return to baseline following stimulation, and recovery time between stimuli was sufficient to allow neurons to undergo subsequent rounds of stimulation (**Figure 4.3b**). We observed no differences between RNAse inhibitor and untreated controls in the overall percent responsiveness to 4 rounds of stimulation (**Figure 4.3c**), suggesting that RNAse inhibitor does not grossly alter neuronal excitability.

Although we previously demonstrated that the Qdots photoluminescence spectra were not broadened during the ligand exchange process, ligand exchange and subsequent DNA-wrapping could still alter Qdots photoluminescence emission properties, for example intensity. Of note, the surface ligands present on the Qdot surface have been shown to play a role in photoluminescence

efficiency (Grandhi, M et al. 2016), and decreases in photoluminescence intensity have been noted following the phase transfer process (Farlow, Seo et al. 2013).

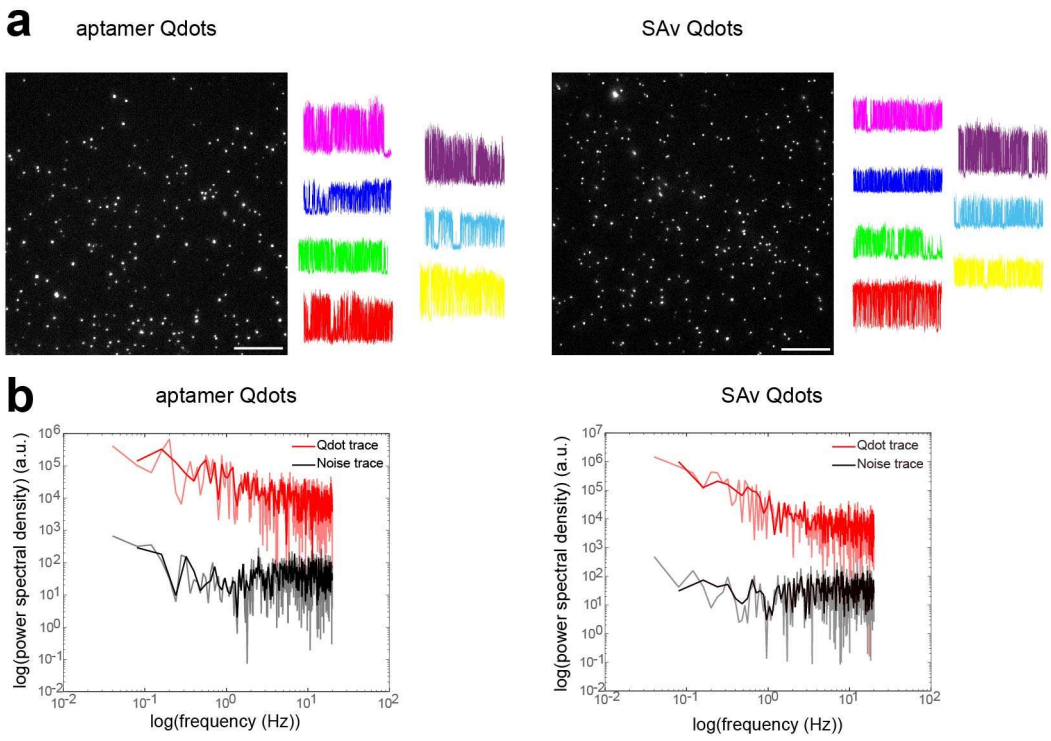

Figure 4.4 **Qdot spectral characterization.**(**a**) Qdots were immobilized in an agarose gel (left) and photoluminescence traces tracked (right). Scale bars, 20 μm. (**b**) Power spectral densities for aptamer Qdots (left) and SAv Qdots (right).

To assess emissive properties at the single Qdot level, we immobilized both ptDNA-wrapped Qdots and SAv Qdots (**Figure 4.4a**), which are commonly used for single particle tracking studies. We first qualitatively examined Qdot 'blinking' (**Figure 4.4a**). The on-off states that are characteristic of Qdots are the result of two processes: light-driven charging and discharging of the nanoparticle core and charging and discharging of electron traps (Galland, Ghosh et al. 2011, Yuan, Gómez et al. 2018). We observed similar photoluminescence traces in time for ptDNA-wrapped and SAv-conjugated Qdots (**Figure 4.4a**). To examine the distribution of spectral intensities, we performed quantal analysis (Zhang, Li et al. 2009) to distinguish single Qdots from multiple Qdots. Gaussian fits to multiplicative increases in peak intensity revealed a

greater number of single particle immobilized Qdots for ptDNA-wrapping, consistent with observations that commercial SAv Qdots often possess 'sticky' surfaces that result in greater degrees of multi-Qdot labeling. Interestingly, we also note that on a per particle basis, photoluminescence intensity is not significantly decreased for ptDNA-wrapped Qdots. We further examined the power spectral densities of ptDNA-wrapped Qdots, which appear similar to those of SAv Qdots (**Figure 4.4b**). Thus, our data indicate that overall photoluminescence properties are not substantially altered during the ligand exchange and subsequent wrapping and hybridization processes.

To validate aptamer-Qdot labelling in neurons, we began by expressing a general membrane label to examine co-localization of Qdots with membrane labelling. For this, we used the genetically encoded fluorescent voltage indicator ASAP1 (St-Pierre, Marshall et al. 2014), expressed in excitatory neurons. The majority of genetically encoded voltage or calcium indicators are designed such that the fluorophore is located within the cytoplasm (Lin and Schnitzer 2016). However, the mechanism of action for ASAP1 is somewhat different, where a circularly permutated GFP is located in the extracellular domain to report fluctuations in voltage across the membrane. Given that our RNA aptamer binds to GFP, we reasoned that this would provide a facile tag that may further enable simultaneous readout of membrane voltage in addition to single-particle positions. We transfected neurons between 7-10 DIV and imaged ASAP1 expression at 12-14 DIV (**Figure 4.5a**). After verifying expression of plasmid DNA, we optimized our labelling approach to minimize incubation time while still allowing sufficient numbers of Qdots in each field of view to generate sample statistics (see Methods, **Figure 4.5b**). Neurons were incubated in a serum-free solution with 4% BSA for 5 min before tracking experiments were performed. Of

note, we also tested using FBS to reduce non-specific binding, but found that labelling density was greatly reduced without outperforming BSA in the overall reduction of non-specific binding.

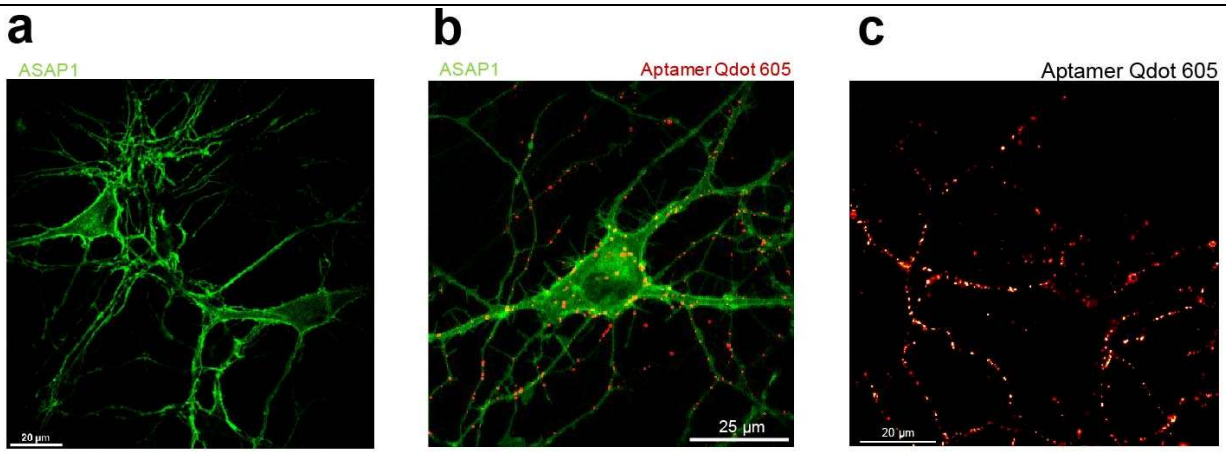

Figure 4.5 **Single particle tracking of membrane bound aptamer-Qdots using the genetically encoded voltage indicator ASAP1.** (**a**) Representative FOV of ASAP1 expression in 12 DIV neurons. (**b**) Representative FOV of ASAP1 expression in 12 DIV neurons with aptamer-Qdot labeling. (**c**) Representative FOV of aptamer-Qdot labeling for single particle tracking. Scale bars as shown. FOV, Field-of-view.

Single particle tracking experiments in neurons were performed over a 60 s duration and at a 10 Hz frame rate (**Figure 4.5c**). Particle trajectories were recovered using previously described tracking algorithms (see Methods) (Jaqaman et al. 2008). We uncovered a heterogeneous distribution of diffusion coefficients for ASAP1-labeled aptamer-Qdots (**Figure 4.6**).

Synaptic vesicle recycling, a process whereby filled synaptic vesicles fuse with a presynaptic active zone, release neurotransmitter, and are then recycled for later reuse, has been well characterized at the molecular level (Südhof 2004). However, the role of synaptic vesicle mobility in maintaining these important and homeostatically regulated processes has yet to be established (Kamin, Lauterbach et al. 2010). We thus set out to demonstrate that, because of their monovalent nature, aptamer-Qdots are useful tools to study synaptic vesicle mobility. To enable the conjugation of aptamer-Qdots to synaptic vesicle proteins, we expressed SV2a-pHluorin (Kwon and Chapman 2011), a pH-sensitive GFP commonly used to study synaptic vesicle fusion

(Sankaranarayanan, De Angelis et al. 2000, Kavalali and Jorgensen 2013), in 7-10 DIV neurons, and performed particle tracking experiments between 12-14 DIV. pHluorins expressed in synaptic vesicle proteins are in part well-suited to report vesicle fusion events due to the location of the GFP chromophore within the vesicle lumen; as with ASAP1, the localization of the GFP molecule to a site on the neuronal surface remains necessary to enable aptamer binding. Additionally, pHluorins are advantageous as tags for single particle tracking due to the relatively lower degree of fluorophore intensity when localized to within the vesicle lumen, where the acidic pH results in effective quenching of fluorophore emission. Alkalinization, for example by addition of NH_4Cl to the imaging solution, allows visualization of SV2a-pHluorin expression. We verified that SV2a-pHluorin expression was localized to synapses by post-hoc immunostaining against the commonly used synaptic marker Synaptophysin.

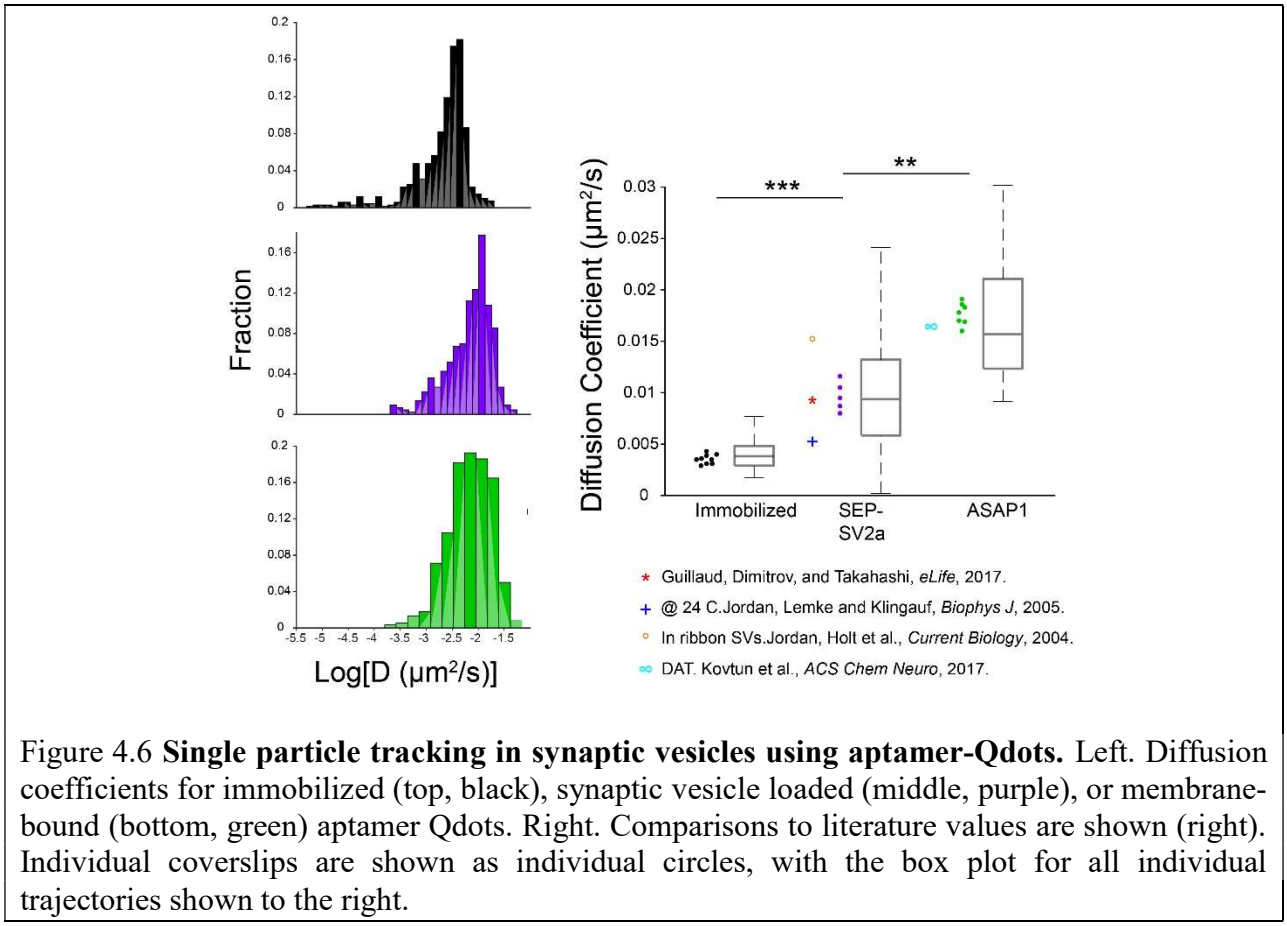

Figure 4.6 **Single particle tracking in synaptic vesicles using aptamer-Qdots.** Left. Diffusion coefficients for immobilized (top, black), synaptic vesicle loaded (middle, purple), or membrane-bound (bottom, green) aptamer Qdots. Right. Comparisons to literature values are shown (right). Individual coverslips are shown as individual circles, with the box plot for all individual trajectories shown to the right.

To assess the utility of monovalent aptamer-Qdots to study synaptic vesicle dynamics, we next performed single particle tracking using aptamer-Qdots loaded into synaptic vesicles (**Figure 4.6**). Notably, based on our earlier results, which suggested that in the presence of RNAse inhibitor, the aptamer would be stable for up to ~2 hours in imaging media, suggested that longer incubation periods would be possible, although whether there would be faster degradation in the presence of cells remained unclear. We used a 45 min incubation to load synaptic vesicles with aptamer-Qdots, an established incubation length to ensure sufficient vesicle turnover. We observed labeling of Qdots that was largely co-localized to SV2a-pHluorin expression, confirming that aptamer labelling remained specific after 45 min incubation, and suggesting that only negligible degradation occurs. We again tracked aptamer-Qdots at a 10 Hz imaging rate. To compare vesicle mobilities, we also performed tracking of immobilized aptamer-Qdots and ASAP1-tagged aptamer-Qdots. We observed largely heterogeneous and unimodal distributions of diffusion coefficients across all 3 conditions, with a tail of small diffusion coefficients for immobilized aptamer-Qdots. Analysis of average diffusion coefficient for individual neurons demonstrates an overall increase in diffusion coefficient for both SV2a-pHluorin and ASAP1 aptamer-Qdots in comparison to immobilized aptamer-Qdots. The range of diffusion coefficients we obtained for SV2a-pHluorin labelling is in good agreement with a Brownian motion analysis-based approach, similar to the one used here, for trajectories obtained by tracking antibody-conjugated Qdots (Guillaud, Dimitrov et al. 2017). Overall diffusion coefficients for aptamer-Qdots, which were imaged at 34 ºC, were also larger than for antibody-conjugated Qdots imaged at room temperature (Jordan, Lemke et al. 2005), in agreement with previous demonstrations that vesicle mobility is temperature-dependent (Renden and Gersdorff 2007, Guillaud, Dimitrov et al. 2017). Confinement of Qdots within synaptic vesicles also results in lower overall diffusion coefficients than membrane

machinery related to active cellular transport. We observed that SV2a-pHluorin tagged aptamer-Qdot mobilities were lower than a monoamine transporter (Kovtun, Sakrikar et al. 2015) – and furthermore that hippocampal synaptic vesicles exhibit lower diffusion coefficients than vesicles at ribbon synapses (Holt, Cooke et al. 2004), in good agreement with previous results.

Lastly, as a proof-of-principle, we demonstrate multicolor monovalent labeling using a SNAP-tagged endocannabinoid receptor (CB1R) paired with a benzylguanine DNA-hybridized Qdots (Em 605) in combination with aptamer-Qdots targeted to a Synaptophysin-pHluorin (Em 545) (**Figure 4.7**).

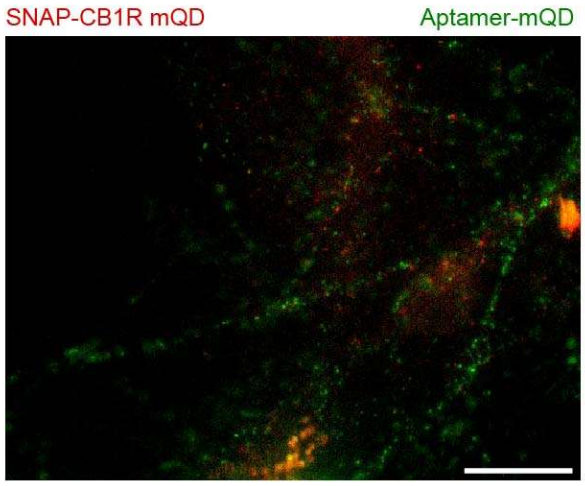

Figure 4.7 Multicolor monovalent quantum dot labeling. Scale bar, 20 μm.

Discussion

We present an approach for tagging cell surface or synaptic vesicle proteins with monovalent Qdots that are hybridized to an RNA aptamer. This method is broadly generalizable to any target of interest where GFP-based expression can be used as a handle for aptamer binding. We demonstrate that monovalency is preserved even after aptamer hybridization, which may be

important at cell surfaces sites where a large protein copy number increases the likelihood of multivalent conjugation. Furthermore, the use of RNA hybridization and aptamer binding as a conjugation strategy may open new doors for the utility of Qdots to examine the mobility of cellular components where generating antibodies against specific targets has proven challenging. DNA or RNA-based cell tagging have been of interest for a variety of applications beyond single particle tracking, and the use of Qdots may enable far greater multiplexing than is possible with traditional fluorophores. For example, using combinatorial combinations of Qdots with DNA barcodes could allow increased diversity in neuronal connectome sequencing – a long-sought advance for neuroscience (Zador, Dubnau et al. 2012).

Here, we further extend the utility of previous efforts to generate monovalent Qdots (Farlow, Seo et al. 2013) that are facile to produce, without complicated conjugation chemistries that would be prohibitive for many biological laboratories. DNA-wrapping of Qdots to achieve steric hindrance, thus conferring monovalency, represents a different approach, with both advantages and challenges ahead. The use of monomeric Streptavidin represents an alternative strategy to achieving a monovalent Qdot. Using this method, a distribution of valencies would be generated and monovalent Qdots are excised following gel electrophoresis (Howarth, Liu et al. 2008). However, the need to electrophoretically isolate Qdots would reduce overall yield, and the interaction between a 6His tag on the monomeric Streptavidin and the Qdot surface is not irreversible, limiting the lifetime of the monovalent complex to on the order of hours. ptDNA-wrapped Qdots production consists of several steps, where the initial ligand exchange step results in thiol-rich surfaces that persist for a period of months. The less labor intensive DNA-wrapping and RNA hybridization processes are limited by DNA and RNA degradation rates, but we have found that it is possible to store DNA-wrapped Qdots at 4 ºC for up to a week without loss of

binding. However, RNA hybridization must be performed immediately prior to imaging due to the relatively limited timeframe before RNA degradation onset (> 2 hours). Future efforts to increase RNA stability, for example by fluorine modification (Lipi, Chen et al. 2016), will extend the working lifetime of aptamer-hybridized Qdots. However, this will require additional rounds of SELEX screening to ensure that a balance is maintained between RNA stability and binding affinity. Alternatively, small-sized probes such as affimers or nanobodies may be hybridized on to monovalent Qdots, enabling tracking of neuronal proteins over extended timeframes.

References

Alivisatos, A. P. (1996). "Semiconductor Clusters, Nanocrystals, and Quantum Dots." Science **271**(5251): 933-937.

Boeneman, K., J. B. Delehanty, K. Susumu, M. H. Stewart, J. R. Deschamps and I. L. Medintz (2012). Quantum Dots and Fluorescent Protein FRET-Based Biosensors. Nano-Biotechnology for Biomedical and Diagnostic Research. E. Zahavy, A. Ordentlich, S. Yitzhaki and A. Shafferman. Dordrecht, Springer Netherlands**:** 63-74.

Boyden, E. S., F. Zhang, E. Bamberg, G. Nagel and K. Deisseroth (2005). "Millisecond-timescale, genetically targeted optical control of neural activity." Nature Neuroscience **8**: 1263.

Chang, J. C., I. D. Tomlinson, M. R. Warnement, A. Ustione, A. M. D. Carneiro, D. W. Piston, R. D. Blakely and S. J. Rosenthal (2012). "Single Molecule Analysis of Serotonin Transporter Regulation Using Antagonist-Conjugated Quantum Dots Reveals Restricted, p38 MAPK-Dependent Mobilization Underlying Uptake Activation." The Journal of Neuroscience **32**(26): 8919-8929.

Chen, F., A. T. Wassie, A. J. Cote, A. Sinha, S. Alon, S. Asano, E. R. Daugharthy, J.-B. Chang, A. Marblestone, G. M. Church, A. Raj and E. S. Boyden (2016). "Nanoscale Imaging of RNA with Expansion Microscopy." Nature methods **13**(8): 679-684.

Chen, T.-W., T. J. Wardill, Y. Sun, S. R. Pulver, S. L. Renninger, A. Baohan, E. R. Schreiter, R. A. Kerr, M. B. Orger, V. Jayaraman, L. L. Looger, K. Svoboda and D. S. Kim (2013). "Ultrasensitive fluorescent proteins for imaging neuronal activity." Nature **499**: 295.

Chen, Y., J. Vela, H. Htoon, J. L. Casson, D. J. Werder, D. A. Bussian, V. I. Klimov and J. A. Hollingsworth (2008). ""“Giant” Multishell CdSe Nanocrystal Quantum Dots with Suppressed Blinking." Journal of the American Chemical Society **130**(15): 5026-5027.

Clapp, A. R., I. L. Medintz, J. M. Mauro, B. R. Fisher, M. G. Bawendi and H. Mattoussi (2004). "Fluorescence Resonance Energy Transfer Between Quantum Dot Donors and Dye-Labeled Protein Acceptors." Journal of the American Chemical Society **126**(1): 301-310.

Dabbousi, B. O., J. Rodriguez-Viejo, F. V. Mikulec, J. R. Heine, H. Mattoussi, R. Ober, K. F. Jensen and M. G. Bawendi (1997). "(CdSe)ZnS Core−Shell Quantum Dots: Synthesis and Characterization of a Size Series of Highly Luminescent Nanocrystallites." The Journal of Physical Chemistry B **101**(46): 9463-9475.

Dahan, M., S. Lévi, C. Luccardini, P. Rostaing, B. Riveau and A. Triller (2003). "Diffusion Dynamics of Glycine Receptors Revealed by Single-Quantum Dot Tracking." Science **302**(5644): 442-445.

Dennis, A. M., W. J. Rhee, D. Sotto, S. N. Dublin and G. Bao (2012). "Quantum Dot–Fluorescent Protein FRET Probes for Sensing Intracellular pH." ACS Nano **6**(4): 2917-2924.

Efros, A. L., J. B. Delehanty, A. L. Huston, I. L. Medintz, M. Barbic and T. D. Harris (2018). "Evaluating the potential of using quantum dots for monitoring electrical signals in neurons." Nature Nanotechnology **13**(4): 278-288.

Efros, A. L. and D. J. Nesbitt (2016). "Origin and control of blinking in quantum dots." Nature Nanotechnology **11**: 661.

Farlow, J., D. Seo, K. E. Broaders, M. J. Taylor, Z. J. Gartner and Y.-w. Jun (2013). "Formation of targeted monovalent quantum dots by steric exclusion." Nature Methods **10**: 1203.

Farzadfard, F. and T. K. Lu (2018). "Emerging applications for DNA writers and molecular recorders." Science **361**(6405): 870-875.

Galland, C., Y. Ghosh, A. Steinbrück, M. Sykora, J. A. Hollingsworth, V. I. Klimov and H. Htoon (2011). "Two types of luminescence blinking revealed by spectroelectrochemistry of single quantum dots." Nature **479**: 203.

Geng, L., Y. K. Qian, R. Madhavan and H. B. Peng (2008). "Transmembrane mechanisms in the assembly of the postsynaptic apparatus at the neuromuscular junction." Chemico-Biological Interactions **175**(1): 108-112.

Giepmans, B. N. G., T. J. Deerinck, B. L. Smarr, Y. Z. Jones and M. H. Ellisman (2005). "Correlated light and electron microscopic imaging of multiple endogenous proteins using Quantum dots." Nature Methods **2**: 743.

Grandhi, G. K., A. M and R. Viswanatha (2016). "Understanding the Role of Surface Capping Ligands in Passivating the Quantum Dots Using Copper Dopants as Internal Sensor." The Journal of Physical Chemistry C **120**(35): 19785-19795.

Guillaud, L., D. Dimitrov and T. Takahashi (2017). "Presynaptic morphology and vesicular composition determine vesicle dynamics in mouse central synapses." eLife **6**: e24845.

Han, M., X. Gao, J. Z. Su and S. Nie (2001). "Quantum-dot-tagged microbeads for multiplexed optical coding of biomolecules." Nature Biotechnology **19**: 631.

Han, Y., J. M. Kebschull, R. A. A. Campbell, D. Cowan, F. Imhof, A. M. Zador and T. D. Mrsic-Flogel (2018). "The logic of single-cell projections from visual cortex." Nature **556**: 51.

Holt, M., A. Cooke, A. Neef and L. Lagnado (2004). "High Mobility of Vesicles Supports Continuous Exocytosis at a Ribbon Synapse." Current Biology **14**(3): 173-183.

Howarth, M., W. Liu, S. Puthenveetil, Y. Zheng, L. F. Marshall, M. M. Schmidt, K. D. Wittrup, M. G. Bawendi and A. Y. Ting (2008). "Monovalent, reduced-size quantum dots for imaging receptors on living cells." Nature methods **5**(5): 397-399.

Jaqaman, K.; Loerke, D.; Mettlen, M.; Kuwata, H.; Grinstein, S.; Schmid, S. L.; Danuser, G., Robust single-particle tracking in live-cell time-lapse sequences. Nature Methods 2008, 5, 695.

Jordan, R., E. A. Lemke and J. Klingauf (2005). "Visualization of Synaptic Vesicle Movement in Intact Synaptic Boutons Using Fluorescence Fluctuation Spectroscopy." Biophysical Journal **89**(3): 2091-2102.

Kalhor, R., K. Kalhor, L. Mejia, K. Leeper, A. Graveline, P. Mali and G. M. Church (2018). "Developmental barcoding of whole mouse via homing CRISPR." Science **361**(6405).

Kamin, D., M. A. Lauterbach, V. Westphal, J. Keller, A. Schönle, S. W. Hell and S. O. Rizzoli (2010). "High- and Low-Mobility Stages in the Synaptic Vesicle Cycle." Biophysical Journal **99**(2): 675-684.

Kavalali, E. T. and E. M. Jorgensen (2013). "Visualizing presynaptic function." Nature Neuroscience **17**: 10.

Kawasaki, A. M., M. D. Casper, S. M. Freier, E. A. Lesnik, M. C. Zounes, L. L. Cummins, C. Gonzalez and P. D. Cook (1993). "Uniformly modified 2'-deoxy-2'-fluoro-phosphorothioate oligonucleotides as nuclease-resistant antisense compounds with high affinity and specificity for RNA targets." Journal of Medicinal Chemistry **36**(7): 831-841.

Kitko, K. E., T. Hong, R. M. Lazarenko, D. Ying, Y.-Q. Xu and Q. Zhang (2018). "Membrane cholesterol mediates the cellular effects of monolayer graphene substrates." Nature Communications **9**(1): 796.

Kovtun, O., D. Sakrikar, I. D. Tomlinson, J. C. Chang, X. Arzeta-Ferrer, R. D. Blakely and S. J. Rosenthal (2015). "Single-Quantum-Dot Tracking Reveals Altered Membrane Dynamics of an Attention-Deficit/Hyperactivity-Disorder-Derived Dopamine Transporter Coding Variant." ACS Chemical Neuroscience **6**(4): 526-534.

Kwon, S. E. and E. R. Chapman (2011). "Synaptophysin regulates the kinetics of synaptic vesicle endocytosis in central neurons." Neuron **70**(5): 847-854.

Lévi, S., C. Schweizer, H. Bannai, O. Pascual, C. Charrier and A. Triller (2008). "Homeostatic Regulation of Synaptic GlyR Numbers Driven by Lateral Diffusion." Neuron **59**(2): 261-273.

Lin, M. Z. and M. J. Schnitzer (2016). "Genetically encoded indicators of neuronal activity." Nature Neuroscience **19**: 1142.

Lipi, F., S. Chen, M. Chakravarthy, S. Rakesh and R. N. Veedu (2016). "In vitro evolution of chemically-modified nucleic acid aptamers: Pros and cons, and comprehensive selection strategies." RNA Biology **13**(12): 1232-1245.

Liu, J., S. K. Lau, V. A. Varma, R. A. Moffitt, M. Caldwell, T. Liu, A. N. Young, J. A. Petros, A. O. Osunkoya, T. Krogstad, B. Leyland-Jones, M. D. Wang and S. Nie (2010). "Molecular

Mapping of Tumor Heterogeneity on Clinical Tissue Specimens with Multiplexed Quantum Dots." ACS Nano **4**(5): 2755-2765.

Mahler, B., P. Spinicelli, S. Buil, X. Quelin, J.-P. Hermier and B. Dubertret (2008). "Towards non-blinking colloidal quantum dots." Nature Materials **7**: 659.

Mandal, S., X. Zhou, N. Eddine Fahmi, S. Lin, H. Yan and N. Woodbury (2018). "Quantum Dot-based Fluorescence Resonance Energy Transfer through Exciton Dynamics in DNA-Templated J-Aggregates." Biophysical Journal **114**(3): 523a.

Mayer, G. (2009). "The Chemical Biology of Aptamers." Angewandte Chemie International Edition **48**(15): 2672-2689.

Medintz, I. L., A. R. Clapp, H. Mattoussi, E. R. Goldman, B. Fisher and J. M. Mauro (2003). "Self-assembled nanoscale biosensors based on quantum dot FRET donors." Nature Materials **2**: 630.

Michalet, X., F. F. Pinaud, L. A. Bentolila, J. M. Tsay, S. Doose, J. J. Li, G. Sundaresan, A. M. Wu, S. S. Gambhir and S. Weiss (2005). "Quantum Dots for Live Cells, in Vivo Imaging, and Diagnostics." Science **307**(5709): 538-544.

Mikasova, L., L. Groc, D. Choquet and O. J. Manzoni (2008). "Altered surface trafficking of presynaptic cannabinoid type 1 receptor in and out synaptic terminals parallels receptor desensitization." Proceedings of the National Academy of Sciences **105**(47): 18596-18601.

Miller, D. A. B., D. S. Chemla, T. C. Damen, A. C. Gossard, W. Wiegmann, T. H. Wood and C. A. Burrus (1984). "Band-Edge Electroabsorption in Quantum Well Structures: The Quantum-Confined Stark Effect." Physical Review Letters **53**(22): 2173-2176.

Park, H., Y. Li and R. W. Tsien (2012). "Influence of Synaptic Vesicle Position on Release Probability and Exocytotic Fusion Mode." Science **335**(6074): 1362-1366.

Peikon, I. D., J. M. Kebschull, V. V. Vagin, D. I. Ravens, Y.-C. Sun, E. Brouzes, J. I. R. Corrêa, D. Bressan and A. M. Zador (2017). "Using high-throughput barcode sequencing to efficiently map connectomes." Nucleic Acids Research **45**(12): e115-e115.

Reed, M. A., R. T. Bate, K. Bradshaw, W. M. Duncan, W. R. Frensley, J. W. Lee and H. D. Shih (1986). "Spatial quantization in GaAs–AlGaAs multiple quantum dots." Journal of Vacuum Science & Technology B: Microelectronics Processing and Phenomena **4**(1): 358-360.

Renden, R. and H. v. Gersdorff (2007). "Synaptic Vesicle Endocytosis at a CNS Nerve Terminal: Faster Kinetics at Physiological Temperatures and Increased Endocytotic Capacity During Maturation." Journal of Neurophysiology **98**(6): 3349-3359.

Sankaranarayanan, S., D. De Angelis, J. E. Rothman and T. A. Ryan (2000). "The Use of pHluorins for Optical Measurements of Presynaptic Activity." Biophysical Journal **79**(4): 2199-2208.

Shipman, S. L., J. Nivala, J. D. Macklis and G. M. Church (2017). "CRISPR–Cas encoding of a digital movie into the genomes of a population of living bacteria." Nature **547**: 345.

Shui, B., A. Ozer, W. Zipfel, N. Sahu, A. Singh, J. T. Lis, H. Shi and M. I. Kotlikoff (2012). "RNA aptamers that functionally interact with green fluorescent protein and its derivatives." Nucleic Acids Research **40**(5): e39-e39.

St-Pierre, F., J. D. Marshall, Y. Yang, Y. Gong, M. J. Schnitzer and M. Z. Lin (2014). "High-fidelity optical reporting of neuronal electrical activity with an ultrafast fluorescent voltage sensor." Nature neuroscience **17**(6): 884-889.

Strober, W. (1997). "Trypan Blue Exclusion Test of Cell Viability." Current Protocols in Immunology **21**(1): A.3B.1-A.3B.2.

Subila, K. B., G. Kishore Kumar, S. M. Shivaprasad and K. George Thomas (2013). "Luminescence Properties of CdSe Quantum Dots: Role of Crystal Structure and Surface Composition." The Journal of Physical Chemistry Letters **4**(16): 2774-2779.

Südhof, T. C. (2004). "THE SYNAPTIC VESICLE CYCLE." Annual Review of Neuroscience **27**(1): 509-547.

Sylwestrak, E. L., P. Rajasethupathy, M. A. Wright, A. Jaffe and K. Deisseroth (2016). "Multiplexed intact-tissue transcriptional analysis at cellular resolution." Cell **164**(4): 792-804.

Tsunoyama, T. A., Y. Watanabe, J. Goto, K. Naito, R. S. Kasai, K. G. N. Suzuki, T. K. Fujiwara and A. Kusumi (2018). "Super-long single-molecule tracking reveals dynamic-anchorage-induced integrin function." Nature Chemical Biology **14**(5): 497-506.

Yuan, G., D. E. Gómez, N. Kirkwood, K. Boldt and P. Mulvaney (2018). "Two Mechanisms Determine Quantum Dot Blinking." ACS Nano **12**(4): 3397-3405.

Zador, A. M., J. Dubnau, H. K. Oyibo, H. Zhan, G. Cao and I. D. Peikon (2012). "Sequencing the Connectome." PLOS Biology **10**(10): e1001411.

Zhang, Q., Y.-Q. Cao and R. W. Tsien (2007). "Quantum dots provide an optical signal specific to full collapse fusion of synaptic vesicles." Proceedings of the National Academy of Sciences **104**(45): 17843-17848.

Zhang, Q., Y. Li and R. W. Tsien (2009). "The Dynamic Control of Kiss-And-Run and Vesicular Reuse Probed with Single Nanoparticles." Science **323**(5920): 1448-1453.

Zrazhevskiy, P. and X. Gao (2013). "Quantum dot imaging platform for single-cell molecular profiling." Nature Communications **4**: 1619

Chapter 5

Conclusions and future directions

The major findings and contributions from each of the preceding sections are detailed below, followed by a broad overview of ways in which the work presented here might motivate or inform future investigations.

Chronic growth on graphene results in alterations in membrane-associated signaling

In *Chapter 1* of this thesis, much of the previous work to date on the topic of graphene and the brain was reviewed. There is increasing interest in the use of graphene-based materials for biological applications. For example, in neuroscience applications, a combination of optical transparency and high carrier mobility make graphene appealing for transparent and flexible electrodes. And ultimately, new device strategies must be explored if one fundamental limitation of current implanted electrodes is to be overcome: traditional electrodes are spatially limited to recording in the vicinity of a physical stud. Recently, however, the use of photocurrents has been explored for both neuronal stimulation (Parameswaran, Carvalho-de-Souza et al. 2018) and recording (Wang, Shi et al. 2018). Because certain 2-dimensional materials such as graphene generate electron-hole pairs in response to optical excitation, this approach would in theory only be spatially limited in recording by the ability to deliver laser light. Development of such new platforms normal proceeds from *in vitro* studies using either cell lines or primary neuronal cultures. Structural changes in response to the presence of a foreign material have been an active area of study.

In *Chapter 2* of this thesis, we took inspiration from experimental device configurations that require chronic growth on graphene to understand the structural and functional changes that one would observe and further to gain mechanistic insight into the underlying mechanisms for any observed changes. We cultured hippocampal neurons, an established system for the study of synaptic transmission *in vitro*, on graphene substrates and characterized morphology and neuronal firing. Neurons on graphene exhibited an increase in firing frequency and a preference for fast vesicle fusion – without large morphological differences – indicative of an increase in synaptic strength (Kitko, Hong et al. 2018). Increased synaptic strength on graphene has more recently been independently confirmed (Pampaloni, Lottner et al. 2018), although the underlying mechanism is proposed to be different. By manipulating membrane cholesterol levels, we uncovered that cholesterol is a key mediator of the observed synaptic potentiation on graphene. We thus propose a model where chronic growth on graphene increases cholesterol levels in neuron, which in turn modulates neurotransmitter release and potentiates receptor signaling.

Prior to the work presented here in *Chapter 2* (Kitko, Hong et al. 2018), there were numerous proposed explanations for a variety of cellular effects in response to chronic culture on graphene. Some of the earliest studies using graphene as a culture substrate focused on stem cells – it was demonstrated that graphene promoted stem cell differentiation and outgrowth. One key difference between these early studies and more recent work, which must be considered, is the use of an extracellular matrix coating. These protein-based coatings are common for cell culture systems, but introduce potential confounds for investigating the direct effect of graphene on cells. 1. They are poly-ionic and introduce additional surface charges which may electrostatically interact with graphene and 2. At physiological temperature, gel-based protein coatings gel – thereby creating a physical gap between graphene and the biological subject of interest. Recent

studies have demonstrated that such matrix coatings are not necessary for chronic growth (Veliev, Briançon-Marjollet et al. 2016, Kitko, Hong et al. 2018, Pampaloni, Lottner et al. 2018).

A key consideration for future work with graphene – but also broadly for nanomaterials to be designed for neuroscience applications - is the formation of the protein corona. Within minutes of exposure to biological media, both 'soft' and 'hard' protein coronas are formed around nanomaterials (Lundqvist, Stigler et al. 2011, Lee, Choi et al. 2015, Lo Giudice, Herda et al. 2016), thus precluding any 'direct' exposure of the nanomaterial surface to a biological surface. As many computational models suggest a variety of interactions between proteins, lipids, and graphene, more studies are warranted to first understand the makeup of the biological corona formed at a graphene surface. The findings of Castagnola et al. (Castagnola, Zhao et al. 2018) are a first step to this end. Although this work did not focus on fluids within the brain, the use of mass spectrometry to precisely quantify both the components of the protein corona and further their percentage makeup are an important step towards understanding the complex relationship between the graphene surface, a protein corona, and cellular effects.

We propose in *Chapter 2* that cholesterol plays an important role in mediating the effects of graphene substrates. K+ ion adsorption on graphene surfaces has more recently also been proposed as a mechanism to induce potentiated signaling on CVD-graphene. Although our later work, presented in *Chapter 3*, suggests that the effect of modulating K+ levels is not substantial, additional work may still help to inform all the potential routes through which graphene could modify membrane signaling – beyond lipid reorganization or changes in extracellular ion availability.

GNFs acutely modulate lipid membrane packing

Based on our results which demonstrate that cholesterol enrichment occurs on graphene substrates after chronic culture, we next sought to determine whether graphene could also acutely alter membrane signaling. We present our findings in *Chapter 3*. Flakes of graphene result in membrane packing increases within an hour, functionally modifying cell signaling processes in a similar manner to the results outlined in *Chapter 2*.

Although we demonstrate in *Chapter 2* that membrane cholesterol is a key mediator of the potentiated signaling we observe on graphene (Kitko, Hong et al. 2018), the plasma membrane is a complex and dynamic microenvironment containing a myriad of molecules, some of whose roles remain undetermined. Thus, in *Chapter 3* we investigated the interaction of GNFs with several additional molecules present in large molar percentages in the cell membrane. In a cell-free system, a fluorescent cholesterol analog exhibited a large overall change in lifetime than fluorescent SM, PC, or PE analogs, suggesting some specificity to the interaction between graphene and cholesterol beyond a hydrophobic interaction. Treatment with GNFs changes lipid membrane packing within 1 hour, resulting in changes in neurotransmitter release and P2YR signaling.

Graphene is now largely accepted to be a biocompatible culture substrate (Veliev, Briançon-Marjollet et al. 2016, Fischer, Zhang et al. 2018, Kitko, Hong et al. 2018). However, there remain concerns as to the overall toxicity of graphene. This stems from early work using prokaryotic cells, which demonstrated that at 100 μg/ml concentrations, flakes of graphene would disrupt membrane integrity, killing bacteria within a few hours of treatment. We have demonstrated that treatment with low concentrations of GNFs does not affect overall cell viability or membrane conductance within 1 hour. Further studies could explore several avenues – 1 hour was sufficient in our work to modify cell signaling, but ultimately longer term toxicity must be characterized. The results presented here suggest that up to 24-hour treatment is not toxic to cells,

but days or even weeks of treatment time may result in toxicity. Future efforts to understand the underlying mechanisms for longer term toxicity (> 18 DIV on G substrates, > 24 h GNFs treatment) will aid in determining the clinical applicability of G/GO-based nanomaterials. And creating a framework for the toxicity of carbon-based nanomaterials will involve resolving any differences or parallels between G/GO and CNTs. For example, lines of evidence that suggest that the presence of residual impurities (e.g. precursor) may be important to overall toxicity for CNTs (Aldieri, Fenoglio et al. 2013), suggest that production methods may play a role. Thus, production methods may be modified to reduce toxicity if necessary.

Targeting GNFs to specific cell surface sites presents an engineering challenge for the future. GO flakes can be easily modified using widely-available conjugation chemistries due to the presence of oxygen groups across the surface. However, if the GNFs surface is important for the nature of its membrane interactions, routes by which the surface can be modified normally result in modification from the graphene structure.

We demonstrate that the effects of GNFs are realized on different timescales for different cell types and different cell signaling pathways (*Chapter 2* & *Chapter 3*). We hypothesize that these differences are due to the ways cholesterol is involved in each cell signaling process. For neurotransmitter release, cholesterol plays an important role in maintaining homeostatic physicochemical membrane properties and molecular organization. There are several possible ways for cholesterol to act, through which vesicle fusion mode preference could be changed and vesicle pool size increased, and future studies could further examine these alternatives. Cholesterol binds the synaptic vesicle proteins synaptophysin and synaptotagmin (Thiele, Hannah et al. 1999), for example, and may thus act to segregate membrane components. Or more directly, cholesterol may play a structural role in changing membrane curvature, altering release properties (Rosa and

Fratangeli 2010). For receptor activation, cholesterol may act through lipid signaling domains or through its role as a ligand for effector proteins. Cholesterol is an important component of lipid-rich domains (Simons and Ehehalt 2002) which serve as concentrating platforms for receptors, which may be stabilized or enlarged after GNFs treatment. And G-protein coupled receptors can be modulated by altered concentrations of membrane cholesterol. Smoothened for example, which is part of the canonical Hedgehog signaling pathway, can be directly activated by cholesterol engaging its extracellular domain (Huang, Nedelcu et al. 2016, Luchetti, Sircar et al. 2016). Future work may distinguish between these possibilities. Computational models are beginning to elucidate the role cholesterol plays in activation for a variety of different receptors (Prasanna, Chattopadhyay et al. 2014, Pluhackova, Gahbauer et al. 2016, Sengupta, Prasanna et al. 2018), and in the future G/GO may be incorporated into such models to provide greater insight into the physics underlying these complex membrane phenomena.

Aptamer-conjugated quantum dots to study synaptic vesicle mobility

Prior to the method developed by Farlow et al. (Farlow, Seo et al. 2013), monovalent Qdots were largely obtained by isolation of the monovalent product from a mixture of valencies, for example by gel purification (Howarth, Liu et al. 2008, Liu and Gao 2011) or magnetic bead separation (Uddayasankar, Zhang et al. 2014). DNA-wrapping represents a more facile method to generate batches of monovalent Qdots that, in our results presented in *Chapter 4*, did not require isolation when the amount of DNA titrated into Qdots was carefully calibrated. Our work extends this approach by using DNA/RNA hybridization to target monovalent Qdots to cell surface or synaptic vesicle sites via GFP expression in the extracellular environment or vesicle lumen, respectively. Using a hybrid aptamer we designed based on a published RNA aptamer (Shui, Ozer

et al. 2012), we found that vesicle mobility was similar with our approach to previous studies (Guillaud, Dimitrov et al. 2017). Future work may extend these results. Synaptic vesicle proteins are commonly used as tags and then results are generalized to overall synaptic vesicle mobility (Lee, Jung et al. 2012, Park, Li et al. 2012, Guillaud, Dimitrov et al. 2017). However, in line with similar approaches to the study of the mobility of different proteins on the cell surface, questions remain as to the idea that different vesicle proteins may have different mobilities. This could be systematically studied using our aptamer-Qdots combined with the large array of synaptic vesicle proteins that are already available with a pHluorin-tag. For example, synaptophysin (Royle, Granseth et al. 2008), VAMP (Sankaranarayanan, De Angelis et al. 2000), and synaptotagmin (Dean, Dunning et al. 2012), among others, have all been used to study vesicle kinetics. And as with any system where proteins are overexpressed, future studies should determine differences in mobility between the 'additive' overexpression model that was used here and a knock-down/knock-out scenario (e.g. via CRISPR). The latter should be more carefully matched to endogenous levels of protein expression and thus may be more representative.

From a nanoparticle surface engineering perspective, one major line of future work which could greatly improve the end result after Qdot-wrapping with DNA is to modify the second PEG, for example, to neutralize the negative surface charges on the final product. Although our results suggest that DNA interacting with the Qdot surface will indeed sterically hinder multiple binding, after the addition of the carboxy-PEG specified by Farlow et al., the overall charge on the wrapped Qdot will still remain negative. This is problematic for any biological usage scenario, as many charged biomolecules can thus electrostatically interact with the ptDNA-Qdot. In cell culture, for example, poly-lysine is a commonly used substrate coating to increase cell adhesion, and is also positively charged - thus a significant amount of non-specific binding would be expected (Cai, Ge

et al. 2014). We find that a combination of extensively washing neurons after Qdot loading and pre-incubation of aptamer-Qdots in a serum-containing solution (4% BSA in loading media) greatly reduces the amount of non-specific binding compared to loading media alone. However, electrostatic interactions still likely result in an increase of hydrodynamic diameter after incubation in serum-containing media. As the size of Qdots must be sufficiently small to enable synaptic vesicle loading, future work should also investigate the increase in hydrodynamic diameter after contact with serum-containing and biological media and attempt to mitigate such increases.

Concluding remarks and future directions

The experiments detailed in this thesis present new ways to both study and manipulate the plasma membrane and plasma membrane-associated signaling pathways. Nanomaterials, with their small size and tailorable properties, offer an exciting new avenue to study the brain.

Ultimately, the success of any new methodology for neuroscience be determined by the ability to integrate it with other complementary tools *in vivo*. The work detailed here, suggesting that graphene has specific effects on membrane signaling, must be extended beyond *in vitro* culture systems to whole tissue. For example, myelinated axons transmit electrical signals across cm length scales within the brain. Myelin is largely composed of cholesterol – which may open the door for many interesting and novel uses of graphene. From a compliance standpoint, given the results presented here, what is the effect of graphene on myelinated structures *in vivo*? This could initially be tested by applying GNFs to whole brain or tissue slices. Transmission electron microscopy would allow high-resolution examination of myelin layers, allowing examination of the effects of GNFs on myelin at unprecedented resolution. From an engineering standpoint, could

an interaction between graphene and sterols or lipids be used to mitigate device integration issues traditionally encountered in brain implantation?

Quantum dots have played an important role in elucidating the motion of transporters, receptors, and synaptic vesicles. Monovalent conjugation may become an increasingly important design feature when designing nanoparticle probes. The work presented in *Chapter 4* builds on longstanding efforts to design production strategies that are readily learned by the average neuroscience laboratory, for example not requiring complex chemical modifications after the initial surface passivation step. Further incorporation of non-traditional tagging approaches may unlock previously unexplored targets. Although the work here we present for nanoparticle tagging is limited to CdSe/ZnS quantum dots, the approaches and design considerations presented are broadly relevant to many types of nanoparticle. For example, upconverting nanoparticles have now been demonstrated to enable optogenetic stimulation in deeper brain regions than previously possible with infrared light delivery only. Ultimately, orthogonal advances are needed to truly enable practical single-particle tracking in deep brain regions: ultra-small nanoparticles that better diffuse, highly specific and long-term stable tags, methods to ensure clearance of non-bound particles, and non-invasive strategies that permit deep brain light delivery.

In conclusion, the work presented in this thesis highlights new potential for nanomaterials in neuroscience or cell signaling applications. Both acute treatment with flakes of graphene and chronic growth on graphene result in specific changes to membrane packing, which result in altered cell signaling. New methods for targeting nanomaterials such as quantum dots to different local sites will yield new insights into the role that protein diffusion or vesicle movement plays in normal physiological function *in vivo*. Richard Feynman's eponymous statement 'there's plenty of room at the bottom' is as true for neuroscience as for any field; some of the smallest features in

the brain, synaptic connections, which play a fundamental role in communication between cells, are of a size well-suited to these ‘bottom-dwelling’ tools.

References

Aldieri, E., I. Fenoglio, F. Cesano, E. Gazzano, G. Gulino, D. Scarano, A. Attanasio, G. Mazzucco, D. Ghigo and B. Fubini (2013). "The Role of Iron Impurities in the Toxic Effects Exerted by Short Multiwalled Carbon Nanotubes (MWCNT) in Murine Alveolar Macrophages." Journal of Toxicology and Environmental Health, Part A **76**(18): 1056-1071.

Cai, E., P. Ge, S. H. Lee, O. Jeyifous, Y. Wang, Y. Liu, K. M. Wilson, S. J. Lim, M. A. Baird, J. E. Stone, K. Y. Lee, M. W. Davidson, H. J. Chung, K. Schulten, A. M. Smith, W. N. Green and P. R. Selvin (2014). "Stable small quantum dots for synaptic receptor tracking on live neurons()." Angewandte Chemie (International ed. in English) **53**(46): 12484-12488.

Castagnola, V., W. Zhao, L. Boselli, M. C. Lo Giudice, F. Meder, E. Polo, K. R. Paton, C. Backes, J. N. Coleman and K. A. Dawson (2018). "Biological recognition of graphene nanoflakes." Nature Communications **9**(1): 1577.

Dean, C., F. M. Dunning, H. Liu, E. Bomba-Warczak, H. Martens, V. Bharat, S. Ahmed, E. R. Chapman and P. Brennwald (2012). "Axonal and dendritic synaptotagmin isoforms revealed by a pHluorin-syt functional screen." Molecular Biology of the Cell **23**(9): 1715-1727.

Farlow, J., D. Seo, K. E. Broaders, M. Taylor, Z. J. Gartner and Y.-w. Jun (2013). "Exclusive formation of monovalent quantum dot imaging probes by steric exclusion." Nature methods **10**(12): 1203-1205.

Fischer, R. A., Y. Zhang, M. L. Risner, D. Li, Y. Xu and R. M. Sappington (2018). "Impact of Graphene on the Efficacy of Neuron Culture Substrates." Advanced Healthcare Materials **7**(14): 1701290.

Guillaud, L., D. Dimitrov and T. Takahashi (2017). "Presynaptic morphology and vesicular composition determine vesicle dynamics in mouse central synapses." eLife **6**: e24845.

Howarth, M., W. Liu, S. Puthenveetil, Y. Zheng, L. F. Marshall, M. M. Schmidt, K. D. Wittrup, M. G. Bawendi and A. Y. Ting (2008). "Monovalent, reduced-size quantum dots for imaging receptors on living cells." Nature methods **5**(5): 397-399.

Huang, P., D. Nedelcu, M. Watanabe, C. Jao, Y. Kim, J. Liu and A. Salic (2016). "Cellular Cholesterol Directly Activates Smoothened in Hedgehog Signaling." Cell **166**(5): 1176-1187.e1114.

Kitko, K. E., T. Hong, R. M. Lazarenko, D. Ying, Y.-Q. Xu and Q. Zhang (2018). "Membrane cholesterol mediates the cellular effects of monolayer graphene substrates." Nature Communications **9**(1): 796.

Lee, S., K. J. Jung, H. S. Jung and S. Chang (2012). "Dynamics of Multiple Trafficking Behaviors of Individual Synaptic Vesicles Revealed by Quantum-Dot Based Presynaptic Probe." PLOS ONE **7**(5): e38045.

Lee, Y. K., E.-J. Choi, T. J. Webster, S.-H. Kim and D. Khang (2015). "Effect of the protein corona on nanoparticles for modulating cytotoxicity and immunotoxicity." International Journal of Nanomedicine **10**: 97-113.

Liu, H. Y. and X. Gao (2011). "Engineering Monovalent Quantum Dot−Antibody Bioconjugates with a Hybrid Gel System." Bioconjugate Chemistry **22**(3): 510-517.

Lo Giudice, M. C., L. M. Herda, E. Polo and K. A. Dawson (2016). "In situ characterization of nanoparticle biomolecular interactions in complex biological media by flow cytometry." Nature Communications **7**: 13475.

Luchetti, G., R. Sircar, J. H. Kong, S. Nachtergaele, A. Sagner, E. F. X. Byrne, D. F. Covey, C. Siebold and R. Rohatgi (2016). "Cholesterol activates the G-protein coupled receptor Smoothened to promote Hedgehog signaling." eLife **5**: e20304.

Lundqvist, M., J. Stigler, T. Cedervall, T. Berggård, M. B. Flanagan, I. Lynch, G. Elia and K. Dawson (2011). "The Evolution of the Protein Corona around Nanoparticles: A Test Study." ACS Nano **5**(9): 7503-7509.

Pampaloni, N. P., M. Lottner, M. Giugliano, A. Matruglio, F. D'Amico, M. Prato, J. A. Garrido, L. Ballerini and D. Scaini (2018). "Single-layer graphene modulates neuronal communication and augments membrane ion currents." Nature Nanotechnology **13**(8): 755-764.

Parameswaran, R., J. L. Carvalho-de-Souza, Y. Jiang, M. J. Burke, J. F. Zimmerman, K. Koehler, A. W. Phillips, J. Yi, E. J. Adams, F. Bezanilla and B. Tian (2018). "Photoelectrochemical modulation of neuronal activity with free-standing coaxial silicon nanowires." Nature Nanotechnology **13**(3): 260-266.

Park, H., Y. Li and R. W. Tsien (2012). "Influence of Synaptic Vesicle Position on Release Probability and Exocytotic Fusion Mode." Science (New York, N.Y.) **335**(6074): 1362-1366.

Pluhackova, K., S. Gahbauer, F. Kranz, T. A. Wassenaar and R. A. Böckmann (2016). "Dynamic Cholesterol-Conditioned Dimerization of the G Protein Coupled Chemokine Receptor Type 4." PLOS Computational Biology **12**(11): e1005169.

Prasanna, X., A. Chattopadhyay and D. Sengupta (2014). "Cholesterol Modulates the Dimer Interface of the β2-Adrenergic Receptor via Cholesterol Occupancy Sites." Biophysical Journal **106**(6): 1290-1300.

Rosa, P. and A. Fratangeli (2010). "Cholesterol and synaptic vesicle exocytosis." Communicative & Integrative Biology **3**(4): 352-353.

Royle, S. J., B. Granseth, B. Odermatt, A. Derevier and L. Lagnado (2008). "Imaging pHluorin-based probes at hippocampal synapses." Methods in molecular biology (Clifton, N.J.) **457**: 293-303.

Sankaranarayanan, S., D. De Angelis, J. E. Rothman and T. A. Ryan (2000). "The Use of pHluorins for Optical Measurements of Presynaptic Activity." Biophysical Journal **79**(4): 2199-2208.

Sengupta, D., X. Prasanna, M. Mohole and A. Chattopadhyay (2018). "Exploring GPCR–Lipid Interactions by Molecular Dynamics Simulations: Excitements, Challenges, and the Way Forward." The Journal of Physical Chemistry B **122**(22): 5727-5737.

Shui, B., A. Ozer, W. Zipfel, N. Sahu, A. Singh, J. T. Lis, H. Shi and M. I. Kotlikoff (2012). "RNA aptamers that functionally interact with green fluorescent protein and its derivatives." Nucleic Acids Research **40**(5): e39-e39.

Simons, K. and R. Ehehalt (2002). "Cholesterol, lipid rafts, and disease." The Journal of Clinical Investigation **110**(5): 597-603.

Thiele, C., M. J. Hannah, F. Fahrenholz and W. B. Huttner (1999). "Cholesterol binds to synaptophysin and is required for biogenesis of synaptic vesicles." Nature Cell Biology **2**: 42.

Uddayasankar, U., Z. Zhang, R. T. Shergill, C. C. Gradinaru and U. J. Krull (2014). "Isolation of Monovalent Quantum Dot–Nucleic Acid Conjugates Using Magnetic Beads." Bioconjugate Chemistry **25**(7): 1342-1350.

Veliev, F., A. Briançon-Marjollet, V. Bouchiat and C. Delacour (2016). "Impact of crystalline quality on neuronal affinity of pristine graphene." Biomaterials **86**: 33-41.

Wang, R., M. Shi, B. Brewer, L. Yang, Y. Zhang, D. J. Webb, D. Li and Y.-Q. Xu (2018). "Ultrasensitive Graphene Optoelectronic Probes for Recording Electrical Activities of Individual Synapses." Nano Letters **18**(9): 5702-5708.